Fundamental Processes in Laser Drilling and Welding

by

Mark Randall Olfert

A thesis

presented to the University of Waterloo

in fulfilment of the

thesis requirement for the degree of

Doctor of Philosophy

in

Physics

Waterloo, Ontario, Canada, 1999

©Mark Randall Olfert 1999

National Library of Canada
Acquisitions and Bibliographic Services
395 Wellington Street
Ottawa ON K1A 0N4
Canada

Bibliothèque nationale du Canada
Acquisitions et services bibliographiques
395, rue Wellington
Ottawa ON K1A 0N4
Canada

Your file Votre référence

Our file Notre référence

The author has granted a non-exclusive licence allowing the National Library of Canada to reproduce, loan, distribute or sell copies of this thesis in microform, paper or electronic formats.

The author retains ownership of the copyright in this thesis. Neither the thesis nor substantial extracts from it may be printed or otherwise reproduced without the author's permission.

L'auteur a accordé une licence non exclusive permettant à la Bibliothèque nationale du Canada de reproduire, prêter, distribuer ou vendre des copies de cette thèse sous la forme de microfiche/film, de reproduction sur papier ou sur format électronique.

L'auteur conserve la propriété du droit d'auteur qui protège cette thèse. Ni la thèse ni des extraits substantiels de celle-ci ne doivent être imprimés ou autrement reproduits sans son autorisation.

0-612-51218-5

Canada

Abstract

Laser penetration processing of a variety of transparent and translucent dielectrics was carried out under varying gravitational levels. Real time differential holographic interferometry was used to measure heat transfer in laser drilling of fused quartz in zero and normal gravity. Measurements were compared with a numerical model based on a prolate spherical coordinate frame. The model agrees well with experiments close to the surface, but overestimates the extent of the heat transport deeper into the quartz.

Modulated beam intensity drilling of liquids is studied. Frequency dependent structures are observed, particularly in glycerol drilling which exhibit transitions to extremely stable resonant states. A potential mechanism for this resonance is presented.

Laser drill hole initiation in glycerol and acrylic is studied. A parametric energy conservation model is developed and found to be well suited as a laser beam intensity diagnostic.

CW Laser drilling of glycerol-water mixtures and gelatin is studied and dynamical behaviour is discussed in terms of material property differences in viscosity and environmental factors associated with gravity.

Table of Contents

Chapter One – Introduction 1

1.1. The Laser as a Tool....1

1.2. Rationale for Study....3

1.2.1. Industrial Significance of Penetration Processing....3

1.2.2. Variable Gravity Experimentation....9

1.3. Beam Processing Overview....10

1.4. Literature Survey: Process Models....15

1.4.1. Energy Conservation Based Models....15

1.4.2. Solid Phase Models....18

1.4.3. Multi-phase Models....21

1.5. Research Thrust....29

1.5.1. Goals of Research....29

1.5.2. Appropriate Materials....32

1.5.3. Structure of Thesis....34

Chapter Two - Experimental Summary 36

2.1. Data Acquisition Platforms....36

2.1.1. KC-135 Flying Laboratory....36

2.1.2. LAMPS Test Bed....40

2.1.3. Industrial Laser Laboratory....40

2.2. Diagnostic Systems....47

2.2.1.Optical Diagnostics....47

2.2.2. Acoustic Recording....54

2.2.3. Post Processing of Data....55

2.3. Experimental Data Set....56

Chapter Three - Solids: Fused Quartz Holography 60

3.1. Motivation....60

3.2. Selection of Interferograms for Analysis....64

3.3. Process Models....70

3.3.1. Choice of Coordinate System....70

3.3.2. General Process Model....74

3.3.3. Numerical Results....76

3.4. Experimental Temperature Distribution....83

3.5. Comparison of Results....89

3.5.1. Comparison between Numerical and Experimental Results....89

3.5.2. Effect of Boundary Conditions.....92

Chapter Four – Laser Drilling of Liquids with a Modulated Beam 93

4.1. Initial Experiments.....94

4.1.1. Experimental Description.....94

4.1.2. Initial Experiments – Glycerol.....98

4.1.3. Initial Experiments- Water.....104

4.2. Experimental Results.....107

4.2.1. Experimental Description.....107

4.2.2. Drilling Glycerol - Structural Modes.....109

4.2.3. Drilling Water – Structural Modes.....117

4.3. Acoustic Data.....122

4.3.1. Acoustic Data Processing.....122

4.3.2. Spectral Analysis of Glycerol Emission.....129

4.3.3. Spectral Analysis of Water Emission.....148

4.4. Process Models.....153

4.4.1. Geometric Relationships to Modulation Frequency.....154

4.4.2. Cylindrical Cavity Collapse Model.....161

4.4.3. Two Temperature Parameter Model.....168

4.4.4. Conical Cavity Collapse Model.....171

Chapter Five – CW Laser Drilling Experiments 175

5.1. Drill Hole Initiation.....176

5.1.1. Glycerol.....176

5.1.2. Acrylic.....183

5.2. Glycerol Drill Hole Dynamics.....189

5.3. Fluid Motion Phenomena.....201

5.3.1. 100% Water.....202

5.3.2. 66% Glycerol – 34% Water Mixture.....202

5.3.3 . 100% Glycerol.....206

5.3.4. Gelatin.....207

Chapter Six – Discussion 212

6.1. Holographic Results.....212

6.2. Laser Drilling With a Modulated Beam.....214

6.3. Initiation of the Drill Hole.....217

6.4. Dynamic Behaviour.....219

6.4.1. Drill Hole Dynamics.....219

6.4.2. Fluid Flow.....220

6.5. Improvements and Further Opportunities.....222

6.5.1. Holographic Imaging and Fringe Analysis.....222

6.5.2. Modulated Beam Drilling.....227

6.5.3. Drill Hole Dynamics.....229

6.6. Closing Remarks.....230

References **233**

Appendix A: Holographic Data Reduction to Temperature Field Information **239**

Appendix B: Prolate Spheroidal Coordinates **247**

Appendix C: Analytical Solution of Heat Conduction in Prolate Spheroidal Coordinates **250**

List of Figures

1.1. Schematic comparison of conventional (multi pass) arc welding techniques to that of laser penetration processing for butt welding of thick plate steel.

1.2 Laser welded reaction annulus for the Chrysler 45RFE transmission. The parts are welded at an average speed of 100mm/s with a 6kW CO_2 laser. With a weld circumference of 11.5 inches, these parts weld in roughly three seconds. (photo courtesy of TRIAM Powerlasers)

1.3 Laser welded door inner for the Chrysler B-van. The hinge end of the door is comprised of 1.6mm galvanneal which is welded to 0.8mm galvanneal. (photo courtesy of TRIAM Powerlasers)

1.4 Parameter matrix associated with laser materials processing over varying intensity (temperature) regimes. The listed parameters are emissivity (ε), absorption coefficient (α), diffusivity (κ), heat capacity (C_p), surface tension (σ), liquid density (ρ), viscosity (η), latent heat of fusion (ΔH_f), and latent heat of vapourisation (ΔH_v). Subscripts refer to solid (s) liquid (l) and vapour (v) phases.

1.5. Typical behaviour of dimensionless ablation pressure and surface tension pressure as a function of the normalised keyhole radius taken from Kroos et al [24]. p is the excess pressure, p_o is the ambient (atmospheric) pressure, a is the keyhole radius, and r_o is the equilibrium keyhole radius.

1.6 Illustration of nature of keyhole wall motion assumed in the keyhole dynamic model of Klein et al [26].

1.7 Side profiles of fusion zones in laser welded steel (A), laser welded paraffin (B), and laser drilling in gelatin (C).

2.1. NASA KC-135 performing microgravity maneuvers over the Gulf of Mexico. The 45° nose up attitude implies that the pane is just commencing the low gravity portion of the maneuver. (Photo courtesy of NASA)

2.2 Schematic representation of ideal flight path of aircraft which generates simulated low and high g environments. Typical flights consist of 40 parabolic maneuvers with each low gravity period lasting approximately 25 seconds.

2.3 Accelerometer profiles of x, y, and z acceleration levels aboard the KC-135 taken over roughly three parabolic maneuvers. The z direction is taken as into the floor of the aircraft, the y direction is along

the fuselage, and the x direction is across the fuselage, parallel to the floor. Accelerations are normalised to g=9.8 m/s^2.

2.4. The Lamps test bed shown mounted aboard the NASA KC-135. Shown from left to right are the power supply support module (PSSM), the laser enclosure module (LEM), and the electronic equipment support module (EESM). Photo courtesy of NASA Johnson Space Center.

2.5 a. Schematic representation of components and beam paths on the upper level optical breadboard. The downward direction of the processing beam is obtained via two steering mirrors from the upward direction exiting the lower level breadboard.

2.5 b. Schematic representation of components and beam paths on the lower optical breadboard inside the LEM. With the exception of the processing area, the CO_2 laser beam is confined within aluminum tubing for safety purposes.

2.6. Spatial beam profile from Lumonics VFA-1700 laser (after Gu [36]).

2.7. Diagram illustrating essential components of system configured for modulated beam drilling of fluids. For electronically modulated beam experiments, the chopper assembly was removed from the beam path.

2.8. Schematic illustration indicating general imaging geometry with respect to processing beam and work piece.

2.9. Simplified top view of the holographic interferometry module showing incidence of both object and reference beams. The CCD camera records the subsequent real time interference patterns to video tape. Processing laser incidence would be into the page in the center of the work piece.

2.10. Two holographic frames of acrylic from a 2 second duration drill highlighting the evolution of the interference fringes and hence the temperature field. The times marked on the images are relative to the beginning of the drill.

2.11. Generation of Moiré fringes (spaced 'P' apart) by rotation of two Ronchi rulings having spacing 'd' through an angle of 'θ' with respect to each other.

2.12. Before and after images of the Moiré deflectometry video of the same acrylic drill referred to in the previous figure. The "after" image corresponds to the "10s" holographic image.

3.1. Optical transmission in one inch thick cubes of soda lime glass (A) and fused quartz (B).

3.2. Comparison of drill hole profiles during normal (A) and low (B) gravity drilling of fused quartz. The surface of the quartz is coincident with the top of the length scale. Dark regions of cooler material evident in normal gravity drilling are quite dynamic and tend to migrate during the drilling.

3.3. HAZ in soda lime glass (A) compared to that in fused quartz (B). The HAZ in the fused quartz image is not visible at this magnification but extends less than 0.5 mm beyond the cavity wall.

3.4: Interferograms obtained during laser drilling of fused quartz in low gravity (corresponding to experiment 1 of *Table* 3.1).

3.5: Interferograms obtained during laser drilling of fused quartz in normal gravity (corresponding to experiment 2 of *Table* 3.1).

3.6: Interferograms obtained during laser drilling of fused quartz in low gravity (corresponding to experiment 3 of *Table* 3.1). In this case, the laser was directed into a preexisting hole.

3.7. Semi-minor axes of four outermost fringes of interferogram plotted against time for a 3 second drill into fused quartz. The vertical line through the data indicates the point at which the laser was turned off.

3.8. Semi-major axes of four outermost fringes of interferogram plotted against time for a 3 second drill into fused quartz. The vertical line through the data indicates the point at which the laser was turned off.

3.9. Calculated semi-major focal length from *Equation* 3.1 and the data of the previous two figures. The measured drill hole depth is marked by the horizontal line and measures 0.92 cm.

3.10. Illustration of distribution of prolate spheroidal finite element mesh in Cartesian space. Note the increased density of grid points near the tip of the prolate spheroidal cavity.

3.11 Results of numerical simulation corresponding to t^*=0.015 (t=2 seconds). The isotherm spacing is ΔT^*=0.001.

3.12 Results of numerical simulation corresponding to t^*=0.038 (t=5 seconds). The isotherm spacing is ΔT^*=0.001.

3.13 Isotherm field generated from holographic data during drilling of fused quartz at t=2 s under normal gravity conditions, corresponding to an initiation type hole.

3.14 Isotherm field generated from holographic data during drilling of fused quartz at t=5 s under normal gravity conditions, corresponding to an initiation type hole.

3.15 Isotherm field generated from holographic data during drilling of fused quartz at t=2 s under low gravity conditions, corresponding to an initiation type hole.

3.16 Isotherm field generated from holographic data during drilling of fused quartz at t=5 s under low gravity conditions, corresponding to an initiation type hole.

3.17 Isotherm field generated from holographic data during drilling of fused quartz at t=5 s under normal gravity conditions, into an existing hole.

3.25 Radial extent of heating measured at the surface after 2 seconds of drilling, compared to results of numerical model.

3.26 Radial extent of heating measured at the surface after 5 seconds of drilling, compared to results of numerical model. In the legend, "init" and "pre-" differentiate initiation from pre-drilled hole experiments.

4.1: Seven consecutive frames of 100% glycerol with a 200 w (pre chopper) incident power and a chopping frequency of 2750 Hz.

4.2 Frame average of 255 individual images in drilling 100% glycerol under the same conditions as in *Figure* 4.1. The grayscale average is on the left (A), and an edge enhanced version is shown on the right.

4.3. Typical images of drill hole structure in glycerol acquired during CW drilling with a laser output of 50 watts. The images A through G are in no particular order. Note the axial symmetry and smooth cavity walls.

4.4 255 frame average of 50 watt CW 100% glycerol drill (A) and associated edge enhanced image (B).

4.5. Six frame averaged images (255 frames/image) for drilling of glycerol with an average of 50 watts. As with water, no strong frequency dependence on drill hole structure can be identified.

4.6. Frame averages in drilling glycerol at an average incident power of 100 w at chopper frequencies from 1000 to 2760 Hz. A smooth transition in structure can be seen taking place going from high to low frequency with evidence of the onset of the transition starting as high as 2660 Hz.

4.7. Eight consecutive frames at 100w average incident laser power in glycerol at a chopper frequency of 1300 Hz. This is in contrast to the appearance of the frame by frame structure seen in the both the higher chopper frequency sequence shown in *Figure* 4.1 and the CW sequence of *Figure* 4.3.

4.8. Frame averaged images taken at different chopper frequencies at 50 watts. (water)

4.9. Frame averages and associated edge enhanced images during CW drilling of water. A large entrapped bubble is present at 60 watts, while only small bubbles are seen at 100 watts.

4.10. Structures typical of stable resonance condition. The images were obtained with 25 watts average power incident on glycerol at modulation frequencies of 1500 Hz (A), 1700 Hz (B), 1900 Hz (C), and 2250 Hz (D).

4.11. Chopper modulated glycerol drilling at 2 kHz with 54 watts incident power. Note the distortion of even the isolated bubbles in images B and C.

4.12. Evolution of structural envelope leading up to resonance at low intensity ($\sim 7\times10^4 w/cm^2$) in 100% glycerol using a mechanically chopped beam. A resonance is clearly evident in the 1.5kHz average.

4.13. Evolution of structural envelope leading up to resonance at medium intensity ($\sim 1.5\times10^5 w/cm^2$) in 100% glycerol using a mechanically chopped beam.

4.14. Evolution of structural envelope leading up to resonance at high intensity (~3×10^5w/cm^2) in 100% glycerol using a mechanically chopped beam.

4.15. Evolution of structural envelope through resonance to destabilisation at low intensity (~7×10^4w/cm^2) in 100% glycerol using a mechanically chopped beam.

4.16. Evolution of structural envelope through resonance to destabilisation at medium intensity (~1.5×10^5w/cm^2) in 100% glycerol using a mechanically chopped beam.

4.17. Evolution of structural envelope through resonance to destabilisation at high intensity (~3×10^5w/cm^2) in 100% glycerol using a mechanically chopped beam.

4.18. Frame averages of water at 70 watts at modulation frequencies between 0 - 3.5Khz.

4.19. Single frame images of "characteristic" profiles for 70 watt drilling under CW conditions (A) and at 3.5Khz (B).

4.20 Frequency dependence of frame averages for modulated beam drilling at a beam power of 120watts in water.

4.21 FFT spectrum of 475Hz chopper modulated drilling in 100% glycerol. The raw composite spectrum is shown in dB form (A), and amplitude ratio form (B). The refined spectrum with electronic and background noise removed (C).

4.22. Detail of *Figure* 4.21c. Note that the spectrum shows several peaks aside from the fundamental frequency associated with the beam modulation at 475Hz.

4.23 Averaged FFT spectrum of 10 seconds of electronic noise. Some frequencies of the more dominant peaks are marked on the plot.

4.24. Spectra of CW drill carried out in glycerol at 50 w average power over a 15 kHz bandwidth (A), and a three kHz bandwidth (B).

4.25 Individual FFT spectra comprising the averaged 50 w CW glycerol drilling spectrum shown in *Figure* 4.24.

4.26. Comparison of broad band emission observed during CW drilling of 100% glycerol at 54, 108, and 212 watts.

4.27. Spectral behaviour of 25watt average power chopped drilling of glycerol leading up to structural resonance condition. The estimated ratio of observed structural conditions is shown at the right of each spectrum. Modulation frequencies are shown in the upper right hand corner of each spectrum, and peaks which extend beyond the scale limits have their respective maxima marked beside them.

4.28. Spectral behaviour of 54 watt average power chopped drilling of glycerol leading up to structural resonance condition. The estimated ratio of observed structural conditions is shown at the right of each spectrum. Modulation frequencies are shown in the upper right hand corner of each spectrum, and peaks which extend beyond the scale limits have their respective maxima marked beside them.

4.29 Spectral behaviour of 106 watt average power chopped drilling of glycerol leading up to structural resonance condition. The estimated ratio of observed structural conditions is shown at the right of each spectrum. Modulation frequencies are shown in the upper right hand corner of each spectrum, and peaks which extend beyond the scale limits have their respective maxima marked beside them.

4.30 Spectral behaviour of 25 watt average power chopped drilling of glycerol from resonant through to post resonant structural behaviour. The estimated ratio of observed structural conditions is shown at the right of each spectrum. Modulation frequencies are shown in the upper right hand corner of each spectrum, and peaks which extend beyond the scale limits have their respective maxima marked beside them.

4.31 Spectral behaviour of 54 watt average power chopped drilling of glycerol from resonant through to post resonant structural behaviour. The estimated ratio of observed structural conditions is shown at the right of each spectrum. Modulation frequencies are shown in the upper right hand corner of each spectrum, and peaks which extend beyond the scale limits have their respective maxima marked beside them.

4.32. Spectral behaviour of 106 watt average power chopped drilling of glycerol from resonant through to post resonant structural behaviour. The estimated ratio of observed structural conditions is shown at the right of each spectrum. Modulation frequencies are shown in the upper right hand corner of each spectrum, and peaks which extend beyond the scale limits have their respective maxima marked beside them.

4.33. Raw signal (upper) and false colour map of temporal evolution of FFT spectrum (lower) during an electronically modulated drill in glycerol. The modulation frequency was 874 Hz and the average power was 106 watts. The colour key for the relative sound level is shown at the right of the figure.

4.34. FFT Spectra of pulsed beam (241Hz) glycerol drilling at 56 and 102 watts average power. The estimated percentage of observed structural resonance is shown in the legend.

4.35. FFT Spectra of Pulsed beam (465Hz) glycerol drilling ranging from 26 through to 175 watts average power. The estimated percentage of observed structural resonance is shown in the legend.

4.36. FFT Spectra of Pulsed beam (607Hz) glycerol drilling ranging from 22 through to 132 watts average power. The estimated percentage of observed structural resonance is shown in the legend.

4.37. FFT Spectra of pulsed beam (875Hz) glycerol drilling ranging from 24 through to 140 watts average power. The estimated percentage of observed structural resonance is shown in the legend.

4.38. Average acoustic emission spectrum for 30 second (accumulated over 3 experiments) duration CW water drilling at an average power of 70 watts over the 0-16kHz band.

4.39. Average acoustic emission spectrum for 30 second (accumulated over 3 experiments) duration CW water drilling at an average power of 70 watts over the 0-5kHz band.

4.40. Summary of acoustic spectra for chopped beam drilling of water over a chopping frequency range from 0.12 – 3.5kHz. FFT data is presented over the 0 – 16 kHz band.

4.41. Summary of acoustic spectra for chopped beam drilling of water over a chopping frequency range from 0.12 – 3.5kHz. FFT data is presented over the 0 – 5 kHz band.

4.42 Bubble diameter vs depth for low intensity modulated beam excitation of glycerol. Least squares fits show the general depth versus diameter trend of the data.

4.43 Bubble diameter vs depth for medium intensity modulated beam excitation of glycerol. Least squares fits show the general depth versus diameter trend of the data.

4.44 Bubble diameter vs depth for high intensity modulated beam excitation of glycerol. Least squares fits show the general depth versus diameter trend of the data.

4.45 Radius vs. frequency for selected spherical harmonic modes associated with surface waves on a spherical bubble of radius R in glycerol generated from *Equation* 4.6. The numbers adjacent to the curves represent the "l'th" state of the spherical harmonic Y_m^l. The resonant state data is overlaid on the spherical harmonic curves, extrapolated from a bubble depth of 3.5mm.

4.46 Bubble radius vs. inverse frequency for bubbles located at a depth of 3.5mm. (Data was obtained by interpolation of data from *Figures* 4.42 to 4.44 through best fit lines to a depth of 3.5mm.)

4.47 Inverse of cavity closing times assuming fundamental mode for water and glycerol based on initial radii of 0.10, 0.15, and 0.20mm (shown in the legend). The solid lines pertain to glycerol while the dashed lines are with for water.

4.48 Comparison of predicted fundamental mode frequencies for collapse of a hole in glycerol having an initial radius of 0.15mm in the presence (D>0) and absence (D=0) of viscosity.

4.49 Images of water drilling (A) and the early stages of glycerol drilling (B) showing tapered structure. Limitations in the video resolution make it impossible to determine the smallest diameter of the drill holes accurately.

4.50 Schematic illustration of drill hole wall model assuming a small linear taper tending towards a smaller diameter root.

5.1. Hole depth vs. time for a CO_2 laser power of 65 Watts incident on solid glycerol cooled to -89°C.

5.2. Drill hole depth vs. time removing the time offset. Curve fit lines are shown on the plot.

5.3 Hole depth vs. time for 75Watt drilling of liquid glycerol in normal gravity. The solid line represents the results of a curve fit to the data using *Equation* 5.6, where in this case α is held constant at 250 m^{-1}.

5.4. Depth vs. time for CO_2 laser drilling of acrylic at 50-60 Watts. Two sets of data have been used.

5.5. Depth vs. time relationships with curve fits for acrylic drilling with LAMPS test bed laser.

5.6. Initial velocity-power relationship for the LAMPS testbed laser. A data point from the Lumonics VFA 1700 laser is also included on the graph.

5.7. Intensity vs. meter power for VFA1700 and CRF1200 lasers.

5.8. Development of drill hole structure in 100% glycerol. Drilling was performed in normal gravity at 80Watts.

5.9 Typical locations of pixel line segments used to generate temporal line profiles.

5.10. Binarized drill hole radius profiles (vertical dimension) versus time (horizontal) for drilling of glycerol at a laser power of 40 Watts in normal gravity. The profiles are normalised to the maximum depth throughout the entire drill. The duration of the time base is approximately 0.80s.

5.11. Binarized drill hole radius profiles (vertical dimension) versus time (horizontal) drilling of glycerol at a laser power of 80 Watts in normal gravity. The profiles are normalised the maximum depth throughout the entire duration of the drilling.

5.12. Binarized drill hole radius profiles (vertical dimension) versus time (horizontal) for drilling of glycerol at a laser power of 80 Watts in low gravity. The profiles are normalised to the maximum depth throughout the entire duration of the drilling.

5.13. Five consecutive frames of low gravity glycerol drilling captured at the 1/30s framing rate of standard NTSC video.

5.14 Frame average of water drilling in normal gravity with liquid flow lines overlaid on the image.

5.15 Sequences of interferograms comparing fluid flow between drilling in normal and zero gravity of a 66% glycerol - 34% water mixture

5.16 Cumulative frame average of several seconds drilling in normal gravity in 100% glycerol liquid. Bubbles suspended within the fluid trace out their paths, revealing the widespread bulk fluid motion induced by the pumping action of the drill hole. The arrows indicate the direction of the flow.

5.17 Drilling of gelatin at 0 and 1.8-g. Laser power: 70 Watts.

5.18 Schematic illustration of drilling at low and high gravity showing the differing flow patterns playing a role in shaping the molten pool.

5.19 Section view of twin toroidal steady state flow pattern established during laser drilling of gelatin in the presence of gravity.
6.1 Distorted fringe pattern associated with mechanical vibrations induced in the system during the high-g maneuver.

6.2 Holographic interferogram obscured by heavy contamination from dust particles.

6.3 Viscosity dependence of glycerol – water mixtures (from [46]). Low temperature values are strongly effected by addition of water.

A.1. Simple one dimensional model of material undergoing expansion as a result of uniform heating.

A.2. Diagram showing geometry of a light ray traversing an axisymmetric index of refraction (temperature) disturbance.

B.1. Contours associated with constant η prolate spheroids, and constant θ hyperboloids, viewed in the *x-z* plane.

List of Tables

1.1 Materials used throughout the course of this research.

2.1: Summary of experimental diagnostics used for each material.

2.2: Summary of processing conditions investigated for each material.

3.1: Experimental conditions for six holographic frames chosen for thermal analysis.

3.2. Fourier time equivalents for two and five second holes in fused quartz.

4.1. Chopped laser drilling of Glycerol.

4.2. Pulsed laser drilling of glycerol.

4.3: Theoretical and measured electronic beam modulation frequencies associated with the VFA-1700 laser.

4.4 Material properties for water from 300 - 372K [46].

4.5 Material properties for glycerol from 300 - 560K [46].

4.6. Predictions of cylindrical collapse model calculations (*Equations* 4.6 and 4.12) using low temperature values for bulk properties and high temperature values for surface properties.

5.1. Curve fit results for solid glycerol drill hole initiation.

5.2. Curve fit estimates of v_o and α for the data of *Figure* 5.5

5.3. Initial velocity for data of *Figure* 5.5.

5.4. Material constants for acrylic (after Miyamoto et al [51]).

List of Symbols

Symbol	Definition	Units
I	Intensity	W/m^2
T	Temperature	°C
a	Steady state keyhole radius (Chapter 1)	mm
c_p	Specific heat at constant pressure	J/kg°C
ρ	Liquid density	kg/m^3
η	Viscosity (Chapter1)	Pa/s
ΔH_f	Latent heat of fusion	J/kg
ΔH_v	Latent heat of vapourisation	J/kg
α	Absorption coefficient	-
κ	Thermal diffusivity	m^2/s
ε	Emissivity	-
r	radius of the drill hole	mm
θ	Angular cylindrical coordinate	radians
γ	Surface tension coefficient	kg/m
P	Coupled laser power	Watts
P_o	Incident laser power	Watts
v	Velocity	m/s
h	Weld depth	mm
K	Thermal conductivity	W/m
U	Normalised velocity	-
Q	Normalised incident power density	-
ω_{nk}	Eigenfrequencies of oscillation	s^{-1}
$\alpha(t)$	radial perturbation term (Chapter1)	mm
$\Delta\tau$	Dimensionless drill hole closing time (Chapter1, 4)	-
A	Dimensionless drill hole radius	-
C	Dimensionless melt pool extent	-
D	Dimensionless viscosity	-
a	Semi-major focal length	mm

b	Semi-major axis	mm
c	Semi-minor axis	mm
η	Prolate spheroidal radial coordinate (Chapter 3)	-
θ	Prolate spheroidal axial angular coordinate from z-axis	radians
Ψ	Prolate spheroidal azimuthal angular coordinate	radians
T^*	Dimensionless temperature	-
Δt^*	Dimensionless time (Chapter 3)	-
L	Sound level	dB
L_C	Composite sound level	dB
L_B	Background sound level	dB
L_E	Electronic noise sound level	dB
A_C	Composite signal amplitude	relative
A_D	Drilling signal amplitude	relative
A_B	Background signal amplitude	relative
A_E	Electronic noise signal amplitude	relative
Δp	Excess pressure	Pa
τ	Dimensionless time (Chapter 4)	-
ν	Kinematic viscosity	Pa/s
$t_o(z)$	Drill hole collapse time (Chapter 4)	s
$f_o(z)$.	Drill hole fundamental mode frequency (Chapter 4)	s^{-1}

The University of Waterloo requires the signatures of all persons using or photocopying this thesis. Please sign below, and give address and date.

Chapter One

Introduction

1.1. The Laser as a Tool

Since the first laser, based on excitation of a ruby rod was developed in 1960 [1], lasers have played an ever increasing role in society. Today, many different lasers exist using a wide variety of active media and covering the spectrum from the infrared to the ultraviolet. The unique properties associated with a laser beam differentiate it from other sources of light and lend lasers to a multitude of applications. Once depicted in fiction only as "death rays" or "laser blasters", lasers have gained widespread use in areas such

as communications, materials processing, spectroscopy, home entertainment, and process monitoring and many others.

In the broad spectrum of laser applications, the work described in this thesis falls within the domain of materials processing. Even this sub domain of laser applications is vast however, and entire texts have been devoted to the subject [2-12]. Any laser assisted process which results in some modification of a target material is a form of laser materials processing, with the vast majority involving thermally driven processes[1].

Within the context of thermally driven materials processing, a materials processing laser must provide adequate intensity to generate the desired thermal changes in the target. What determines adequate intensity is dependent on the material, the laser/material coupling coefficient, and the type of material processing operation. The work in this thesis falls specifically into the subset known as penetration processing. As the name implies, this type of processing relies on a laser intensity which is high enough to vapourise a cavity and hence penetrate deeply into the target material. A suitable laser system for the purpose of this research is the well established CO_2 gas laser.

Long known for its high beam intensity capability, the CO_2 laser operates in the

[1]In fact, there are methods of laser materials processing which generate essentially no thermal damage. Ultraviolet lasers such as Excimer lasers can have sufficient photon energy to break bonds in many organic compounds and thus, material can be removed via photochemical ablation as opposed to thermal vapourisation.

infrared at a wavelength of 10.6 μm. Many implementations are available, giving output powers ranging from watts to tens of kilowatts in both CW or pulsed modes of operation. Two different CO_2 laser sources, the Melles Griot CRF 1200 and the Lumonics VFA 1700 were used throughout the course of this research. They will be described in the following chapter.

1.2. Rationale for Study

1.2.1. Industrial Significance of Penetration Processing

Laser penetration processing is an area of industrial interest with many applications in welding, cutting, and drilling of materials. As a drilling or cutting tool, the laser has a distinct advantage over conventional methods in terms of tool wear. With well designed beam delivery systems, laser welding is virtually maintenance free in comparison to industrial counterparts such as Tungsten Inert Gas (TIG), Metal Inert Gas (MIG), or resistive welding[2].

[2] Though laser penetration processing is truly a non contact process, some measures must be taken to prevent beam delivery optics from being damaged by vapour reaction flow from the target material. Beam delivery nozzles incorporating coaxial and/or Transverse gas flow circumvent this problem.

In some cases, laser penetration processing provides considerable labour savings over more conventional techniques. For example, butt welding of thick plate steel can be accomplished in a single pass autogeneously with a high power laser (no filler material required) and with no special joint preparation such as filleting. Conventional arc welding usually requires considerable joint preparation, and multiple passes using filler material. *Figure* 1.1 schematically illustrates the difference between a laser penetration weld and a conventional arc weld, viewed as a cross section perpendicular to the weld line.

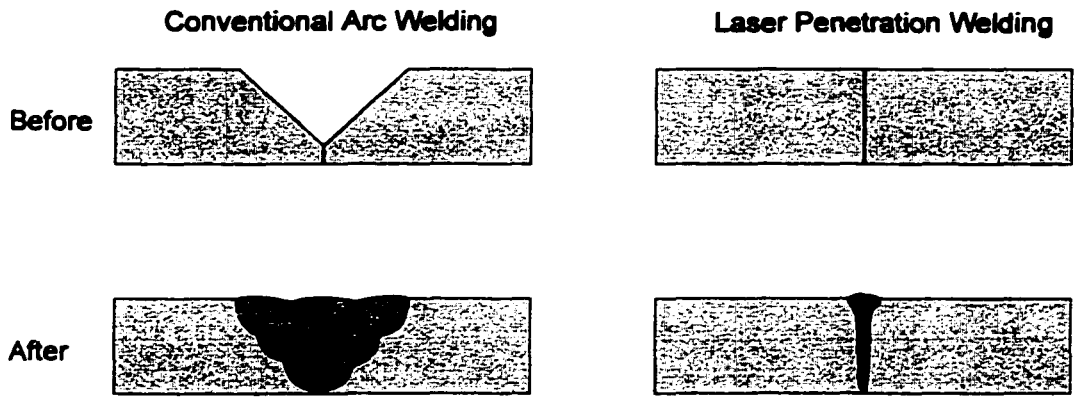


Figure 1.1. Schematic comparison of conventional (multi pass) arc welding techniques to that of laser penetration processing for butt welding of thick plate steel.

Compared to conventional techniques, laser penetration welds deliver substantially lower heat into the parent material which results in extremely low part distortion. This makes the laser an ideal tool for welding applications involving precision

components. Not surprisingly, laser welding has found a permanent place in the manufacturing of automotive transmission components. *Figure* 1.2 shows a component found in a Chrysler transmission which is typically suited to laser welding. An annulus is welded to a hub and subsequently precision machined. Because of the low distortion associated with the laser weld, thinner material can be used and post machining balancing is often eliminated as well. In addition, the processing speed associated with laser penetration welding (typically 5-8 meters/minute), is simply unattainable using conventional processes such as plasma, mig, or tig welding.

More recently, the automotive industry has expanded its application base for laser welding to body parts. Lasers are being used to weld roofs to cars [13], to hem doors and hoods [14] and to make tailored blanks [15]. The latter application involves joining two different sheets together of differing thickness and/or properties *prior* to being formed. Parts formed from tailored blanks are as strong, if not stronger, and much lighter than predecessors based on monolithic blanks. The opportunities for tailored blanks are virtually boundless, as essentially one hundred percent of a vehicle's body and chassis originates as stamped (formed) blanks. Excluding class A surfaces (the outer skin of the vehicle), all component blanks within a vehicle can be considered candidates for laser welding. Some of the types of parts already in production include frame rails, door inners, shock towers, and body sides (aperture frames). *Figure* 1.3 shows a laser welded

door inner for the Chrysler B-van. A section highlighting the weld is shown at the right of the figure.

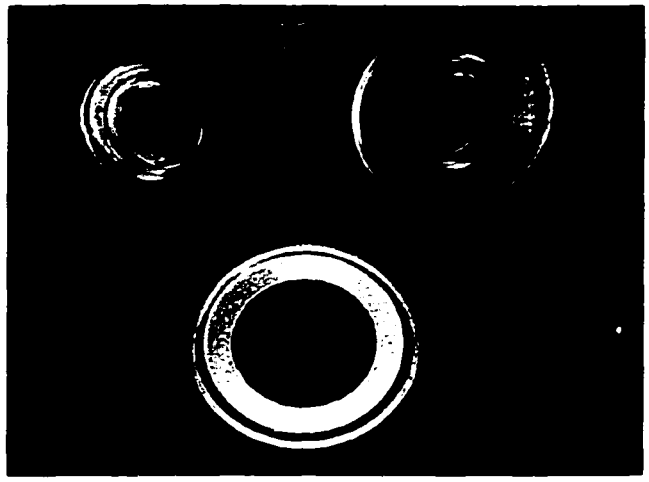


Figure 1.2 Laser welded reaction annulus for the Chrysler 45RFE transmission. The parts are welded at an average speed of 100mm/s with a 6kW CO_2 laser. With a weld circumference of 11.5 inches, these parts weld in roughly three seconds. (photo courtesy of TRIAM Powerlasers)

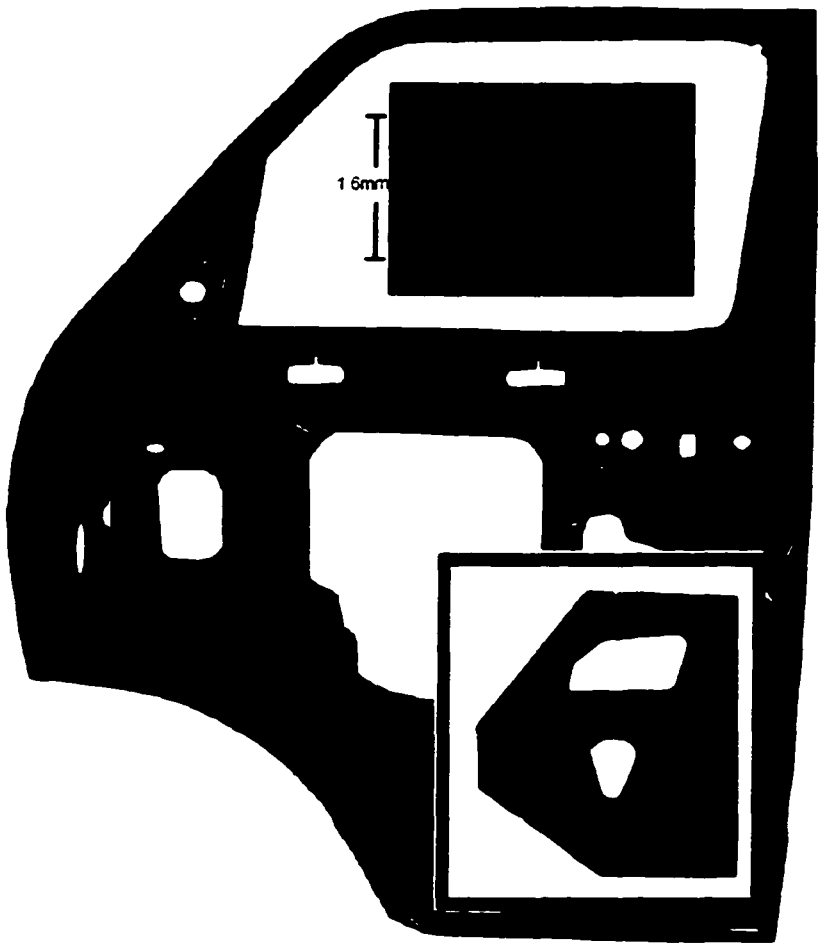


Figure 1.3 Laser welded door inner for the Chrysler B-van. The hinge end of the door is comprised of 1.6mm galvanneal which is welded to 0.8mm galvanneal. (photo courtesy of TRIAM Powerlasers)

Other applications are too numerous to list, but suffice it to say that laser penetration processing has firmly established itself and is continuing to grow in extent industrially. Producing a quality weld such as illustrated in *Figure* 1.3 can be a difficult task however. In terms of the process dynamics, laser penetration processing easily ranks as the most complex of all of the forms of laser material processing. Laser penetration processing of most materials involves a dynamic system consisting of up to four phases (solid, liquid, vapour, and plasma), which interact with each other and the beam in a complex manner. Not surprisingly, much of the expertise in laser penetration processing is of an empirical nature. Viability of new applications or even expanding existing applications often requires lengthy trial and error investigation which may or may not provide fruitful results.

The benefits of predictive models for penetration beam processing are obvious, and hence much effort has gone into modeling of the various mechanisms involved. The ultimate goal of researchers in the field is to have a comprehensive model which accounts for all of the physical mechanisms within the process. As yet, a truly comprehensive analytical model does not exist, but numerous simplified models have been proposed which can be used to describe penetration processing over specific limited parametric ranges. The basic principles of these models will be summarized up to the present state in the following sections of this chapter.

1.2.2. Variable Gravity Experimentation

Much of the experimentation carried out for this thesis was either in a reduced (near zero) or high (near two) gravity environment. The reasoning for investigating penetration processing under varying gravity conditions is two fold.

Firstly, the development of space station Freedom as a long term orbiting microgravity laboratory has prompted investigation into viable technologies for tasks including station structural fabrication, repair and maintenance. The space station will also provide a platform to investigate the potential uses of lasers in the only recently established field of microgravity materials processing [16]. Within this context, any new data involving penetration processing in a reduced gravity environment would enhance the relatively small database of such experimentation.

Secondly, due to the complexity of the process, models are limited to only partial descriptions of the process dynamics. With the ability to isolate and vary the gravity variable, its specific effects and relative role in the process dynamics can be monitored. Ideally experimentation would lead to a thorough understanding of the role that gravity plays in the greater scheme of penetration processing, and both space *and* ground based laser penetration processing would benefit.

1.3. Beam Processing Overview

Before reviewing the relevant literature on this research, it is useful to clarify the mechanics and variables involved in laser penetration processing. *Figure* 1.4 illustrates graphically the buildup of parameters which influence the dynamics as the beam intensity (and hence processing temperature) varies. The first process variable is the intensity distribution in the beam $I(r,\theta,t)$, with r and θ, representing the spatial coordinates relative to the beam axis, and t representing the time coordinate. Even with laser intensity sufficient to produce the keyhole phenomenon, target material first undergoes a sequence of heating processes prior to formation of the keyhole. This sequence is described below.

Initially, laser radiation couples with the target material through the emissivity (ε) and the absorption coefficient (α). The emissivity itself is generally a function of the laser wavelength (λ), the angle of incidence (ϕ), and the temperature (T), while the absorption coefficient is wavelength and temperature dependent. The radiation absorbed through the above mechanisms is converted to heat with its flow governed by solid state diffusion and material properties such as the diffusivity (κ) and heat capacity (C_p), both dependent on temperature as well. The process however, can still be considered single phase during this stage. Processes which are constrained to the solid state regime include laser heating, and laser annealing.

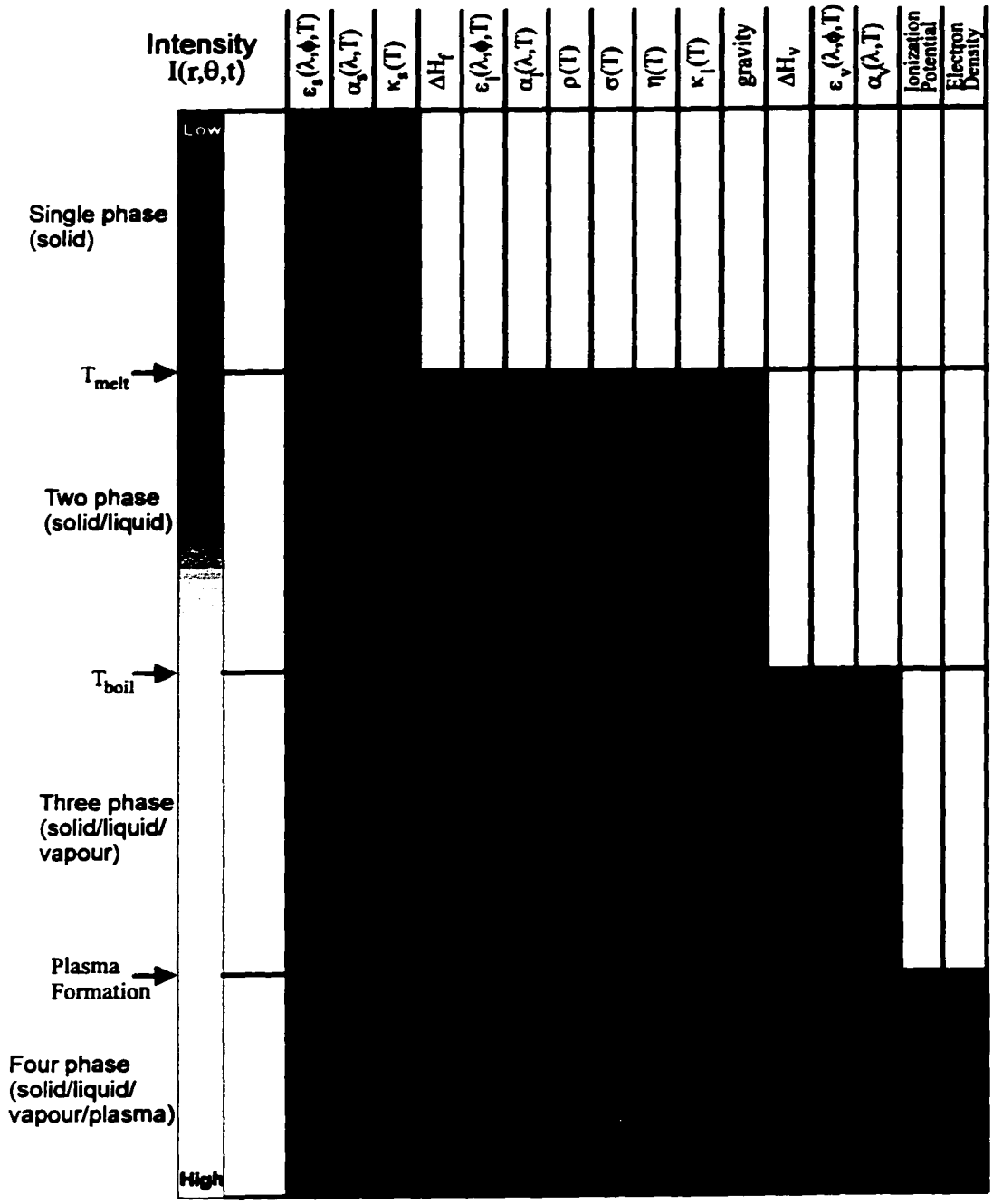


Figure 1.4 Parameter matrix associated with laser materials processing over varying intensity (temperature) regimes. The listed parameters are emissivity (ε), absorption coefficient (α), diffusivity (κ), heat capacity (C_p), surface tension (σ), liquid density (ρ), viscosity (η), latent heat of fusion (ΔH_f), and latent heat of vapourisation (ΔH_v). Subscripts refer to solid (s) liquid (l) and vapour (v) phases.

With sufficient beam intensity, the surface temperature reaches the melting point, introducing several new elements to the process[3]. Energy considerations require that the latent heat of fusion (ΔH_f) be accounted for, and in addition, the presence of liquid complicates thermal transfer through a variety of convection mechanisms. New variables associated with the liquid phase, all dependent on temperature, are introduced in the form of the surface tension (σ), liquid density (ρ), and viscosity (η). Fluid flow mechanisms include Marangoni flow [17], and density driven convection. As well, all of the material properties considered in the solid phase heating have a liquid phase counterpart which must be considered. Gravity also enters as a variable contributing to density driven convection. At this stage, the system technically consists of solid, liquid, and vapour phases, however the vapour component is not yet significant. Laser processing applications which generate a melt zone without significant vapourisation (i.e. not *rapid* boiling) include conduction mode welding, laser alloying, and laser cladding.

At high beam intensity, the temperature at the surface of the target will reach the boiling temperature and the latent heat of vapourisation (ΔH_v) must be considered. Convective processes in the vapour further require the temperature dependent properties of vapour density and viscosity, while the direct beam-vapour interaction involves

[3] Certain materials such as acrylic are spared the many complications associated with fluid phase presence by virtue of a fortuitously located triple point. Atmospheric pressure laser processing results in direct sublimation of target material. The greatly simplified dynamics of this type of system is one of the main reasons why acrylic is widely used for characterizing laser beam quality and intensity.

introducing the wavelength and temperature dependent vapour phase absorption coefficient. Gravity now plays a larger role in the convective processes due to vapour entrapment in the fluid. Though the laser is inducing vapourisation at this stage, the regime is *not necessarily* a keyhole processing regime. In order to generate a keyhole structure, the beam intensity must be sufficient to induce rapid boiling of the melt. Simply put, the vapourisation rate must provide enough localized excess pressure on the surface of the fluid to generate a vapour filled cavity within the material[4].

No new material constants are introduced at this point, but radical changes in the surface geometry and high speed vapour flow within the keyhole complicate the analysis and vapour pressure induced hydrodynamic flow further complicates the process. Within this regime, the system dynamics truly involve solid, liquid and vapour phases. With all of the variables and physical mechanisms present at this point, it should be no surprise that keyhole regime laser material processing is often unstable. It is within *this* regime that the research in this thesis is carried out.

For completeness however, it should be mentioned that the complexity of the interaction mechanisms can extend beyond that of the three phase keyhole regime.

Higher intensity processing generates a plasma through an avalanche ionization process

[4] In reality, adding a changing surface geometry to the list of parameters in play complicates both absorption processes and fluid flow patterns. This will be touched upon briefly in the section titled "Keyhole /Drill hole Development".

[18]. The presence of the plasma increases the local temperature and pressure, and depending on the electron density within the plasma and the beam wavelength, either beam reflection, absorption or transmission can occur. While these effects are present and important in many industrial laser keyholing processes, they are not a factor in this research and will not be further considered.

Even in the absence of plasma effects, many temperature, geometry, and wavelength dependent variables are required to describe an even greater number of interaction mechanisms which themselves are interdependent. To date, a *comprehensive* analytical model of penetration beam welding and cutting considering all variables and process mechanisms does not exist. Though the number of variables is great, and the interaction mechanisms are simply too numerous to include in a single model, all processing regimes tend to establish a hierarchy of relative contributions from the various mechanisms involved.

An example of the changing importance of physical mechanisms throughout different processing regimes is gravity driven density convection which generally plays a small role in welding under conduction limited conditions, but becomes significant as the conduction limited regime passes into the boiling regime. Models developed to date only consider a few of the most dominant process mechanisms under given conditions, but often provide good agreement with experiment over a reasonable range of processing

variables. Some of these models are summarized below.

1.4. Literature Survey: Process Models

The extent of process variables considered and complexity of a given model depends on the predictive goals defined for the model. The following sections will be broken down into categories indicating the prime physical focus of these models.

1.4.1. Energy Conservation Based Models

Models based on energy conservation are perhaps the most simplistic, but they are often sufficient to predict aspects of laser penetration processing such as drill hole/keyhole establishment rates, or penetration to welding speed ratios. Though these models ignore all dynamic effects, they can provide technicians in an industrial laser job shop with starting points when setting up for different applications.

Keyhole/Drill hole Development:

Because dynamical effects are ignored in energy conservation models, they are incapable of tracking the process which transforms a planar target surface into a deep

vapour filled cavity in the interaction region. Generally, in order to achieve penetration, the laser intensity must be sufficient to induce rapid boiling of the target material. Removal of material and recoil pressure from the vapour streaming away from the surface produces a depression within the melt pool. At some point the increasing concavity of the melt pool surface provides positive feedback to the continuation of the process by effectively enhancing the laser-material coupling through multiple reflections [19]. Deep penetration weld energy coupling efficiencies can in fact reach nearly one hundred percent [20], when the aspect ratio of the keyhole is high, and the material is not thin.

Assuming that the laser intensity is high enough to induce rapid boiling, then a simple energy balance will yield the velocity of the vapour front into the material [21],

$$v = \frac{\varepsilon I}{\rho(H_f + H_v + c_p \Delta T)} \qquad 1.1$$

where ε is the effective emissivity at the laser wavelength, I the incident intensity (W/m^2), ρ the density (kg/m^3), H_f and H_v the latent heats of fusion and vapourisation (J/kg), c_p the specific heat capacity at constant pressure (J/kg°C), and ΔT the temperature difference between the boiling point of the material and the initial temperature (°C). The model assumes that all of the vapourised material is removed from the cavity and that all energy is directed into the vapourisation process. Hence, equation 1.1 represents an upper limit to the velocity of the vapour front.

Duley [21] extended the application of equation 1.1 to a time varying laser intensity $I(t)$ where the now time dependant velocity can be integrated to obtain the drill hole depth $z(t)$.

$$z(t) = \int_0^t v(t)dt = \frac{1}{\rho(H_f + H_v + c_p\Delta T)}\int_0^t \varepsilon I(t)dt \qquad 1.2$$

The model is applicable to systems in which the effects of heat transfer to the solid are small in comparison with the vapourisation. In terms of material properties, one way of quantifying this is to say that the model is valid for drill hole depths which are much greater than the characteristic distance of heat penetration, i.e. $z(t) >> \sqrt{\kappa t}$, where κ is the thermal diffusivity of the material (m^2/s).

Weld penetration/ Speed estimation:

Banas [22] developed a simple energy conservation model which is applicable to laser penetration welding. The laser output power P_o couples to the material through an effective emissivity (ϵ),[5] resulting in an absorbed power $P=\epsilon P_o$. This absorbed energy rate is then equated to the melt volume generation rate as follows:

[5] Recall that the emissivity of a material is dependent on the wavelength, temperature, and the angle of incidence. The effective emissivity for deep penetration processing can approach unity even for a material which ordinarily exhibits high reflectivity to the beam. This will be discussed further in the section on keyhole formation.

$$P = 2r_o hv(\rho C_p(T_M - T_o) + \Delta H_f) \quad 1.3$$

where $2r_o$ is the weld width, h is the weld depth, v is the weld velocity, ρ is the material density, C_p is the heat capacity of the solid, T_M-T_o is the temperature difference between the melt and the surrounding solid, and ΔH_f is the latent heat of fusion of the material. With the penetration depth as an input, a relatively straightforward calculation then determines a P/v power-velocity ratio required to achieve the desired penetration.

Some limitations of the model become apparent at this point however. Since P/v becomes unbounded as $v \rightarrow 0$ (i.e. as welding→drilling), this implies that either the keyhole depth becomes unbounded or the power required to generate a given depth approaches zero, which is clearly non physical. The reason that the model breaks down at lower velocities is primarily due to the neglect of heat conduction into the solid. A relative measure of the extent of heat conduction to welding speed is the Peclet number (vr_o/κ). The above model is only applicable when the Peclet number is much greater than one.

1.4.2. Solid Phase Models

The next level of complexity involves models which consider solid state heat transfer. Often temperature fields can be reasonably predicted using models which only

consider solid state heat conduction. Analytical solutions to a variety of fundamental heat transfer problems from Carslaw and Jaeger's text [23] have more than once demonstrated their use in solving temperature distributions in welding problems.

The basis for these models is the time dependent heat conduction equation:

$$\nabla^2 T = \frac{1}{\kappa}\frac{\partial T}{\partial t} \tag{1.4}$$

For steady state models, this reduces to,

$$\nabla^2 T = 0 \tag{1.5}$$

Swift-Hook and Gick [20] provided the first analytical solution of the heat equation applying to penetration beam processing, treating the problem as that of a line source of heat moving at a velocity (v) through a plate of finite thickness. The line source was specified to be the same length as the plate thickness, simulating a full penetration welding scenario. Radiative heat losses from the lower and upper surfaces were assumed to be negligible and the solution was hence two-dimensional. Mean or averaged values of the materials properties were assumed. Solution of the steady state heat conduction problem for this geometry gives the following expression for a quantity, X, defined by the authors as the normalized power input per unit depth,

$$X = \frac{P}{aS} = 2\pi \frac{e^{-Ur\cos\theta}}{K_o(Ur)} \tag{1.6}$$

P represents the total absorbed power (assumed evenly distributed), a is the plate thickness, r and θ are the cylindrical coordinates (relative to the beam axis as "z"), U is the normalised velocity, $U=v/2\kappa$, $K_0(Ur)$ is a modified Bessel function of the second kind, and S is the heat function, related to the temperature through the integration

$$S = \int_0^T K dT \tag{1.7}$$

Though the phase changes were not explicitly accounted for in the solution (in terms of the latent heats), it was assumed that phase changes took place along the isotherms (i.e. along constant S) associated with the melting temperature and the boiling temperature. One of the drawbacks associated with analytical models which only consider solid state heat conduction is that solutions generally become unbounded at the heat source. Swift-Hook and Gick's model is no exception with the presence of a logarithmic singularity in the Bessel function at $Ur=0$.

The authors proceed to solve for the maximum width of the weld pool b, which is expressed in terms of the normalized melting width defined as

$$Y = vb / \kappa = 2Ub \tag{1.8}$$

which is a function of Ur involving the modified Bessel functions of the second kind and its derivative. The solution of the maximum pool width also provides a means of removing the θ dependence from the normalized power input expression, reducing it to a function of Ur alone. A plot of the normalized melting width (also referred to as the

normalized speed-width) versus the normalized power input is then generated analytically using small and large *Ur* expansions of the modified Bessel functions. One of the predictions from the model indicates that the maximum fraction of beam power which could be used just to generate the melt pool was 0.48. Comparison of the model with electron beam welding data indicated that the experimental processing was occurring near maximum efficiency. The same was true of higher power (~20kW) laser welds, but lower power and thin plate laser welds indicated much lower efficiencies overall.

Swift-Hook and Gick did note effects such as the generation of a plasma within the keyhole, but they did not account for any of the previously touched on beam-plasma interactions. While lasers may be capable of generating similar intensities as electron beams, the latter is essentially unaffected by the presence or absence of a plasma.

1.4.3. Multi-phase Models

Multiphase models consist of any models which consider more than one phase explicitly within the model. As this constitutes a considerably large body of research, only a few of the most relevant models will be mentioned. Relevance within the context of this thesis implies that the model delivers insight into keyhole/drill hole morphology and dynamics. The summaries that follow all relate to modeling the structure(s) of the

laser keyhole and associated melt flow. They are grouped into two categories: Steady state and dynamic.

Steady State/Quasi-steady State Keyhole Models:

Andrews and Atthey [24] presented a model in 1976 wherein the steady state keyhole profiles were computed for the idealized case of a stationary laser beam incident normally on a semi-infinite liquid surface[6]. Assuming axi-symmetric (irrotational) flow of both vapour and liquid phases, the authors use a simplified energy conservation expression and Bernoulli's equation across the phase boundary (including both gravitational and surface tension effects) to deduce an expression for the surface of the keyhole (drill hole) $z=s(r)$. When surface tension is neglected, the surface of the keyhole is described by a first order differential equation of the form,

$$\frac{dS}{dR} = \sqrt{-(1+Q^2/S)} \qquad 1.9$$

where the capitalization of letters implies normalised variables and Q represents a normalised incident power density which also includes terms associated with density, gravity and latent heat of vapourisation. The authors define a boundary condition $S(R_o)=0$ and assume that if R_o is defined as the maximum radius of the incident beam,

there is nothing beyond R_o capable of maintaining a depression in the surface. The solution takes the shape of a somewhat convex conical cavity with a cusp at r=0.

When the effects of surface tension are considered, the solution involves a second order nonlinear differential equation which must be solved numerically. The resulting solutions differ from the earlier results in several ways. The surface tension smoothes out the cusp at r=0, as well as extending the range of the surface depression beyond R=R_o again due to the smoothing effects of the surface tension. More striking however is the difference in penetration depth predictions, where the inclusion of surface tension restricts the maximum penetration depth to one third of that predicted without surface tension considered.

Keyhole Dynamics:

The dynamics of the keyhole itself have been discussed by Kroos [25,26,27], Gratzke [25,26], Simon [25,26,27], Klein [27], Vicanek [26,27], and Decker [27]. In the first paper of this series, the stability of a cylindrical keyhole which fully penetrates the thickness of the target material is considered from the point of view of energy conservation and pressure balance. The hydrodynamic pressure due to fluid flow around

[6] This "idealized" state is actually quite well suited to a large body of the research in this thesis where drilling of a variety of liquid materials is studied.

the keyhole, and the hydrostatic pressure due to gravity were neglected in this treatment so that the resulting balance involved just ablation and surface tension pressures. The energy balance was represented with the absorbed energy flux density being equated to the sum of the flux densities associated with ablation of material and that due to solid state heat conduction.

Solution of the pressure balance equation yields two self consistent solutions for the keyhole radius, one stable and one unstable providing that the laser intensity is sufficiently above the threshold for maintaining a keyhole in the material. Typical behaviour of the two pressure components is illustrated in *Figure* 1.5

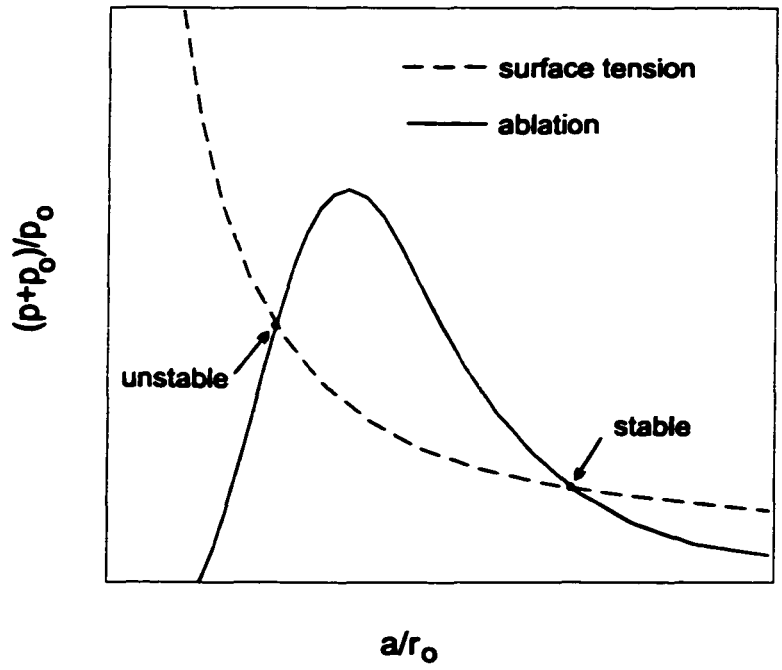


Figure 1.5. Typical behaviour of dimensionless ablation pressure and surface tension pressure as a function of the normalised keyhole radius taken from Kroos et al [25]. p is the excess pressure, p_o is the ambient (atmospheric) pressure, a is the keyhole radius, and r_o is the equilibrium keyhole radius.

The amplitude of the ablation pressure curve is related to laser intensity, and hence the authors were able to calculate the threshold power per unit thickness of material for formation of a stable keyhole by using the lowest ablation pressure curve which intersects the surface tension pressure curve for a given material.

The equilibrium states predicted from the first publication [25], also infer that perturbations from the equilibrium state will result in a dynamic keyhole. The authors extend the work of their first publication to consider the effects of radial oscillations of a cylindrical keyhole [26]. The model assumes a keyhole of radius $r_1(t)$ surrounded by a

cylindrical melt pool of radius $r_2(t)$ in which there exists a radial flow field designated by $u(r,t)$. The flow field satisfies the Navier-Stokes equation for irrotational flow and the authors first seek a solution to determine the collapse time of the keyhole given the initial conditions of a stable state at t=0 and a sudden removal of ablation pressure for t>0 (i.e. laser turned off at t=0). After considerable non-dimensionalisation and substitution, the keyhole collapse time is represented in non-dimensional form by the following integral

$$\Delta\tau = \frac{1}{4}\int_0^1 \left(\frac{\ln(1+C/A)}{1-\sqrt{A}+\sqrt{1+C}-\sqrt{A+C}} \right)^{1/2} dA \qquad 1.10$$

which in terms of real time t is given by $\Delta\tau = t \Big/ \left(\frac{\rho r_o^3}{\gamma} \right)^{1/2}$, r_o being the keyhole radius at t=0, ρ the melt density, and γ the surface tension of the melt. The parameters A and C are given by $A(\tau) = \left(\frac{r_1(t)}{r_o} \right)^2$, and $C = \frac{r_2^2(0)}{r_0^2} - 1$. From earlier work by Dowden et al [28] the authors determine that $C \approx 10$ is appropriate for the term which effectively represents the keyhole volume to melt ratio, and upon numerical integration of equation 1.10 find that $\Delta\tau \approx 1$. When material properties are inserted and dimensional time is computed this yields $\Delta t \cong 0.1$msec for Al, Fe, and Cu.

The authors then proceed to study the effects of perturbations about the stable solution point referred to in *Figure* 1.5. Through a standard linear stability analysis, the

model which still only considers radial oscillations of the entire keyhole, predicts that perturbations from the stable keyhole radius will oscillate over a band of frequencies with a peak amplitude in the 500-700Hz range.

In a third publication [27], this work was further extended to include the excess pressure associated with gas flow out of the keyhole. Furthermore, the constraints on the motion of the keyhole wall were relaxed to allow radial, axial and azimuthal modes of oscillation as shown in *Figure* 1.6.

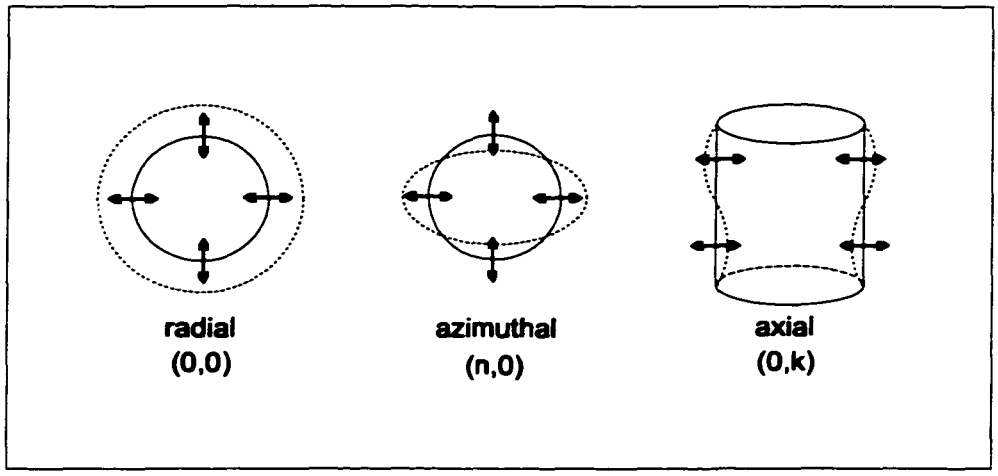


Figure 1.6 Illustration of nature of keyhole wall motion assumed in the keyhole dynamic model of Klein et al [27].

The oscillatory motion of the keyhole was assumed to be a combination of eigenstates in which the keyhole surface for a single state would be represented by

$$r_{n,k}(t) = a + \cos(n\phi)\cos(kz)\alpha(t) \qquad 1.11$$

where a is the steady state solution, $\alpha(t)<<a$ is the perturbation term, and n and k are the azimuthal and axial mode numbers of the oscillation. The ground state (n=k=0) in this treatment is analogous to the radial oscillations discussed in the previous paper [26].

Rather than attacking the problem via solving the equation of motion, Klein et al [27] derive expressions for the kinetic and potential energy and subsequently solve for the eigenfrequencies of oscillation using the Lagrangian method. The authors first consider the ground mode frequency ω_{00} under the same processing conditions as in the earlier paper and find that consideration of the vapour streaming from the keyhole significantly alters the results so that the previous estimate of frequencies near 600 Hz are found to be near 1500 Hz.

A general expression for the eigenfrequencies ω_{nk} was derived which is explicitly dependent on the surface tension of the melt, the average melt density, the equilibrium radius of the keyhole, and the three components involved in the pressure balance. The first few eigenfrequencies were calculated for pure iron under a gaussian beam of radius r_o=150μm. The frequencies group together in bands associated with a given azimuthal mode as the thickness of the material increases beyond about 2mm. The frequency bands associated with the n=1,2,3 azimuthal modes fall between 1 and 10 kHz increasing in order with mode number.

The solution implies that an infinite number of eigenstates are possible in principle, however Klein et al [27] point out that the lifespan of these perturbation based oscillations will be limited by various dissipative forces. The computed damping rate associated with viscous forces was used to estimate the lifetimes of the eigenstates. Using properties for iron, the authors determine that the viscous damping discriminates higher order states. As an example, the (0,0) state will persist for 50-100ms, (over 50 full cycles), while the (3,3) state is predicted to persist for 1-10ms (about 10 cycles).

In closing, Klein et al cite experimental results that lend support to the model, including direct evidence of spectral emissions between 4 and 10 kHz linked directly to keyhole oscillations [29]. In a second, a study of variable frequency beam power modulation revealed a correlation between an observed resonance in the plasma and stabilisation of the welding depth [30].

1.5. Research Thrust

1.5.1. Goals of Research

The general goal of this research is to further the understanding of the fundamental process dynamics of laser drilling and welding. As indicated in *Figure* 1.4,

the number of interdependent parameters involved in typical penetration processing of metals is intimidating to say the least. Rather than studying this extremely complicated system and attempting to infer the effect of certain variables, it is first desirable to simplify the treatment as much as possible. By using low laser intensity ($\leq 10^6 w/cm^2$), plasma formation does not take place, reducing the number of parameters by two and limiting the dynamics to that of a three phase system. While limiting the intensity of the beam eliminates the ability to carry out penetration processing in most metals, penetration processing of dielectric media is still easily achievable.

Although the material properties of metals and dielectrics differ a great deal, penetration dynamics are dominated by physical convection processes within the melt pool. These dynamics play a large role in the resulting fusion zone. *Figure* 1.7 shows side views of fusion zones in laser welding of steel (A), laser welding of paraffin (B), and laser *drilling* of gelatin (C). All three exhibit similar morphological structure, indicating that drilling and welding of dielectrics may involve similar dynamical behaviour.

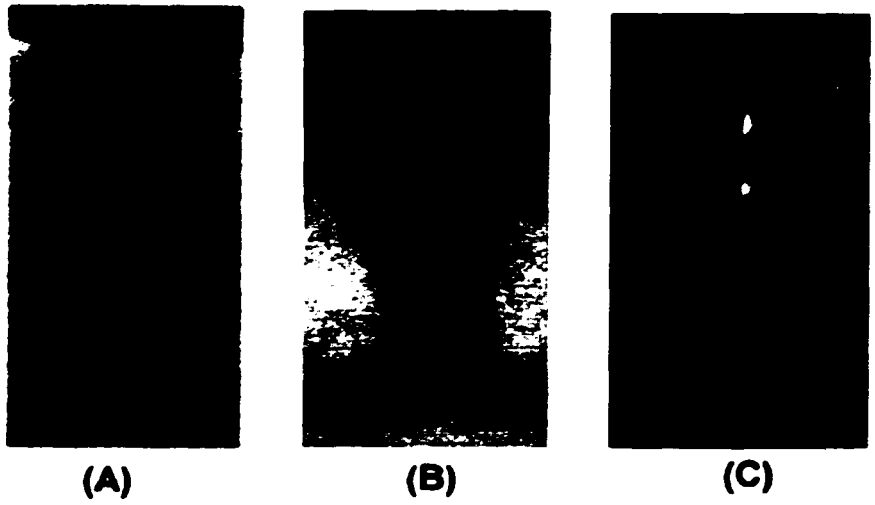


Figure 1.7 Side profiles of fusion zones in laser welded steel (A), laser welded paraffin (B), and laser drilling in gelatin (C).

Limiting the beam intensity has other benefits beyond eliminating the plasma effects on the process. Many dielectrics are optically transparent, or at least translucent to such a degree that direct observation of the profile of the keyhole and surrounding molten material can take place. Another benefit of low intensity processing is that the laser itself becomes portable enough to facilitate experimentation aboard the NASA KC135 microgravity laboratory, thus allowing the process to be further simplified by controlling buoyancy.

Further simplification of the process dynamics is achieved by reducing the weld speed to zero. Laser drilling has a geometric advantage over laser welding in that it possesses cylindrical symmetry (assuming symmetry exists in the laser beam intensity

profile). For this reason, the vast majority of the experimental work involves drilling.

A final simplification which applies to much of the experimental data set is the removal of the solid phase boundary. All of the solid state parameters vanish, as well as the latent heat of fusion. By performing laser "drilling" of a dielectric liquid in the absence of gravity, the sixteen contributing parameters to the process highlighted in *Figure* 1.4 are reduced to seven.

The work of this thesis is divided into two major efforts. The first involves studying heat transfer associated with laser drilling of fused quartz under variable gravity conditions. By using holographic techniques (described in chapter two), heat transfer from laser drilling into the fused quartz can be quantitatively measured. The second effort involves a considerably broader study of penetration processing cavity and fluid dynamics, also in variable gravity, using a variety of materials. By performing similar experiments across a variety of differing materials, influence of various material parameters on the process dynamics may be ascertained.

1.5.2. Appropriate Materials

Materials which are suited to this research should ideally be transmissive over the 400-700 nm, wavelength range and highly absorptive at the laser wavelength of 10.6μm.

In fact, the vast majority of optically transparent materials obey this requirement. Excluding salts such as NaCl and KCl, or exotic materials such as zinc selenide, one would be hard pressed to find a visibly transparent material which does not absorb at 10.6μm. Some candidate materials meeting the above requirements can be eliminated for reasons of health, safety, or availability, but this still leaves a wide selection of potential candidates. The challenge is to select a limited number of media which yield the most information. The extent of materials used throughout the course of this research are summarized in *Table* 1.1. The rationale for the choice of material is given in the table.

Table 1.1 Materials used throughout the course of this research.

Material	Rationale for choice
Acrylic	Commonly used for diagnostic of laser beam mode quality. Readily available.
Fused Quartz	Subject of earlier laser processing work in both normal and reduced gravity [16, 31]. Excellent optical quality for holographic imaging.
Soda Lime Glass	Subject of earlier laser processing experimentation [32]. Melt pool more analogous to typical industrial applications.
Paraffin	Readily available. Ease of post processing sectioning. Similar to plastics experimented on by Mueller [33].
Water	Two phase system. Readily available. Previously studied by Mueller [34]. Safe.
Gelatin	Allows comparison of water experiments to a system which acts as a pseudo three phase system.
100% Glycerol (liquid)	Two phase system. Readily available. High viscosity compared with water allows study of effect of viscosity on process. Soluble in water which allows mixtures to be studied.
100% Glycerol (solid)	Allows study of three phase glycerol system in comparison to two phase system
66% Glycerol	Two phase system. Allows viscosity effect to be studied. Some analogy to metallic alloy.
50% Glycerol	Two phase system. Allows viscosity effect to be studied. Some analogy to metallic alloy.

1.5.3. Structure of Thesis

The remainder of the chapters are dedicated to describing the equipment, experiments, and results of the previous few years work. Chapter 2 describes in detail the experimental systems, including experimental hardware, diagnostic techniques, extent of data set, and environmental/processing conditions.

In Chapter 3, a detailed analysis of real time differential holographic interferometry of fused quartz drilling in low and normal gravity is presented. The experimental data, and temperature field analysis from the data are presented first, followed by analytical and numerical models which are developed using prolate spheroidal coordinates.

Chapter 4 focuses on modulated beam intensity drilling of water and glycerol. These experiments involved drilling into water and glycerol with a pulsing laser beam under normal gravity conditions. This avenue of investigation was prompted by the keyhole dynamic predictions of the German group summarized in section 1.4.3 [25-27]. Interesting structural effects on the drill hole are observed as the pulsing (beam modulation) frequency is varied. In the case of the glycerol, under certain conditions, unique and very stable drill hole structures can be achieved which are attributed to a resonant coupling with the modulated beam. The fact that the structures are *stable* is of great interest, as process instability represents a major pitfall in the development of any

industrial application. Imaging and acoustic data associated with both resonant and non-resonant behaviour is presented. The mechanism of this coupling is investigated through numerous drill hole dynamic models, which are compared with both structural and acoustic data.

Chapter 5 provides further insights into the dynamics associated with laser drilling. The process of drill hole initiation is investigated in solid and liquid glycerol and fitted to a simple intensity attenuation model. The same model is applied to acrylic drilling, which demonstrate excellent consistency. Drill hole dynamics are discussed for one hundred percent glycerol based on high speed imaging data in both low and normal gravity. A cyclic process is identified in both instances but with distinctly different periods. Fluid motion phenomena in the liquid surrounding the drill hole is investigated briefly for all of the fluid mixtures as well as gelatin. Differences are described, and related to differences in fluid viscosity.

Chapter 6 summarizes and discusses the results of the research. As is the case with any experimentation, as many questions arise as answers, and potential avenues for further investigation are discussed.

Chapter Two

Experimental Summary

2.1. Data Acquisition Platforms

2.1.1. KC-135 Flying Laboratory

Much of the experimental data was acquired in either low (milli-g) or high (~1.8g) gravity environments, made possible with the NASA KC-135 flying laboratory. The KC-135 is shown in *Figure* 2.1. Variable gravity conditions are simulated aboard the KC-135 by flying a parabolic trajectory. *Figure* 2.2 schematically illustrates an "ideal" parabolic

flight path and resulting acceleration levels in the frame of reference of the

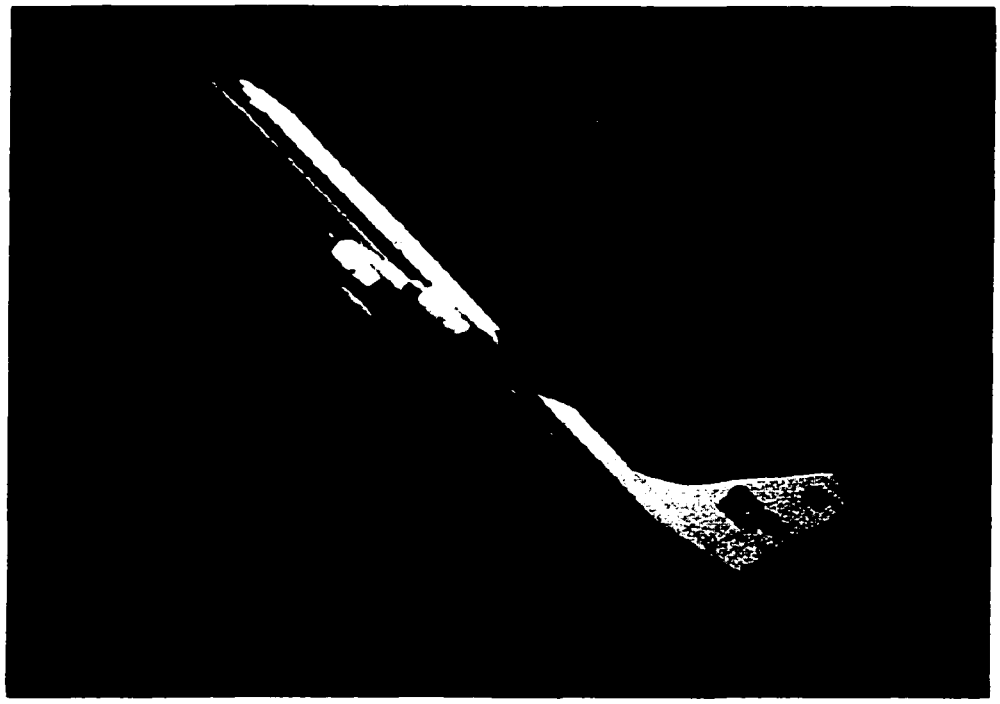


Figure 2.1. NASA KC-135 performing microgravity maneuvers over the Gulf of Mexico. The 45° nose up attitude implies that the pane is just commencing the low gravity portion of the maneuver. (Photo courtesy of NASA)

aircraft. Transition of the acceleration levels occurs at the inflection points with low gravity conditions during concave down regions of the trajectory, and high gravity conditions during concave up regions.

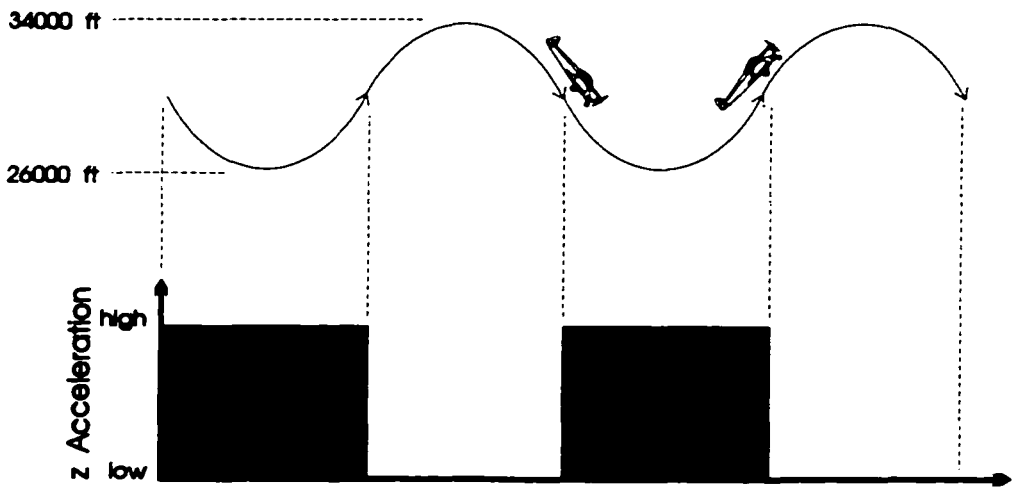


Figure 2.2 Schematic representation of ideal flight path of aircraft which generates simulated low and high g environments. Typical flights consist of 40 parabolic maneuvers with each low gravity period lasting approximately 25 seconds.

In actual KC-135 flights, control and geometric limitations reduce the quality of the low and high acceleration maneuvers. Full control of the aircraft is accomplished through manipulation of just four parameters described as pitch, roll, yaw, and thrust. The yaw and roll of the aircraft are the only parameters under automatic control. The pilot and co-pilot operate the pitch and throttle controls manually throughout both the low and high *g* maneuvers which inevitably limit the quality of the reduced gravity[7].

[7] It is interesting to note that with a human element in the control of the aircraft, each flight crew tends to generate their own unique acceleration versus time signature. In fact, frequent KC-135 flyers can often recognize the cockpit crew from a given flight based on the acceleration vs. time records.

A typical flight consists of 40 parabolas with each full cycle lasting approximately 70 - 80 seconds. Defining the magnitude of the acceleration due to gravity on the surface of the earth to be $g \equiv 9.8$ m/s^2 (directed anti-parallel to the z axis of a Cartesian reference frame on the surface), then typical z components of acceleration during low gravity maneuvers are $a_z \leq 0.01g$. Periods of relatively clean low gravity can be sustained for 20 to 25 seconds each cycle. *Figure* 2.3 shows typical plots of the three axes' acceleration components versus time over several parabolas.

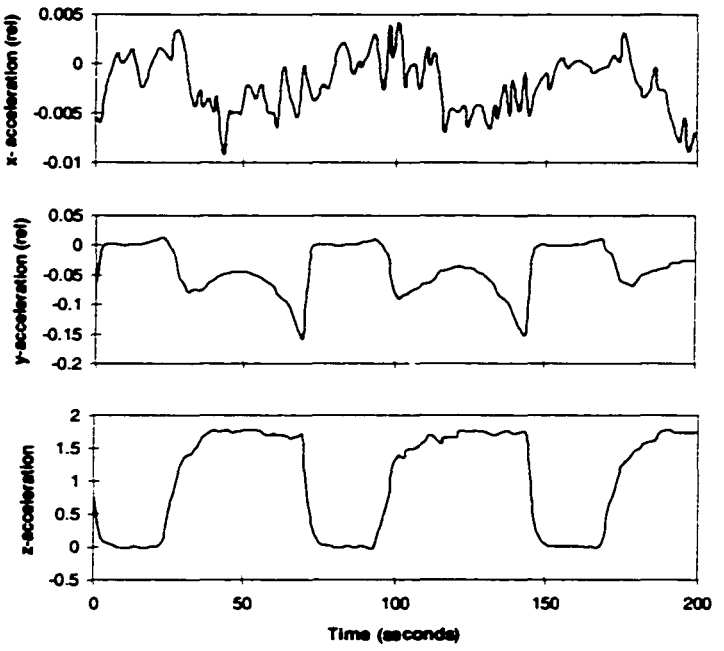


Figure 2.3 Accelerometer profiles of x, y, and z acceleration levels aboard the KC-135 taken over roughly three parabolic maneuvers. The z direction is taken as into the floor of the aircraft, the y direction is along the fuselage, and the x direction is across the fuselage, parallel to the floor. Accelerations are normalised to g=9.8 m/s^2.

Power to supply onboard experiments primarily comes from 28 V.D.C. generators which is the aviation standard. Standard 110/220 Volt AC is supplied via onboard power inverters. Uninterruptable power supplies are optionally provided to supply critical minimal load devices such as computers.

The entire interior of the aircraft is lined with foam padding for safety reasons, and the floor provides a grid of threaded holes to which experimental platforms can be mounted. All experimental systems flown on the KC-135 must conform to an extensive set of structural, safety and electrical guidelines set out by NASA [35][8].

2.1.2. LAMPS Test Bed

The majority of the laser drilling experiments were performed on a specially designed platform called the LAMPS (Laser Assisted Material Processing in Space), test bed. The success of rudimentary laser materials processing experiments initiated by Duley and Mueller [36] under the Canadian Space Agency's User Development Program (UDP) prompted the design and construction of the LAMPS test bed. The test bed was designed to be a general purpose laser material processing workstation coupled with

[8]KC-135 *passengers* must also pass extensive tests before being allowed to fly. These include a USAF class III medical examination, a high altitude indoctrination course (hypobaric chamber), and security checks.

sophisticated diagnostics and control. Space and power limitations were placed on the system in order to comply with NASA regulations for compatibility with the KC-135.

The system, consisting of three modules, is built around a Melles Griot CRF-1200 CO_2 laser rated at 120 watts maximum CW output with typically greater than 90% TEM_{00} mode content [37]. The three modules are the Laser Enclosure Module (LEM), the Power Supply Support Module (PSSM), and the Electronic Equipment Support Module (EESM). The complete LAMPS test bed is shown mounted aboard the KC-135 in *Figure* 2.4.

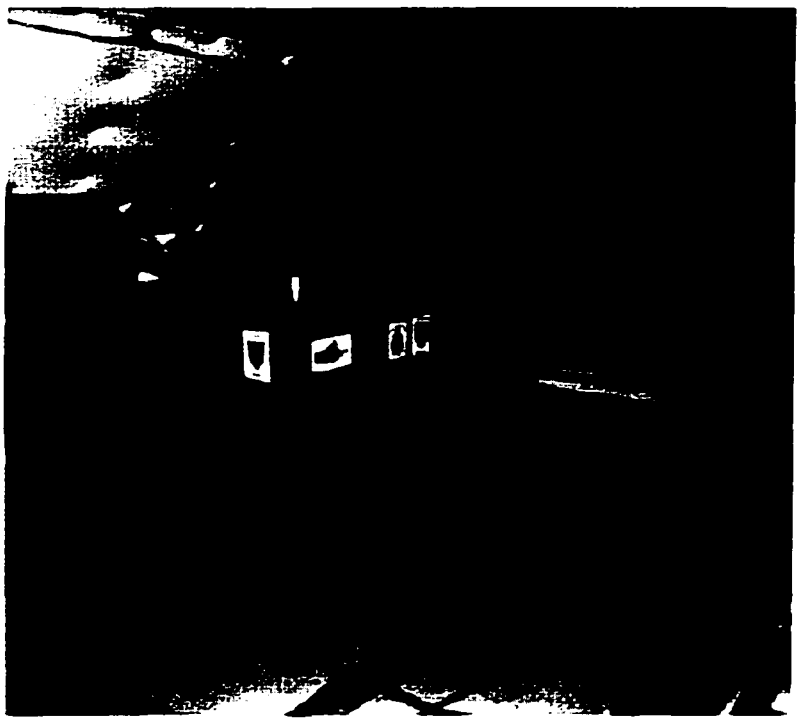


Figure 2.4. The Lamps test bed shown mounted aboard the NASA KC-135. Shown from left to right are the power supply support module (PSSM), the laser enclosure module (LEM), and the electronic equipment support module (EESM). Photo courtesy of NASA Johnson Space Center.

The main module is the LEM, which houses all of the materials processing equipment and diagnostic sensors mounted on two stacked Newport optical breadboards. The materials processing equipment includes the CO_2 laser head, the beam delivery unit (BDU), shield gas system, the focusing assembly (using a 5 inch ZnSe planoconvex lens), and a servo driven Aerotech sample positioner. The diagnostics include a helium neon (HeNe) beam locating laser aligned coaxially with the CO_2 beam, a three axis accelerometer, a laser power detector, and three optical diagnostic subsystems in the form of direct imaging, Moiré deflectometry and real time differential holographic interferometry of which any two could be in use at one time. The optical diagnostics will be discussed in detail in section 2.2.1.

Components in the optical subsystems include a second HeNe laser, numerous optics and mirrors to direct and shape the HeNe beam, a Newport model HC-300 thermoplastic holographic camera, a Moiré deflectometry module, and two Panasonic GP-CD60 CCD video cameras. The hardware layout of the LEM is detailed in *Figure* 2.5 which shows a schematic top view layout of the upper and lower optical bread boards. The entire bread board assembly is mounted to the base of the LEM enclosure with damped shock isolation mounts.

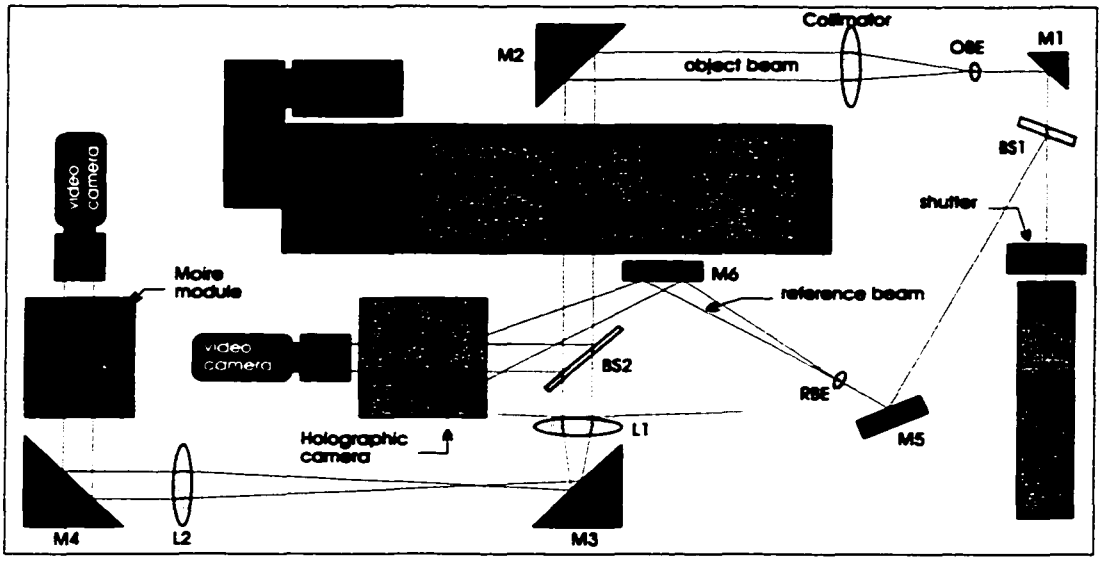


Figure 2.5 a. Schematic representation of components and beam paths on the upper level optical breadboard. The downward direction of the processing beam is obtained via two steering mirrors from the upward direction exiting the lower level breadboard.

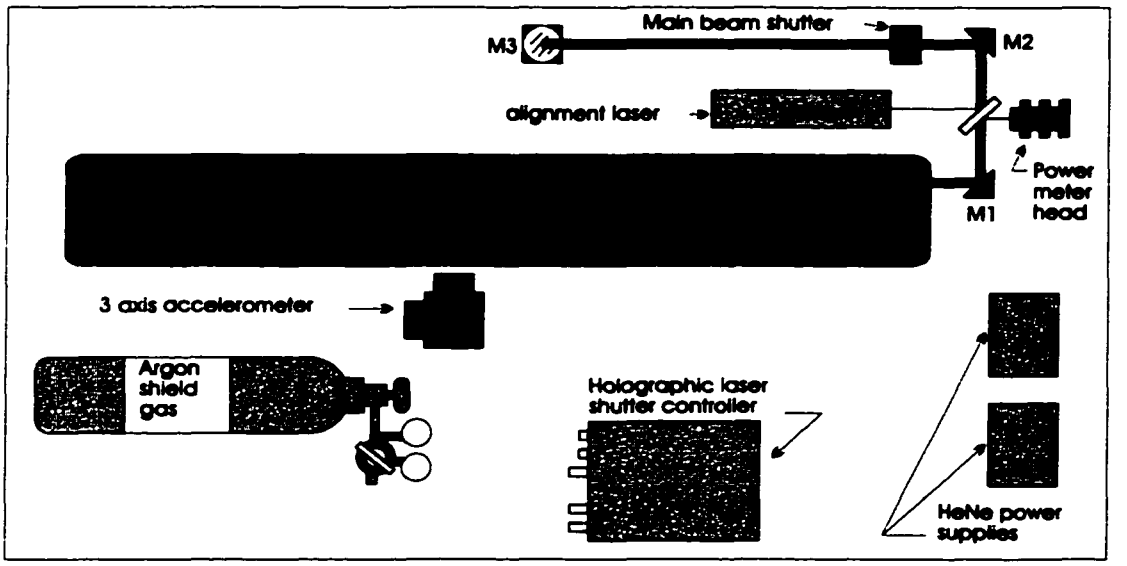


Figure 2.5 b. Schematic representation of components and beam paths on the lower optical breadboard inside the LEM. With the exception of the processing area, the CO_2 laser beam is confined within aluminum tubing for safety purposes.

The EESM contains all of the control and support hardware required for the test bed. This includes the holographic camera controller, the video camera controllers, two VHS video cassette recorders, a Unidex servo controller, the CO_2 laser controller, the laser power meter, a video data monitor (switchable between the two video channels), and a PC to control the majority of the hardware and data acquisition. All critical systems including the CO_2 laser, the main laser shutter, the holographic camera, and the motion controller have manual override control accessible through the EESM in the event of a system malfunction.

The PSSM supplies the power and coolant to the CO_2 laser head. Cooling of the laser head is achieved via a closed loop heat exchanger using distilled water as coolant.

Once the modules are connected together, the LAMPS test bed provides the user with a self contained "plug in" laser materials processing research facility complete with a wide range of advanced diagnostics capabilities. The only external connections required are a 30 amp 115 V.A.C. service, and a means of fume evacuation. Fume evacuation is provided by modified charcoal filtered shop vacuum for ground based experiments. During aircraft based experiments, the fume evacuation is accomplished through use of an overboard vent available on the aircraft.

2.1.3. Industrial Laser Laboratory

Experiments involving time modulated beam drilling of liquids utilized a laser processing facility built around a Lumonics VFA-1700 fast axial flow industrial CO_2 laser. The exact mode content of the beam was unknown, but a beam profile shown in *Figure* 2.6 indicates a considerable presence of the Gaussian TEM_{00} mode.

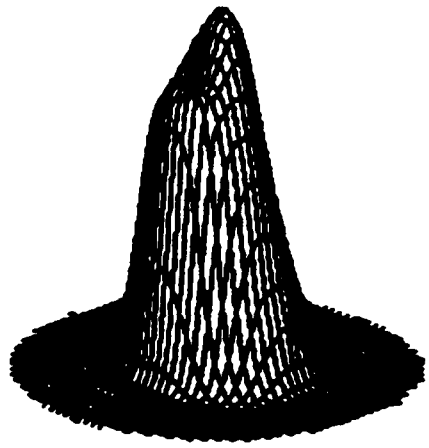


Figure 2.6. Spatial beam profile from Lumonics VFA-1700 laser (after Gu [38]).

The beam was directed normally at the free surface of the target liquid through a 5 inch ZnSe lens such that the focal plane was located at the liquid surface. Modulation of the beam was accomplished in two ways: 1) Electrical modulation of the discharge plasma via the laser controller on a fifty percent duty cycle allowed modulation at discrete

frequencies (limited by the controller design) up to 1 kHz. 2) Mechanical modulation of the beam via a rotating fifty percent duty cycle chopping wheel located between the focusing optic and the target allowed modulation of the beam at frequencies from 100 Hz to 3600 Hz. A diagram of the apparatus indicating the essential components is shown in *Figure* 2.7. The specific design of the elements in the apparatus differed over two sets of experiments and the detailed differences will be described in Chapter 4, which is dedicated to modulated beam processing.

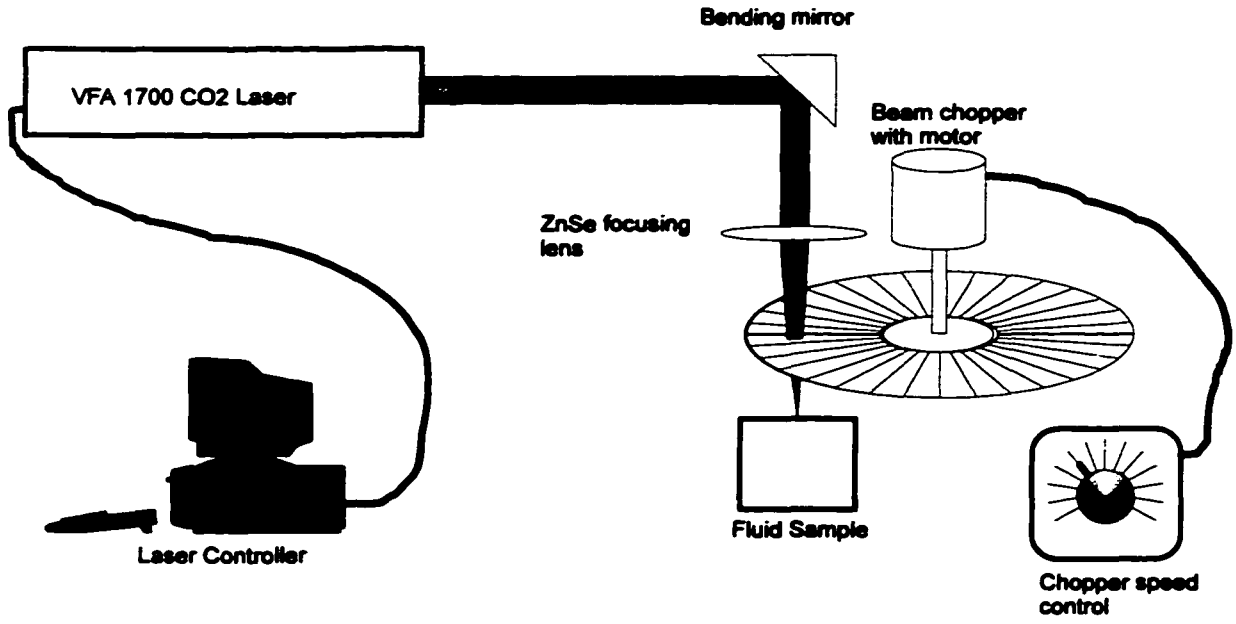


Figure 2.7. Diagram illustrating essential components of system configured for modulated beam drilling of fluids. For electronically modulated beam experiments, the chopper assembly was removed from the beam path.

2.2. Diagnostic Systems

2.2.1. Optical Diagnostics

General:

Of the three imaging techniques available on the LAMPS test bed, only direct imaging was available in the experiments performed in the industrial laser lab. All of the imaging techniques share a common perspective with respect to the work piece, with the imaging taking place on an axis perpendicular to the axis of the processing beam[9]. *Figure* 2.8 diagrammatically illustrates the general imaging geometry, ignoring optical hardware specific to each technique. With this configuration, the three diagnostics allow observation of dynamical and thermal behaviour of laser processing in a plane containing the processing beam and perpendicular to the optic axis of the imaging camera, provided the target material is optically transparent.

On the LAMPS test bed there are only two cameras and two VCR's available, hence only two of the three techniques may be employed at once. The characteristics of each technique are summarized below.

[9]The z-x geometry is actually the only truly shared geometry for all of the imaging diagnostics. The extra relay optics and bending mirrors between the Moiré module and the object have the effect of inverting the y-axis of the image. Thus, the left and right sides of the two video channels are interchanged.

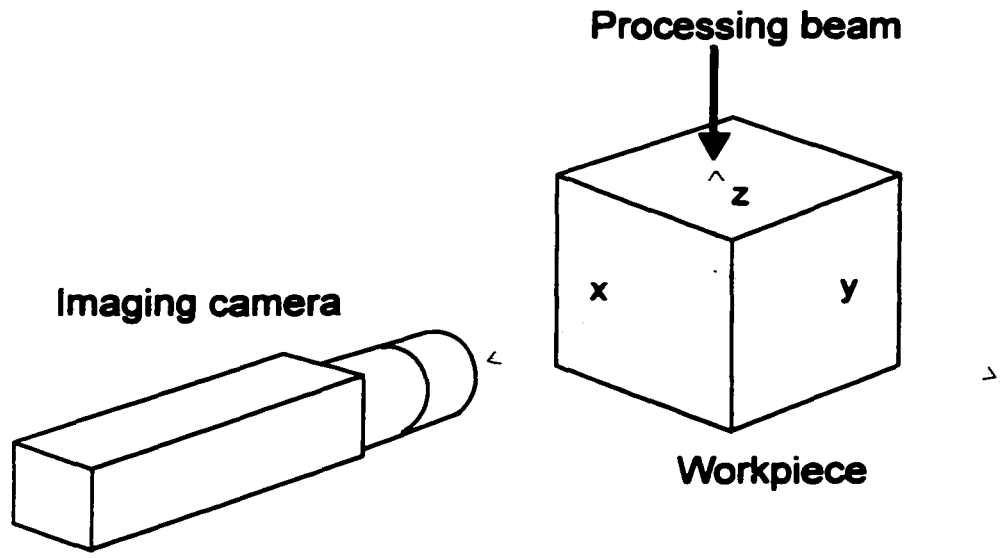


Figure 2.8. Schematic illustration indicating general imaging geometry with respect to processing beam and work piece.

Holographic interferometry:

The actual holographic technique employed in LAMPS is known as real time differential holographic interferometry. The essence of the technique involves comparison of plane coherent wave fronts which have passed through the media of interest before and during the thermal processing. The optical path of light passing through a medium depends on its index of refraction which is a function of the temperature of the medium (for monochromatic light). Thus, if one were to project on to a screen the superposition of the plane waves associated with passage through

undisturbed and thermally disturbed fused quartz for example, a two dimensional interference pattern would result due to phase differences in the two wave fronts.

With holographic imaging techniques, one can record the phase and amplitude field information of an undisturbed plane wave after passage through the medium of interest on a holographic plate. A simplified sketch of the holographic arrangement for recording (and subsequent viewing) the plane wave front is shown in *Figure* 2.9. The undisturbed plane wave can then be reconstructed by illumination of the developed holographic plate by the original reference beam.

If the geometry of the arrangement is kept intact, then an interferogram representing the optical path difference (OPD) field between undisturbed and thermally disturbed material will be generated by the combination of the now disturbed object wave front with the reconstructed undisturbed wave front. Fortunately, the design of the Newport HC-300 holographic camera allows in situ development of the hologram and thus the geometry can be exactly preserved. The evolving fringe field is then imaged via a ccd camera (as indicated in *Figure* 2.9) and recorded to video tape, allowing the evolution of the OPD field to be followed in real time. Holographic imaging of an acrylic block after laser processing is shown in *Figure* 2.10.

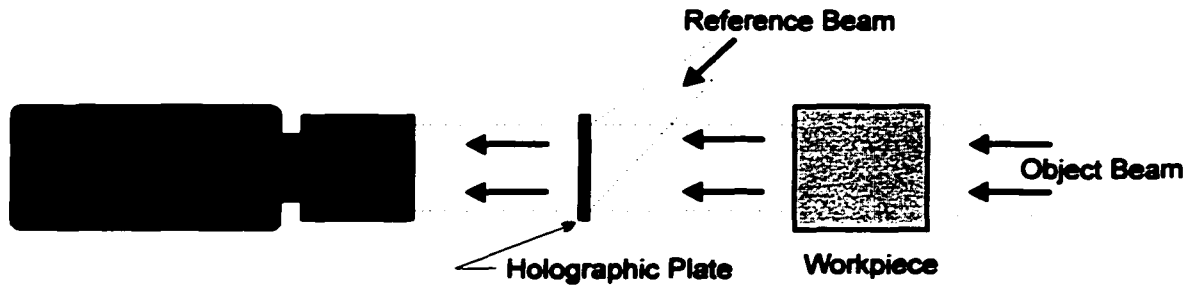


Figure 2.9. Simplified top view of the holographic interferometry module showing incidence of both object and reference beams. The CCD camera records the subsequent real time interference patterns to video tape. Processing laser incidence would be into the page in the center of the work piece.

As mentioned previously, the OPD field is related to variations in index of refraction within the thermally processed material which are in turn related to the temperature changes within the material. In general, the exact relationship between the interferogram fringes (a two dimensional fringe field) and the three dimensional thermal field within the material is not tractable. However, by imposing restrictions on the nature of the processing which give rise to cylindrical symmetry, the temperature field can be extracted from the interferogram data. To this end, the nature of the processing must be restricted to a stationary process (i.e. drilling), and the work piece dimensions must be such that the radius associated with the most distant fringe falls within the boundaries of the work piece. Even with cylindrical symmetry the reduction of a given fringe pattern to a temperature field is computationally very intensive. A brief description of the data reduction method is given in Appendix A.

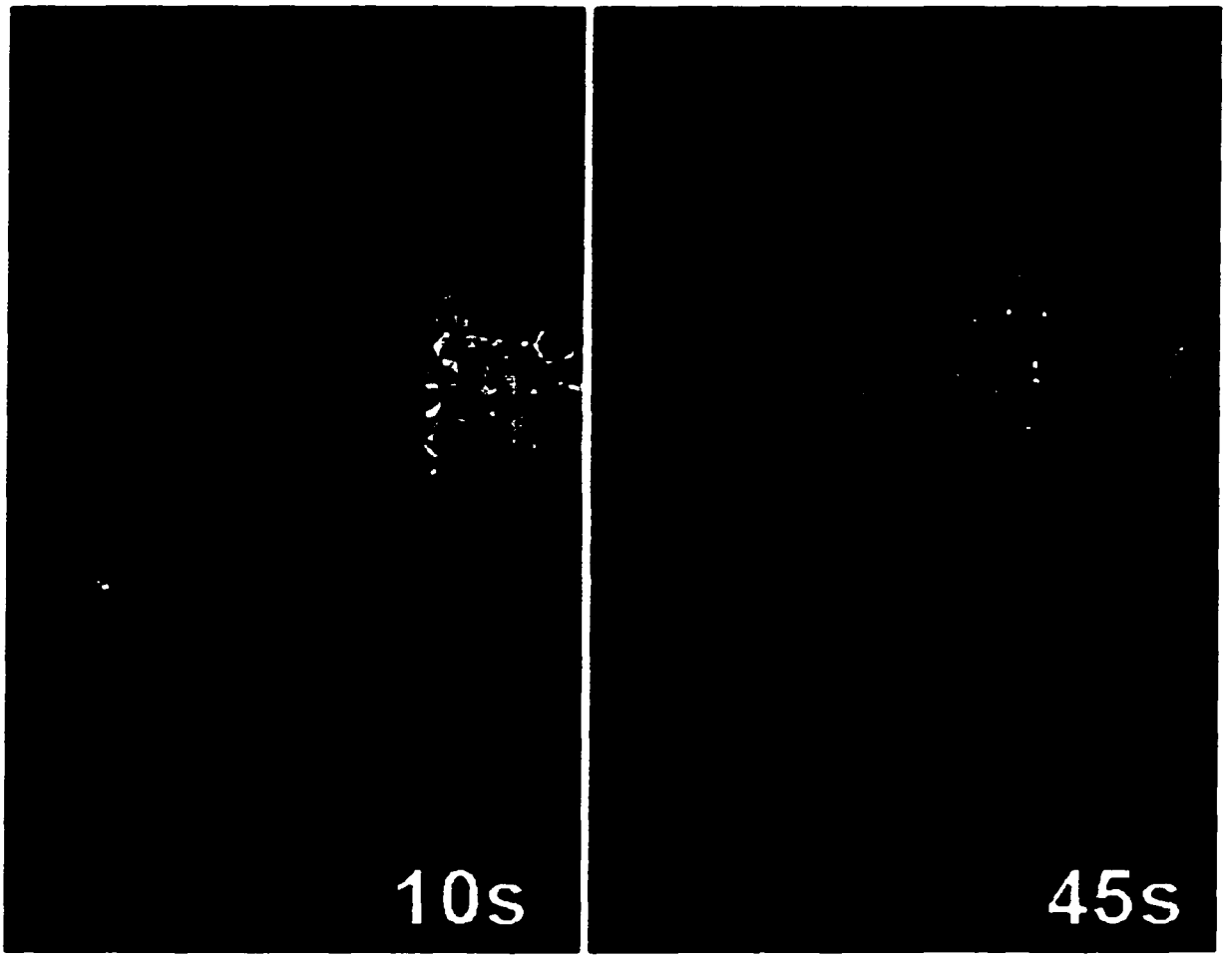


Figure 2.10. Two holographic frames of acrylic from a 2 second duration drill highlighting the evolution of the interference fringes and hence the temperature field. The times marked on the images are relative to the beginning of the drill.

Moiré Deflectometry:

The Moiré deflectometry technique involves passing a collimated coherent beam through the work piece (the phase object), through a pair of Ronchi rulings spaced a

prescribed distance apart and imaged onto a diffuser screen. The gratings, spaced at 8 line pairs per millimeter produce a Moiré fringe pattern when they are rotated with respect to each other as shown in *Figure* 2.11. Subsequent changes in the phase object arising from thermal processing will be reflected by perpendicular deflections of the Moiré fringe pattern. *Figure* 2.12 shows Moiré patterns obtained from the LAMPS test bed before and after laser drilling of an acrylic block. As is the case in holographic fringe interpretation, Moiré fringe deflections can be reduced to temperature field data as long as the processing conditions are cylindrically symmetric.

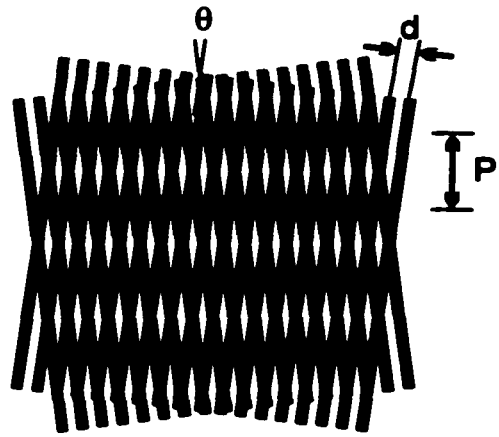


Figure 2.11. Generation of Moiré fringes (spaced 'P' apart) by rotation of two Ronchi rulings having spacing 'd' through an angle of 'θ' with respect to each other.

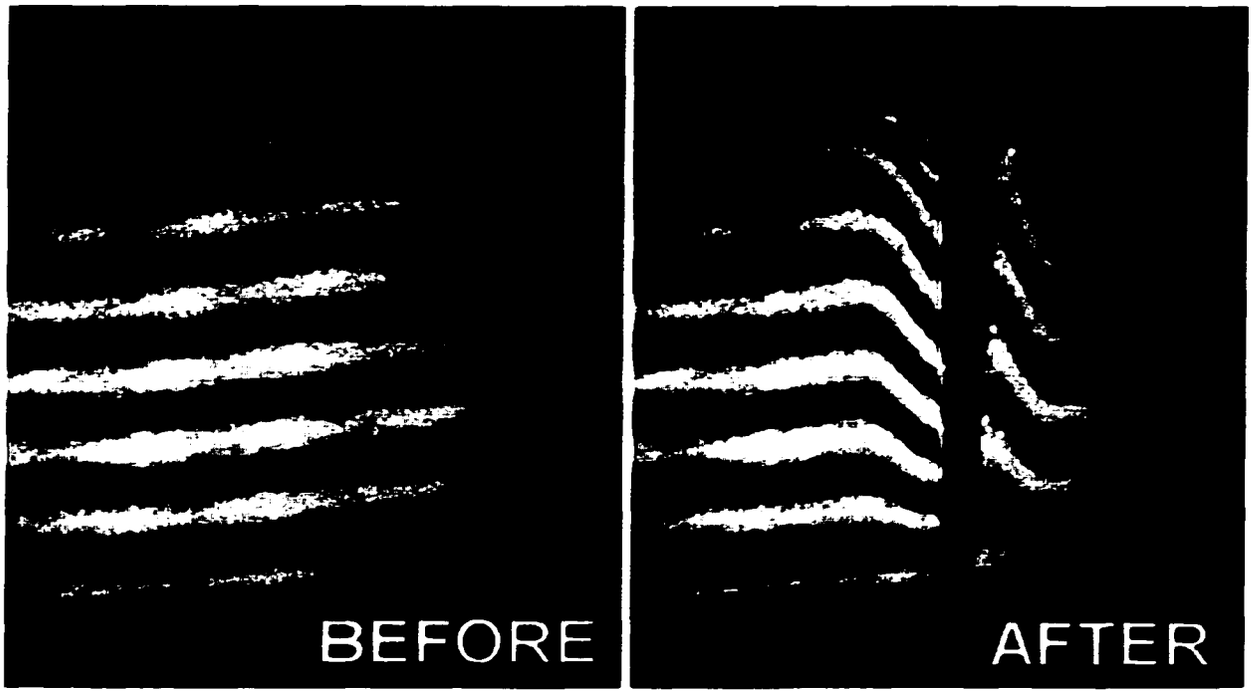


Figure 2.12. Before and after images of the Moiré deflectometry video of the same acrylic drill referred to in the previous figure. The "after" image corresponds to the "10s" holographic image.

Direct Imaging:

Of the imaging techniques, direct imaging was most often used. Though not capable of extracting temperature field data, the direct imaging technique allows direct observation of drill hole (or keyhole) profiles as they evolve. Furthermore, the requirement of complete transparency of the work piece, crucial to the previous two optical diagnostics is reduced to one of translucence, allowing observation of an extended set of materials.

On LAMPS, the majority of the direct imaging was performed with the ccd camera for holographic imaging by removing the holographic plate and replacing the collimated laser beam light source with a diffuse white light source from a halogen lamp. For experiments performed in the industrial laser lab, the camera was mounted directly in front of the work piece with a light source in the rear in the configuration shown in *Figure* 2.8.

A small amount of data was acquired on direct imaging of fluid drilling with a 16 mm movie camera capable of 500 Hz framing rate. High speed film data was subsequently transferred to video tape for analysis.

2.2.2. Acoustic Recording

Acoustic emissions during laser processing were monitored in modulated beam experiments. A fully enclosed fluid cell having only orifices for the processing beam and gas inlet was fitted with an electret microphone above the surface of the fluid. The walls and ceiling of the vessel were lined with acoustic damping foam above the surface to reduce noise and natural vessel resonance. Acoustic signals were concurrently recorded with the direct imaging video to one of the Hi Fi audio channels of the VCR through a microphone preamplifier. The audio bandwidth was nominally 20 Hz to 20 kHz, but in

practice acoustic spectra tended to diminish at frequencies above approximately18 kHz..

2.2.3. Post Processing of Data

Imaging Data:

Imaging data from video tape was manipulated with the aid of video digitizer (frame grabber) boards and software. Processing ranged from simple enhancement of an individual frame for display to lengthy frame sequence averaging. Scale for the video data was provided by an acrylic calibration block scored with a 5.00 mm square grid which would be recorded in the processing plane before commencement of a given set of experiments.

Holographic imaging data from which temperature field data was to be extracted was sent to the National Optics Institute (NOI) where software on Sun workstations had been specifically developed to perform the computationally intensive analysis described in Appendix A.

Acoustic Data:

Recorded acoustic data was post processed primarily with a National Instruments data acquisition card interfaced to a PC. Raw audio data was digitized at 44.1 kHz

sampling rate, then fed through a 2048 point fast Fourier transform filter utilizing a hamming window yielding a 2048 discrete point sound level spectrum in dB ranging from 0 to 22050 Hz. Individual FFT's required approximately 1 second of sound signal, and hence each drilling experiment yielded about 10 FFT's. A detailed description of the steps taken to isolate the drilling only component of the acoustic spectrum will be presented in chapter 4.

2.3. Experimental Data Set

Because of the wide array of materials and parameters, the best way to present the parameters involved in the specific materials of the data set is in a tabular form. *Table* 2.1 lists the materials and indicates the extent of the diagnostics used for each. *Table* 2.2 summarizes the environmental and processing conditions each of the materials were subjected to.

Table 2.1: Summary of experimental diagnostics used for each material.

	Experimental Diagnostics			
Material	Direct imaging	Holographic imaging	Moiré Deflectometry	Acoustic Monitoring
Acrylic	✓	✓	✓	
Fused Quartz		✓	✓	
Soda Lime Glass		✓	✓	
Paraffin	✓			✓*
Gelatin	✓	✓	✓	✓*
Water	✓	✓	✓	✓**
Glycerol (100%)	✓	✓	✓	✓**
Glycerol (66%)	✓	✓	✓	✓*
Glycerol (50%)	✓	✓	✓	✓*

* Data acquired without anechoic enclosure around sample. (i.e. rough measurements only)

** Anechoic chamber data acquired only for ground based experiments involving primarily modulated beam experiments.

Table 2.2: Summary of processing conditions investigated for each material.

	g-level (1g = 9.8m/s^2)			laser operating mode		
Material	Low (<0.01g)	Normal (1g)	High (1.8±.1g)	CW	Pulse train	Single shot
Acrylic	✓	✓	✓	✓	✓	✓
Fused Quartz	✓	✓	✓	✓		
Soda Lime Glass	✓	✓		✓		
Paraffin	✓	✓	✓	✓		
Gelatin	✓	✓	✓	✓		
Water	✓	✓	✓	✓	✓	✓
Glycerol (100%)	✓	✓	✓	✓	✓	
Glycerol (66%)	✓	✓	✓	✓		
Glycerol (50%)	✓	✓	✓	✓		

All of the processing was carried out with the laser incidence parallel to the gravitational acceleration vector (for normal and high g processing). The beam was focused with a five inch (127 mm) focal length planoconvex ZnSe optic with the focal plane nominally located at the surface of the specimen. Uncertainty in the surface-focal plane coincidence was typically ± 0.5 mm for solids and ±1.5 mm for liquids[10]. Beam waist dimensions were typically 0.25 to 0.30 mm in diameter, with the smaller associated with the LAMPS based laser and the larger with the VFA-1700. Intensity ranges depended on the material, but overall, the intensity ranged from 4×10^4 to 3×10^5 W/cm^2.

[10] The higher uncertainty associated with the focal plane for liquids arises due to the free nature of the "free" surface. Penetration processing of liquids generates small surface waves emanating from the drill hole analogous to the waves on a smooth pond generated by tossing pebbles into it. However, most of the variation comes from flight based experiments where unavoidable lateral accelerations can cause shifts of up to a millimeter in the free surface location at the point of incidence.

All of the experiments were carried out in air, over a temperature range from 15°C to 30°C. The ground based experiments were all carried out at standard atmospheric pressure (1atm.), while the KC-135 based experiments were all performed at the ambient cabin pressure of 0.8 ATM.

Detailed results of the experiments will be provided in chapters three and four for the solids and liquids respectively.

Chapter Three

Fused Quartz Holography

3.1. Motivation

The availability of the holographic optical diagnostic system in LAMPS which allows visualisation (and quantification) of temperature fields generated by laser processing is unprecedented, and as such, any number of appropriately transparent candidates would be of interest to investigate. Isothermal fields derived from experimental data can be compared directly with theoretical models to gain an improved

understanding of the presently uncertain process dynamics. However, due to the prohibitive cost involved in reducing raw holographic interferogram data to temperature fields, resource limitations restrict a *full* thermal analysis to only a few video frames. These restrictions limit the material to one which could provide the best insight into the effect of process variables, ideally a material which exhibits dynamic and morphological similarities to an industrially relevant material.

With only the above restrictions to guide the choice, soda lime glass emerges as a good choice since it has been previously studied during laser welding [39][11]. Unfortunately, optical inhomogeneities in soda lime glass cubes rendered them unusable for quantitative analysis. This distortion in soda lime glass is shown in *Figure* 3.1a and compared to transmission through a cube of fused quartz in *Figure* 3.1b.

The main process variable of interest is the gravitational acceleration which gives rise to all of the buoyancy driven dynamics within the melt pool. What is desired is a transparent material with good optical quality, which also exhibits g-level dependent behaviour during laser processing.

[11] The striking similarity between keyhole welding of steel and soda lime glass observed by Arata's group provided the motivation for investigating this material.



A B

Figure 3.1. **Optical transmission in one inch thick cubes of soda lime glass (A) and fused quartz (B).**

Acrylic provides the optical quality required for holographic investigations, but as the laser interaction primarily involves direct sublimation of the target material, a lack of liquid makes acrylic processing insensitive to gravity.

In fused quartz, specimens can have exceptional optical quality and earlier studies of drilling of fused quartz in a variable gravity environment by Mueller et al [16] indicate that the drill hole wall temperature distribution is dependent on the gravitational acceleration. Direct imaging of the molten material surrounding the drill hole reveals that the presence of gravity tends to generate considerably more dynamic thermal behaviour while in low gravity the drill hole temperature profile tends to be stable and uniform. *Figure* 3.2 highlights the typical visual differences between drill holes in normal and low gravity drilling in fused quartz.

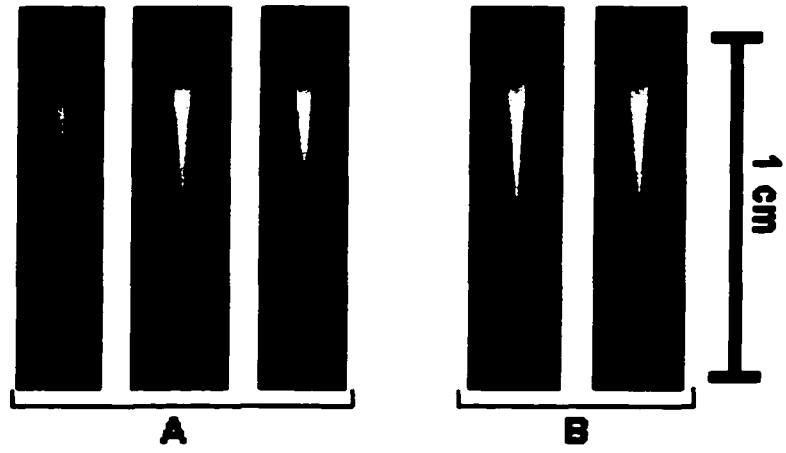


Figure 3.2. Comparison of drill hole profiles during normal (A) and low (B) gravity drilling of fused quartz. The surface of the quartz is coincident with the top of the length scale. Dark regions of cooler material evident in normal gravity drilling are quite dynamic and tend to migrate during the drilling.

These considerations suggest that fused quartz is a good candidate for full holographic analysis, but in choosing fused quartz, we likely sacrifice to some degree a similarity in process dynamics to those of industrial materials. This can be seen from the profile of the heat affected zone (HAZ) in soda lime glass compared to that of fused quartz in *Figure* 3.3. The HAZ associated with the lime glass is made visible by virtue of extensive stress fracturing and takes a form not unlike HAZ profiles viewed along the bead of laser welded metal. The HAZ in quartz is not apparent in the figure but higher magnification reveals a region of optical distortion surrounding the drill hole extending ~ 0.5 mm beyond the drill hole wall. Even with this limitation, fused quartz was found to be the best candidate for a full thermal analysis.



A B

Figure 3.3. HAZ in soda lime glass (A) compared to that in fused quartz (B). The HAZ in the fused quartz image is not visible at this magnification but extends less than 0.5 mm beyond the cavity wall.

3.2. Selection of Interferograms for Analysis

The involved nature of the data reduction from interferogram to isotherms, placed tight constraints on the number of video frames which could be fully analysed. Ultimately, only six interferograms were chosen corresponding to three separate drilling experiments under varying conditions. *Table* 3.1 summarizes the experimental conditions for the six video frames chosen.

Table 3.1: Experimental conditions for six holographic frames chosen for thermal analysis.

Experiment	Laser Power	Drill Type	g-level	Time
1	105±5 watts	initiation	low	2 seconds
1	105±5 watts	initiation	low	5 seconds
2	91±4 watts	initiation	normal	2 seconds
2	91±4 watts	initiation	normal	5 seconds
3	91±4 watts	pre-drilled	normal	2 seconds
3	91±4 watts	pre-drilled	normal	5 seconds

The column labeled "Drill Type" indicates two types of drilling, defined as "initiation" and "pre-drilled". The initiation drills entail directing the focused laser on a previously unirradiated surface at time t=0 with the drill hole subsequently developing to its full depth over the next two to three seconds. In contrast, experiments labeled pre-drilled involved directing the focused laser into an existing hole, drilled with the same laser power. The rationale for drilling into a preexisting hole stems from the nature of the model used to approximate the process, as will be described in section 3.3. In terms of the model, the pre-drilled experiments are more closely approximated by the model, which assumes a static structure for the drill hole.

The choice of the frames is intended to provide the maximum flexibility in terms of comparative analysis. The key experiment for comparative analysis is experiment 2 from *Table* 3.1. Experiments 1 and 2 provide the opportunity to identify differences in thermal transport which arise primarily due to gravity while experiments 2 and 3 highlight differences in thermal transfer associated with different initial drill hole

geometry. Finally, two temporal points for each of the three separate drilling experiments provides another set of data for the cross comparisons described above, as well as a measure of the rate of thermal diffusion in each experiment.

The choice of t=2 s as the initial time point was somewhat arbitrary, but tightly spaced interference fringes during the early stages of drilling allowed only the extent of the outermost fringe to be resolved. It was observed that after two seconds, fringes had spread to the extent that between 3-5 of the outermost fringes were easily resolved. Furthermore, by the 2 second mark, holes which had been initiated from the surface had reached 90% or more of their full depth implying that a steady state condition was being established.

t=5s was chosen to match the length of the laser pulse, and t longer than this would only serve to complicate analysis, as boundary conditions at the hole wall undergo abrupt changes when the laser source is terminated.

Interferograms of the three experiments are shown in *Figures* 3.4, 3.5, and 3.6. The diminished brightness of the t=5 s interferograms is attributable to laser shut off at the end of drilling. The top of the fused quartz is coincident with the top of the centimeter scale marks. The laser drilling process is assumed to produce a cylindrically symmetric thermal disturbance, and hence the families of fringes in the interferograms take a form similar to that of prolate (elongated) half spheres.

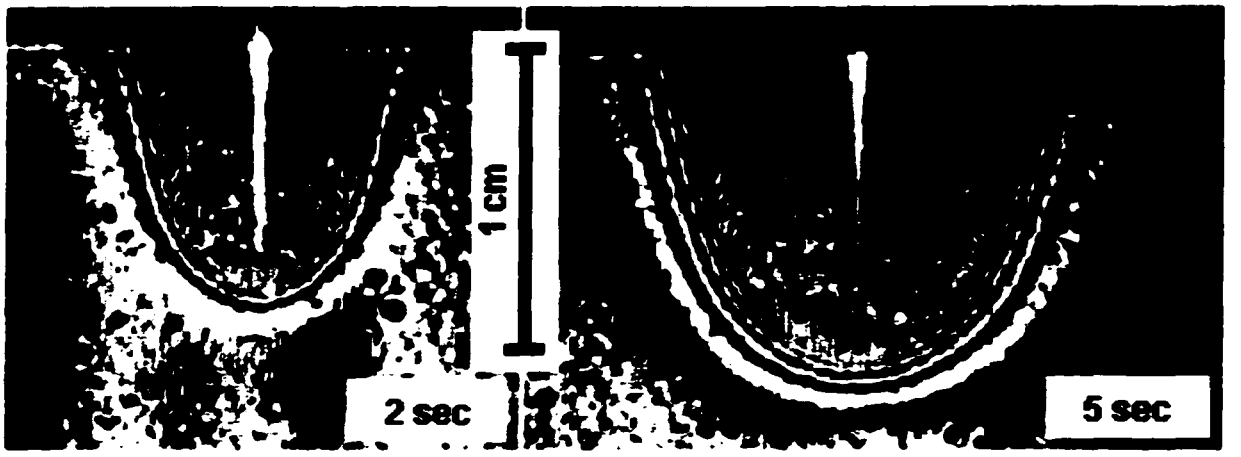


Figure 3.4: Interferograms obtained during laser drilling of fused quartz in low gravity (corresponding to experiment 1 of *Table* 3.1).

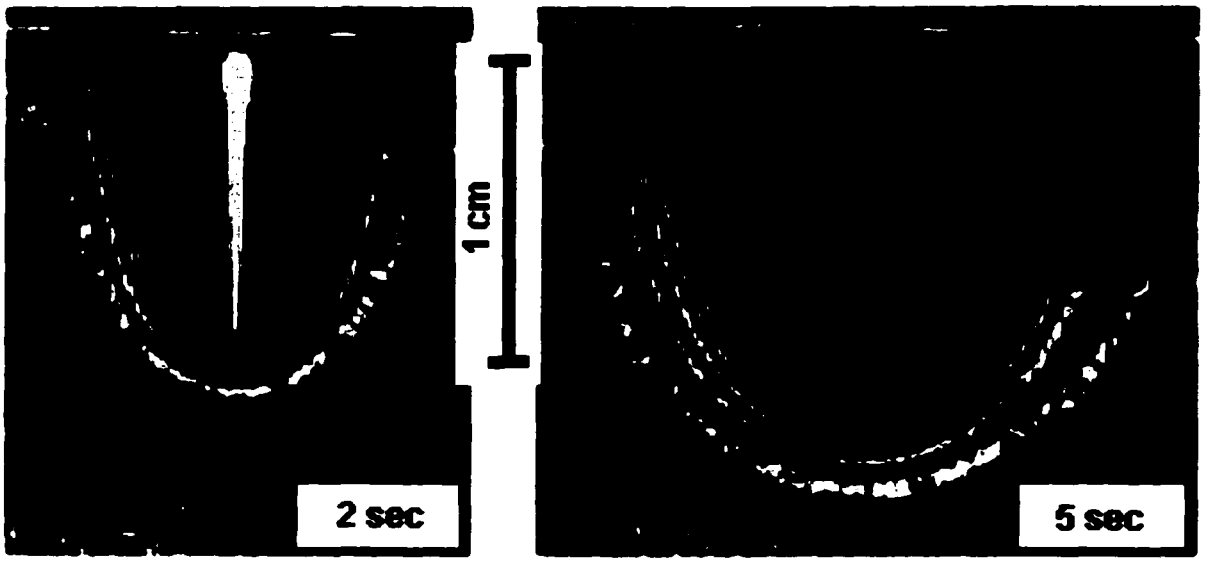


Figure 3.5: Interferograms obtained during laser drilling of fused quartz in normal gravity (corresponding to experiment 2 of *Table* 3.1).

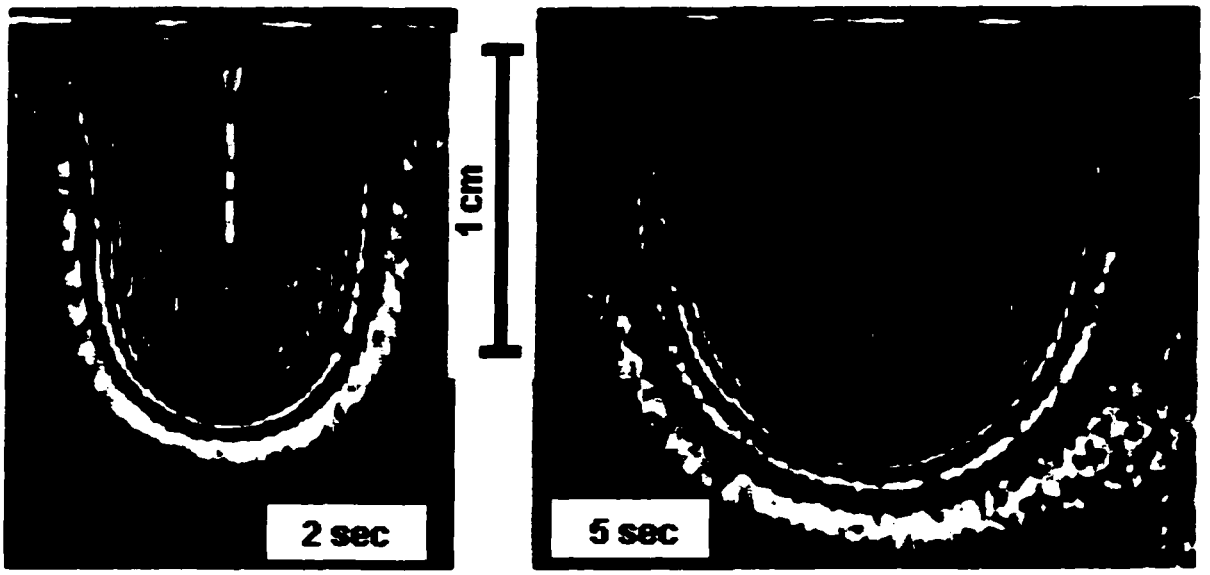


Figure 3.6: Interferograms obtained during laser drilling of fused quartz in low gravity (corresponding to experiment 3 of *Table* 3.1). In this case, the laser was directed into a preexisting hole.

Comparatively, fringe fields in experiments 1 and 2 in both normal and low gravity exhibit similar overall structure. The only apparent differences are in the extent of the outermost fringes, with the normal gravity fringe field extending somewhat farther than the low gravity fringe field. Oddly, the low gravity experiment was performed with 15% higher incident power from the laser.

It should be noted however that the low and normal gravity experiments were all carried out with the laser power supply set at the same output level. Changes in laser

power possibly arose through physical changes in the resonator geometry[12] which would alter the mode content of the beam. The laser (specified to have greater than 90% TEM_{00} content) may have provided higher powers at a given power supply setting in low gravity but in a mixed mode form which would affect the focusability and effective absorption of the beam in the quartz. Unfortunately, low gravity beam profiles were not acquired to confirm this possibility.

Comparing fringe fields associated with initiation and pre-drilled *normal gravity* experiments (experiments 2 and 3), the major difference appears in the elongation of the fringes. As would be expected, fringes associated with the pre-drilled experiment show greater radial evolution deep in the hole since thermal transfer along the full length of the hole is simultaneously initiated at t=0. The extent of the fringes near the surface of the quartz compares well between the two normal gravity experiments.

[12] The resonator cavity in the Melles Griot CRF-1200 laser is constructed of glass, and hence is relatively susceptible to minor deformation brought on through changes in gravitational acceleration.

3.3. Process Models

3.3.1. Choice of Coordinate System

As mentioned in section 3.2, the interferometric fringes observed in the drilling of fused quartz take on the shape of elongated or prolate half spheres. The isotherms can be expected to exhibit similar behaviour. If this is in fact the case, then the thermal behaviour within the framework of prolate spheroidal geometry may reduce to a one dimensional problem, simplifying matters greatly. The coordinate transformation relating the more familiar circular cylindrical coordinate system (r, Ψ, z) to prolate spheroidal coordinates (η, θ, Ψ) is detailed in Appendix B. Here, only the results of the transformations will be used. The best coordinate analogies to those of the prolate spheroidal frame are in the spherical polar system (r, θ, Ψ) where r represents the radial coordinate, θ represents the axial angular coordinate measured from the positive *z* axis, and Ψ represents the azimuthal angular coordinate measured from the positive *x* axis. The azimuthal coordinate Ψ remains untransformed from its original form in cylindrical coordinates spanning the range $\Psi \in [0..2\pi]$. The θ coordinate in the prolate spheroidal system is analogous to the polar coordinate in spherical coordinates, spanning the same range $\theta \in [0..\pi]$. Unlike it's spherical counterpart however, surfaces generated by setting θ=constant are hyperboloids (rather than cones). In a similar manner, the η coordinate is

radial-like and shares the same domain as the radial coordinate ($\eta \in [0..\infty]$) but surfaces generated by setting η=constant are not surprisingly prolate spheroidal rather than spherical. Furthermore, rather than reducing to a single point at the origin, setting η=0 results in a line of length $2a$ centered at the origin directed along the z axis. The parameter a in fact defines the semi-major focal length of the entire family of η=constant prolate spheroids. A diagram showing contours of η=constant, and θ=constant is shown in appendix B, *Figure* B.1.

The fact that the shape of η=constant contours is parametrically dependent on the semi-major focal length a makes it possible to quantify the fit of fringe field families to families of η=constant for a given semi-major focal length a. The experimental data appears to fit satisfactorily into a prolate spheroidal coordinate framework by simple inspection of the interferogram data. However, for a given family of elongated spheroids to satisfy $\eta_i = const$, there are specific relationships between major and minor axes which must be adhered to. From Appendix B, we have the following relationship relating the semi-major focal length to semi-major and semi-minor axes of a given prolate spheroid,

$$b_i^2 - c_i^2 = a^2 = const \qquad 3.1$$

where b_i and c_i represent the semi-major and semi-minor axis lengths respectively of the i'th prolate spheroid in the family. All three quantities in *Equation* 3.1 can be directly

measured from the interferograms. The semi-major focal length was assumed to be approximately equivalent to the depth of the hole and measured directly from the quartz with a traveling microscope. The semi-minor and semi-major axes were determined from measurement of the fringes on the interferograms. Semi-minor axis estimates were complicated somewhat due to an outward inflection of the fringes near the surface (see *Figures* 3.4-6) likely associated with additional surface heating from the beam wings. The trends of the fringes before the inflection were extrapolated to the surface to estimate the semi-minor axes. The measured semi-minor and semi-major axes for several of the outermost fringes are plotted as a function of time in *Figures* 3.7 and 3.8 respectively for a ground based initiation type drill of 3 seconds duration.

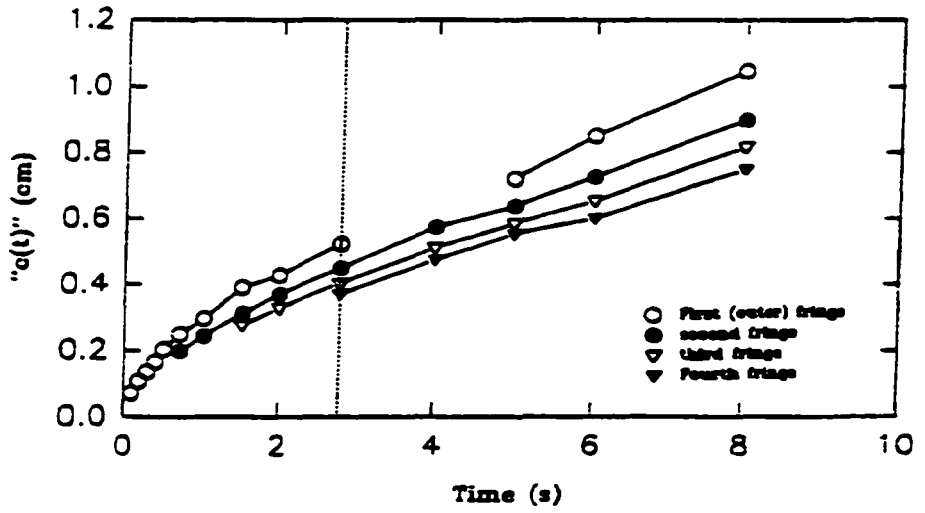


Figure 3.7. Semi-minor axes of four outermost fringes of interferogram plotted against time for a 3 second drill into fused quartz. The vertical line through the data indicates the point at which the laser was turned off.

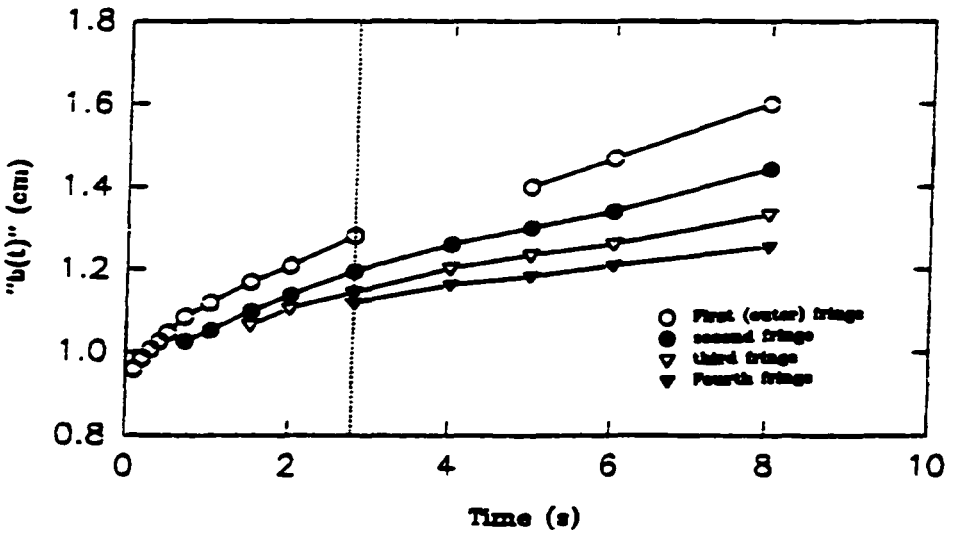


Figure 3.8. Semi-major axes of four outermost fringes of interferogram plotted against time for a 3 second drill into fused quartz. The vertical line through the data indicates the point at which the laser was turned off.

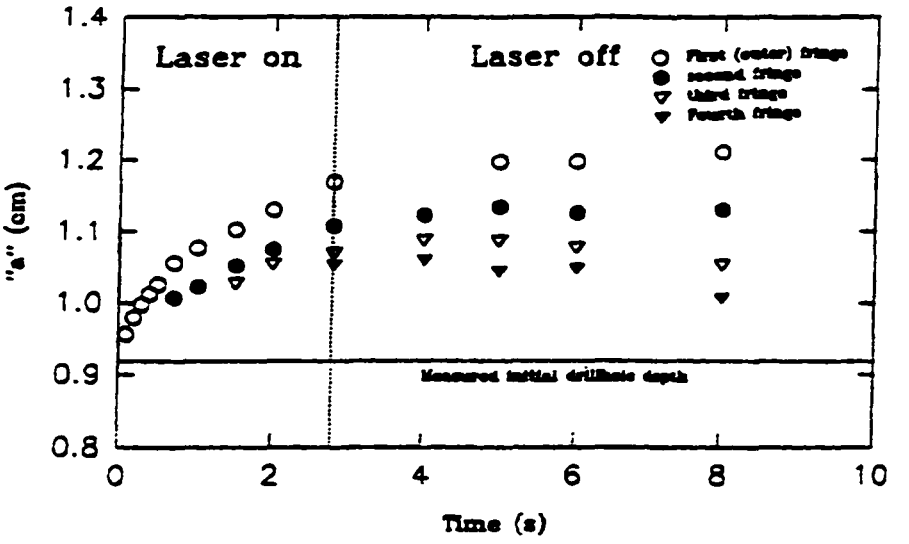


Figure 3.9. Calculated semi-major focal length from *Equation* 3.1 and the data of the previous two figures. The measured drill hole depth is marked by the horizontal line and measures 0.92 cm.

Figure 3.9 shows a plot of the calculated semi-major focal length a for the measurements performed in the previous two figures. A horizontal line indicates the directly measured value for a obtained with a traveling microscope. The family of isotherms do not appear to conform strictly to the prolate spheroidal geometry, but the four outermost fringes do all fall within approximately 10% of an average calculated semi-major focal length of 1.05 cm for the entire duration of the drilling. This calculated result exceeded the measurement of the drill hole length of 0.92 cm by 15%. Though the fringe data does not represent a perfect fit to prolate spheroidal geometry, the fit is reasonable, and one should also recall that the fringe field itself does not represent the temperature field. For these reasons, a solution space in prolate spheroidal coordinates was deemed appropriate. The semi-major focal length parameter was chosen to be 1.0 cm for reasons of simplicity and as a compromise between the direct measurements and calculation results mentioned above. Both the analytical and numerical models described in the following sections will be solved within a prolate spheroidal framework.

3.3.2. General Process Model

The heat transfer captured holographically was a transient process, and hence requires solution of the more complex time dependent heat conduction (diffusion) equation. The familiar diffusion equation,

$$\nabla^2 T = \frac{1}{\alpha}\frac{\partial T}{\partial t} \qquad 3.2$$

where T is the temperature (in degrees Kelvin) and α is the thermal diffusivity constant (in m^2/s). To solve *Equation* 3.2 in prolate spheroidal coordinates one requires the Laplacian [40]:

$$\nabla^2 = \frac{1}{a^2(\sinh^2\eta + \sin^2\theta)}\left[\frac{\partial^2}{\partial\eta^2} + \coth\eta\frac{\partial}{\partial\eta} + \frac{\partial^2}{\partial\theta^2} + \cot\theta\frac{\partial}{\partial\theta}\right] + \frac{1}{a^2\sinh^2\eta + \sin^2\theta}\frac{\partial^2}{\partial\psi^2} \qquad 3.3$$

The quartz drilling possesses circular symmetry along the z axis, and hence, $T = T(\eta, \theta, t)$ only. This allows the latter term in *Equation* 3.3 to be dropped, so the diffusion equation reduces to:

$$\frac{1}{a^2(\sinh^2\eta + \sin^2\theta)}\left[\frac{\partial^2 T}{\partial\eta^2} + \coth\eta\frac{\partial T}{\partial\eta} + \frac{\partial^2 T}{\partial\theta^2} + \cot\theta\frac{\partial T}{\partial\theta}\right] = \frac{1}{\alpha}\frac{\partial T}{\partial t} \qquad 3.4$$

To complete the solution of Equation 3.4, boundary conditions are required to solve for the arbitrary constants in the solution. The processing acts on effectively a semi-infinite half space in which the surface (in air) can be approximated as an adiabatic boundary. In terms of the prolate spheroidal coordinates, this amounts to the following boundary condition:

$$\frac{\partial T}{\partial\theta} = 0, \qquad \theta = \frac{\pi}{2} \qquad 3.5$$

Another adiabatic boundary condition which arises due to circular symmetry is

$$\frac{\partial T}{\partial \theta} = 0, \qquad \theta = 0, \pi \tag{3.6}$$

In the infinite field, the temperature is assumed to be undisturbed from its initial state, implying a Dirichlet boundary condition [41]:

$$T = T_{\infty}, \text{ or } T - T_{\infty} = 0, \qquad \text{as } \eta \rightarrow \infty \tag{3.7}$$

Drilling vapourises a narrow cavity into the quartz along the z axis which can be considered as an isothermal prolate spheroidal half cavity with $\eta = 0$. This means that the length of the isothermal cavity effectively represents the semi-major focal length a, and implies the final boundary condition:

$$T = T_o, \qquad \eta = 0 \tag{3.8}$$

The problem was solved analytically using the separation of variables technique, but proved to be non-physical. The complete analytical solution is presented in Appendix C, but will be discussed no further in this thesis.

3.3.3. Numerical Results

Numerical modeling was carried out using code originally developed for heat transfer in oblate spheroidal geometry [42]. As might be expected, the transformations

giving rise to oblate spheroidal geometry are very similar to those for prolate spheroidal geometry. The conformal transformation required to generate oblate spheroidal geometry is as follows:

$$w = z + ir = a\sinh(\eta + i\theta) \qquad 3.9$$

Comparison of *Equation* 3.9 with *Equation* B.1 of Appendix B reveals that all that separates the two coordinate systems from each other is the exchange of a sinh for a cosh in the transformation equation. As a result, conversion of the finite element code to prolate spheroidal geometry was very straightforward.

The purpose of modeling drilling in fused quartz drilling in prolate spheroidal coordinates is to maximize the match up of the heat flow geometry and the finite element mesh geometry. Heat flow which is strongly two or three dimensional (within a given coordinate system) requires a much finer FEA mesh to maintain accuracy than that which is close to one dimensional [43].

The model assumes identical boundary conditions as those given in *Equations* 3.5 .. 3.8 with the exception that the $\eta = 0$ boundary condition is replaced with a non zero value for η. The exact value for the boundary of the cavity $\eta = \eta_0$ is user specified in the form of the semi-major focal length a, and the aspect ratio of the cavity, defined as c/b, with a, b, and c as defined in appendix B. The temperature field output is dimensionless, ranging from 0 to 1 and defined as

$$T^* = \frac{T - T_\infty}{T_0 - T_\infty}, \qquad 0 \le T^* \le 1 \tag{3.10}$$

where T is the absolute temperature, T_∞ is the infinite field absolute (room) temperature, and T_0 is the drill hole wall temperature. The radial and depth coordinates of the solutions are dimensionless, being normalised to the semi-major focal length a. The time input is dimensionless as well, and expressed as the Fourier number, defined in this problem as:

$$t^* = \frac{\alpha t}{a^2} \tag{3.11}$$

The semi-major focal length a, and the aspect ratio c/b were determined by direct measurement with a traveling microscope. These parameters were found to be consistent across the range of processing performed and were:

$$a = 1.0cm\,, \qquad c/b = 50 \tag{3.12}$$

Calculation of the appropriate Fourier number to match the 2 and 5 second experimental drills proved to be somewhat more involved. The finite volume model assumes a constant thermal diffusivity α, while in reality, the diffusivity is temperature dependent. As a result, an average value for α was calculated based on available manufacturer's data [44] and was found to be $\alpha = 7.65 \times 10^{-3}$ cm^2/s based on thermal conductivity and heat capacity data between 0-950°C. Based on the averaged α and the measured dimension a, *Equation* 3.11 can be solved for t^*. Calculated values are given in

Table 3.2.

Table 3.2. Fourier time equivalents for two and five second holes in fused quartz.

time (seconds)	Fourier number*
2	0.015
5	0.038

* Based on characteristic length of 1 cm and $\alpha=7.65\times10^{-3}cm^2/s$.

Further inputs to the model included time step size, Δt^* and the number of time steps. $\Delta t^* = 5\times10^{-5}$ was chosen for both Fourier numbers which when started at $t^*= 0$, required 300 time steps to reach $t^*= 0.015$ and 760 steps to reach $t^*= 0.038$. The mesh spacing was also adjustable, and it was found that a grid consisting of 80 η by 40 θ divisions gave satisfactory results without requiring excessive computation time. The distribution of the mesh points in Cartesian space is illustrated in *Figure* 3.10. The numerical model was tested against the known solution for spherical geometry with the following parameters: $b/c = 1.01$, $N_\eta = 80$, $N_\theta = 40$, and t^* ranging from 6×10^{-5} - 4×10^{4}. The results of the numerical simulation fell within 0.6% of the results for the exact solution, validating the accuracy of the converted code.

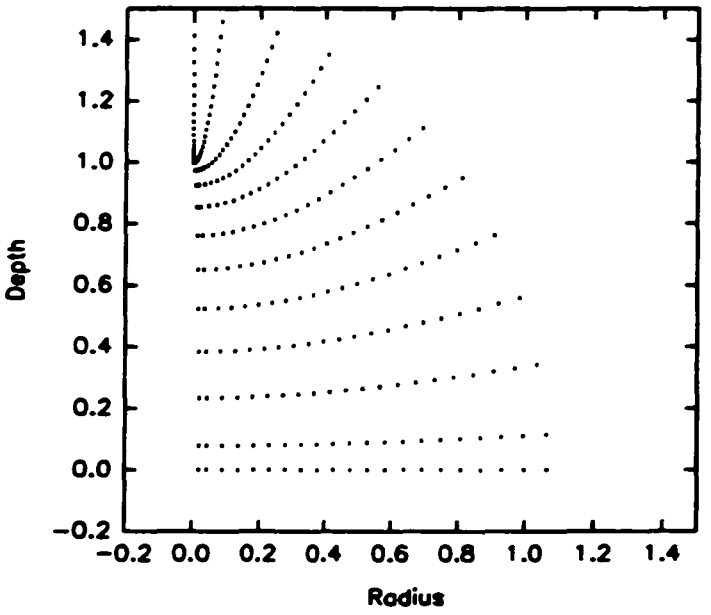


Figure 3.10. Illustration of distribution of prolate spheroidal finite element mesh in Cartesian space. Note the increased density of grid points near the tip of the prolate spheroidal cavity.

The results of numerical simulations using the prolate spheroidal parameters specified previously for the 2 and five 5 drills are shown in *Figures* 3.11 and 3.12. The isothermal fields were generated from dimensionless r, z, T^* data using surface and topographic plotting software[45].

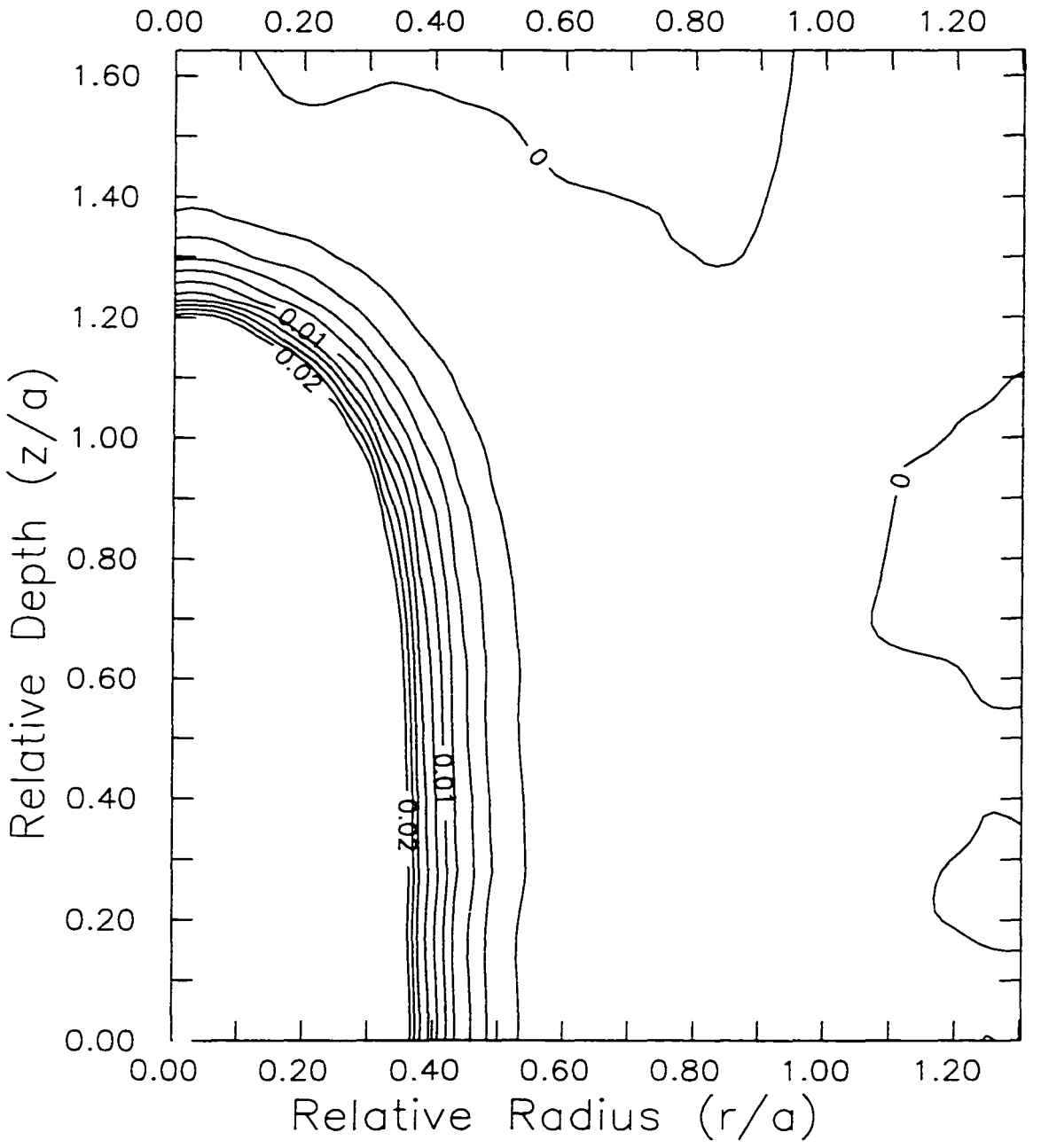


Figure 3.11 **Results of numerical simulation corresponding to t^*=0.015 (t=2 seconds). The isotherm spacing is ΔT^*=0.001.**

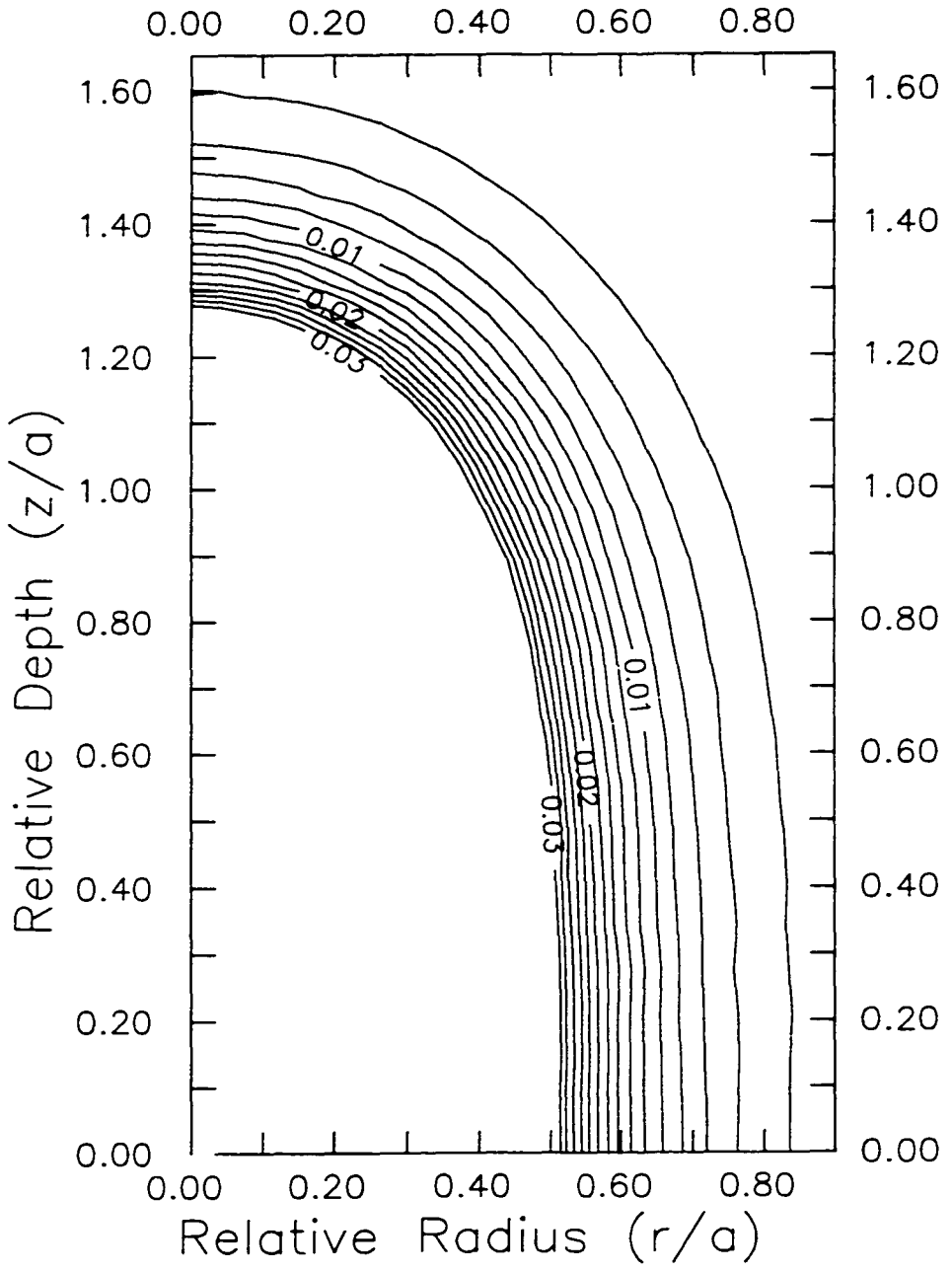


Figure 3.12 Results of numerical simulation corresponding to t^*=0.038 (t=5 seconds). The isotherm spacing is ΔT^*=0.001.

As expected, the simulation corresponding to a 5 second drill shows thermal changes which extend further into the medium than for the simulation corresponding to the 2 second drill. Simulation results indicate an almost depth independent radial thermal field until well over 50% of the hole depth.

3.4. Experimental Temperature Distribution

Analysis of the interferograms of *Figures* 3.4, 3.5, and 3.6 was carried out over the regions of resolvable fringes according to the techniques described in chapter 2 and Appendix A. Unfortunately, the number of resolvable fringes associated with the 2 second interferogram of the pre-drilled ground based experiment was insufficient to yield temperature results. In fact, unresolved fringes evident in all of the interferograms of *Figures* 3.4-3.6 limit thermal calculations to regions at some distance from the hole.

The National Optics Institute provided results of the analysis in the form of (dimensioned) r, z, and T data. For comparison with results of the simulations, the data was non-dimensionalised. *Figures* 3.13-3.17 show the isothermal fields generated by the data. Horizontal line segments on each plot indicate the distribution of data points and each figure is accompanied by a scaled down image of the raw interferogram indicating the region covered by the analysis. The orientation of the interferograms is rotated to

match those of the isothermal plots. Ambient temperature was 26°C for the low gravity experiment, and 23°C for normal gravity experiments.

The isotherms generally follow smooth contours centered around the drill hole axis, with a tapering trend towards smaller radii at greater depths. Radial fluctuations in temperature give rise to a wavy appearance on some of the plots, but this behaviour appears linked to the discrete spacing of the data points in the *z* direction.

Drilling under low gravity (*Figures* 3.15-3.16) resulted in somewhat lessened radial and depth extent of heating when compared to their normal gravity counterparts of *Figures* 3.13- 3.14, indicating perhaps a lower temperature process in the drill hole during drilling under low gravity. It should be pointed out however that differences in the measured laser power for the experiments (summarized in *Table* 3.1) would tend to favour just the opposite effect.

Differences in temperature fields between drilling an initiated hole and drilling into a preexisting hole can be seen by comparing *Figures* 3.14 and 3.17. The extent of the thermal fields compare well near the surface, but the initiated hole exhibits much greater tapering of the isotherms as the hole proceeds deeper into the quartz.

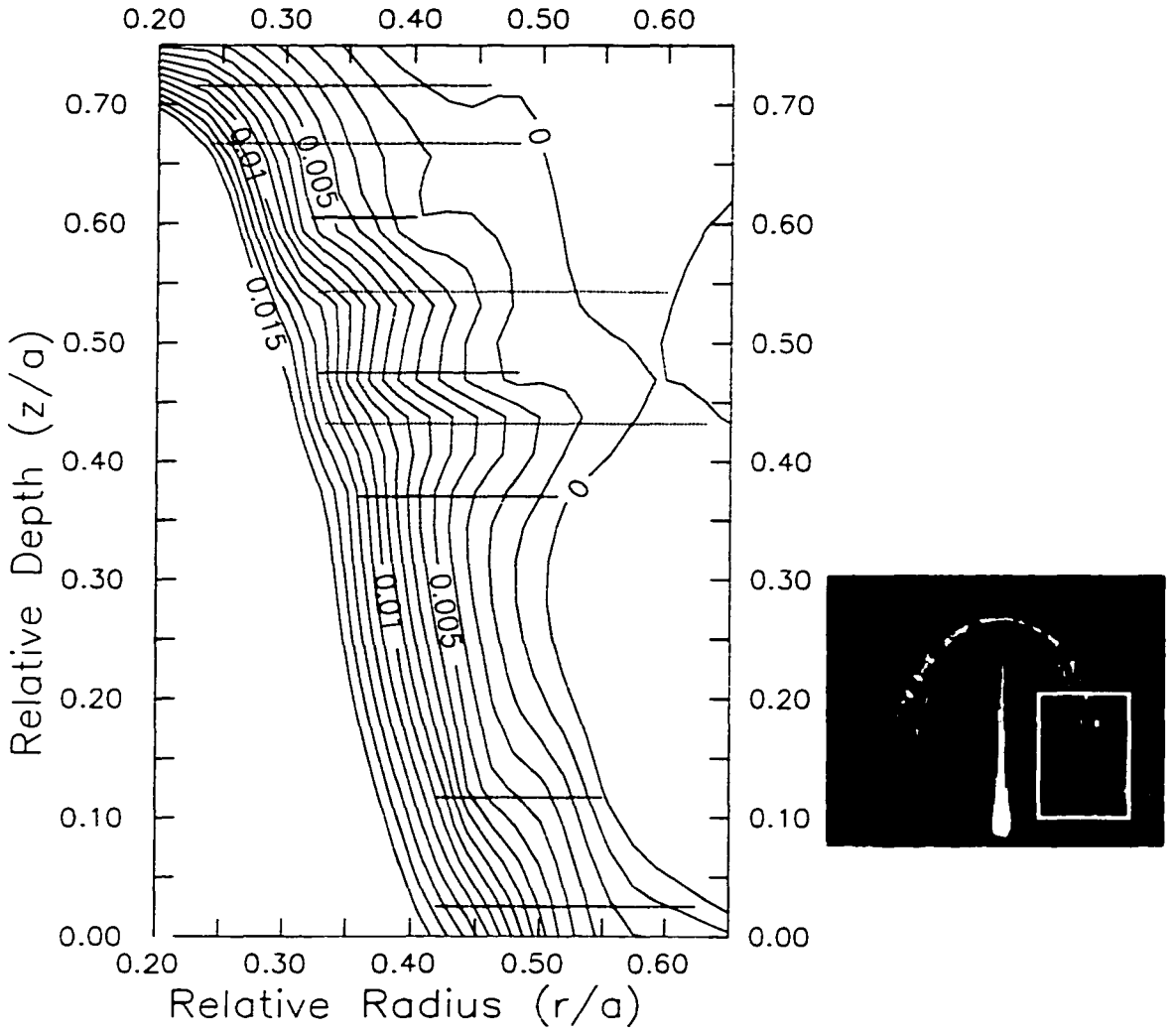


Figure 3.13 **Isotherm field generated from holographic data during drilling of fused quartz at t=2 s under normal gravity conditions, corresponding to an initiation type hole.**

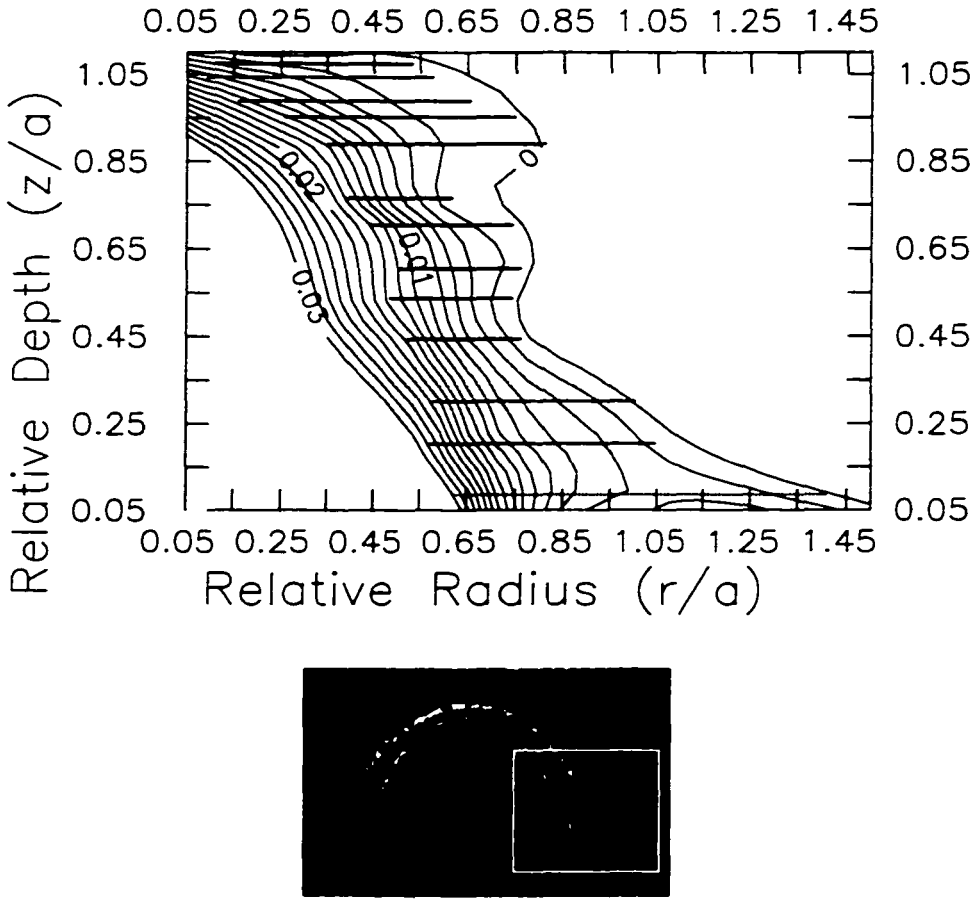


Figure 3.14 **Isotherm field generated from holographic data during drilling of fused quartz at *t*=5 s under normal gravity conditions, corresponding to an initiation type hole.**

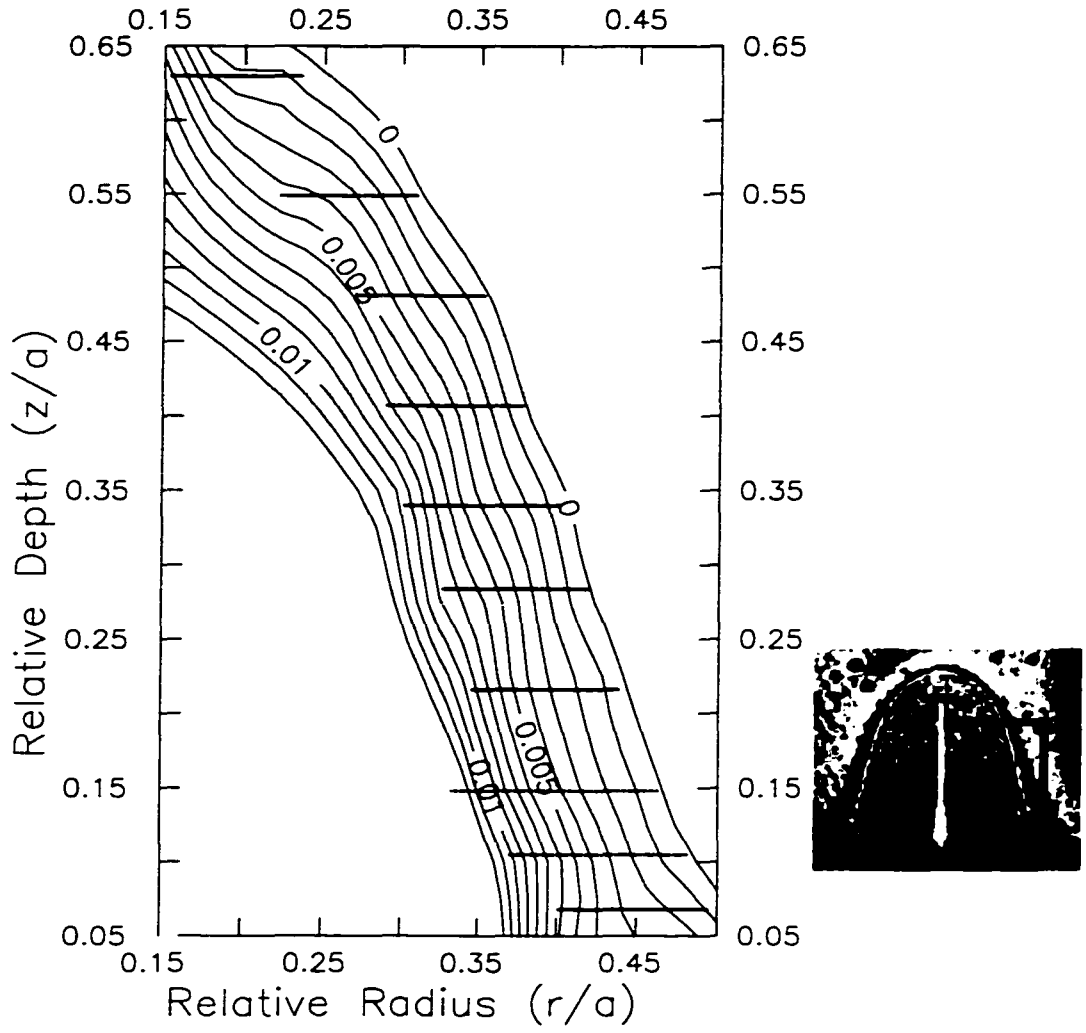


Figure 3.15 **Isotherm field generated from holographic data during drilling of fused quartz at t=2 s under low gravity conditions, corresponding to an initiation type hole.**

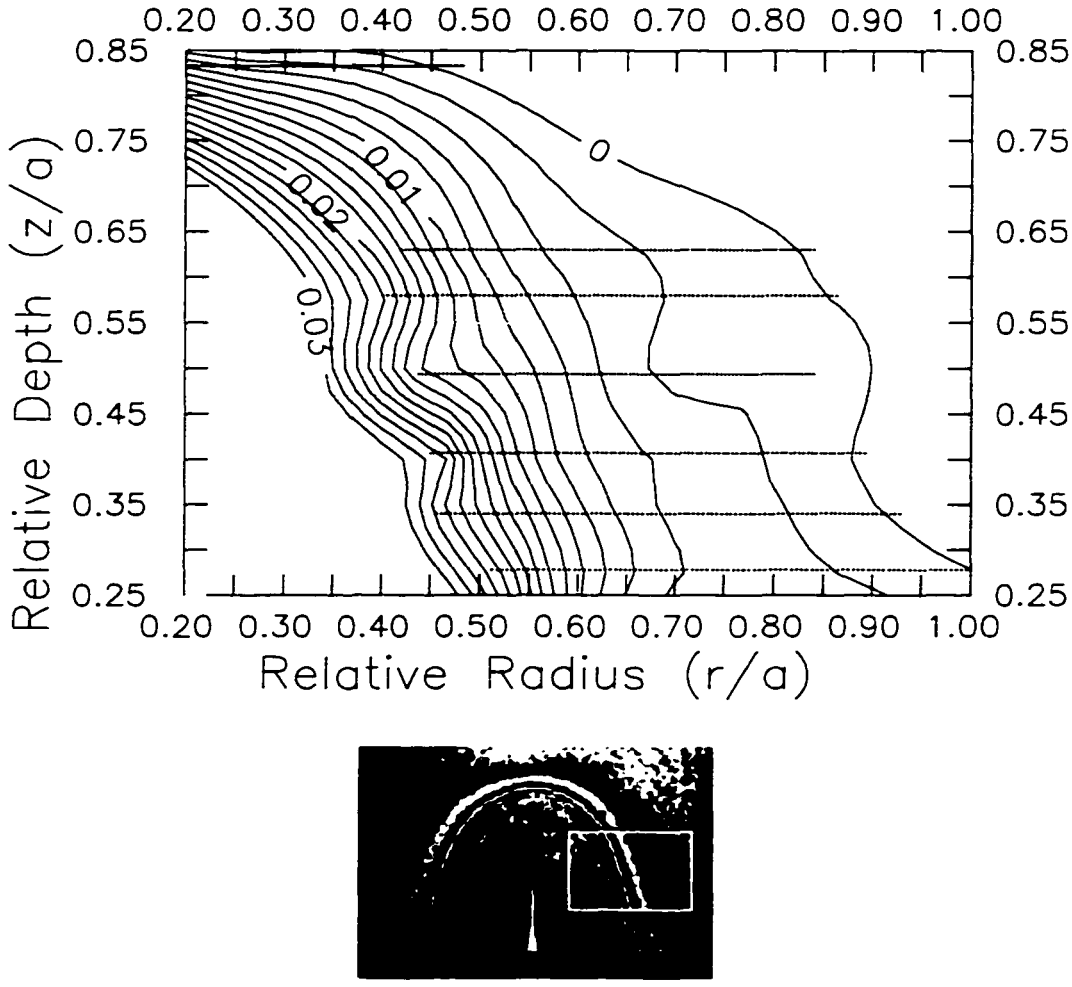


Figure 3.16 **Isotherm field generated from holographic data during drilling of fused quartz at *t*=5 s under low gravity conditions, corresponding to an initiation type hole.**

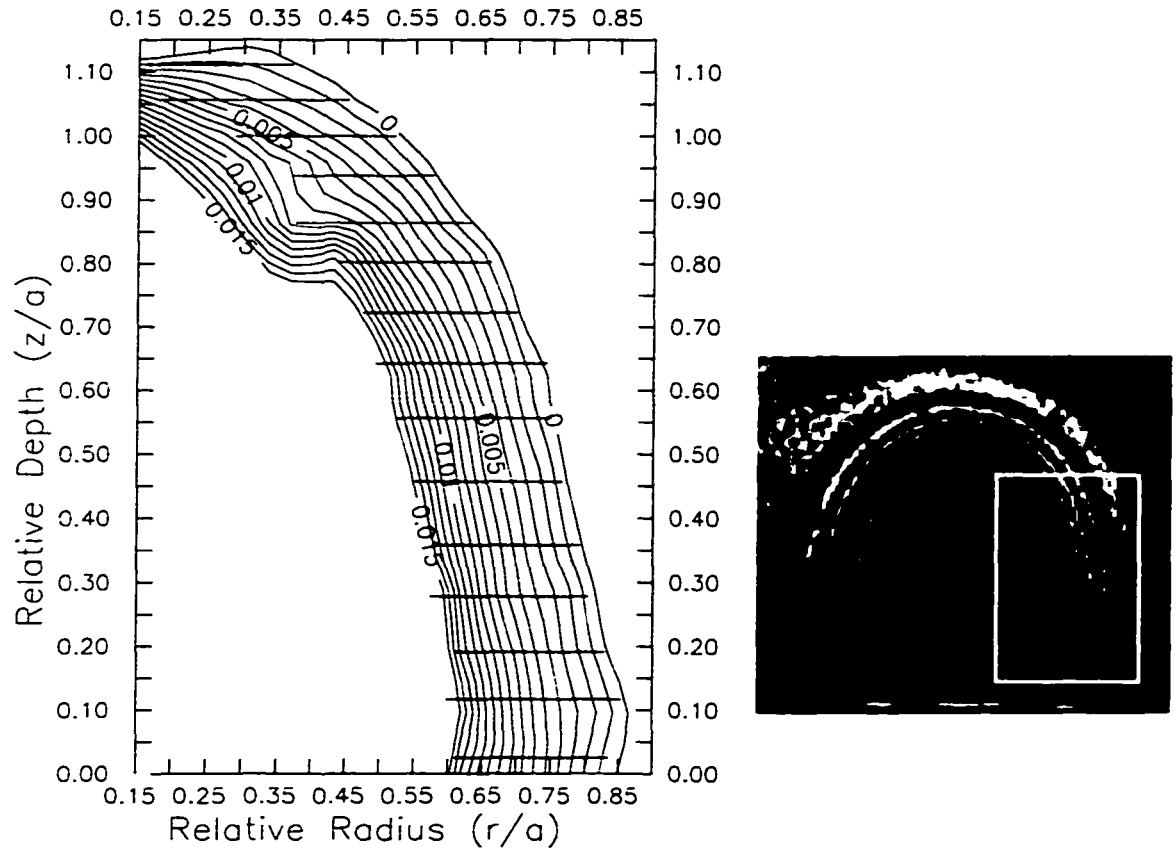


Figure 3.17 Isotherm field generated from holographic data during drilling of fused quartz at t=5 s under normal gravity conditions, into an existing hole.

3.5. Comparison of Results

3.5.1. Comparison Between Numerical and Experimental Results

The most informative region to compare experimental and numerical isotherms is in the immediate vicinity of the drill hole wall. Tightly spaced $T(z)$ variations along the

length of the cavity evident during drilling in normal gravity will not be represented in temperature fields measured distant from the drill hole. Unfortunately, experimental limitations restrict measurements to these distant regions from the drill hole and as such, only the macroscopic behaviour of the experiments can be compared with the numerical model.

In comparison to the numerical model, measured temperature fields all exhibit a larger amount of taper towards the root of the hole and less penetration. This is expected for initiated hole experiments given that the depth of the hole does not fully mature until ~ 2 seconds into the irradiation. Even the pre-drilled hole experiment shows somewhat more taper in the temperature lines than in the numerical model. The surface (z=0), is the only depth in the experimental data which can yield a realistic comparison to the numerical model, given that only near the surface was the drill hole exposed to laser radiation from t=0. Isotherms from the experimental data were extrapolated to the surface and plotted with those of the numerical model in Figure 3.18 for the 2 second laser exposures and in Figure 3.19 for the 5 second laser exposures. Not surprisingly, the best experimental fit to the model comes from the t=5 second laser irradiation into the preexisting hole.

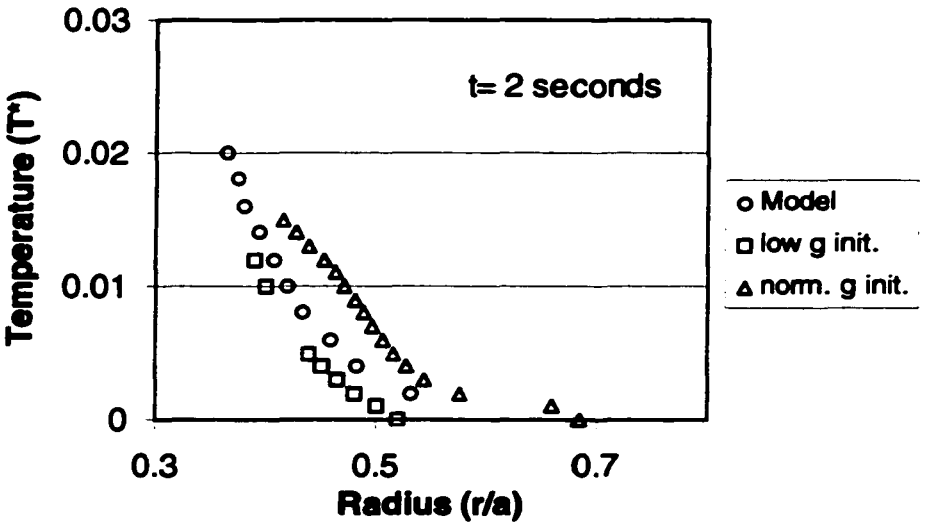


Figure 3.25 Radial extent of heating measured at the surface after 2 seconds of drilling, compared to results of numerical model.

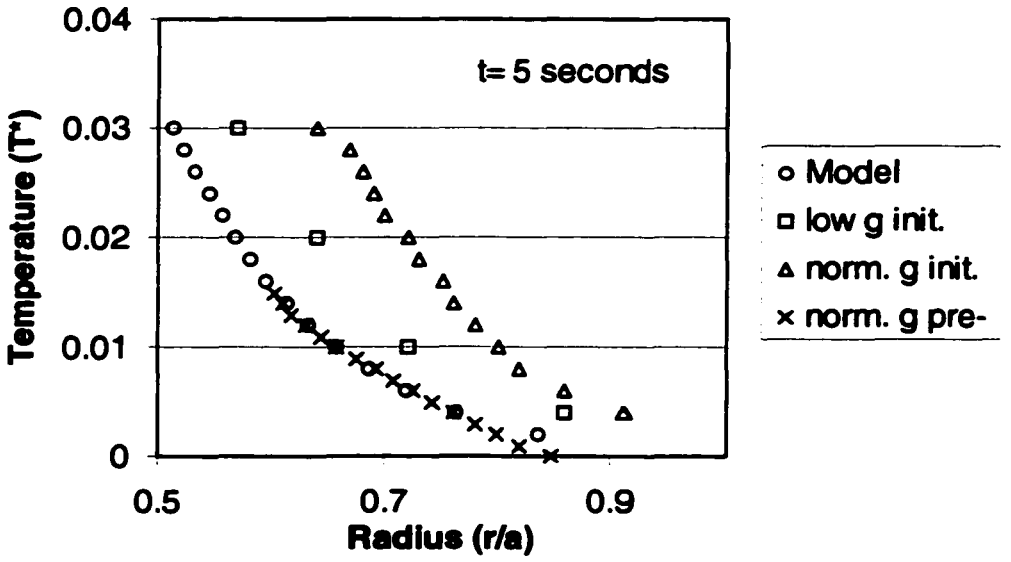


Figure 3.26 Radial extent of heating measured at the surface after 5 seconds of drilling, compared to results of numerical model. In the legend, "init" and "pre-" differentiate initiation from pre-drilled hole experiments.

3.5.2. Effect of Boundary Conditions

Perhaps the most obviously unrepresentative boundary condition involves the isothermal boundary condition at $\eta = \eta_o$. This boundary condition has two major differences from the experiments. The first is associated with the temporal nature of the thermal disturbance. In all but one data set, drilling was initiated from the surface, and propagation of the cavity to full length took between 2 and 3 seconds. Effectively this introduced a variable semi-major focal length $a = a(t)$. Even for heating of a preexisting drill hole, the isothermal assumption was invalidated by the fact that it would take of the order of 2 or more seconds to heat the hole to a uniform temperature. This is equivalent to replacing $T(\eta = \eta_0, t) = T_0$ with $T(\eta = \eta_0, t) = T(t)$.

The second major difference from the isothermal boundary condition can be attributed to the geometry of the isotherm, as the hole geometry does not follow the prescribed prolate spheroidal shape assumed in the boundary condition. *Figure* 3.3B shows a magnified view of a typical drill hole in fused quartz indicating more of a hyperbolic conical structure than prolate spheroidal. Given this hole geometry, it is not surprising that the interferograms exhibit outward inflections of the fringes near the surface.

Chapter Four

Laser Drilling of Liquids with a Modulated Beam

This chapter summarizes the results of laser drilling experiments performed in fluids with an intensity modulated laser beam. The work is motivated by the work of the German group [25-27], whose keyhole dynamic model predict that collapse dynamics may result in bands of eigenfrequencies, representing wave modes on a cylindrical keyhole. By drilling into liquids, the physical system is greatly simplified by removing the solid phase boundary and by eliminating hydrodynamic effects associated with a translating molten pool.

In total, two series of experiments were performed. In the first, a preliminary

investigation was carried out using a simple beam chopper. The observation of an interesting structural dependence on modulation frequency observed in 100% glycerol drilling prompted a second more systematic series of experiments using an improved modulation apparatus, and included acoustic data recorded during drilling.

This series showed a frequency dependent structure in both glycerol, and water. The nature of this dependence which had initially been observed in glycerol showed abrupt structural phase changes resembling jumps between resonant and non-resonant states. The results of the two series of experiments are described in the following two sections. Observations and data associated with the latter series of experiments have been fitted to a simple model.

4.1. Initial Experiments

4.1.1. Experimental Description

The apparatus used has been described in chapter 2 and is shown schematically in *Figure* 2.7. In the initial series of experiments, the chopper consisted of a simple AC fan motor driving a disk which was constructed of aluminum with a diameter of 200 mm and 50 wedge shaped fins measuring 3.6 degrees. These fins were separated by equivalent

sized gaps, yielding a 50% duty cycle pulse train. The chopping frequency was monitored with a photodetector and a frequency counter.

The laser beam was directed normally at water and glycerol, using an incident (pre chopper) power of 100 watts, with one additional experiment carried out at 200 watts. The surfaces of the fluids were located at the focus of the beam where the beam waist diameter was ~0.05cm, resulting in incident intensities of 1.3×10^4 watts/cm^2, and 2.5×10^4 watts/cm^2 respectively for the 100 watt and 200 watt incident powers before the chopper. Averaged over the 50% duty cycle associated with the modulation, the *average* intensity delivered to the fluids was 6.4×10^3 w/cm^2 and 1.3×10^4 w/cm^2 respectively for 100 and 200 watt powers.

Penetration processing (drilling) of the water and glycerol was carried out over a chopper frequency range limited to <2.9kHz. The transverse profile of the drill hole was monitored by a CCD camera and videotaped at 30 frames per second in the imaging configuration shown in *Figure* 2.7. Video data was subsequently processed with a frame grabber and image processing software capable of image enhancement and averaging.

The dynamic nature of the hole structure in fluids was such that conventional 30 frame per second video was too slow to follow the evolution of the structure in detail. Even in glycerol drilling, which appeared to be the least dynamic, drill hole structure in any given frame often appeared unrelated to that in neighbouring frames. *Figure* 4.1

highlights this showing seven consecutive frames of glycerol drilling. The seemingly random nature of the frame to frame structure makes it impractical to examine data one frame at a time and implies that a frame averaging approach might prove more useful. By averaging numerous individual frames, favoured structures can be highlighted while random structures are de-emphasized. *Figure* 4.2 shows an example of one such frame average. This average was performed on frames from the same hole as in *Figure* 4.1.

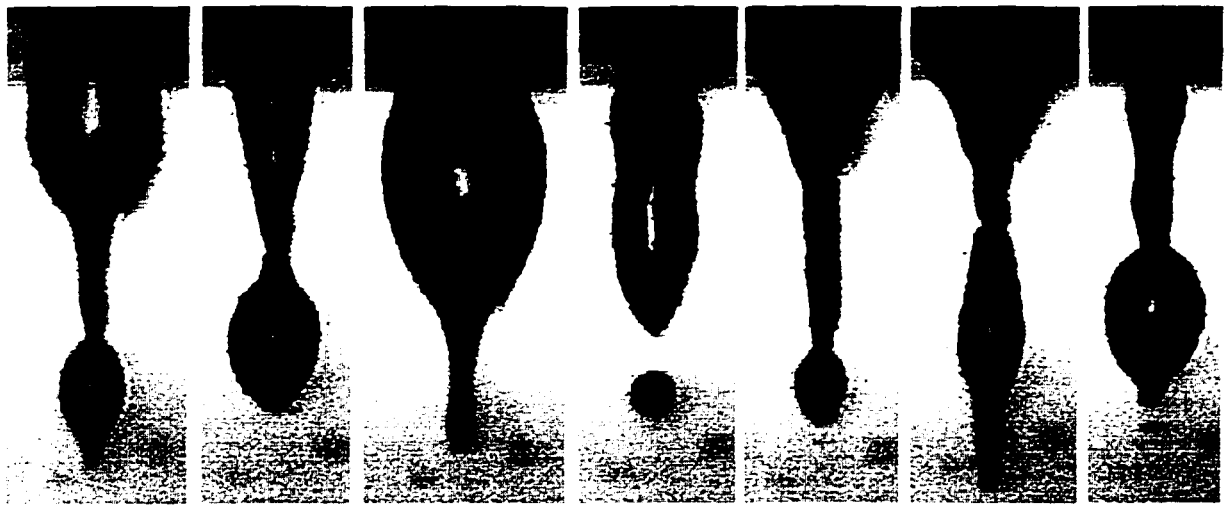


Figure 4.1: Seven consecutive frames of 100% glycerol with a 200 w (pre chopper) incident power and a chopping frequency of 2750 Hz. Frames were spaced 1/30 seconds apart.

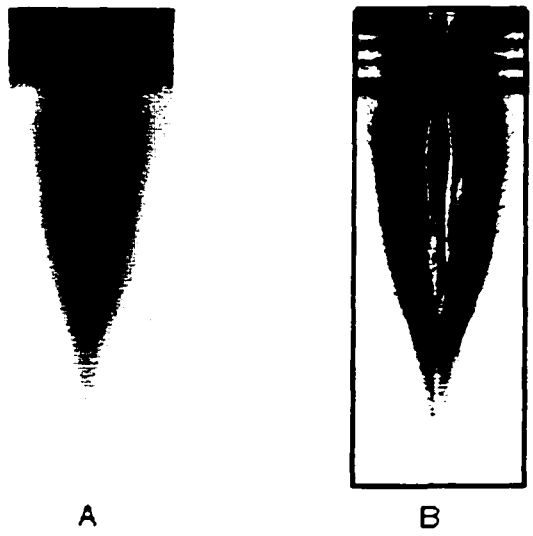


Figure 4.2 Frame average of 255 individual images in drilling 100% glycerol under the same conditions as in *Figure* 4.1. The grayscale average is on the left (A), and an edge enhanced version is shown on the right.

An edge detection algorithm[13] subsequently applied to the frame average (*Figure* 4.2b), helps to define the outer envelope of the cavity radius as a function of depth, as well as to enhance recurring structures within the hole. In this particular case, a long slender hourglass like shape can be observed extending from the surface into the drill hole near the optic axis which appears remarkably similar to the drill hole structure associated with laser drilled acrylic.

13 The edge detection algorithm used was from the standard filter library available in PhotoShop ™ version 2.5.

4.1.2. Initial Experiments - Glycerol

As is the case for water, the baseline for comparison of the glycerol experiments are non-modulated or CW drills. All CW drills into glycerol showed the characteristic rapid dynamics of the drill hole structure which had been observed in previous studies [46,47]. A series of images of video frames from a CW drill into glycerol is shown in *Figure* 4.3. The beam axis is apparent in each of the images and the surface is located at the top of the length scale. Interestingly, the overall symmetry and style of the hole structure appears very similar to that shown in *Figure* 4.1. *Figure* 4.4 shows the averaged and edge detected images associated with the CW drilling.



Figure 4.3. Typical images of drill hole structure in glycerol acquired during CW drilling with a laser output of 50 watts. The images A through G are in no particular order. Note the axial symmetry and smooth cavity walls.

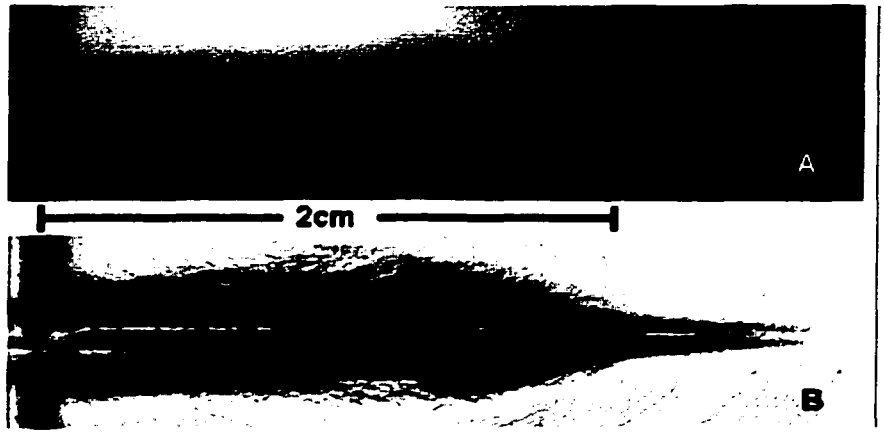


Figure 4.4 255 frame average of 50 watt CW 100% glycerol drill (A) and associated edge enhanced image (B).

In the first of two experiments performed on glycerol, drilling was carried out at an average incident power of 50 watts over the full range of chopper frequencies. As found in drilling water, frame averages performed on data at different frequencies indicated no major differences in the structure of the drill hole envelope. The frame averaged data and associated edge filtered counterparts are shown in *Figure* 4.5. At higher chopper frequencies, the radius of the outer envelope of the drill hole shows a smooth growth and decay progressing from the surface to the tip of the drill hole with a single maximum located approximately at mid depth. Subsequent frame averages at lower frequencies indicate little change with the exception that the maximum radius of the envelope appears to be biased towards shallower depth. Aside from the average at the highest frequency, the maximum radius of the envelope tends to reside near 0.33 of the full depth of the hole.

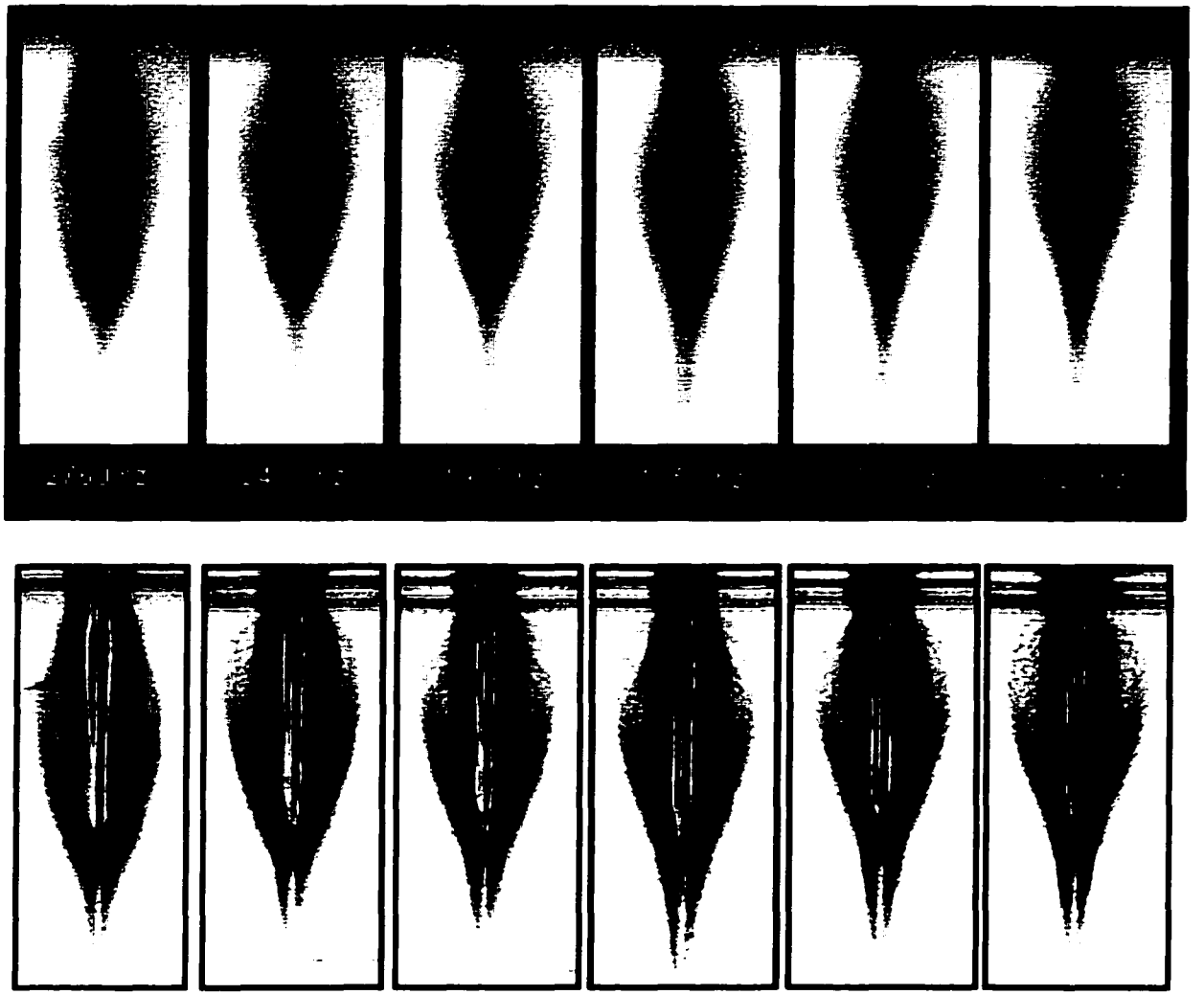


Figure 4.5. Six frame averaged images (255 frames/image) for drilling of glycerol with an average of 50 watts. As with water, no strong frequency dependence on drill hole structure can be identified.

When glycerol drilling was carried out at 100 watts, a completely different behaviour was observed (*Figure* 4.6). At the highest chopper frequency, a distinctive difference in the envelope structure can be seen. At 100 watts, the envelope shows a rapid subsurface radial growth to a maximum near 10% penetration. The subsequent tapering

of the envelope to the tip of the hole then proceeds almost linearly. More significant however is the distinctive phase transition which occurs at 100 watts as the chopper frequency is lowered. At a chopper frequency only 100 Hz below 2760 Hz, the initiation of a structural transition can be observed in the frame averaged data. The edge filtered image obtained at 2660 Hz suggests that a preferential shape starts to form close to the surface and as the frequency is reduced further, images clearly show a shallow bubble has formed. At frequencies below 1300 Hz, virtually all evidence of the original deep phase has disappeared from the frame averages. The relative size of the large shallow bubble was observed to grow as the modulation frequency was lowered, perhaps in response to an increased energy per pulse associated with lower modulation frequency.

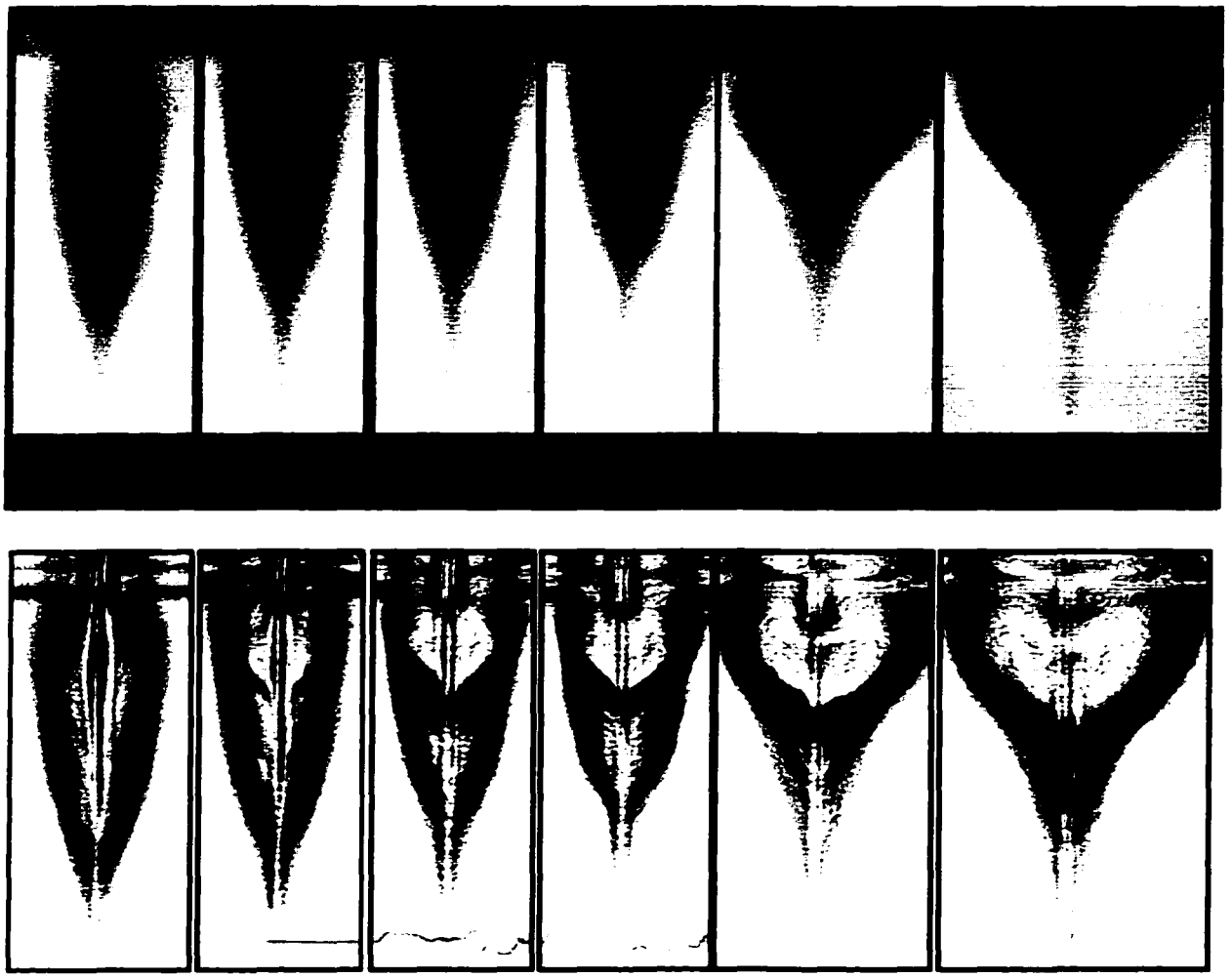


Figure 4.6. Frame averages in drilling glycerol at an average incident power of 100 w at chopper frequencies from 1000 to 2760 Hz. A smooth transition in structure can be seen taking place going from high to low frequency with evidence of the onset of the transition starting as high as 2660 Hz.

Examination of the evolution of the structure on a frame by frame basis near the low frequency limit supports the evidence of a structural transition. Such a sequence obtained at a chopping frequency of 1.3 kHz is shown in *Figure* 4.7.

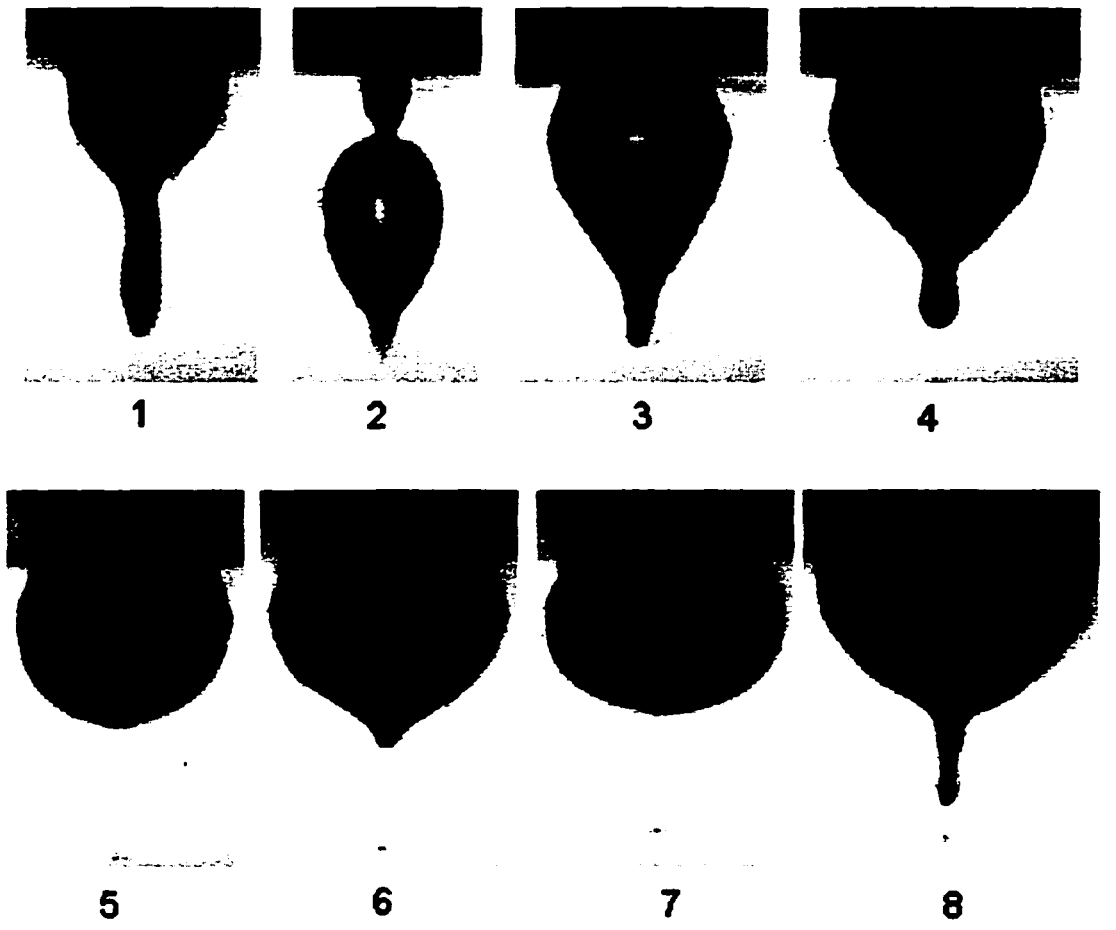


Figure 4.7. Eight consecutive frames at 100w average incident laser power in glycerol at a chopper frequency of 1300 Hz. This is in contrast to the appearance of the frame by frame structure seen in the both the higher chopper frequency sequence shown in *Figure* 4.1 and the CW sequence of *Figure* 4.3.

4.1.3. Initial Experiments - Water

The first water experiment, at an average power of 50 watts generated drill hole

structures which show little dependence on chopper frequency. Over frequencies ranging from < 200 Hz to > 2700 Hz, the frame averaged data results consistently show an inverted tear drop like envelope (*Figure* 4.8).

CW drilling of water produces a typically conical envelope of the drill hole extent. If the incident power is lower than ~80w then the conical envelope is augmented with evidence of a quasi-stable bubble trapped at the tip as previously observed by Mueller [16]. *Figure* 4.9 illustrates frame averages of CW water drilling at powers both above and below the bubble entrapment threshold.

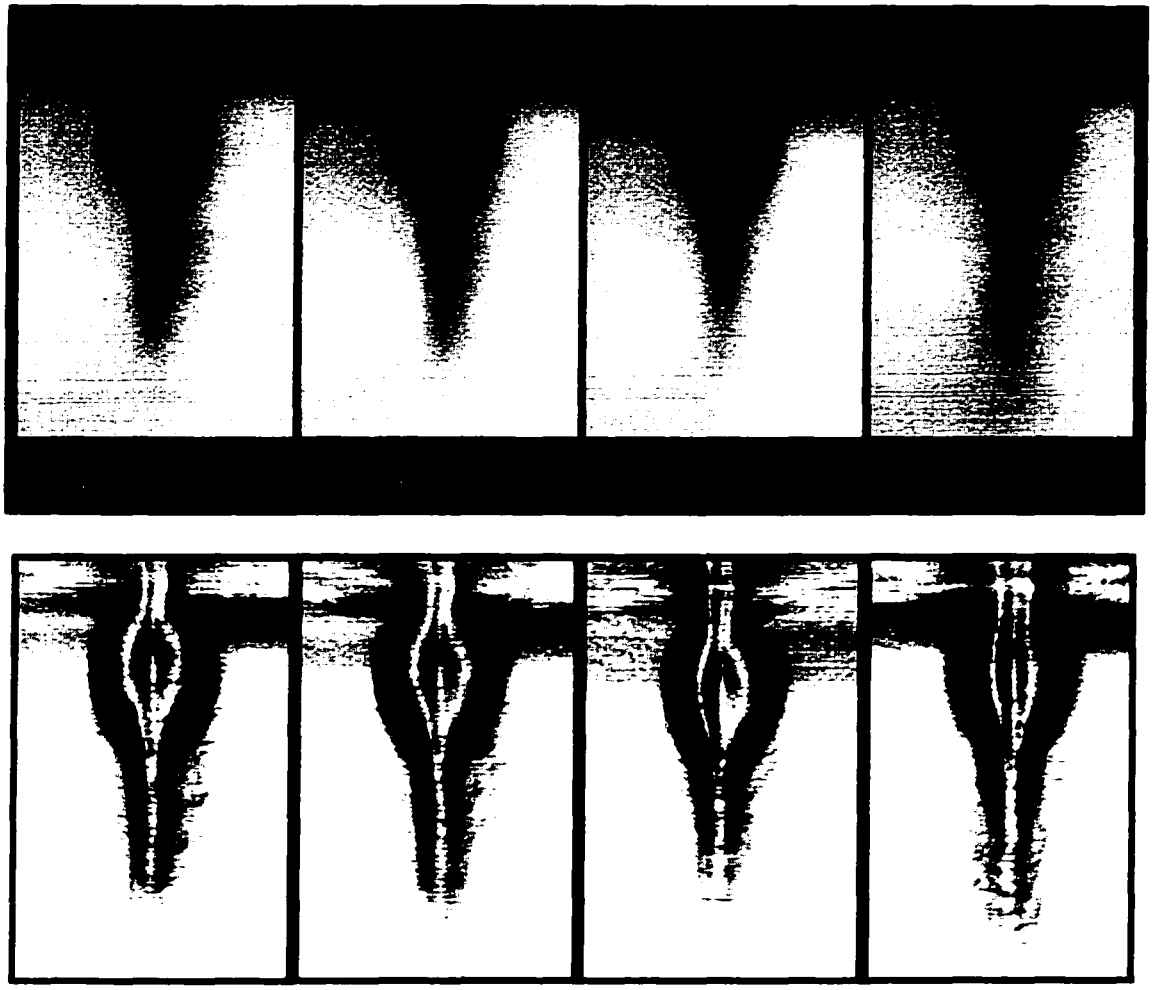


Figure 4.8. Frame averaged images taken at different chopper frequencies at 50 watts. (water)

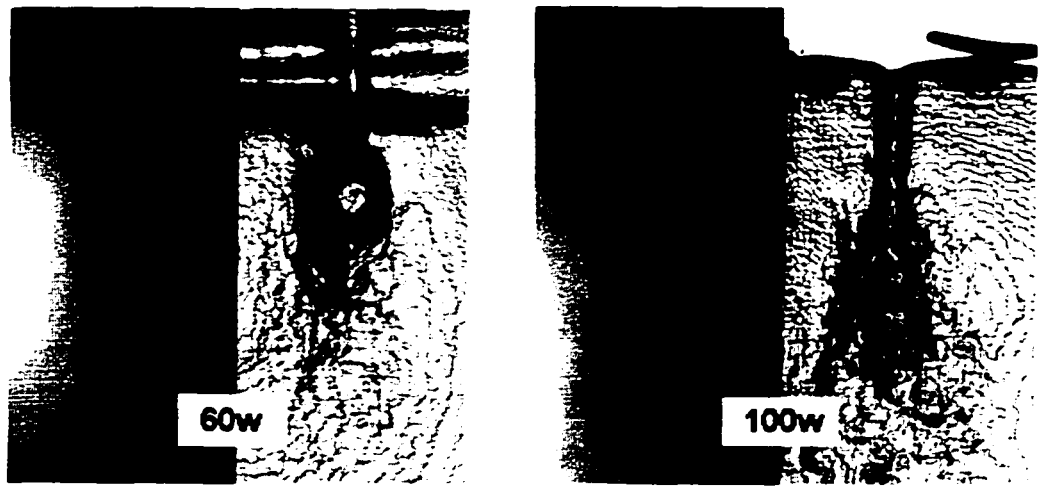


Figure 4.9. Frame averages and associated edge enhanced images during CW drilling of water. A large entrapped bubble is present at 60 watts, while only small bubbles are seen at 100 watts.

4.2. Experimental Results

4.2.1. Experimental Description

The initial experiment was repeated with the following modifications: A new mechanical chopper was designed based on a variable speed DC motor. A combination of built in SCR control and external line control through a Variac provided improved chopping frequency stability to within ±10Hz. A smaller diameter chopper wheel consisting of twelve 15 degree anodized aluminum blades spaced 15 degrees apart replaced the 50 blade wheel used in the previous experiments. Even with a reduction in

the number of blades by a factor of four, the higher rotational rate of the DC motor resulted in an increase in the upper frequency limit to over 3500 Hz. The exceptional controllability of the motor speed also extended the lower frequency limit to 100 Hz. During mechanical chopping experiments, the wheel was located again between the focusing optic and the fluid at a location where the ratio of beam diameter to chopper gap was approximately 0.25.

In order to identify systematic errors arising from the mechanical chopper, experiments were repeated by electronically modulating the laser beam. With the VFA-1700, the maximum modulation frequency which would provide *full* modulation of beam power based on a 50% duty cycle was 1Khz. This was accomplished internally through the laser controller by specifying the duty cycle in terms of a 4Khz clock. The 1Khz modulation would then be generated by setting a "two on, two off" duty cycle for the laser controller. Lower modulation frequencies are subject to limitation imposed by the discrete nature of the duty cycle specification so that low frequencies based on 50% duty cycle are limited to 666, 500 and 250 Hz[14].

Acoustic emissions from the drill hole were recorded on one of the hi-fi stereo channels of the video recorder through a Realistic electret microphone and preamplifier combination. According to the manufacturers specifications, the VCR audio response is

14 These frequencies are all relative to the "4kHz" reference clock of the laser controller. It will become apparent as the acoustic spectral data is presented that the actual clock frequency is lower than this.

from 20-20000Hz, and the microphone response is flat up to at least 17kHz. Acoustic data was therefore assumed to have a flat frequency response to 15kHz. To minimize external noise, the fluid chamber was fully enclosed with the microphone located in the air space above the fluid surface. The inner surfaces of the chamber above the fluid line were also lined with acoustic damping foam to minimize contributions from any natural resonances associated with the container.

Drilling of glycerol and water was carried out between 0Hz (CW), and 3.6kHz using both modulation techniques whenever possible. The laser output ranged from ≤50 to 350 watts, and gave 22-175 watts *average power* after modulation.

4.2.2. Drilling Glycerol – Structural Modes

The main purpose of the series of modulated beam experiments was to map out in greater detail the structural phase evolution initially observed in 100% glycerol. Experimental data was grouped into bins according to frequency and power ranges and the behaviour of the drill hole morphology could be classified into three distinct states: 1) dynamic non-resonant structure associated with low frequency modulation and lower laser power; 2) stable resonance structure; 3) de-stabilized resonance, associated with higher frequency modulation and high laser power. The duration of each irradiation was

ten seconds and it was quite common to observe more than one of the above modes in a given experiment. *Tables* 4.1 and 4.2 summarize the extent of data acquired while drilling glycerol using a modulated beam. Observed states seen during each irradiation period are indicated by symbols. To facilitate comparison, frequency range has been categorized as 1 - 16 and power ranges are labeled by the letters A to D.

Table 4.1. Chopped laser drilling of Glycerol.

1	0	∅	∅	∅
2	100 - 130	∅	∅	∅
3	200 - 325	∅	∅	∅
4	400 - 550	∅	∅	∅
5	600 - 850	∅	∅	∅⊕
6	900 - 1100	∅	∅⊕	∅⊕
7	1200 - 1350	∅⊕	∅⊕	∅⊕
8	1400 - 1600	∅⊕	⊕⊗	⊕
9	1700 - 1800	∅⊕	⊕⊗	⊕
10	1900 - 2000	⊕	⊕⊗	⊕⊗
11	2200 - 2300	⊕	⊗	⊕⊗
12	2450 - 2550	⊕	⊗	⊕⊗
13	2700 - 2800	⊕	⊗	⊕⊗
14	2950 - 3050	⊕⊗	⊗	⊕⊗
15	3200 - 3300	⊕⊗	-	⊕⊗
16	3450 - 3650	⊗	⊗	⊗

KEY: ∅... non resonant dynamic structure
⊕... stable resonant structure
⊗... destabilized resonance
- ...no data available

Table 4.2. Pulsed laser drilling of glycerol.

3	200 - 325	-	Ø	Ø	-
4	400 - 550	Ø	Ø	ØΘ	ØΘ
5	600 - 850	Ø	ØΘ	ØΘ	ØΘ
6	860 - 1100	Ø	ØΘ	ØΘ	ØΘ⊗

Qualitatively, only the low frequency sub resonance structures show similar characteristics as in previous experiments. These structures follow the typical behaviour observed during CW drilling (*Figure* 4.3).

As the modulation frequency approaches a resonance from below, the smooth structured dynamically evolving hole transforms periodically into a single quasi-stable spherical structure with surface ripples with waves of considerable amplitude at times. *Figure* 4.10 shows a sequence of images exhibiting this structure.

Size variations evident in the bubble profiles in *Figure* 4.10 are dependent on both the beam modulation frequency and the depth of the bubble below the liquid surface. The latter dependence is such that the bubble size grows as it approaches the surface. This may be caused by a decreasing hydrostatic pressure term acting to close the bubble. *Figure* 4.10 also shows clearly that bubble size tends to decrease as the modulation

frequency increases.

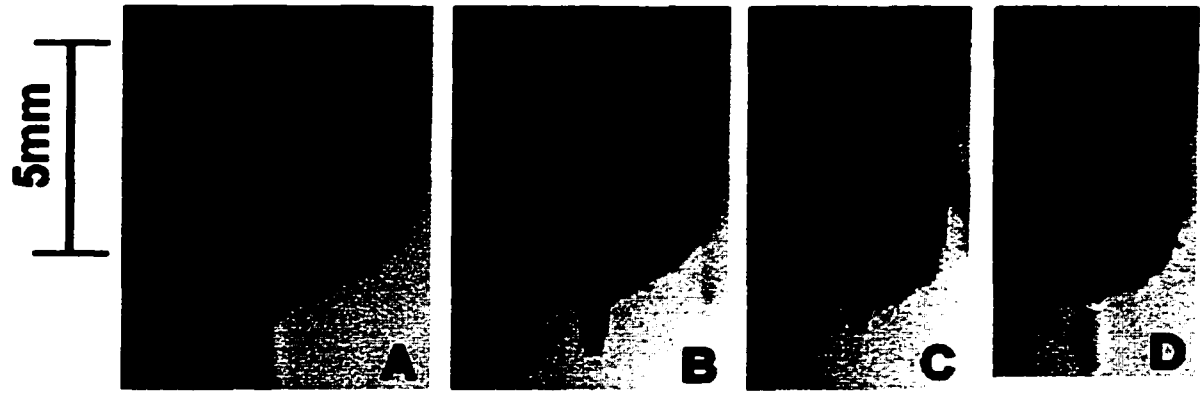


Figure 4.10. Structures typical of stable resonance condition. The images were obtained with 25 watts average power incident on glycerol at modulation frequencies of 1500 Hz (A), 1700 Hz (B), 1900 Hz (C), and 2250 Hz (D).

At high frequencies, the hole structure de-stabilizes and no spherical modes are observed. Unlike the low frequency non-resonance drilling however, drill hole structure tends to be highly non-symmetric, consisting of smaller highly distorted bubbles forming, collapsing, and often appearing to be laterally ejected from the hole. Distortions in the primary bubbles are similar to those of bubbles in the resonant states, indicating that the high frequency de-stabilized states may not simply be beyond the band of resonance, but rather de-stabilized by some other process. *Figure* 4.11 indicates some of the typical structural behaviour associated with de-stabilized resonance states.

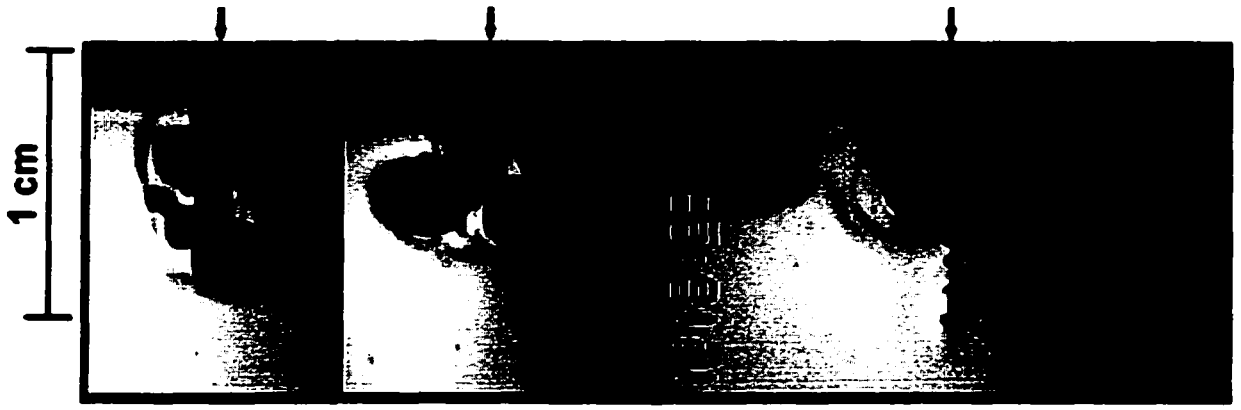


Figure 4.11. Chopper modulated glycerol drilling at 2 kHz with 54 watts incident power. Note the distortion of even the isolated bubbles in images B and C.

As in the previous series of experiments, a frame averaging approach was adopted to analyze data in more detail. Data was divided into pre- and post-resonant structural groups, and further subdivided according to beam intensity. The approach to the structural resonance state for the low, medium, and high intensity drilling is shown in *Figures* 4.12, 4.13, and 4.14 respectively. Drilling of low intensity shows a very striking bimodal mode in the frame averages when compared to high intensity, but this bimodal structure is observed at all intensity levels.

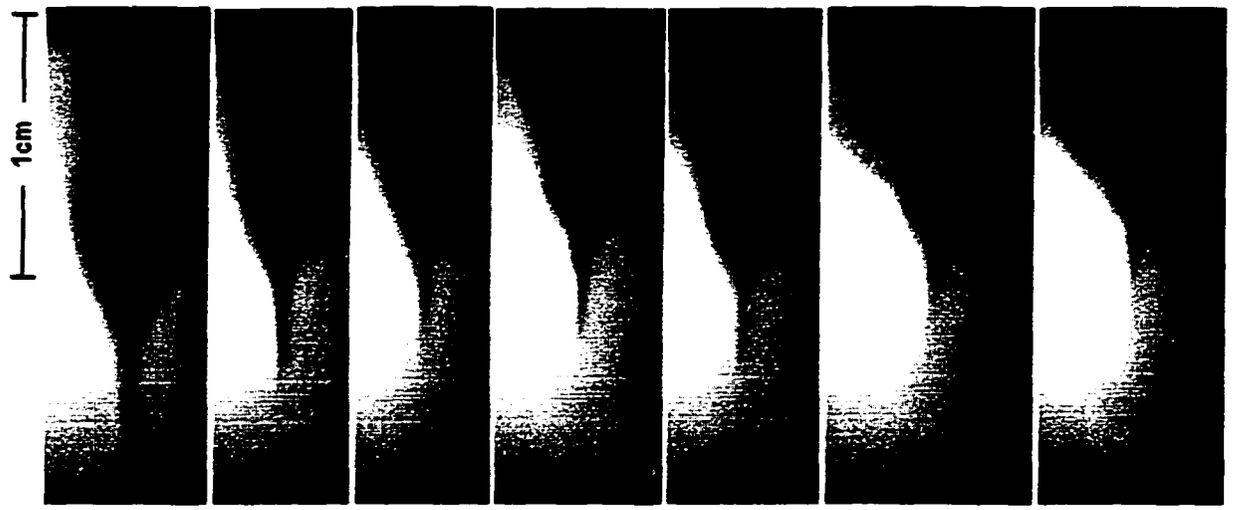


Figure 4.12. Evolution of structural envelope leading up to resonance at low intensity (~7×10^4w/cm^2) in 100% glycerol using a mechanically chopped beam. A resonance is clearly evident in the 1.5kHz average.

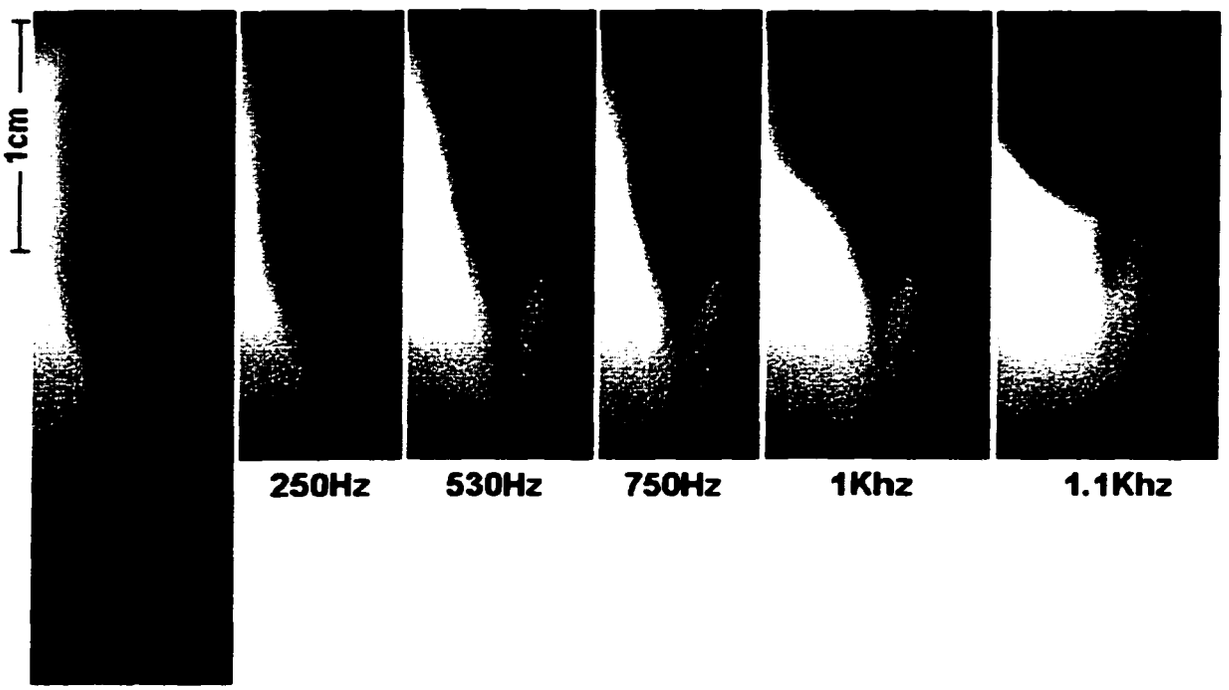


Figure 4.13. Evolution of structural envelope leading up to resonance at medium intensity (~1.5×10^5w/cm^2) in 100% glycerol using a mechanically chopped beam.

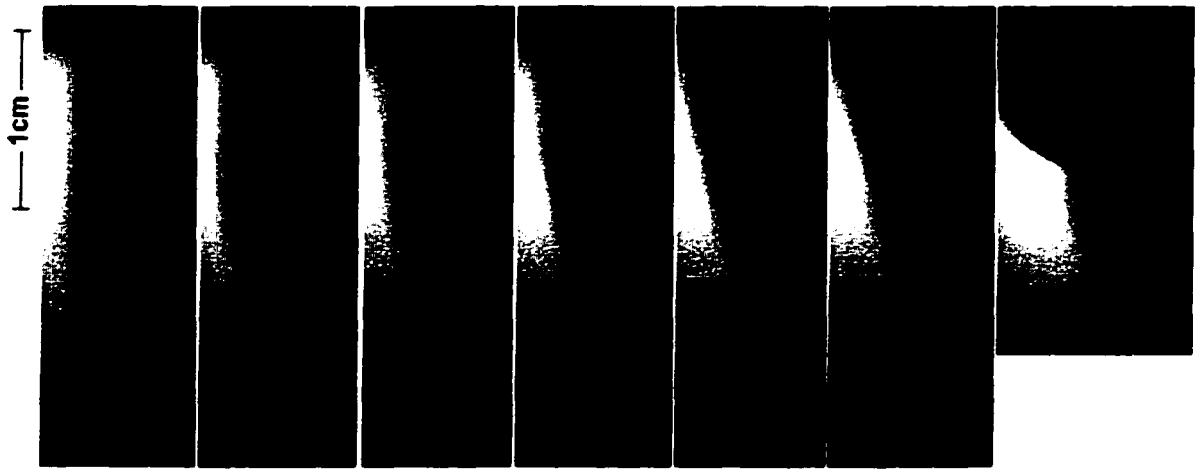


Figure 4.14. Evolution of structural envelope leading up to resonance at high intensity (~3×10^5w/cm^2) in 100% glycerol using a mechanically chopped beam.

The post-resonant or destabilised resonance transitions at the three incident laser intensities are summarized in *Figures* 4.15, 4.16, and 4.17. At all three intensities one sees a bimodal envelope similar in appearance to those of the sub resonance frame averages. The similarities in the pre- and post-resonant structural averages are not likely due to similar process dynamics. Frame by frame, post-resonant structures are typified by random asymmetries which often proceed to the extent that a lateral detachment of large bubbles occurs (see *Figure* 4.11). The blurred appearance of the post-resonance averages is due to such random effects.



Figure 4.15. Evolution of structural envelope through resonance to destabilisation at low intensity (~7×10^4w/cm^2) in 100% glycerol using a mechanically chopped beam.



Figure 4.16. Evolution of structural envelope through resonance to destabilisation at medium intensity (~1.5×10^5w/cm^2) in 100% glycerol using a mechanically chopped beam.

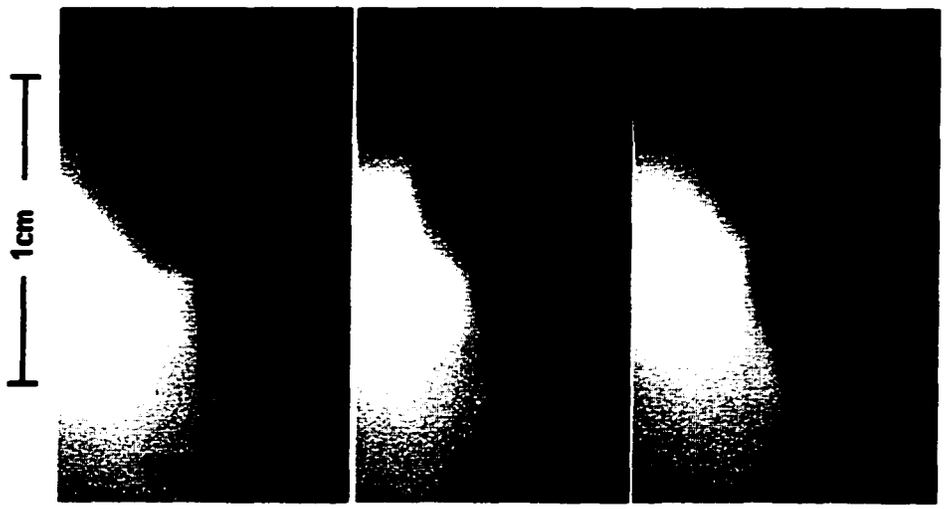


Figure 4.17. Evolution of structural envelope through resonance to destabilisation at high intensity (~3×10^5w/cm^2) in 100% glycerol using a mechanically chopped beam.

4.2.3. Drilling Water – Structural Modes

Because the first series of experiments on water had indicated little modulation dependence, follow-up experiments were not as comprehensive as those for glycerol. This proved to be rather unfortunate as the extended frequency range provided by the improved apparatus allowed observation of the transformation of the structural envelope from the conical CW type shown in *Figure* 4.9 to a shape similar to the teardrop shaped envelopes seen in *Figure* 4.8. Two full frequency surveys were carried out under only mechanical beam modulation; one at 70±5, and the other at 122±5 watts (pre-chopper

power).

Figure 4.18 highlights the evolution in the frame averaged drill hole envelopes in the water interaction at 70 watts. The envelope appears to move through three distinct structural phases over the full range of frequencies. At frequencies below ~200Hz, the envelope can be described as conical, closely resembling that of CW drilling, but with significantly enhanced penetration. This enhanced penetration itself is quite interesting, considering that modulation results in an average power deposition only 50% that during CW drilling. In fact, *all* of the modulation frequencies studied gave superior penetration when compared to CW irradiation of water. Between 200Hz and 1Khz, the hole envelope takes the shape of an inverted teardrop, with a noticeable bimodal form as frequency increases to ≥500Hz. By 1Khz, the bimodal teardrop has evolved to a relatively featureless and almost cylindrical envelope, with only a slight taper favouring a wider root. Above 1Khz, the envelope stabilizes into a structure consisting of a bubble superposed in the middle of an otherwise conical cavity.

Though the higher frequency frame averages resemble those of the CW frame averages somewhat, it should be pointed out that the excitation processes are far from analogous to each other. *Figure* 4.19 compares single frame images of CW and high frequency modulation drilling. In CW excitation, the bubble is located near the root of the conical drill hole, while at 3.5 kHz, a larger bubble is located in the middle of the

conical cavity. Another striking difference between the two regimes is the extent of bubble ejection from the root of the hole. CW excitation produces large numbers of bubbles, with many too small to be resolved by the video camera. These are injected into the water at up to five times the average drill hole depth. Conversely, high frequency modulation drilling produces relatively few detached bubbles, and the few that are produced are large enough to be clearly resolved. These bubbles rarely exceed three times the drill hole depth. The transition from one regime to the other takes place between 100 –200Hz.

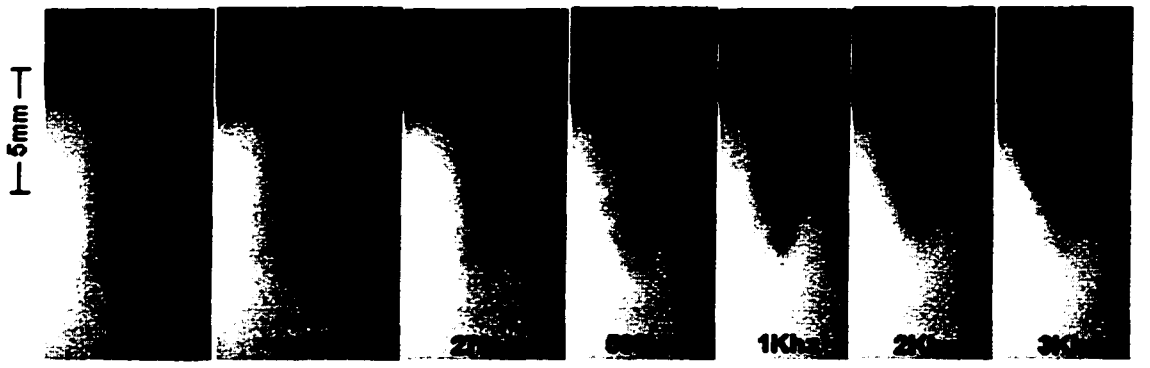


Figure 4.18. Frame averages of water at 70 watts at modulation frequencies between 0 - 3.5Khz.

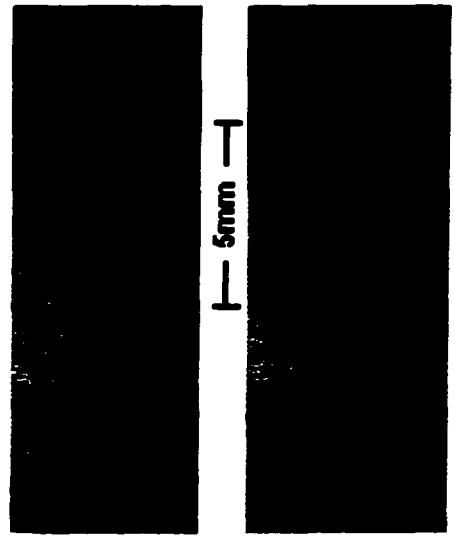


Figure 4.19. Single frame images of "characteristic" profiles for 70 watt drilling under CW conditions (A) and at 3.5Khz (B).

In contrast to the 70 watt experiments, excitation at 120 watts produced a much simpler frequency dependence in the structural envelope. A summary of the envelope shapes is shown in *Figure* 4.20. At low frequencies, the behaviour appears identical to that at 70 watts, with the exception of the absence of an entrapped bubble at the root of the hole. As before, a transition occurs near 200 Hz in which the conical envelope and high rate of bubble ejection are replaced by an inverted teardrop shaped envelope. This is where the similarities cease between 70 and 120 watt results, as unlike the lower power experiment, the 120 watt hole envelope does not undergo any *major* structural phase transitions at higher frequencies. No evidence of a bimodal structure appears at any of

the modulation frequencies. Rather, the aspect ratio of the single mode teardrop simply increases in width with increasing frequency.

Though the two follow-up experiments performed on water exhibit a different dependence on modulation frequency, it is worth noting that results of the 120 watt experiment appears to be consistent with the first series of experiments performed at 100 watts in water. The two types of structural evolution may be linked to the bubble entrapment threshold described earlier. The two experiments performed above the stability threshold power agree with each other while the single study below the stability threshold shows a different behaviour, however not enough data exists to confirm or refute this possibility.

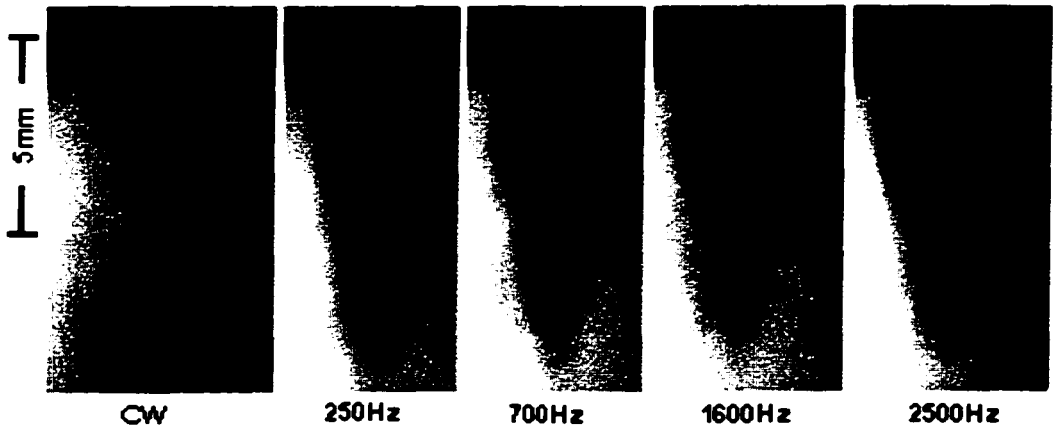


Figure 4.20 Frequency dependence of frame averages for modulated beam drilling at a beam power of 120watts in water.

4.3. Acoustic Data

4.3.1. Acoustic Data Processing

The addition of acoustic recording of the drilling process adds a significant new dimension to the study of the modulated beam process dynamics. Structural phase changes in the drill hole can be correlated with fast Fourier transform spectra of the associated acoustic data. A general description of acoustic data acquisition and processing techniques were described in chapter 2, but specific details of the data processing remain to be described.

The main challenge in interpreting the acoustic information is in extracting only that portion of the data associated with the drilling process. The audio data is a composite signal which consists of both pure drill hole emission and noise. In an attempt to better isolate the spectrum associated with laser processing, background noise was recorded before each experiment. Assuming that the spectral content of the background noise contained no transient signals, the drilling spectrum could be extracted by subtraction.

Raw FFT spectra were computed in decibel form, where sound level is defined as

$$L = 10\log\left(\frac{I}{I_0}\right) \tag{4.1}$$

and I is sound intensity while I_0 is an arbitrarily defined reference intensity[15]. The composite spectrum consists of three components; drilling, background noise, and electronic noise, with the first of these to be isolated. Background noise is comprised of ambient and systematic acoustic signals included in the composite signal. Electronic noise is an unfortunate artifact arising from the proximity of the recorder to the laser controller. Assuming that the amplitudes of each component combine additively, then the amplitude of the composite spectrum can be expressed as $A_C=A_D+A_B+A_E$, where the subscripts refer to the composite (C), drilling (D), background (B), and electronic (E), components, respectively. Spectral data give these levels in decibels, which becomes

$$L_C = 10\log\left(\frac{A_C}{A_0}\right)^2 = 20\log\left(\frac{A_D + A_B + A_E}{A_0}\right) \tag{4.2}$$

$$L_B = 20\log\left(\frac{A_B}{A_0}\right) \tag{4.3}$$

$$L_E = 20\log\left(\frac{A_E}{A_0}\right) \tag{4.4}$$

where A_0 is a reference amplitude which is unknown but consistent between the three spectra. The amplitude ratios A_X/A_0 can be obtained from spectral data and then drilling

15 The reference intensity has by international agreement been defined as the standard human threshold of audibility where $I_0 = 10^{-12}$ w/m^2.

amplitude ratio can be found as follows

$$\frac{A_D}{A_0} = 10^{L_C/20} - 10^{L_B/20} - 10^{L_E/20} \qquad 4.5$$

It should be pointed out that the mathematical arguments made above are valid only for similar members of the respective 2048 point spectra. That is to say that each variable should be associated with a subscript 'j' where j ranges from 1 to 2048.

Though it would be a straightforward task to convert the isolated drilling spectrum back to decibel units, presentation of the data in terms of the amplitude ratio results in spectra which are far easier to interpret. *Figure* 4.21 shows a single spectrum at various stages of this process. The raw composite spectrum in dB is shown in *Figure* 4.21A, while the same spectrum in amplitude ratio form is shown in *Figure* 4.21B. *Figure* 4.21C then shows the same spectrum in amplitude ratio form with the background and electronic noise removed as described above. *Figure* 4.22 shows a more detailed view of the region of the majority emissions.

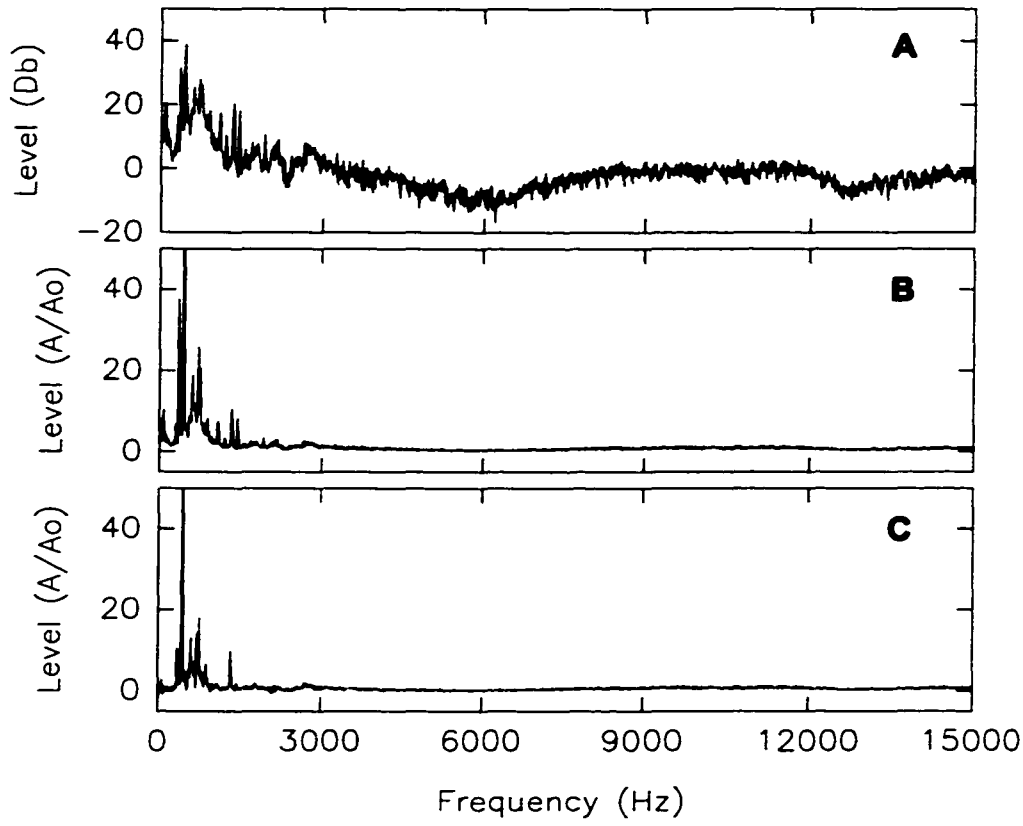


Figure 4.21 FFT spectrum of 475Hz chopper modulated drilling in 100% glycerol. The raw composite spectrum is shown in dB form (A), and amplitude ratio form (B). The refined spectrum with electronic and background noise removed (C).

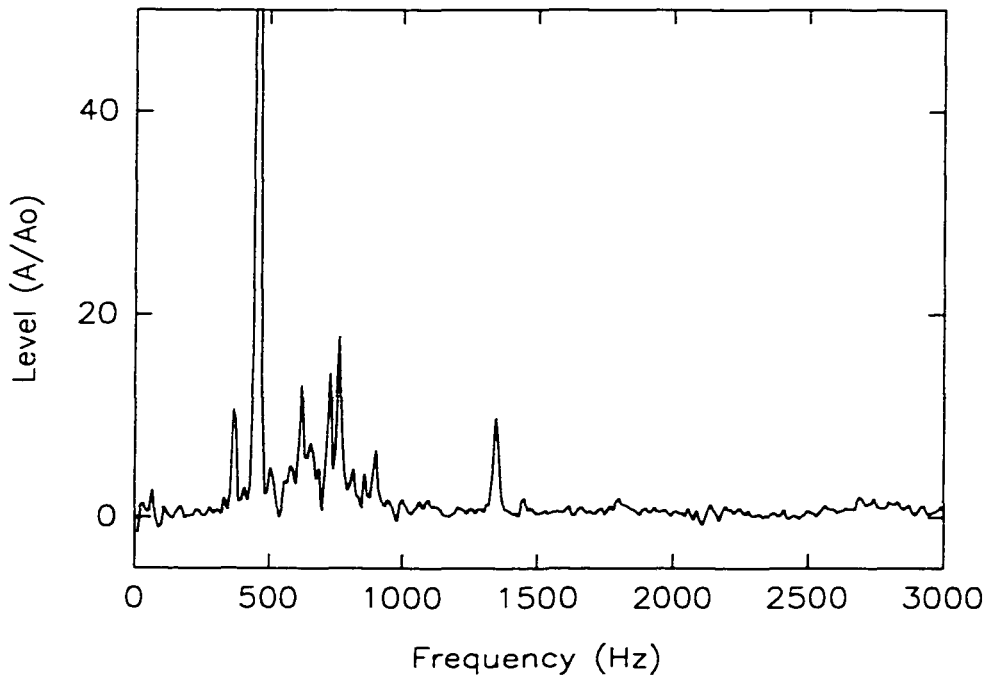


Figure 4.22. Detail of *Figure* 4.21c. Note that the spectrum shows several peaks aside from the fundamental frequency associated with the beam modulation at 475Hz.

Noise reduction in the isolated spectrum is apparent, but is not perfect as noise levels in the raw spectra are never a perfect match to the recorded noise spectra, resulting at times in noise related artifacts. Processed spectra can show negative values at isolated frequencies if the combined background and noise components exceed the composite signal for a given element of the 2048 point spectrum. In the absence of external process or environmental variability, negative spectral signals are negligible. Significant negative spectral features however are instructive and indicate that at that particular frequency, the combined electronic and background noises exceeded that of the composite signal. These

negative spectral peaks can sometimes be identified with specific systematic or environmental signals. For example, a slight shift in chopper motor RPM between background and drilling acoustic sampling will result in an enhanced peak at the modulation frequency and the appearance of a false absorption line immediately adjacent to it. Furthermore, electronic background removal was based on the assumption that spectral content and noise amplitude was constant throughout the experiments and although this may be valid, frequency components comprising the electronic noise background should be regarded with extra caution. A spectrum associated with electronic noise is presented in *Figure* 4.23 with its major peaks identified. Frequencies above 5kHz are not shown on the plot and do not contribute significantly to the signal. Processed spectra which show negative peaks or absorption lines at noise frequencies suggest that an overcompensation of the electronic noise may have occurred. The opposite is not necessarily true however. Positive spectral features at electronic noise frequencies *may* be the result of undercompensation, but may also represent true emission signals from the drilling process.

Detailed analysis of the data shown in *Figure* 4.23 reveals that all of the major spectral components in the electronic noise signal appear to be associated with harmonics of the 60 Hz line frequency. The dominant frequency in the noise is associated with the fifth harmonic at 360Hz, more than twice as strong as all other frequencies. Also noteworthy is the fact that the top four contributors to the signal at 360, 720, 1080, and

1440Hz, while being harmonics of the 60Hz line frequency also represent a sequence of harmonics of 360Hz. Hence, peaks in the drilling spectrum associated with 360Hz and its harmonics may be spurious.

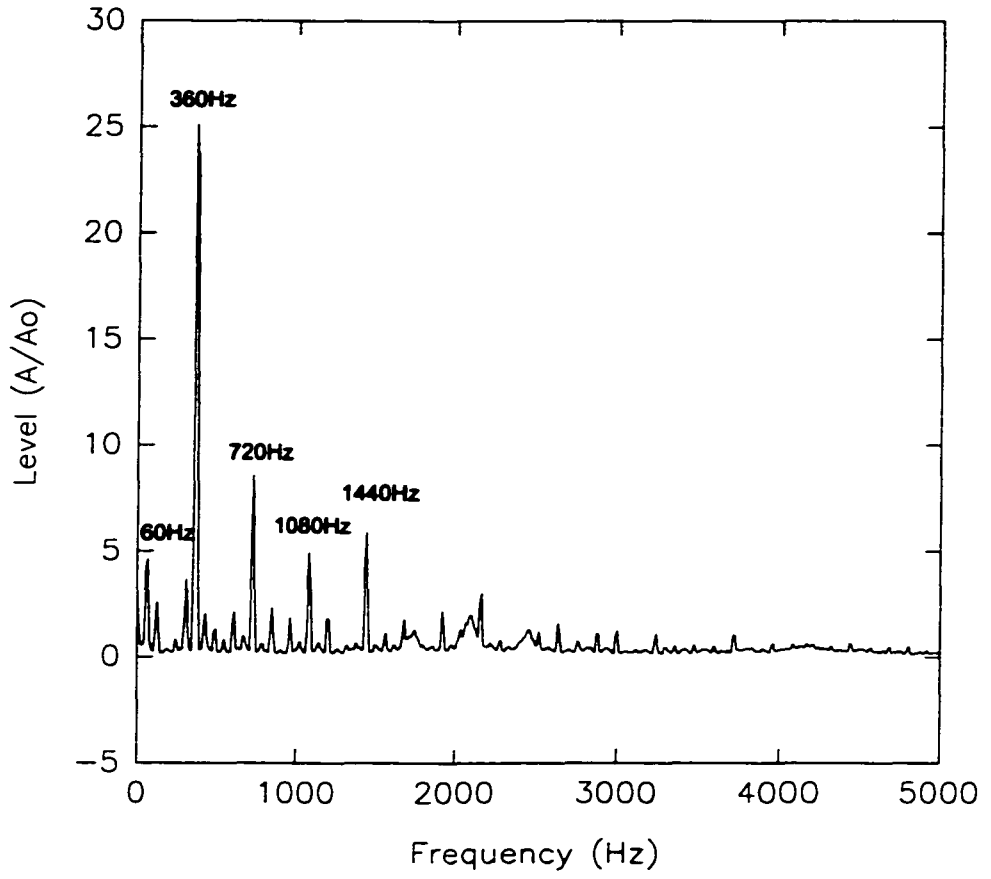


Figure 4.23 Averaged FFT spectrum of 10 seconds of electronic noise. Some frequencies of the more dominant peaks are marked on the plot.

4.3.2. Spectral Analysis of Glycerol Emission

Continuous Wave Emissions

An FFT spectrum averaged over ten seconds of CW drilling data at 54 watts average power is shown in *Figure* 4.24a. Most emission is contained within the 0 - 3 kHz range as shown in *Figure* 4.24b. Spectral structure consists of relatively sharp peaks at 300, 360, 610, 920, 1440, and 2160Hz in conjunction with a broad band feature ranging from about 500 to 1000Hz, and peaking near 670Hz. Given the limitations above due to electronic noise, the only features that can be firmly identified with drill hole emissions are the broad band peak centered at 670Hz, and the sharp peaks at 610, 850, and 920Hz.

Further investigation into the nature of the broad band feature reveals that it consists of a variety of intermittent signals within a band between 300Hz and 1.2 kHz. The averaged spectrum is reduced in *Figure* 4.25 to ten component spectra, each representing about one second of drilling. These show that rather than one broad emission peak appearing between 500 and 1000Hz, spectra reveal an intermittent enhanced spectral content within that range. The fact that a definite emission band results in longer duration FFT averaged spectra, with no such evidence at shorter time scales suggests that the

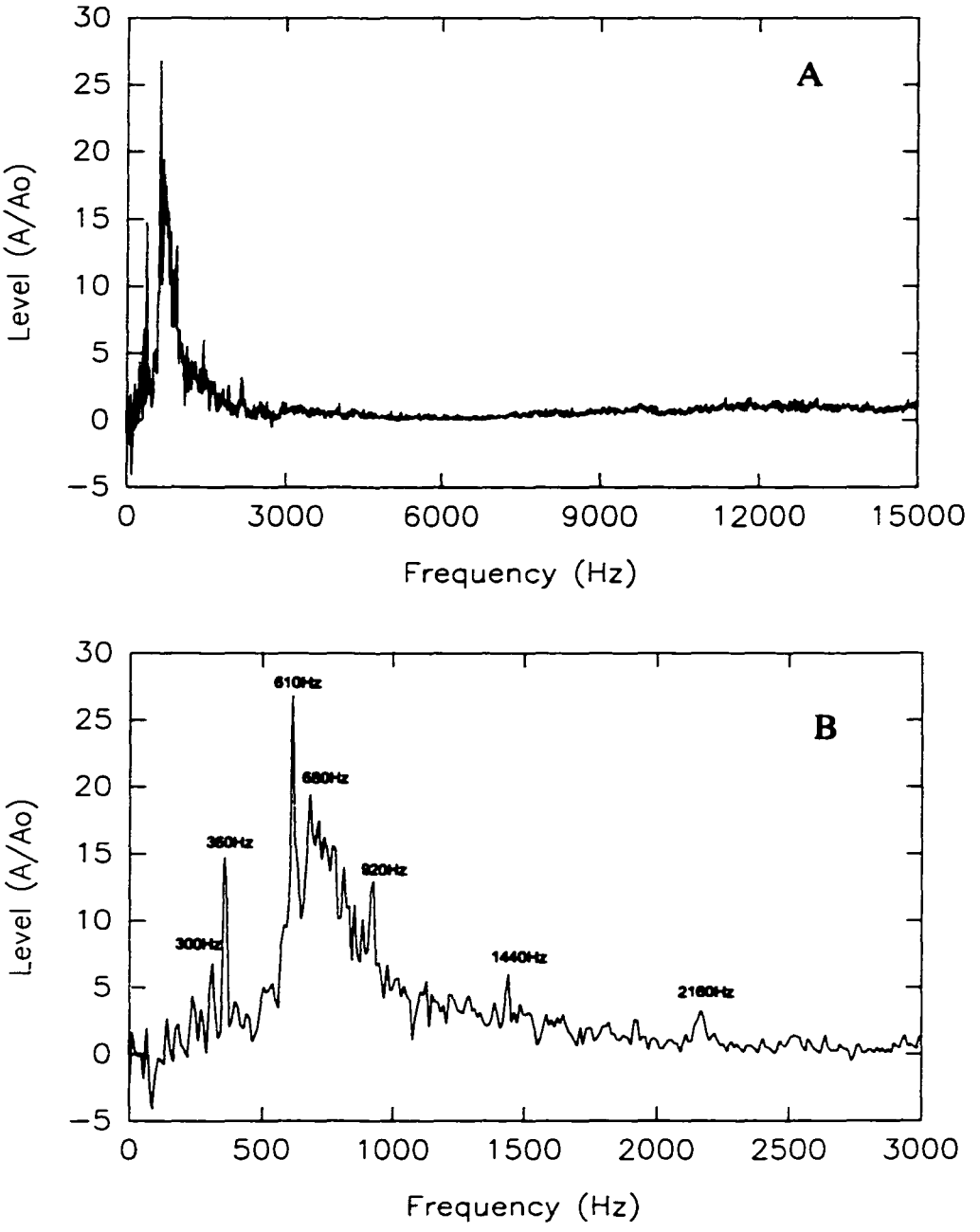


Figure 4.24. Spectrum of CW drill carried out in glycerol at 50 w average power over a 15 kHz bandwidth (A), and a three kHz bandwidth (B).

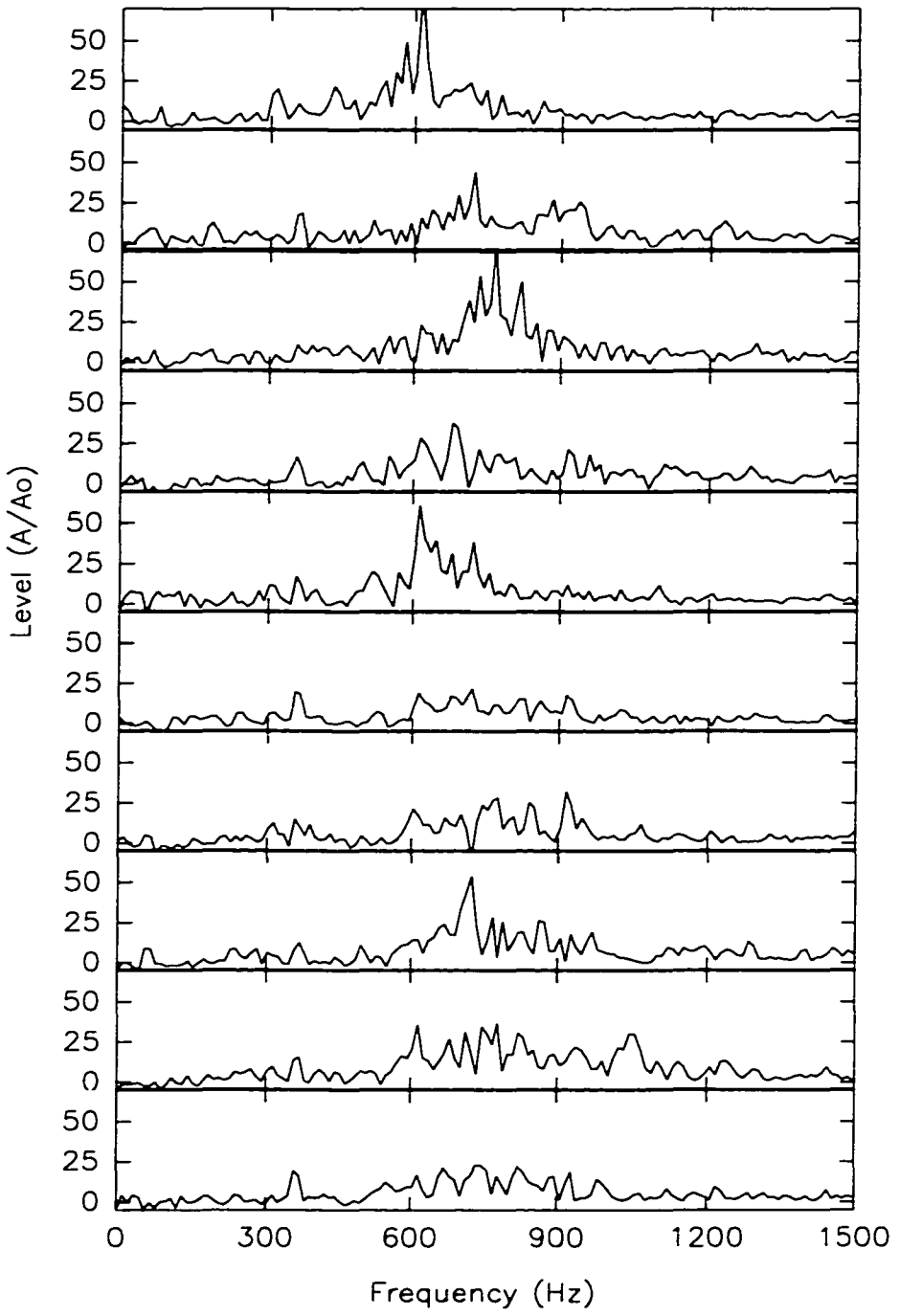


Figure 4.25 **Individual FFT spectra comprising the averaged 50 w CW glycerol drilling spectrum shown in** *Figure* 4.24.

process may be randomly jumping between a group of allowable "eigenmodes" centered near 670Hz. The peak of the band at 670Hz would then represent the most stable eigenstate of the system.

The spectral response of the CW glycerol drilling also appears to be independent of incident laser intensity. A comparison of spectra obtained during 54, 108, and 212 watt CW drilling of glycerol is shown in *Figure* 4.26. The two higher power spectra exhibit apparent absorption lines at 360Hz, suggesting that overcompensation of the electronic noise has occurred. All three spectra show the broad emission peak between 500 and 1000Hz. 212 and 54 watt drills share the same broad 670Hz peak, while the 108 watt spectrum shows a peak near 735 Hz.

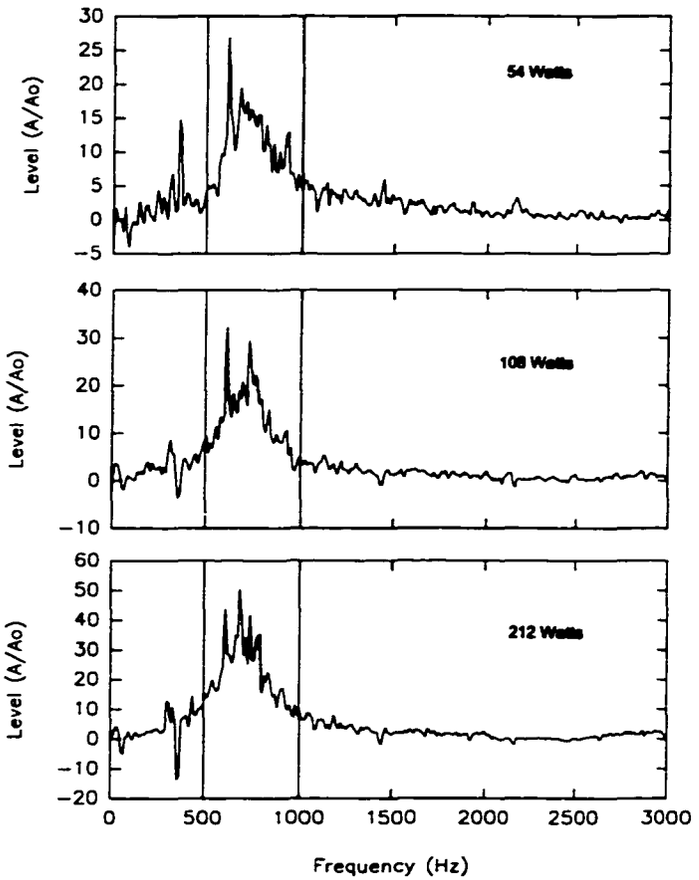


Figure 4.26. Comparison of broad band emission observed during CW drilling of 100% glycerol at 54, 108, and 212 watts.

Chopped Modulation:

The acoustic spectral data will first be presented in the same way as those in the previous section, grouped according to laser power level, and further divided into pre- and post-resonant domains. Accompanying these spectra are estimates of the percentage content of each of the three structural phases (pre-resonant, resonant, and post resonant).

Rather than adjusting the scale of each spectrum to encompass the dynamic range of the data, a single range common to all of the spectra has been used for simplification, but because of this, numerous peaks are truncated. For completeness, all such peaks have their maximum level recorded. *Figures* 4.27, 4.28, and 4.29 summarize the acoustic spectral behaviour of the 25, 54, and 106 watt average power chopped beam drilling leading up to resonance. *Figures* 4.30, 4.31, and 4.32 summarize the acoustic spectral behaviour of the 25, 54, and 106 watt average power chopped beam results from resonance to higher frequency.

It is difficult to identify distinguishing common features in these data which differentiate post- and pre-resonance from resonance. It appears that the second harmonic experiences attenuation somewhere between the pre and post resonant structural states, but it does not follow a consistent pattern throughout the structural resonance phase. All of the highest frequency spectra show an increase in broad band noise starting at around 5.5kHz as well as an increase in signal between 0 and 1000Hz. The higher frequency noise is presumed to be an artifact associated with turbulence generated by the chopper blades. This turbulence generated an audible "hiss" easily perceptible at higher frequencies of modulation. The low frequency noise may be the result of an asymmetry or imbalance in the chopper disc which would induce acoustic frequencies as low as the rotation frequency of the motor. For the chopper used in this series of experiments, the rotation frequency of the motor is 1/12 that of the modulation frequency.

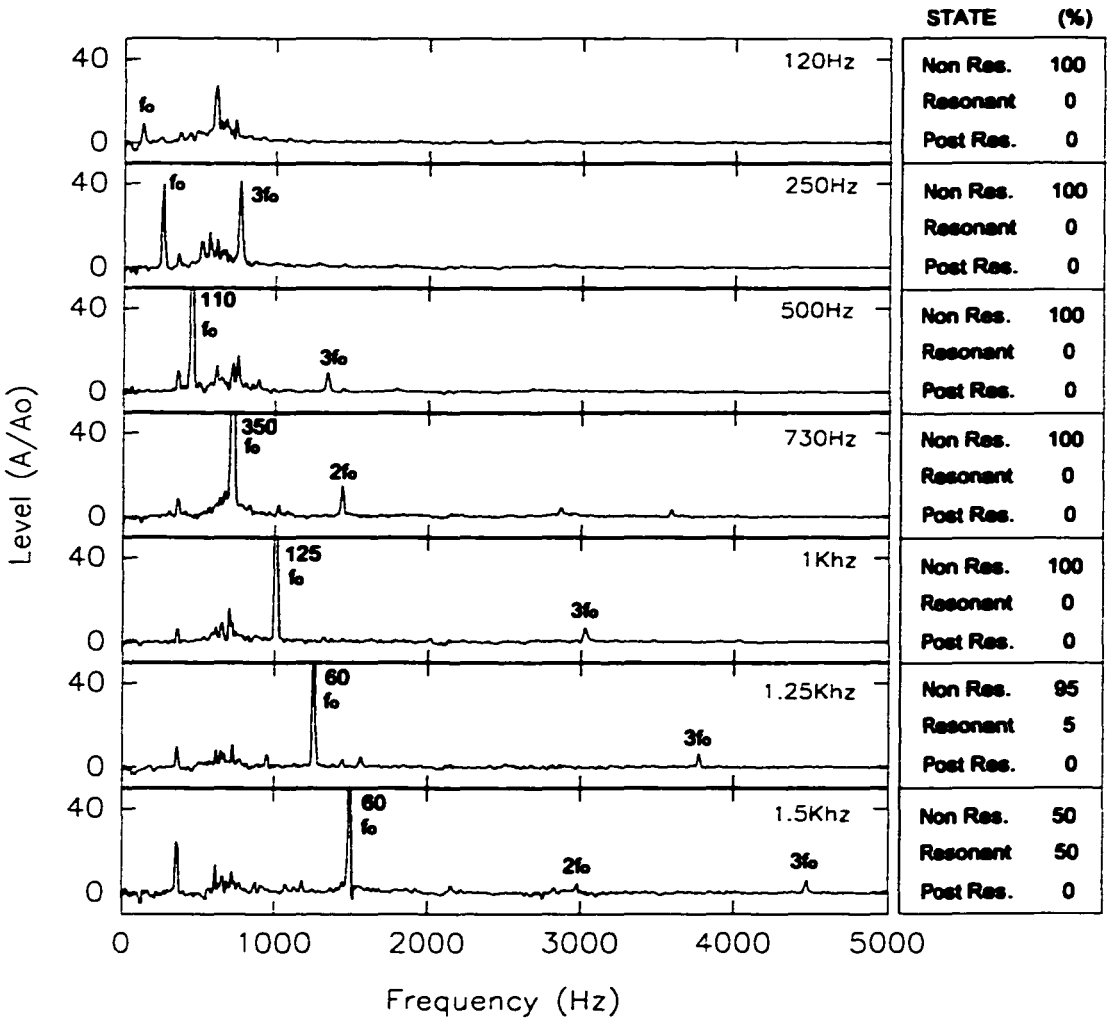


Figure 4.27. Spectral behaviour of 25watt average power chopped drilling of glycerol leading up to structural resonance condition. The estimated ratio of observed structural conditions is shown at the right of each spectrum. Modulation frequencies are shown in the upper right hand corner of each spectrum, and peaks which extend beyond the scale limits have their respective maxima marked beside them.

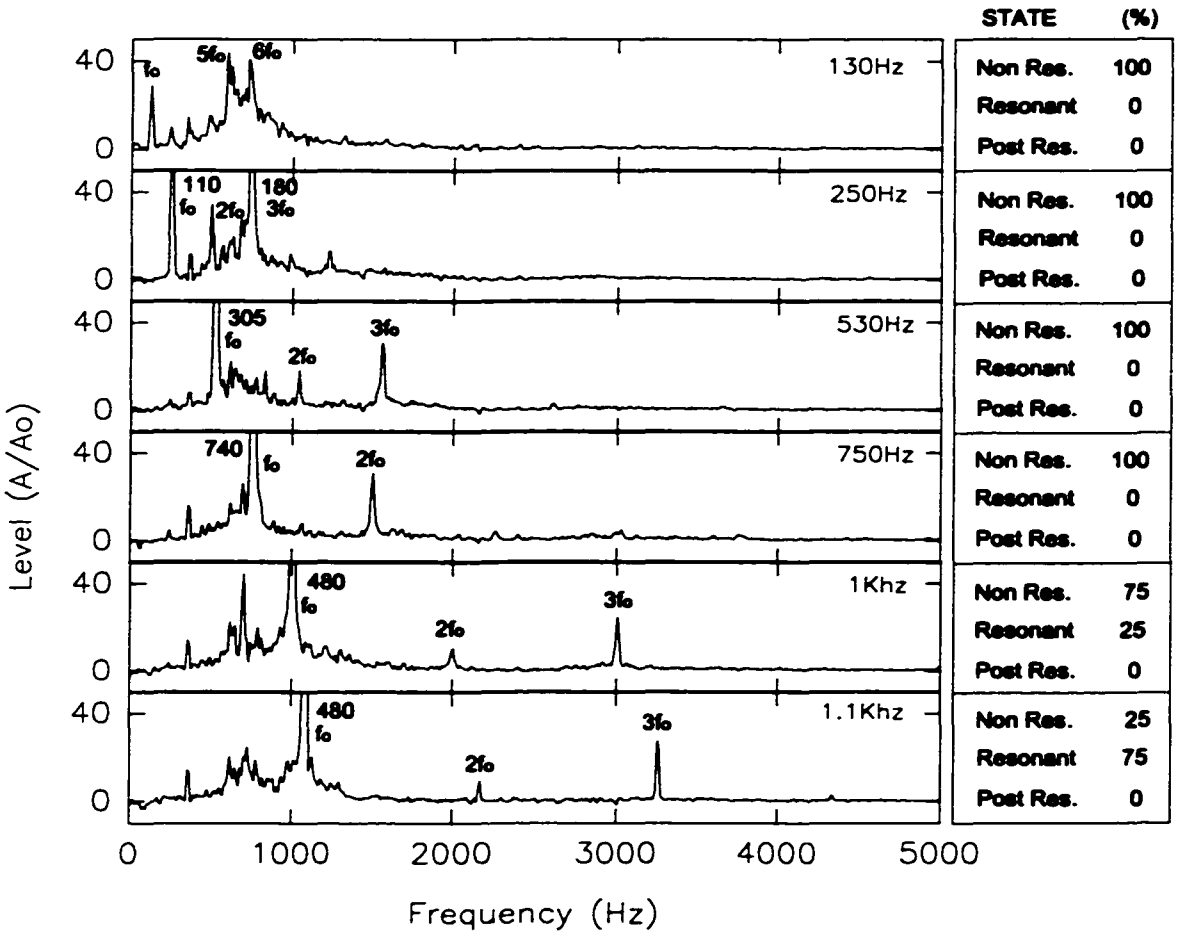


Figure 4.28. Spectral behaviour of 54 watt average power chopped drilling of glycerol leading up to structural resonance condition. The estimated ratio of observed structural conditions is shown at the right of each spectrum. Modulation frequencies are shown in the upper right hand corner of each spectrum, and peaks which extend beyond the scale limits have their respective maxima marked beside them.

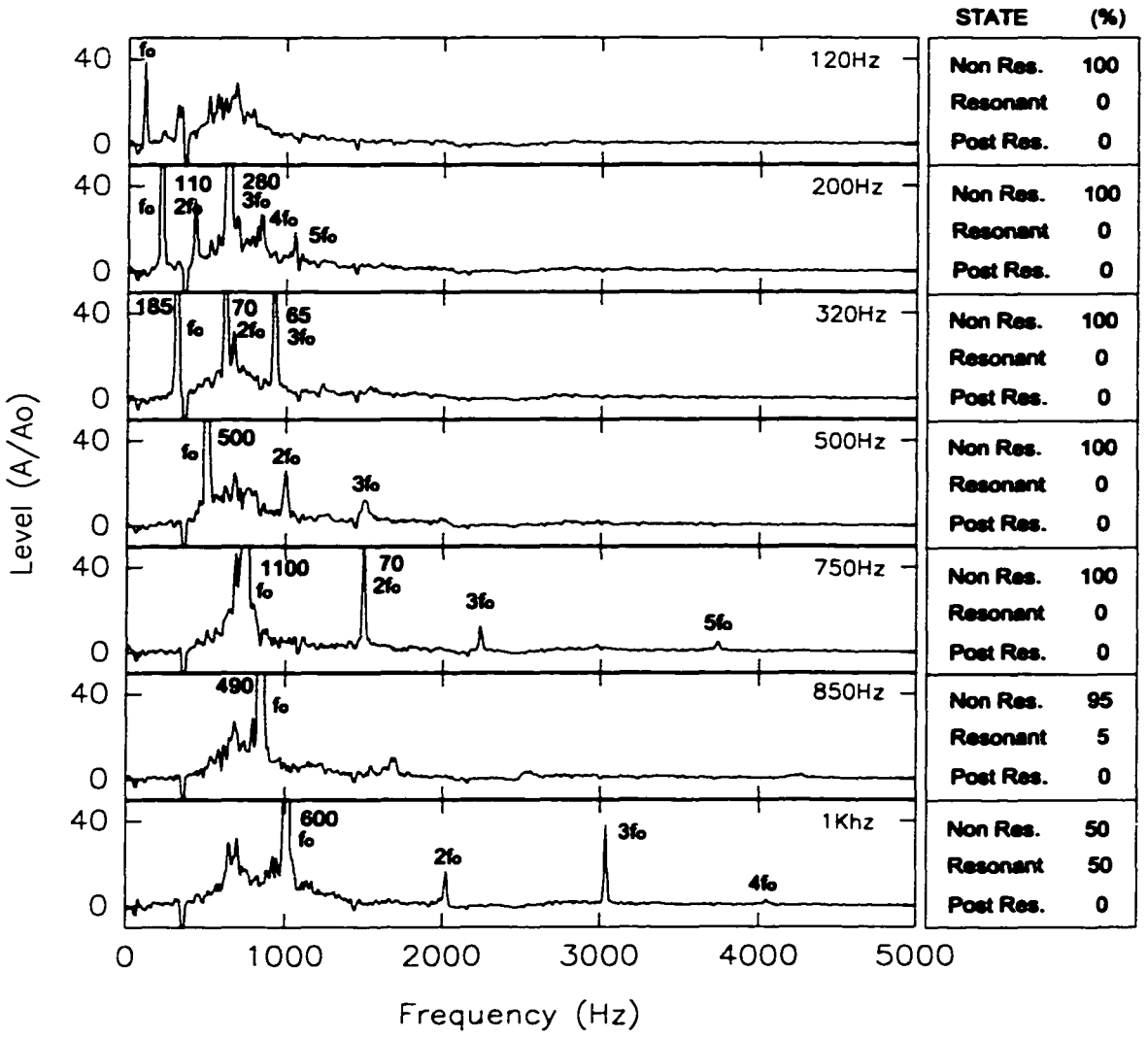


Figure 4.29 Spectral behaviour of 106 watt average power chopped drilling of glycerol leading up to structural resonance condition. The estimated ratio of observed structural conditions is shown at the right of each spectrum. Modulation frequencies are shown in the upper right hand corner of each spectrum, and peaks which extend beyond the scale limits have their respective maxima marked beside them.

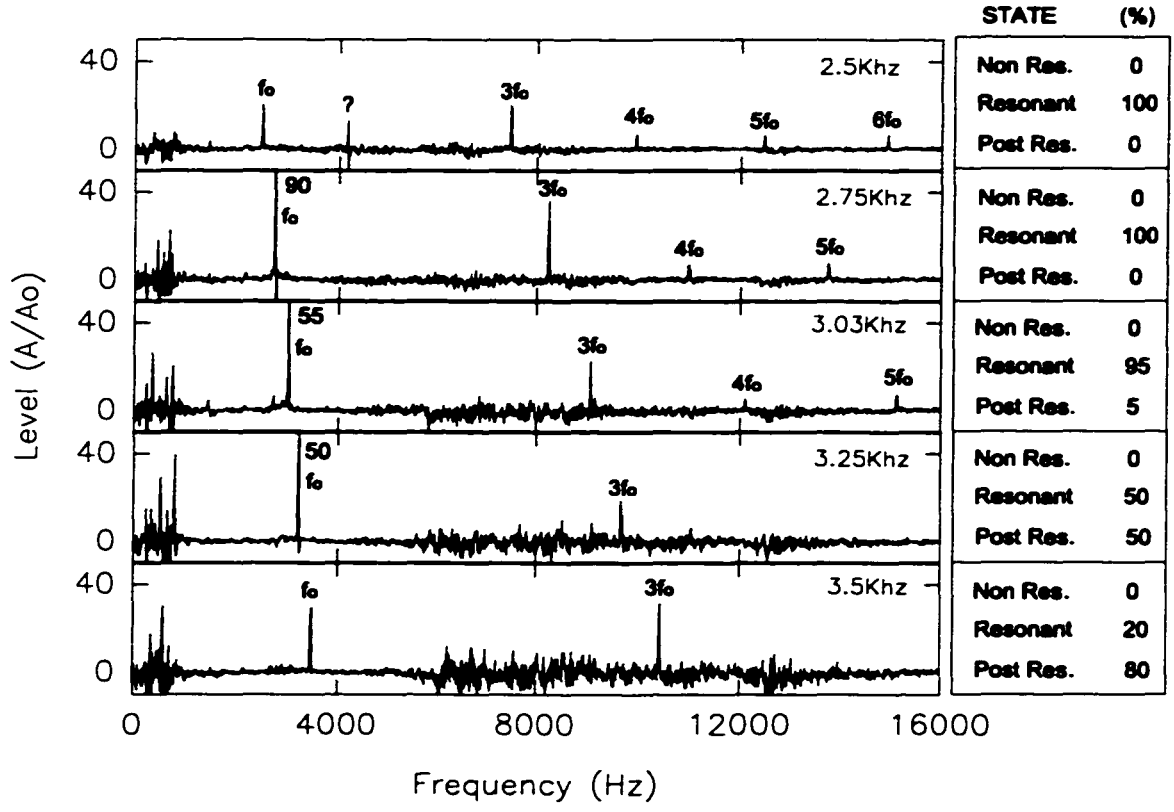


Figure 4.30 Spectral behaviour of 25 watt average power chopped drilling of glycerol from resonant through to post resonant structural behaviour. The estimated ratio of observed structural conditions is shown at the right of each spectrum. Modulation frequencies are shown in the upper right hand corner of each spectrum, and peaks which extend beyond the scale limits have their respective maxima marked beside them.

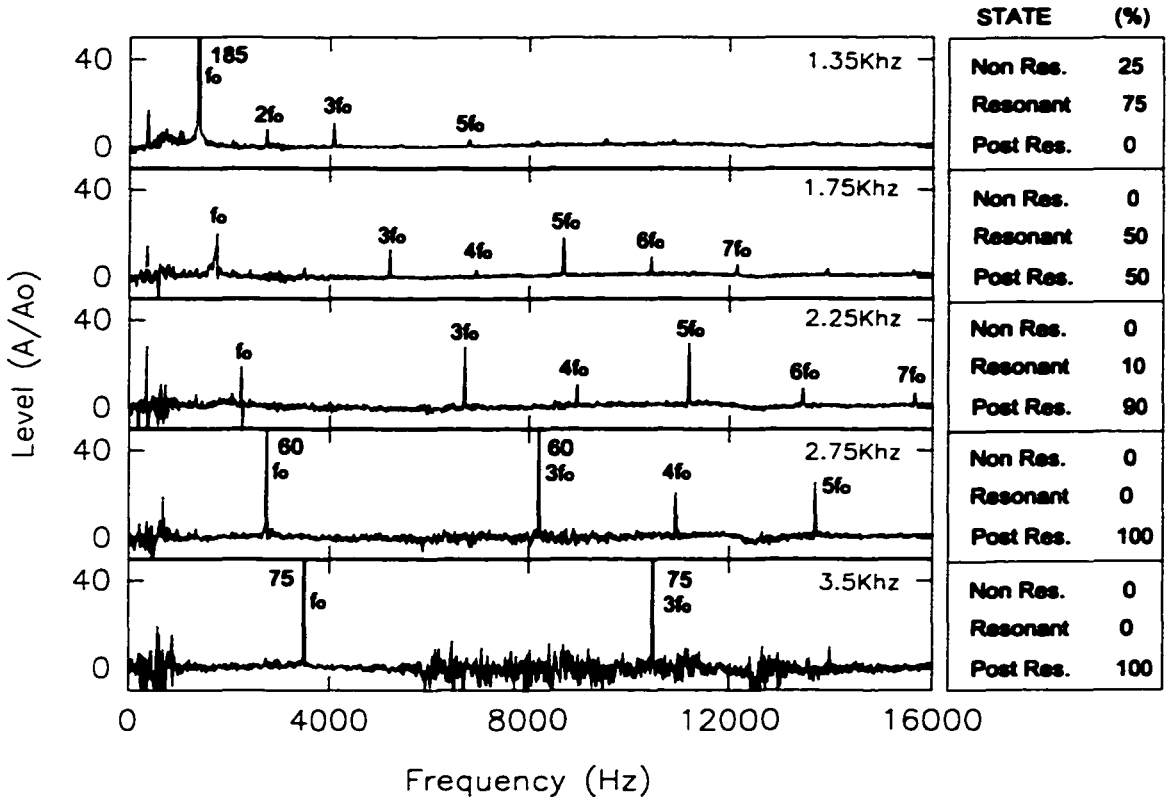


Figure 4.31 Spectral behaviour of 54 watt average power chopped drilling of glycerol from resonant through to post resonant structural behaviour. The estimated ratio of observed structural conditions is shown at the right of each spectrum. Modulation frequencies are shown in the upper right hand corner of each spectrum, and peaks which extend beyond the scale limits have their respective maxima marked beside them.

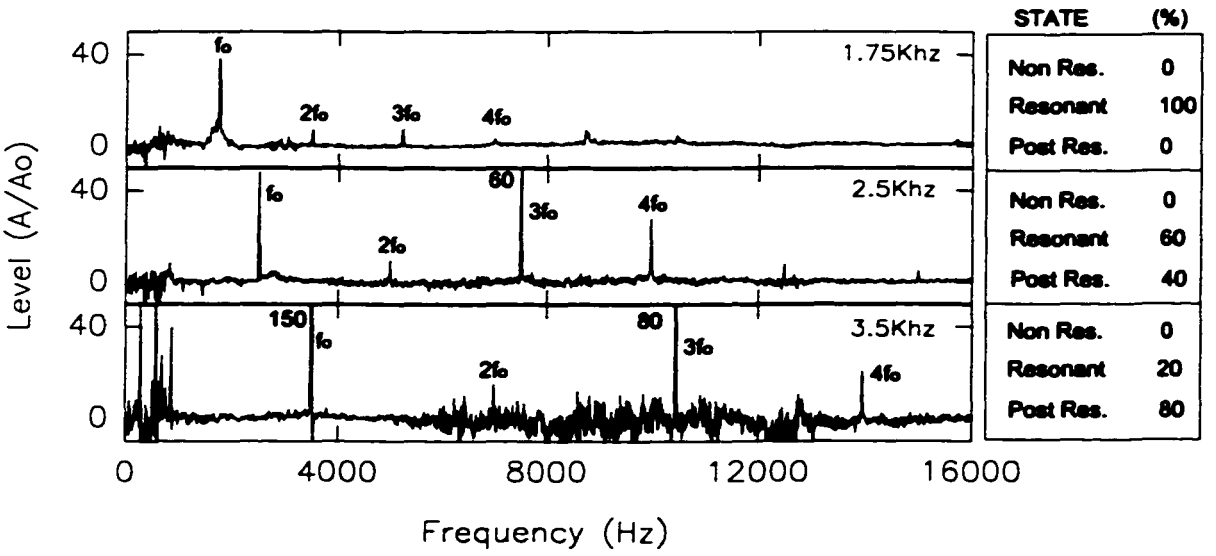


Figure 4.32. Spectral behaviour of 106 watt average power chopped drilling of glycerol from resonant through to post resonant structural behaviour. The estimated ratio of observed structural conditions is shown at the right of each spectrum. Modulation frequencies are shown in the upper right hand corner of each spectrum, and peaks which extend beyond the scale limits have their respective maxima marked beside them.

One limitation associated with the averaged spectra shown above is that results which exhibit mixed mode behaviour are not accurately represented by averaging. Alternatively, through mapping the temporal evolution of the FFT, a direct contrast between resonant and non-resonant like behaviour can be realized under similar experimental conditions. *Figure* 4.33 shows such a temporal FFT map with frequency spanning the y-axis, time along the x-axis, and the relative sound level represented with sixteen colours. This particular experiment initially exhibited stable resonant structure, then transformed into a non-resonant structure. The transition point near 2.0 sec. is quite

clear in the plot. The resonant mode exhibits a strong broad peak at the modulation frequency with evidence of several higher harmonics up to the sixth harmonic. The non-resonant mode has a strong narrow peak associated with the modulation frequency, and also shows evidence of higher harmonics at up to six times the fundamental. Other striking differences between the modes include an enhanced third harmonic observed in the resonant mode, supporting the observations from averaged spectra, and an apparent overall shift of the power spectrum towards the modulation frequency during resonance[16].

16 The sound level spectrum is *not* a power spectrum but is simply related to it by squaring the sound level data. Hence the shifts in frequency distribution of the sound level data will be mirrored in the power spectrum.

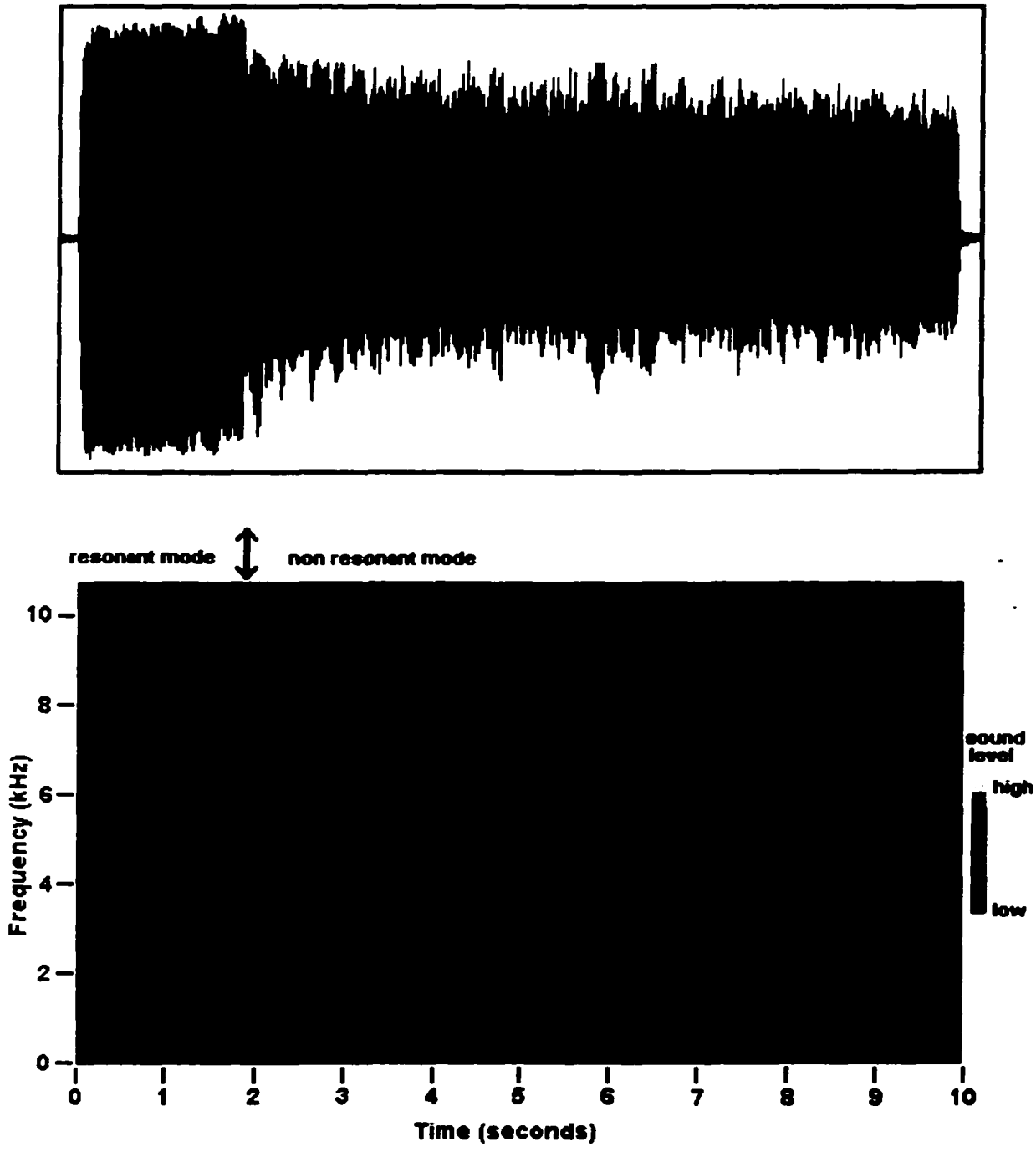


Figure 4.33. Raw signal (upper) and false colour map of temporal evolution of FFT spectrum (lower) during an electronically modulated drill in glycerol. The modulation frequency was 874 Hz and the average power was 106 watts. The colour key for the relative sound level is shown at the right of the figure.

Pulsed Modulation Emissions:

Electronically modulated drilling was somewhat restricted in terms of bandwidth, and choices of frequencies within the smaller bandwidth were limited to discrete frequencies by the laser controller. Despite this however, the electronic modulation technique possessed some distinctive advantages over its mechanical counterpart. First, because modulation was achieved entirely without mechanical motion, the background noise became negligible. Second, since modulation frequencies fall at discrete values, this facilitates easy comparison between resonant and non-resonant behaviour associated with different intensity drilling at the same frequency. Furthermore, electronic noise previously present was eliminated. The resulting FFT spectra were found to be noise free and hence required no post-processing.

Resulting spectra, though limited in driving frequency range, provide the cleanest spectral output of all experimental data. In fact, pulsed drilling FFT data best highlights spectral differences between resonant and non-resonant drilling. As described earlier, electronic modulation is achieved by specifying a single duty cycle in terms of an integer number of internal controller clock cycles. To retain consistency with the mechanical modulation, only 50% duty cycle outputs were used. *Table* 4.3 summarizes the practical frequency outputs available from the laser controller with a 50% duty cycle. Actual Frequency Output is based on direct measurements of the FFT spectra. Surprisingly,

internal clock rates calculated from the FFT measurements resulted in values ranging from 3500 to 3856Hz depending on the modulation frequency. Most importantly however, the frequency stability for a given pulse specification was excellent, leading to FFT spectra with extremely sharp and narrow emission lines.

Table 4.3: Theoretical and measured electronic beam modulation frequencies associated with the VFA-1700 laser.

Total Internal Clock Cycles (#on+#off)	Theoretical Frequency Output (Hz)	Actual Frequency Output (Hz)	Calculated Internal Clock (Hz)
2+2	1000	875	3500
3+3	666	607	3642
4+4	500	465	3720
8+8	250	241	3856

At a modulation frequency of 241 Hz, no structural resonance states were observed. Spectra obtained during drilling at 56 and 102 watts are compared in *Figure* 4.34. The spectral peaks reach levels of more than 100, however as in the previous sections, peaks are truncated at 50 to focus on the region occupied by the typical CW emission envelope and to also provide a similar scale compared to the rest of the FFT spectra. If one ignores the frequency contributions from the modulation frequency and its harmonics, emission spectra closely follow those obtained in CW drilling (*Figure* 4.26). The CW like signal level also exhibits the intensity independence demonstrated in CW

drilling.

At higher modulation frequencies it was possible to induce structural resonance in the drill hole. *Figures* 4.35, 4.36, and 4.37 compare spectra at 465, 607 and 875 Hz respectively. Key ingredients to each of the three figures are spectra which are associated with no structural resonance. These non-resonant emissions were observed only at low intensity and serve as baselines for comparison to the resonant emission. As for 241 Hz, the non-resonant emission envelopes (excluding the modulation frequency and its harmonics) closely resemble CW data.

At higher intensities where resonant behaviour is observed to varying degrees, the CW-like emission envelopes undergo drastic changes, which appear to be related to both the modulation frequency and the relative percentage of observed resonance. Most of the effects appear related to the main CW emission band between 500 Hz and 1 kHz. Resonant structures show increased emission in the 0.5-1 kHz band which are not observed under non-resonant conditions (*Figure* 4.34). Enhanced output is also observed from 1 - 2 kHz and between 2.7 - 3 kHz.

Within the 0.5-2 kHz band, resonant state emissions exhibit a general enhancement over those in the non-resonant state and lines associated with the modulation are broadened to varying degrees. This behaviour is consistent with the frequency response associated with a damped driven harmonic oscillator.

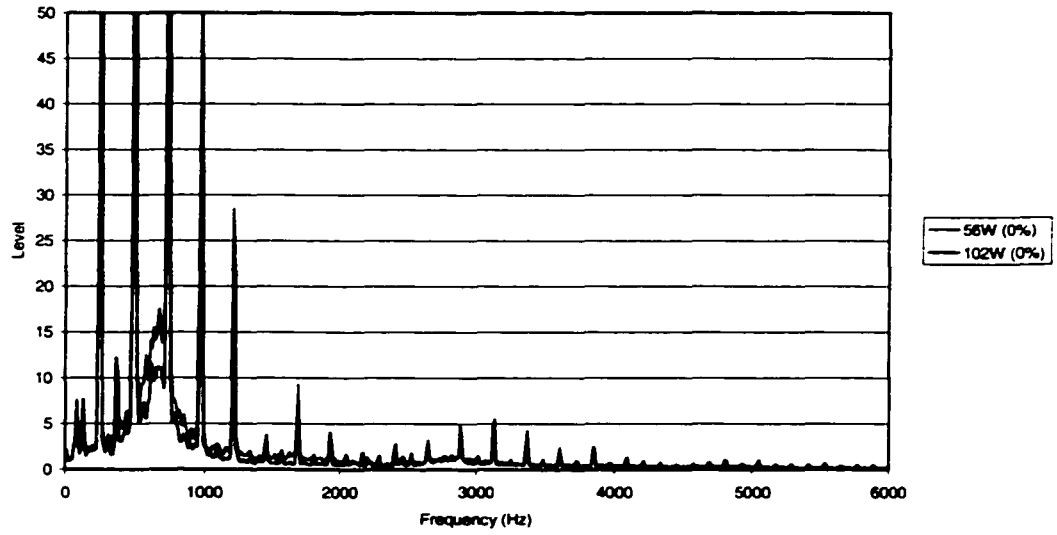


Figure 4.34. FFT Spectra of pulsed beam (241Hz) glycerol drilling at 56 and 102 watts average power. The estimated percentage of observed structural resonance is shown in the legend.

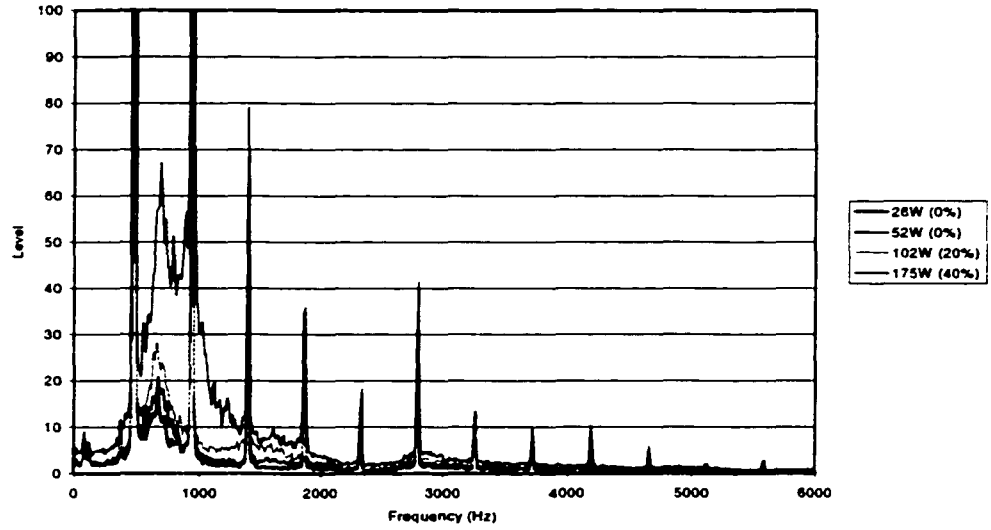


Figure 4.35. FFT Spectra of Pulsed beam (465Hz) glycerol drilling ranging from 26 through to 175 watts average power. The estimated percentage of observed structural resonance is shown in the legend.

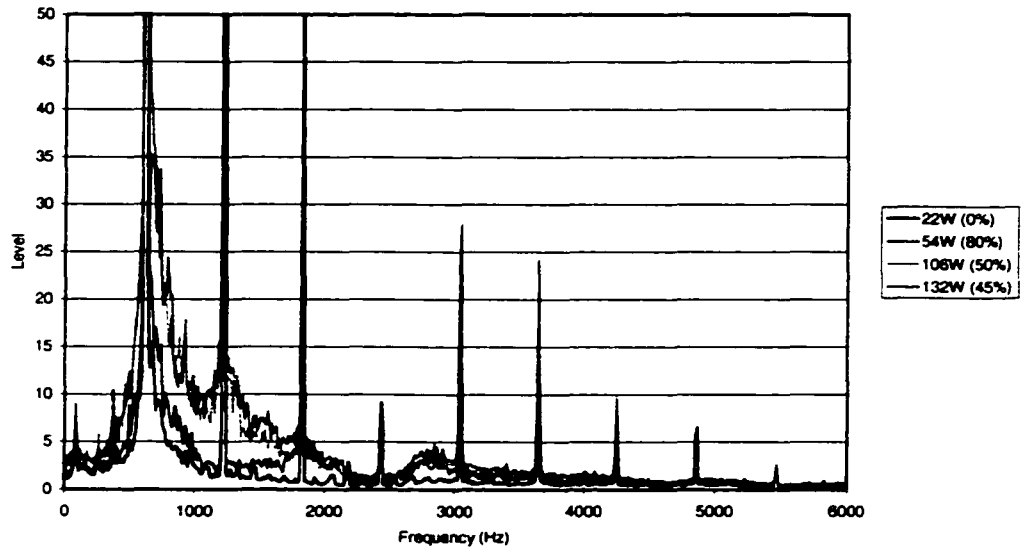


Figure 4.36. FFT Spectra of Pulsed beam (607Hz) glycerol drilling ranging from 22 through to 132 watts average power. The estimated percentage of observed structural resonance is shown in the legend.

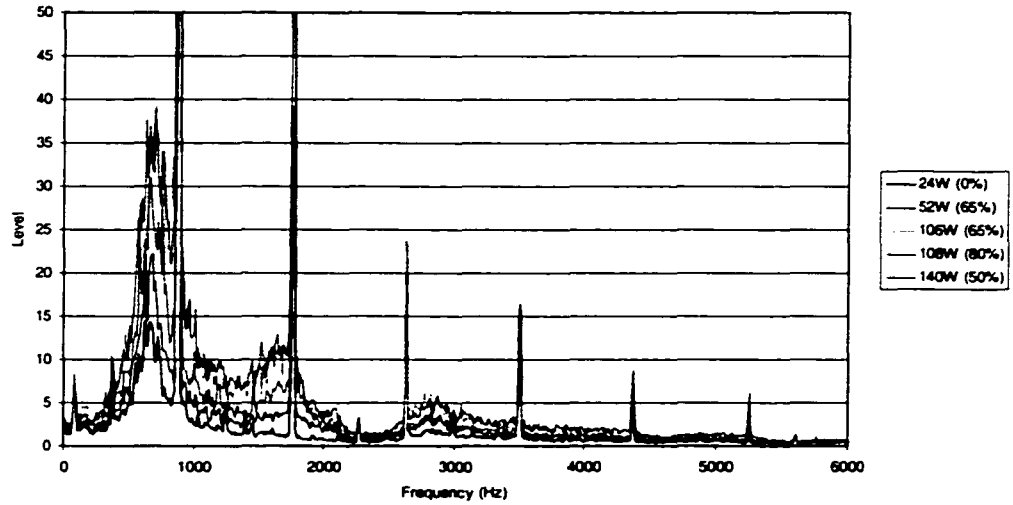


Figure 4.37. FFT Spectra of pulsed beam (875Hz) glycerol drilling ranging from 24 through to 140 watts average power. The estimated percentage of observed structural resonance is shown in the legend.

4.3.3. Spectral Analysis of Water Emission

The only acoustic data collected on water drilling was at 70 watts average power. Spectra all exhibit diminished levels of acoustic emissions from 0 to 16 kHz compared to similar results for glycerol. *Figures* 4.38 and 4.39 show the emission spectrum associated with CW drilling of water at 75 watts power over the 0-15kHz and 0-5kHz bands respectively. Spectra are averaged over approximately thirty seconds. Emission from water show diminished intensity compared to those of glycerol. The largest peak occurs at 360Hz, and is assumed to be attributed to electronic noise. The continuum band of emission shows increased output between 500 and 1000Hz as well as enhancement near 3kHz, as seen in the emission spectra of glycerol. In fact, aside from exhibiting a generally lower intensity, the behaviour of water at frequencies up to about 7kHz appears interchangeable with that of glycerol. Unlike glycerol however, water shows two broad bands between 7-12kHz and 13-16kHz, indicating the presence of much higher frequency structural oscillations.

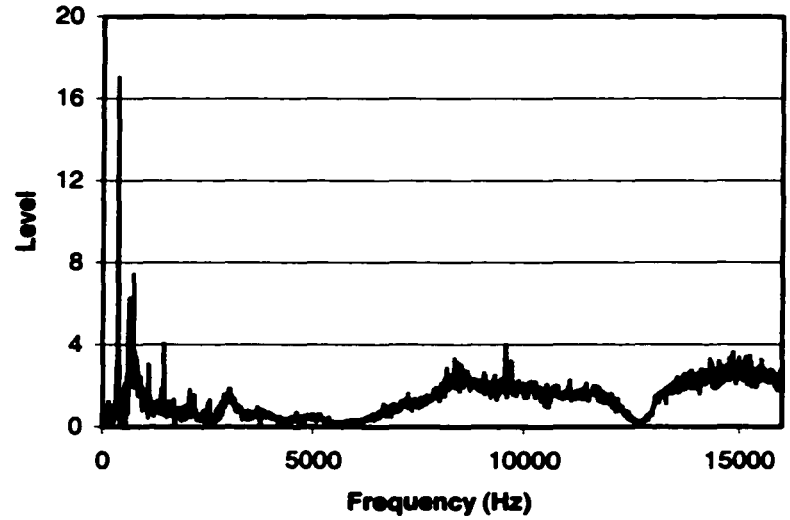


Figure 4.38. Average acoustic emission spectrum for 30 second (accumulated over 3 experiments) duration CW water drilling at an average power of 70 watts over the 0-16kHz band.

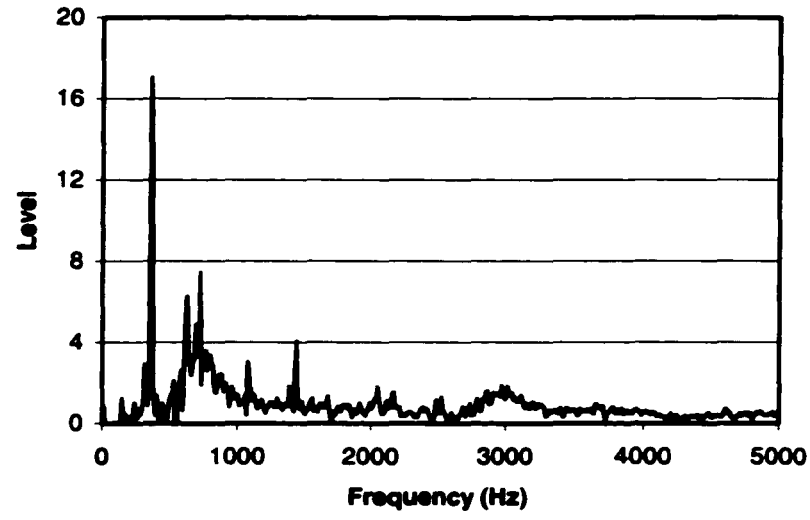


Figure 4.39. Average acoustic emission spectrum for 30 second (accumulated over 3 experiments) duration CW water drilling at an average power of 70 watts over the 0-5kHz band.

Modulated beam spectra are summarized in *Figures* 4.40, and 4.41 for 0-16 and 0-5kHz bands respectively. All show strong emission at the modulation frequency. Higher harmonics are observed in some of the spectra, but not in a consistent pattern. It appears that harmonics which lie within the enhanced bands observed during CW drilling are enhanced so that if a harmonic happens to lie between 500-1000Hz, 2800-3200Hz, 7000-12000Hz, or 13000-16000+ Hz, it will show up on the emission spectrum. Outside of these bands, only the fundamental mode possesses the strength to be detected.

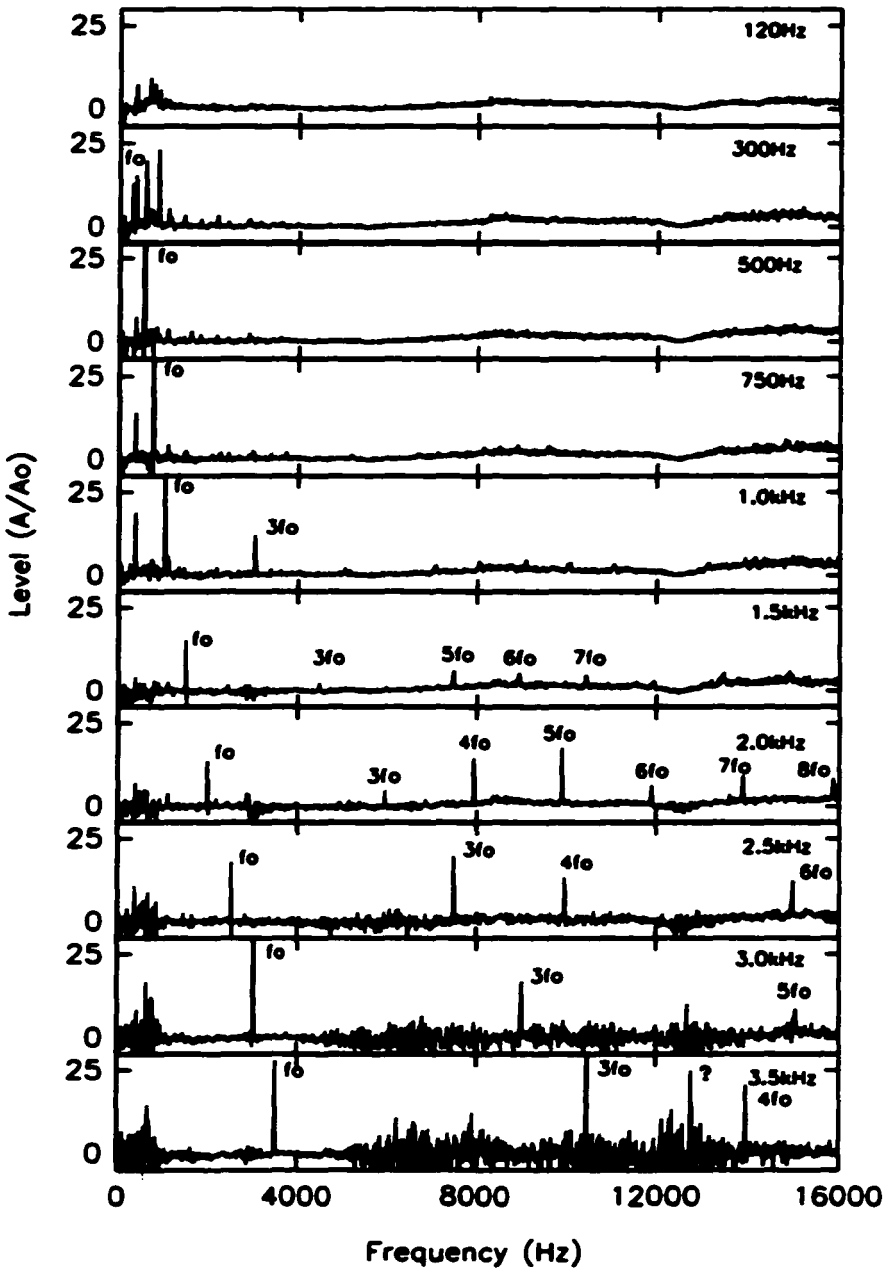


Figure 4.40. Summary of acoustic spectra for chopped beam drilling of water over a chopping frequency range from 0.12 – 3.5kHz. FFT data is presented over the 0 – 16 kHz band.

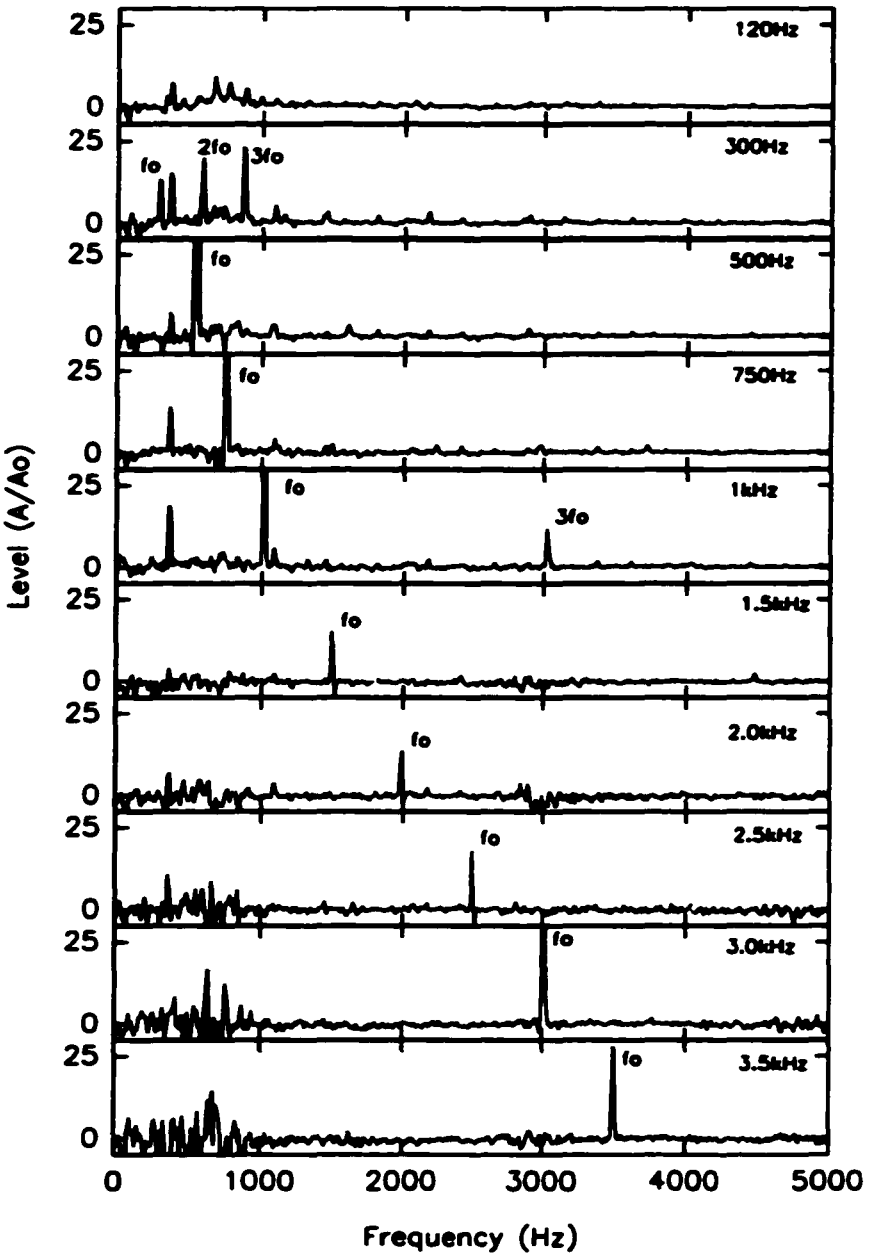


Figure 4.41. Summary of acoustic spectra for chopped beam drilling of water over a chopping frequency range from 0.12 – 3.5kHz. FFT data is presented over the 0 – 5 kHz band.

4.4. Process Models

The data summarized in this chapter highlight what appears to be resonant behaviour associated with the laser drilling of glycerol using a modulated laser beam. The experimental observables which indicate this are the appearance of stable bubble structures together with enhanced acoustic emission in the 0-4kHz band. As previously mentioned, the stability of the resonant mode is of great interest from the point of view of industrial applications. Modeling this two phase process may provide new insight into mechanisms which could stabilise industrial laser welding and drilling processes.

Several questions are posed by these observations: What is the mechanism that drives the resonance in glycerol? If this behaviour is a resonance condition, then why does it appear over a continuous range of modulation frequencies and what causes the destabilisation of the resonant behaviour at higher frequencies? Why is this behaviour apparently not evident in water drilling? The goal of this section is to develop a preliminary model, or models which attempt to answer these questions.

The onset of resonant behaviour is easily related to the modulation frequency from visual inspection. The stability of the resonant state cavity itself makes it possible to study such parameters as the depth and radius of the quasistable bubble. The first approach will focus on mapping the geometric relationship between bubbles in the

resonant state and the modulation frequency.

4.4.1. Geometric Relationships to Modulation Frequency

The preliminary observation of resonant states at different modulation frequencies (highlighted in *Figure* 4.10) indicate that the size of the bubble is related in some way to the modulation frequency. Since the bubble phenomenon is quite stable in the resonant state, quantitative data can be acquired as a function of the modulation frequency. The quantitative data regarding the bubble geometry include the radius of the bubble and its depth. This information was obtained from individual video frames, but due to the sheer number of frames showing resonant structure, measurements were limited to roughly ten discrete samplings evenly distributed in time during each data set.

Bubble radii vs. depth are plotted in *Figures* 4.42 through 4.44, for low, medium and high intensity experiments. Data points are grouped according to the modulation frequency and it was observed that in all cases when resonance appeared, bubble geometry evolved towards larger shallower structures as time evolved.

The resonant state bubbles nearly always show a texture which is periodic, implying the presence of one or more spherical harmonic wave states on the surface of the bubble. Landau and Lifshitz [48] have solved the problem of surface waves on a

spherical droplet (or bubble). The solution involves a linear combination of volume spherical harmonic functions, $r^l Y_m^l(\theta,\phi)$, where r represents the radius of the bubble/droplet and $Y_m^l(\theta,\phi)$ are Laplace's spherical harmonics. The solution gives rise to discrete eigenfrequencies ω_l which are $2l+1$ fold degenerate[17], given by

$$\omega_l^2 = \frac{\alpha l(l-1)(l+2)}{\rho R^3} \qquad 4.6$$

Where α represents the surface tension of the liquid, ρ the density, and R the steady state radius of the bubble.

17 The index l in the spherical harmonic determines the frequency, and since the index m takes the values $0, \pm1, \pm2, \ldots, \pm l$, there exists a $2l+1$ fold degeneracy in the eigenfrequencies.

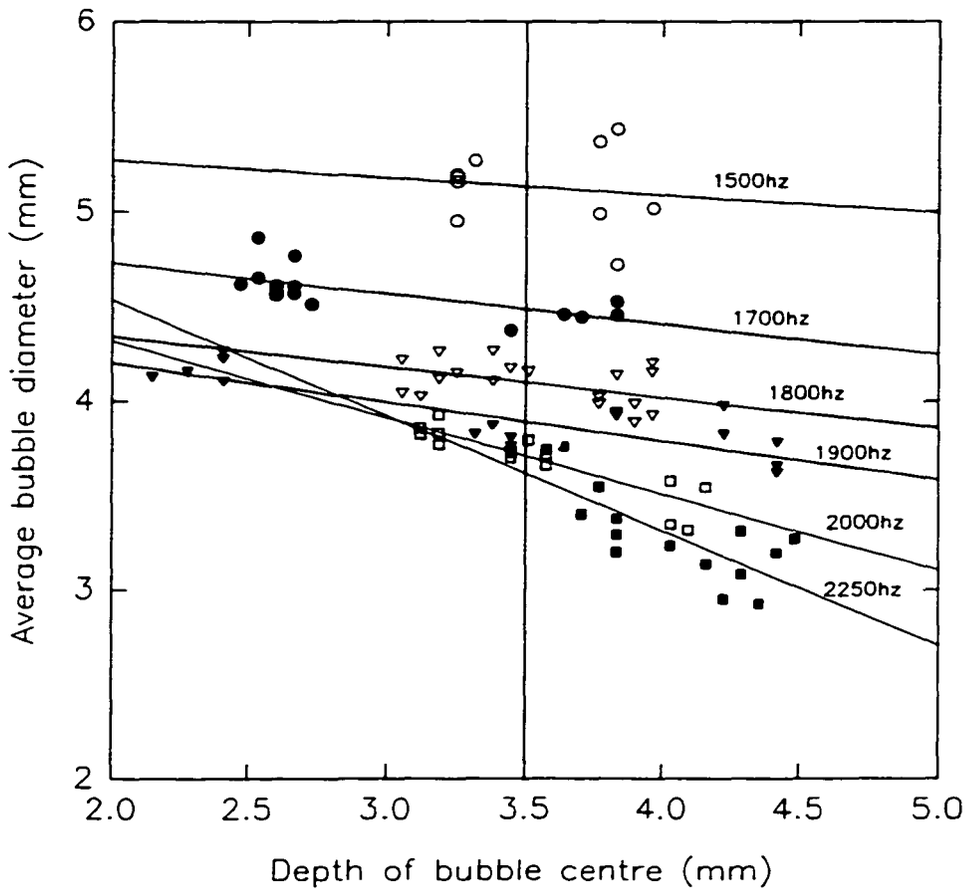


Figure 4.42 **Bubble diameter vs depth for low intensity modulated beam excitation of glycerol. Least squares fits show the general depth versus diameter trend of the data.**

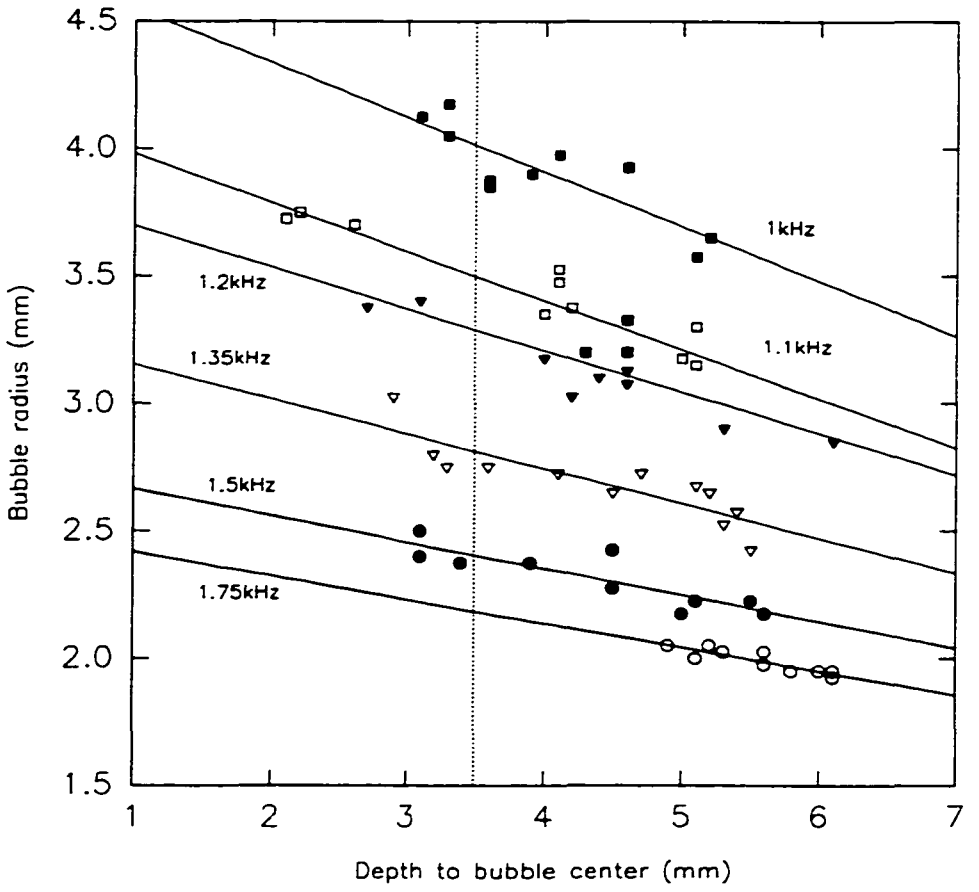


Figure 4.43 Bubble diameter vs depth for medium intensity modulated beam excitation of glycerol. Least squares fits show the general depth versus diameter trend of the data.

Aside from material constants, the only functional dependence of the eigenfrequency is on the radius of the bubble. In order to extract a similar dependence from the experimental data of *Figures* 4.42 - 4.44, r measured at z=3.5mm was extrapolated for each frequency group and for each intensity level. *Figure* 4.45 compares the frequency-bubble size dependence of selected spherical harmonic modes to

the experimental data (at a depth of 3.5mm). A density of 1250 kg/m^3 and surface tension coefficient of 0.069 N/m were used in the calculation of the eigenfrequency curves.

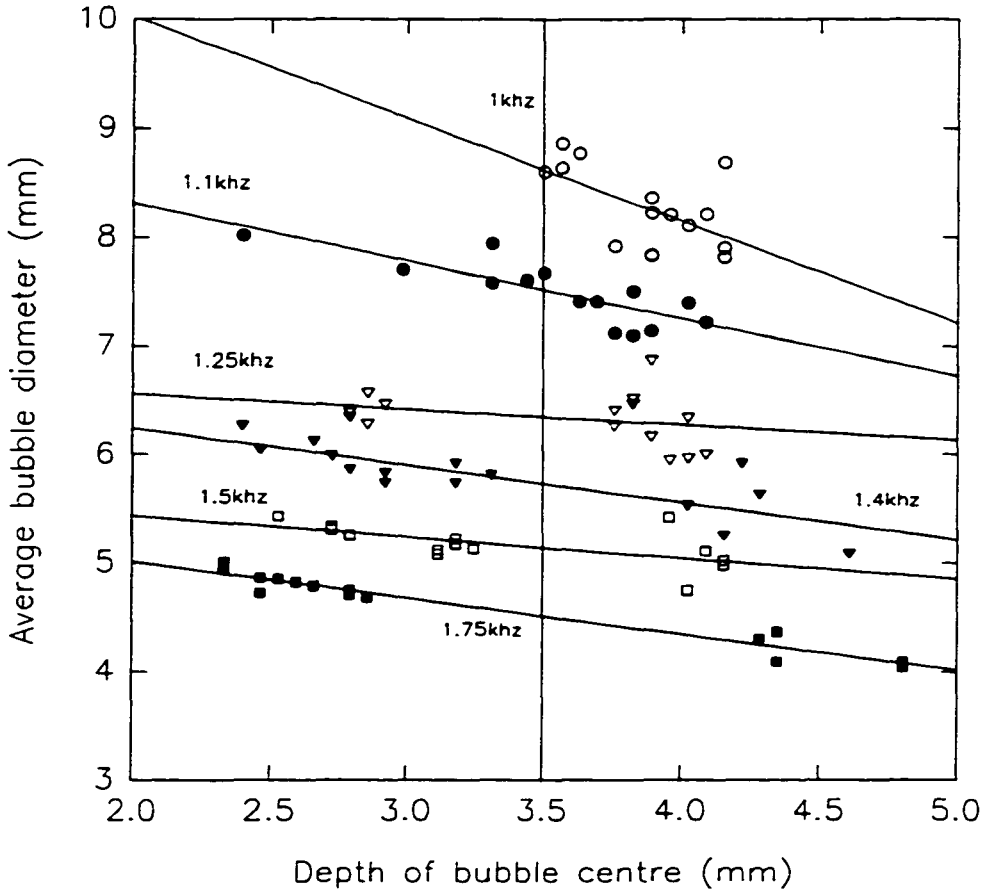


Figure 4.44 Bubble diameter vs depth for high intensity modulated beam excitation of glycerol. Least squares fits show the general depth versus diameter trend of the data.

Several noteworthy observations come from *Figure* 4.45. The experimental data sweep through a range of four eigenfrequencies (l=8, 9, 10, 11) which indicates that the

resonant condition is not the result of coupling with a preferred eigenstate of the bubble. More striking however is the fact that the experimental data, taken from three completely different intensity regimes, appear to conform to the same frequency-radius dependence. This suggests that the mechanism(s) generating the quasistable bubble is intensity *independent.* Recall that in section 4.3.2, spectra of CW emission from glycerol also showed no dependence on intensity.

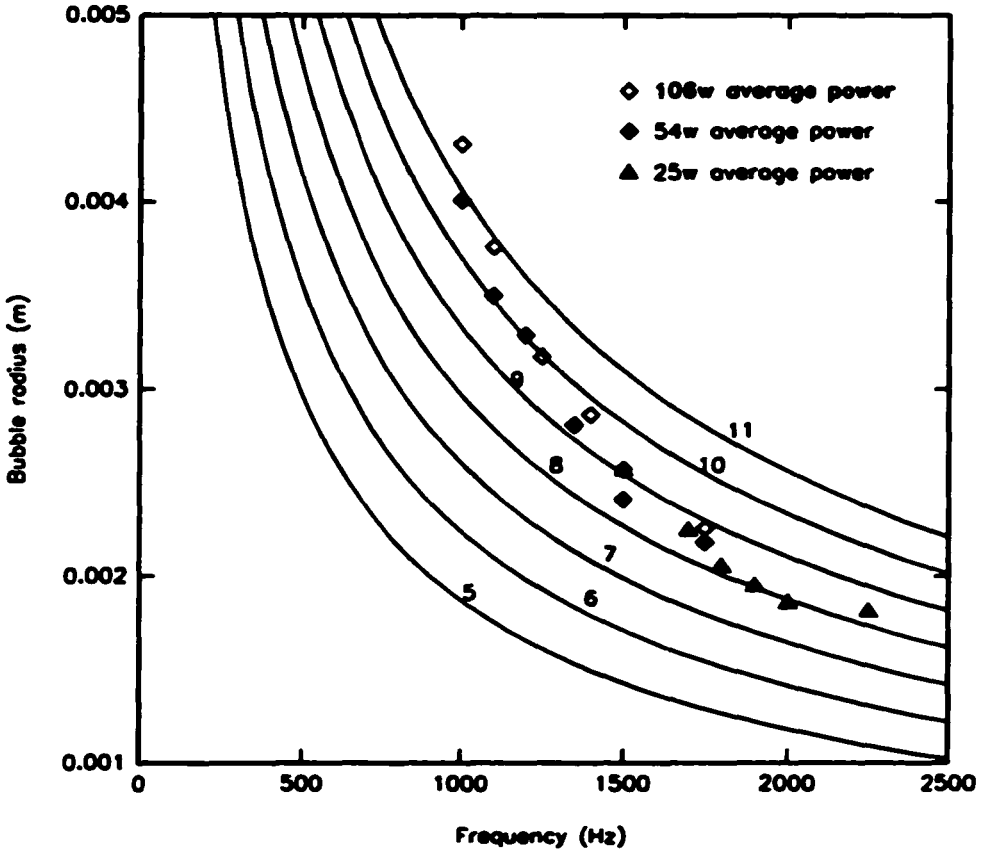


Figure 4.45 Radius vs. frequency for selected spherical harmonic modes associated with surface waves on a spherical bubble of radius R in glycerol generated from *Equation* 4.6. The numbers adjacent to the curves represent the "l'th" state of the spherical harmonic Y_m^l. The resonant state data is overlaid on the spherical harmonic curves, extrapolated from a bubble depth of 3.5mm.

The close conformance of the experimental data across varying laser intensities can also be seen in *Figure* 4.46 where the data is presented in the form of bubble radius versus inverse frequency. Bubble radii clearly exhibit a linear dependence on the inverse frequency, independent of laser intensity. At this time both the intensity independence and the linear bubble radius-inverse modulation frequency cannot be explained and further investigation is required. In the following sections, the resonant behaviour will be modeled in terms of the natural collapse times of the drill holes.

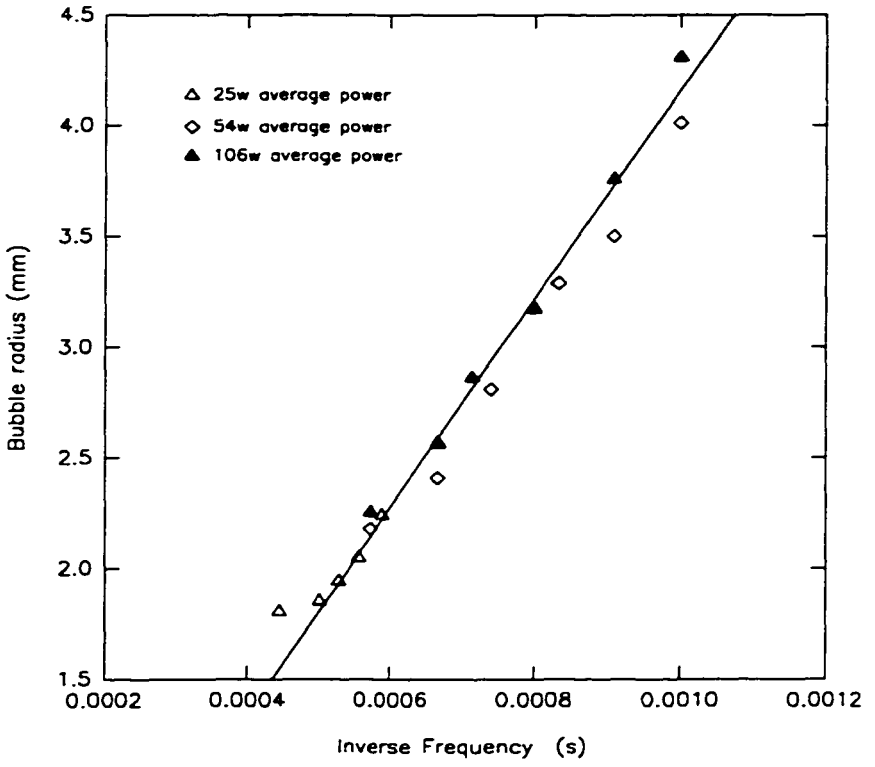


Figure 4.46 Bubble radius vs. inverse frequency for bubbles located at a depth of 3.5mm. (Data was obtained by interpolation of data from *Figures* 4.42 to 4.44 through best fit lines to a depth of 3.5mm.)

4.4.2. Cylindrical Cavity Collapse Model

As discussed in chapter 1, Kroos et al [25-27], solve an expression for the collapse time of the keyhole (drill hole) in the absence of viscosity to determine the lower limit of the keyhole closing time. The assumption underlying this approach is that the inverse of the collapse time yields a frequency attributable to the ground state or fundamental mode of oscillation of the drill hole. These authors simplify the equation of motion by neglecting effects due to viscosity. Because of the obvious difference in viscosity between water and glycerol it would be desirable to develop solutions which take this quantity into account.

The equation originally solved by Kroos et al (*Equation* 1.10) results from simplification of an equation which contains an explicit dependence on the viscosity of the melt pool. The full equation of motion describing the keyhole *prior* to this simplification is reproduced below.

$$\frac{\ddot{A}}{4}\ln\left(\frac{C+A}{A}\right)-\frac{(\dot{A})^2}{8A}\left(1-\frac{A}{A+C}\right)+D\frac{\dot{A}}{A}\left(1+\frac{A}{A+C}\right)=P(\tau)-\frac{1}{\sqrt{A}}\left[1+\left(\frac{A}{A+C}\right)^{1/2}\right] \qquad 4.7$$

A is a dimensionless form of the keyhole radius, C is a dimensionless parameter which indicates the radial extent of the molten material, D is a dimensionless measure of the viscosity, and $P(\tau)$ is a dimensionless pressure term which accounts for the excess pressure $\Delta p(t)$, maintaining the cavity against the closing pressures. *Equation* 4.7 is in the

form of a second order nonlinear differential equation in A, where the dots represent differentiation with dimensionless time τ. The terms are defined below.

The dimensionless radius is expressed in terms of the time dependent keyhole radius

$$A(\tau) = \left(\frac{r_1(t)}{r_o} \right)^2 \tag{4.8}$$

where $r_1(t)$ is the radius of the keyhole wall, and r_0 is the initial keyhole wall radius at t=0. Dimensionless time, τ, is defined as

$$\tau = t \Big/ \left(\frac{\rho r_o^3}{\gamma} \right)^{1/2} \tag{4.9}$$

where ρ is the melt density, and γ is the coefficient of surface tension. Dimensionless pressure, $P(\tau)$, is given by

$$P(\tau) = \frac{\Delta p(t) r_o}{\gamma} \tag{4.10}$$

with $\Delta p(t)$ described above. C describes the radial extent of the melt pool, and is given by

$$C = \frac{r_2^2(0)}{r_0^2} - 1 \tag{4.11}$$

where $r_2^2(0)$ represents the initial radius of the melt pool. The final parameter requiring definition is the viscosity

$$D = \nu\left(\frac{\rho}{\gamma r_o}\right)^{1/2} \qquad 4.12$$

with ν representing the *kinematic* viscosity of the melt.

Analogous to the approach taken by Kroos et al [25], the inverse of the collapse time of a cylindrical cavity of radius r_o will be sought and used to determine the frequency of the fundamental mode of the drill hole. To accomplish this, *Equation* 4.7 must be solved. By assuming a static cylindrical cavity exists at t=0 and setting the ablation pressure term to zero ($P(\tau)$=0) in *Equation* 4.7 the cavity will undergo collapse. The boundary conditions describing this are as follows

$$A(0) = 1, \qquad \dot{A}(0) = 0 \qquad 4.13$$

Given the complexity of *Equation* 4.7, it must be solved numerically. *Equations* 4.7 and 4.13 were solved using the numerical differential equation solving function within *Mathematica*. As a check, the solution derived by Kroos et al based upon *Equation* 1.10 was reproduced using *Equations* 4.7 and 4.13, setting D=0 and using a variety of values of the parameter C similar to those displayed by Kroos et al. The Mathematica results were indistinguishable from those of Kroos et al, validating both the syntax of the input equations and the accuracy of the Mathematica output.

In order to solve Equation 4.7 for glycerol and water, a variety of thermophysical properties are required for each liquid. Temperature dependent material properties of

both glycerol and water were obtained using material properties computation software [49]. The relevant properties for water and glycerol are tabulated below in *Tables* 4.4 and 4.5. The data spans the temperature range from 300 K to the respective boiling temperatures of water and glycerol. To simplify the comparison of water and glycerol results, a normalised temperature is introduced and defined as

$$T^* = \frac{T - 300}{T_{boil} - 300}. \qquad 4.14$$

Table 4.4 Material properties for water from 300 - 372K [49].

Temperature (Kelvin)	Normalised Temperature	Liquid density (kg/m^3)	Dynamic Viscosity (Pa/s)	Surface Tension (N/m)
300.00	0	9.95E+02	8.46E-04	7.36E-02
308.00	0.11	9.94E+02	7.07E-04	7.21E-02
316.00	0.22	9.91E+02	6.03E-04	7.06E-02
324.00	0.33	9.89E+02	5.22E-04	6.90E-02
332.00	0.44	9.85E+02	4.59E-04	6.74E-02
340.00	0.55	9.82E+02	4.09E-04	6.58E-02
348.00	0.66	9.77E+02	3.68E-04	6.42E-02
356.00	0.77	9.73E+02	3.34E-04	6.26E-02
364.00	0.88	9.68E+02	3.05E-04	6.10E-02
372.00	1	9.62E+02	2.81E-04	5.94E-02

Table 4.5 Material properties for glycerol from 300 - 560K [49].

Temperature (Kelvin)	Normalised Temperature	Liquid density (kg/m^3)	Dynamic Viscosity (Pa/s)	Surface Tension (N/m)
300.00	0	1.30E+03	5.27E-01	1.28E-01
328.89	0.11	1.26E+03	1.06E-01	1.16E-01
357.78	0.22	1.22E+03	2.39E-02	1.03E-01
386.67	0.33	1.19E+03	9.07E-03	9.05E-02
415.56	0.44	1.16E+03	4.72E-03	7.90E-02
444.44	0.55	1.14E+03	2.97E-03	6.81E-02
473.33	0.66	1.12E+03	2.11E-03	5.80E-02
502.22	0.77	1.11E+03	1.61E-03	4.86E-02
531.11	0.88	1.09E+03	1.28E-03	4.00E-02
560.00	1	1.08E+03	1.05E-03	3.20E-02

Solution of *Equation* 4.7 requires specification of the parameters C, and D, which are in turn dependent on the initial drill hole radius r_o, the outer melt radius r_2, the liquid density, the liquid viscosity (kinematic), and the surface tension coefficient. The radial parameters r_o, and r_2 contain the highest degree of uncertainty. The drill hole radius is not well defined because of its dynamic and often tapered form, and the outer melt radius does not exist in the 2-phase system. Because of this uncertainty, the sensitivity of these parameters to the closing time result must be discussed.

The melt boundary in the glycerol and water systems is defined by the rectangular container walls which measure 50mm×100mm. With the drill hole centered in the container, the smallest unbounded cylindrical volume has a radius of 25mm. An upper limit to r_2 would be the circle bounded by the long dimension of the container, leading to a radius of 50mm. This represents an uncertainty of 100% in the r_2 parameter. To test

the sensitivity of this variation on the closing time result, the lower and upper limits for r_2 were used to compute the closing times for a water cavity with an initial radius of r_o=0.2mm, and normalised temperature T^*=1. Closing time results ranged from 8.13×10^{-4} -7.63×10^{-4}s , representing less than 7% change in the results over a 100% change in the r_2 input parameter. The closing time was hence determined to be insensitive to the outer melt radius and it was arbitrarily fixed at r_2=35mm for the remainder of the computations.

In a similar manner, assuming the initial cavity radius may range from r_o=0.1-0.2mm, there is again a 100% uncertainty in the input parameter. Closing times for water having an outer melt radius of r_2=35mm and T^*=1 were computed using upper and lower values for the initial cavity radius, resulting in closing times ranging from 2.97×10^{-4} - 7.89×10^{-4}s, representing a 166% change in the output for a 100% variance in the input. The closing time was hence determined to be sensitive to the initial cavity radius and for this reason the results have been calculated for several values of r_o. The results are shown in *Figure* 4.47 for both water and glycerol. The results are presented in terms of the inverse of the closing time (i.e. the fundamental mode frequency) versus normalised temperature.

Initial drill hole radii of 0.10, 0.15, and 0.20mm were used in conjunction with the temperature dependent material properties and an outer melt radius of 3.5cm. The water

demonstrates a very weak and almost linear dependence on the normalised temperature, decreasing monotonically with increasing temperature. Starkly contrasting this is the glycerol behaviour which demonstrates a strong increasing trend at lower temperatures, having a maxima near T^*=0.2 followed by a somewhat weaker decreasing trend up to the boiling point.

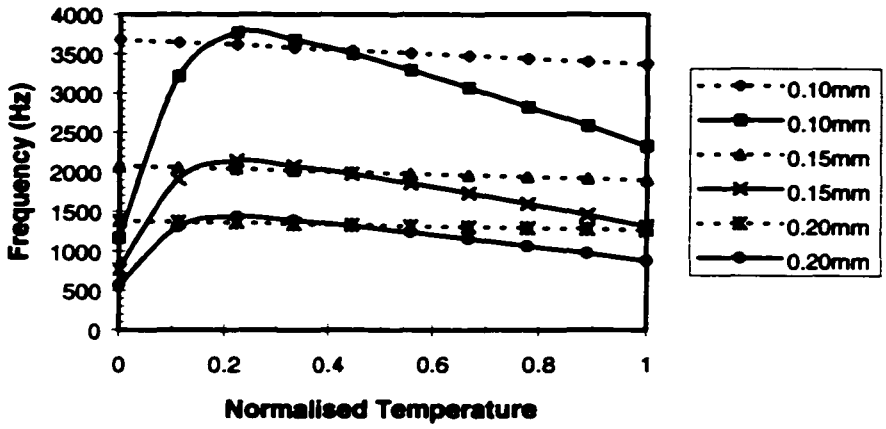


Figure 4.47 Inverse of cavity closing times assuming fundamental mode for water and glycerol based on initial radii of 0.10, 0.15, and 0.20mm (shown in the legend). The solid lines pertain to glycerol while the dashed lines are with for water.

It is interesting to note that for all initial radii, glycerol and water are predicted to share identical closure times *at two specific normalised temperatures.* Furthermore, as the initial drill hole radius increases, the predicted fundamental mode frequencies decrease and the relative differences between the glycerol and water frequencies becomes

smaller. The calculations based on r_o=0.2mm, for example, show similar fundamental mode frequencies over a large fraction of the normalised temperature span. Model results seem to imply that both glycerol and water should tend to exhibit resonant behaviour for modulated beams in the 0-3.5kHz range. The only striking difference between the numerical results for water and glycerol is at the low end of the temperature range, but one might argue that since the keyholing process is based on rapid boiling of the material, this discrepancy at low temperature is meaningless. While the keyhole is generated and maintained via rapid vapourisation at the *surface*, the majority of the liquid between the r_1 and r_2 boundaries is at or near room temperature. Even the surface of the collapsing drill hole wall is not maintained at the boiling temperature since the model assumes the beam to be extinguished at t=0 and some cooling will occur during the collapse. The model computes each point assuming an isothermal fluid body. Clearly this is not the case, and the model should be modified to reflect this.

4.4.3. Two Temperature Parameter Model

The problem can be divided into one involving surface related effects and bulk related effects. The surface tension coefficient is the only parameter which is directly involved with surface effects. The bulk related parameters include viscosity and liquid density. One can see how the low temperature discrepancies between water and glycerol

are indeed related to the *bulk* parameter of viscosity by simply removing the viscosity term from the numerical calculations. *Figure* 4.48 compares the fundamental mode frequency of glycerol with an initial radius of 0.15mm both with and without the inclusion of the viscosity term in *Equation* 4.7. The two curves become essentially indistinguishable from one another above a normalised temperature of 0.3. Because the viscosity of glycerol is so large at or near room temperature the predicted collapse times grow dramatically. Since viscosity is a bulk property, we may assume it to be at its room temperature value and hence we should expect dramatic differences in resonant frequencies between water and glycerol.

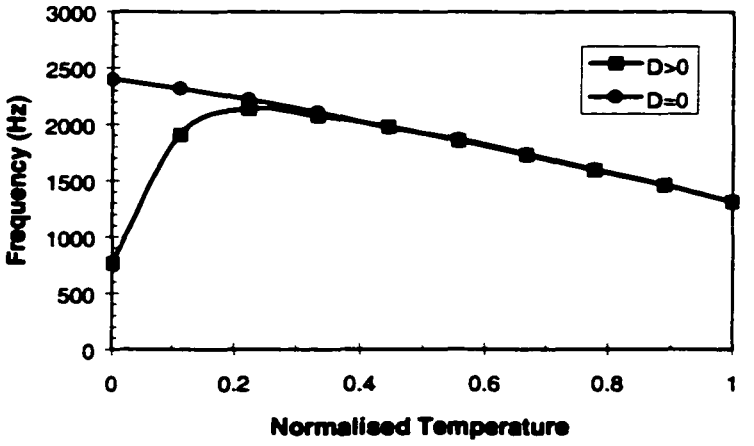


Figure 4.48 Comparison of predicted fundamental mode frequencies for collapse of a hole in glycerol having an initial radius of 0.15mm in the presence (D>0) and absence (D=0) of viscosity.

Using only low temperature values for the fundamental mode frequency is inaccurate also. A better approach to the numerical problem may be to use $T^*=0$ values for viscosity and density and $T^*=1$ values for the coefficient of surface tension. The results of the model using the two temperature parameters is summarized in *Table* 4.6.

Table 4.6. Predictions of cylindrical collapse model calculations (*Equations* 4.6 and 4.12) using low temperature values for bulk properties and high temperature values for surface properties.

Initial drill hole radius r_o (mm)	Water fundamental mode frequency (Hz)	Glycerol fundamental mode frequency (Hz)
0.10	3308	297
0.15	1864	199
0.20	1244	149

Using this approach, the fundamental mode frequencies are all somewhat lowered in comparison to the $T^*=0$ values from *Figure* 4.47. However, because the surface tension coefficient for glycerol is strongly dependent on T^*, the difference in mode frequencies between water and glycerol grows larger and tends to increase with decreasing initial radius. With an initial radius of 0.1mm these frequencies differ by more than 3kHz, which may explain why stable resonant structures were not observed in water.

While this model appears to adequately address the issue of the onset of

resonance, it does little to explain the fact that this seems to proceed through a range of frequencies. One of the underlying assumptions of the above model is that the hole is perfectly cylindrical. This is clearly not the case, and since the cavity collapse time (fundamental mode frequency) is strongly dependent on the initial radius, variation from cylindrical geometry should be considered.

4.4.4. Conical Cavity Collapse Model

The cylindrical cavity collapse model posed above represents only a zeroth order approximation to a real drill hole. Large scale departures from cylindrical geometry make the collapse time calculations intractable, but if the difference in geometry can be regarded more as a perturbation of the cylindrical geometry, the mathematics associated with the cylindrical collapse can be preserved.

Drill holes in water tend to assume a tapered geometry, similar to those in the early stages of glycerol drilling. *Figure* 4.49 shows this geometry. While the taper is clear from these images, resolution limits the estimation of the minimum radius to within ±0.05mm.

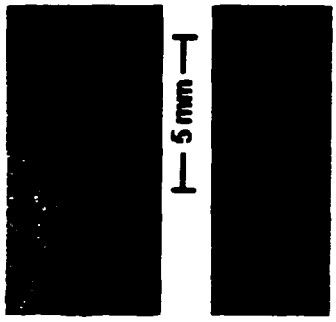


Figure 4.49 Images of water drilling (A) and the early stages of glycerol drilling (B) showing tapered structure. Limitations in the video resolution make it impossible to determine the smallest diameter of the drill holes accurately.

If the cylindrical geometry is modified to incorporate a small degree of taper, a more representative picture of the drill hole wall can be obtained without sacrificing the simplicity of the collapse time calculations. *Figure* 4.50 shows this model for the drill hole wall assuming a simple linear taper. As long as $\frac{dr}{dz}$ is small, the collapse dynamics of a cylinder should still hold, but as there *is* some taper, the collapse does not take place uniformly, but rather proceeds along the length of the drill hole from root to surface. The collapse time for a point at a depth z can be estimated by simply substituting $r(z)$ for the initial radius in *Equation* 4.7. A continuous variation in $r(z)$ from the root of the drill hole to the surface will then result in a range of collapse times $t_o(z)$ and hence a band of fundamental mode frequencies $f_o(z)$.

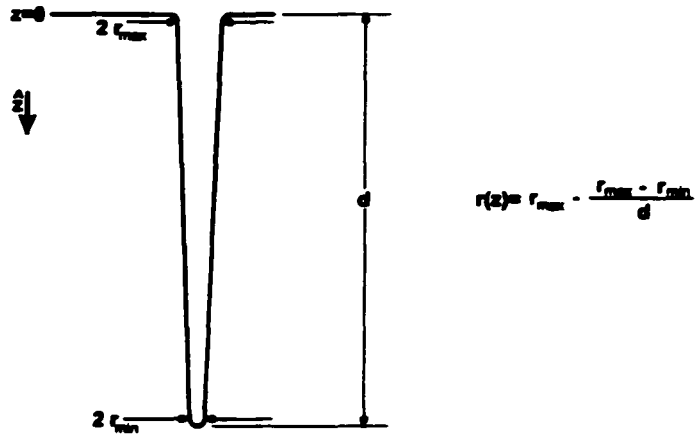


Figure 4.50 Schematic illustration of drill hole wall model assuming a small linear taper tending towards a smaller diameter root.

As an example, consider a tapered drill hole having a surface radius r_{max}=0.10mm, and a root radius r_{min}=0.01mm. In glycerol, using the two temperature properties this results in closure of the root within 3.3×10^{-4} seconds and full closure after 3.3×10^{-3} seconds yielding frequencies between 300Hz and 3kHz.

A tapered drill hole geometry predicts a band of resonant frequencies, in agreement with observation, and also suggests that because the closure frequency is a function of depth, resonant coupling of the modulated laser beam should depend on depth according to the modulation frequency. Within a continuum resonance band, higher modulation frequencies are expected to interact with deeper (narrower) regions of the cavity. This also qualitatively agrees with the frequency dependent depth of the bubble, (*Figures* 4.42, 4.43, and 4.44) observed in the glycerol drilling where the depth of the

stable resonant bubbles increases as the modulation frequency increases.

Chapter Five

CW Laser Drilling Experiments

To gain further insight into the process dynamics of laser processing, continuous wave (CW) drilling of acrylic, solid glycerol, glycerol-water mixtures, and gelatin have been examined.

In the first section of this chapter, drill hole initiation in glycerol and acrylic are modeled using energy conservation and parametric curve fitting. In the remaining sections, some of the dynamical aspects of laser drilling are presented and qualitatively modeled.

5.1. Drill Hole Initiation

5.1.1. Glycerol

Solid Glycerol:

Drilling of solid glycerol was performed only in normal gravity. The purpose of the experiment was to facilitate a direct comparison to drilling of the liquid. Differences in the behaviour between drilling with two and three phases provides insight into the significance of the role that the solid-liquid phase boundary plays in the drilling process.

According to the literature surveyed, the normal melting point of pure glycerol is listed at close to 18°C. In reality, cooling of the material below 18 °C did not induce a true solidification, but rather only increased the overall viscosity. By cooling glycerol to near the temperature of dry ice (-89 °C) a quasi solid state was obtained. Using the Lumonics VFA-1700 laser, drill hole dynamics were monitored via the standard direct imaging technique described in chapter two, and acoustic emission was monitored with an electret microphone. No acoustic noise reduction measures were used in this experiment. Drilling was carried out at an incident power of 65±5 watts with a spot diameter of 0.6±.05 mm at the surface of the target material resulting in an incident intensity of $2.3\times10^8 \pm 0.55\times10^8$ watts/m^2.

Drill hole development in solid glycerol was sufficiently slow to be seen within the 30Hz video framing rate and plots of hole depth as a function of time are shown in Figure 5.1. The development of the hole was tracked over the course of thirty video frames. Inconsistent development of the drill holes is evidenced by plateaus and occasional reduction in the depth of the cavity. This arises due to instabilities in the liquid layer surrounding the drill hole.

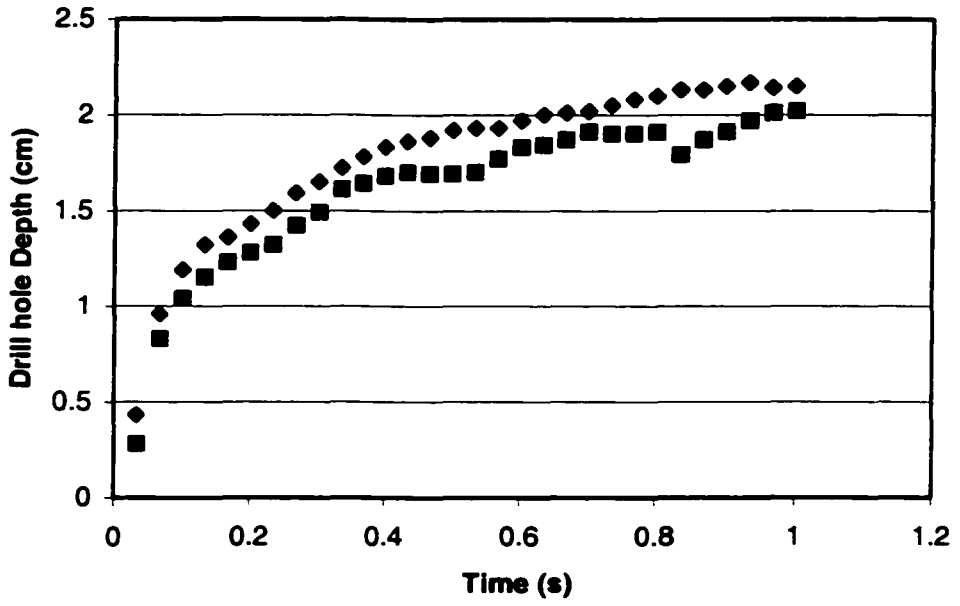


Figure 5.1. Hole depth vs. time for a CO_2 laser power of 65 Watts incident on solid glycerol cooled to -89°C.

One can obtain a lower bound for the surface laser intensity by computing the

minimum initial drill hole propagation speed into the material. With a simple $v = d / t$ velocity relationship, the minimum propagation speed of the vapour front (i.e. tip of the drill hole) can be inferred by dividing the drill hole depth observed in the first frame by 1/30 sec. This number is between 0.084 and 0.129 m/s based on the data in *Figure* 5.1. and infers a minimum surface intensity of the laser beam from the simple energy conservation model result expressed in *Equation* 1.1 which is rewritten here as an expression for the minimum intensity.

$$I_o = \rho(H_f + H_v + c_p \Delta T) v_0 / \varepsilon \qquad 5.1$$

The required material properties for glycerol were taken from numerous sources. A liquid density of ρ=1170kg/m^3 is used, representing the average over the 300-550K temperature range[49]. Latent heats of fusion and vapourisation are ΔH_f=200.6 kJ/kg [50], and ΔH_v=663 kJ/kg [51] respectively. An intermediate value (at T=140°C) for heat capacity was used, C_p=3.01kJ/kg•K [52], while the temperature difference is assumed to be given by the difference between the boiling point of glycerol [52] and the temperature of dry ice [49], ΔT=290-(-89)=379°C. ε is assumed to be unity. Using these values in *Equation* 5.1, the minimum incident intensity is in the range 2-3 x10^8 W/m^2 (over the range of minimum velocities measured) and is consistent with the direct calculations carried out at the beginning of the section. It should be noted however that the above approaches assume a flat topped intensity distribution, which is not the case for the lasers

used in the experimentation (refer to *Figure* 2.6).

By analysing the overall drill hole depth vs. time curve, the peak surface laser intensity can be obtained if it is assumed that the beam follows a Beer-Lambert type attenuation with increasing penetration into the material

$$I(z) = I_o e^{-\alpha z} \tag{5.2}$$

as seen in drilling of dielectrics [53,54]. From *Equation* 1.1,

$$v(t) = \frac{dz}{dt} = \frac{\varepsilon I_o e^{-\alpha z}}{\rho(H_f + H_v + c_p \Delta T)} \tag{5.3}$$

This is a first order differential equation and hence requires one initial condition to facilitate a unique solution. This condition is the initial drill hole velocity, which is from *Equation* 1.1, replacing I and v with I_o and v_o,

$$v_o = \frac{\varepsilon I_o}{\rho(H_f + H_v + c_p \Delta T)} \ . \tag{5.4}$$

Solving *Equation* 5.3 in conjunction with the initial value given by *Equation* 5.4 gives

$$z(t) = \frac{\ln(1 + \alpha v_o t)}{\alpha} \ . \tag{5.5}$$

The only unknowns in the expression for $z(t)$ are the absorption coefficient, and the initial velocity.

In principle, the initial velocity and absorption coefficient can be found by curve fitting *Equation* 5.5 to the experimental data. However, the drill hole depth data of *Figure* 5.1 contains unknown t=0 offsets as the video frames are unsynchronised with the beginning of drilling. As a result, *Equation* 5.5 requires an additional constant to reflect this. Rewriting *Equation* 5.5 to include the offset time t_o, we get

$$z(t) = \frac{\ln(1 + \alpha v_o (t - t_o))}{\alpha} \qquad 5.6$$

The three parameter dependant function of *Equation* 5.6 was fitted to the data of *Figure* 5.1 and the results are summarized in *Table* 5.1 . *Figure* 5.2 shows the data of *Figure* 5.1 replotted with the respective time offsets removed, and the curve fits superposed on the data.

Table 5.1. Curve fit results for solid glycerol drill hole initiation.

	Initial velocity v_o (m/s)	Attenuation coeff. α (m^{-1})	Offset time t_o (s)
Drill #1	0.829±0.065	242±5	0.0240±0.0012
Drill #2	0.676±0.088	258±10	0.0271±0.0018
Average	0.753±0.077	250±8	-

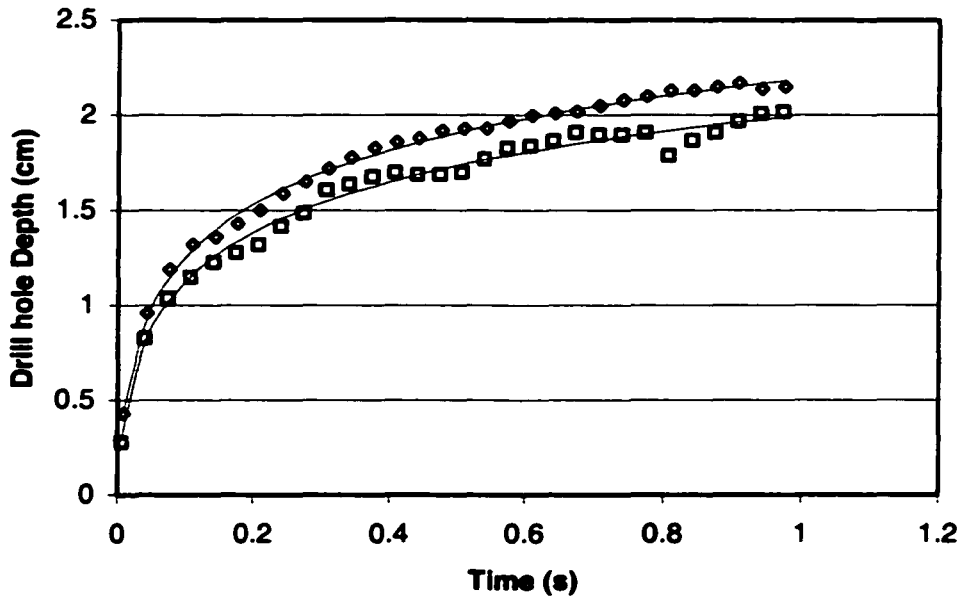


Figure 5.2. Drill hole depth vs. time removing the time offset. Curve fit lines are shown on the plot.

The average initial velocity of more than 0.75 m/s exceeds that predicted by the uniform intensity calculation since the actual laser beam mode is closer to a Gaussian distribution (see *Figure* 2.5). The resultant surface intensity predicted by this approach obtained from the initial velocity is I_o=1.8x10^9 W/m^2.

Liquid Glycerol:

The role played by the absence of a solid phase boundary can be seen in drilling liquid glycerol. Video data suggests that drilling in a liquid is a considerably different

phenomenon from that in a solid. At the standard video framing rate, the initiation of the drill hole is impossible to track, as the first frame often appears to be a near fully mature cavity. When recorded at 500Hz with a high speed camera however, the development of the drill hole can be tracked. The initiation of one such hole drilled at a laser power of 75 Watts is shown in *Figure* 5.3. The curve fitting technique used in the previous sections was applied to the data but was a poor fit to the data. In fact, the measured minimum initial velocity of 6.8m/s exceeds that of the solid phase experiments by nearly 10 times.

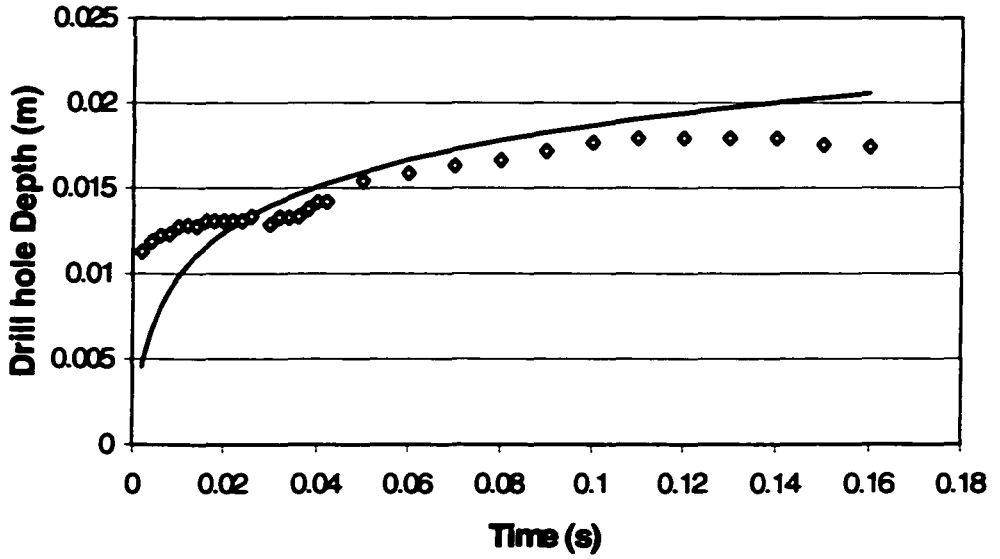


Figure 5.3 Hole depth vs. time for 75Watt drilling of liquid glycerol in normal gravity. The solid line represents the results of a curve fit to the data using *Equation* 5.6, where in this case α is held constant at 250 m^{-1}.

The differences between the liquid and solid phase drilling primarily stem from convective processes. Unlike in solid phase drilling, the cavity wall is relatively free to

expand in the liquid phase. Convective processes driven by ablation pressure allow the cavity to laterally expand much faster than through pure vapourisation of material.

5.1.2. Acrylic

The drilling of acrylic with a laser beam has long been used as a qualitative diagnostic for determining the shape and intensity of the incident radiation [55,56]. This arises from sublimation rather than a melting and vapourisation process, so that laser drilling into acrylic is not complicated by fluid dynamic processes associated with the melt. A method of quantification of the laser intensity has been published by Miyamoto et al [54] which involves scanning the focused beam across an acrylic surface at a known velocity, then sectioning and measuring the depth of the vapourised groove. Using energy conservation, the intensity of the laser beam can be found.

A curve fitting technique used earlier in drilling of glycerol can also be applied to acrylic and can provide a quantitative intensity estimate for the processing beam. This technique also provides a comparison between the beam quality for the Lumonics and Melles Griot lasers. Experiments involving short duration drills into acrylic in normal gravity were carried out using both the VFA 1700 and CRF 1200 lasers.

Drilling with the VFA laser was performed in single pulses of 0.2 seconds

duration. The development of the drill hole was monitored with a ccd camera and recorded on video tape without synchronisation. This of course resulted in the problem of frame to drill start synchronization. Two holes were analyzed for acrylic at an incident power of between 50 and 60 Watts. The resulting $z(t)$ relationship is shown in *Figure* 5.4 along with the results of the curve fit to the data. The fit to the data in *Figure* 5.4 estimates the initial velocity to be v_o=0.405 ± 0.012 m/s, with an attenuation coefficient estimated at α=117 ±2 m^{-1}. The quality of the fit to these data is extremely good.

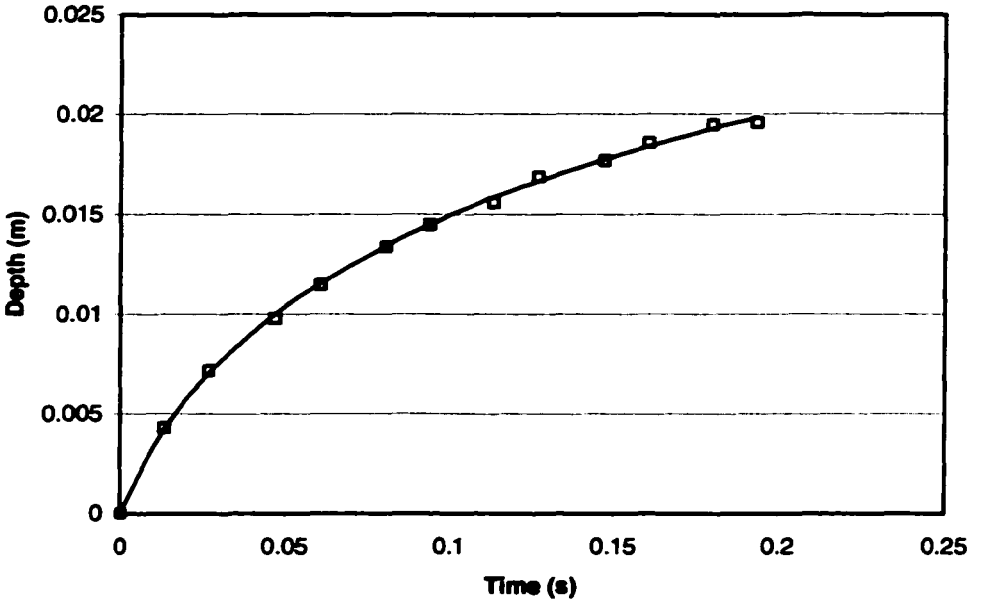


Figure 5.4. Depth vs. time for CO_2 laser drilling of acrylic at 50-60 Watts. Two sets of data have been used.

With the LAMPS platform laser, drill holes were generated using a series of five 10 ms bursts. The resulting video data contained a stop action record of the drill hole development spaced 10 ms apart. By measuring the depths of the drill holes during the pauses between successive pulses, synchronization problems could be eliminated so that all of the drill holes were normalised to t=0. *Figure* 5.5 shows the average depth vs. time associated with each of three laser power levels. The curve fit results for each of the power levels, assuming a zero intercept are summarized in *Table* 5.2.

Table 5.2. Curve fit estimates of v_o and α for the data of *Figure* 5.5

Meter Power P (W)	Initial velocity estimate v_o (m/s)	Attenuation coefficient α (m^{-1})
46	0.21 ±0.01	132 ±21
63	0.295 ±0.004	114 ±3
95	0.394 ±0.009	105 ±5

The initial velocity estimate showed the expected increase with laser power, and the attenuation coefficient was consistent with the value of α=117 m^{-1} estimated from the VFA 1700 experiments. Fits using this value of α are shown in *Figure* 5.5 and initial velocity estimates are summarized in *Table* 5.3.

Table 5.3. Initial velocity for data of *Figure* 5.5.

Meter power P (W)	Initial velocity estimate v_o (m/s)
46	0.205 ±0.003
63	0.298 ±0.001
95	0.418 ±0.004

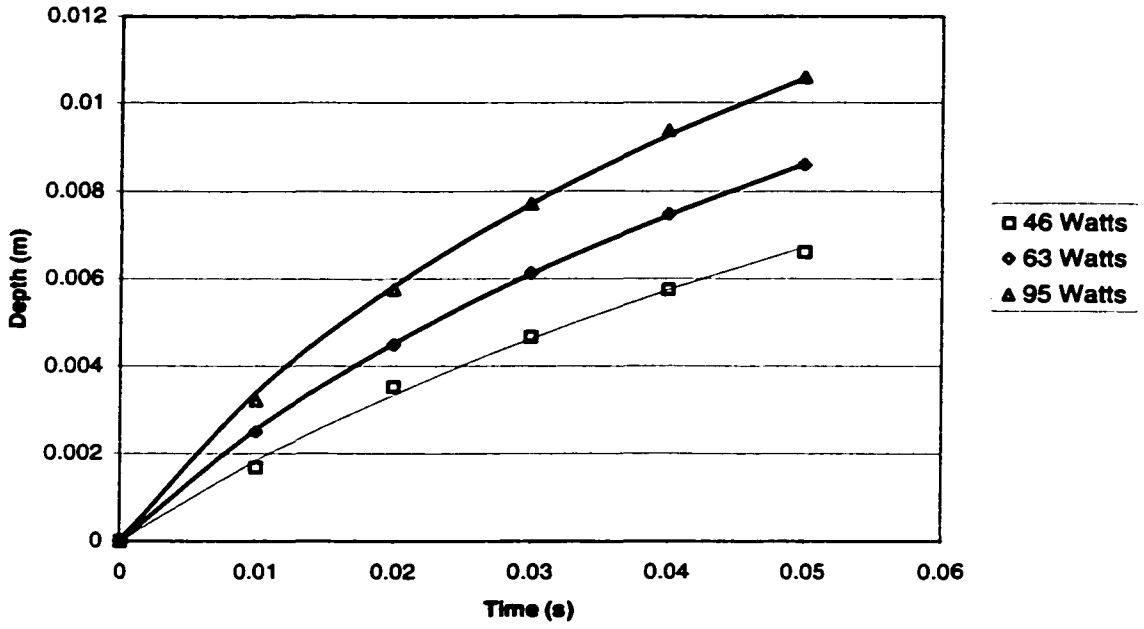


Figure 5.5. Depth vs. time relationships with curve fits for acrylic drilling with LAMPS test bed laser.

From *Equation* 5.6, a linear relationship between P and v is expected if the emissivity remains constant throughout the power range used. *Figure* 5.6 shows the

dependence of the initial velocity on the power for the LAMPS experiments. A single $v_o(P)$ point associated with the VFA 1700 experiments is also included on the plot. The power-initial velocity relationship is linear for the LAMPS test bed laser but the data point for the VFA 1700 is off this line. This is due to the different mode structures the lasers used. It is surprising that the VFA 1700 drills at a rate faster than the sealed Melles Griot unit, implying that the mode quality of the Lumonics laser is better. Given that the Melles Griot laser is specified to produce greater than 90% TEM_{00} content this is unlikely. It is likely that the source of this discrepancy arises from the measurement of power of the Lumonics laser as the thermopile based power meter is operating very close to its lower limit of detection for the series of experiments performed throughout this research.

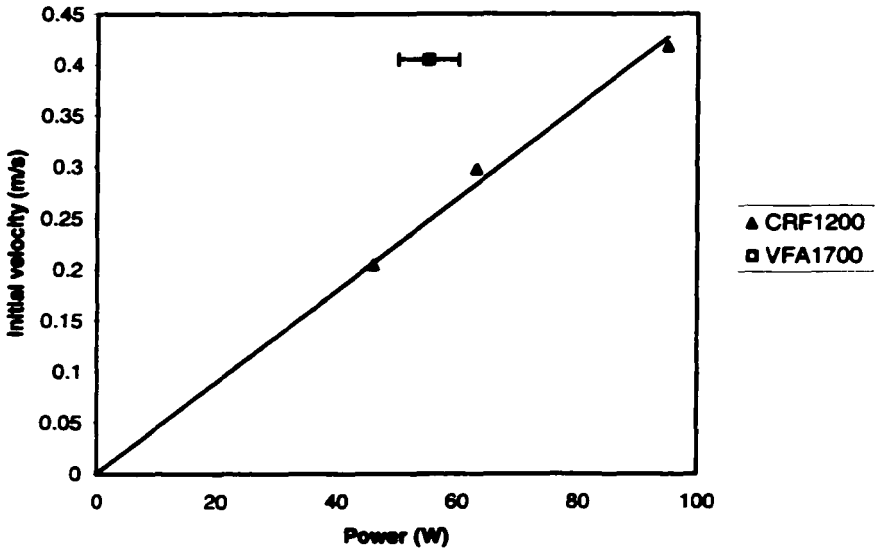


Figure 5.6. Initial velocity-power relationship for the LAMPS testbed laser. A data point from the Lumonics VFA 1700 laser is also included on the graph.

The intensity of the beam can be obtained from *Equation* 5.6 and is shown in *Figure* 5.7. The material constants are taken directly from the work of Miyamoto et al [54] (*Table* 5.4).

Table 5.4. Material constants for acrylic (after Miyamoto et al [54]).

Mass Density (kg/m^3)	Latent heat of vap. ΔH_v (J/kg)	Avg. Heat capacity c_v (J/kg°C)	Sublimation Temp. T_v (°C)
1190	2.52×10^6	160	300

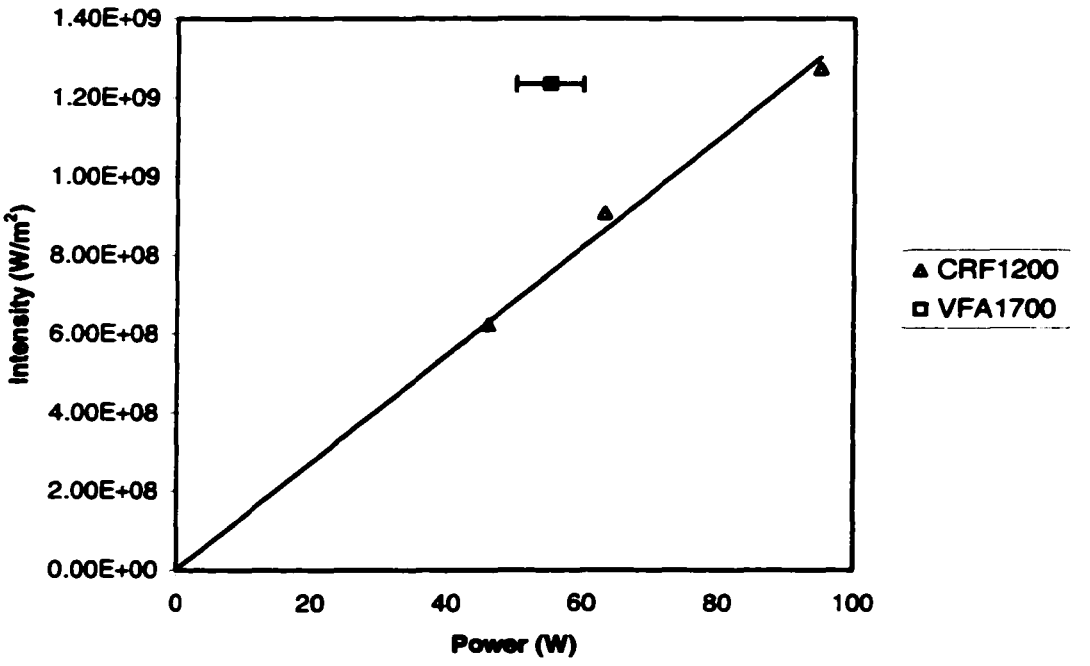


Figure 5.7. Intensity vs. meter power for VFA1700 and CRF1200 lasers.

5.2. Glycerol Drill Hole Dynamics

Laser drilling of glycerol-water mixtures was studied with the aid of a high speed 16mm movie camera which captured the dynamics of the interactions at 500 frames per second. Solutions of pure water, 50% glycerol-water, and 100% glycerol were

photographed during laser drilling but only the pure glycerol solution provided slow enough dynamics to be followed at the 500Hz framing rate. The prime difference between these liquids is their viscosity, which introduces a damping effect into the dynamics and instabilities associated with the laser drilling process. At room temperature, pure glycerol is more than 10 times more viscous than a 50/50 glycerol/water mixture and more than 600 times more viscous than pure water. The viscosity effectively acts as a low pass filter on the drill hole wall dynamics.

The development of a drill hole associated with drilling under normal gravity into pure glycerol is shown in Figure 5.8. (Because the initiation of the drilling is in no way synchronized with the film framing, the error in the time labels can be as much as 2ms). By 10ms into the drill, the drill hole has already clearly passed from a regime of longitudinal cylindrical-like growth to one of lateral expansion centered at a single subsurface point (i.e. inflation of a bubble has begun). The rate of increase of penetration slows significantly and the lateral expansion continues centered about the original perturbation. Within 100ms, the cylindrical hole has transformed into a long slender hole with a large elliptical bubble along its length as well as smaller scale r(z) variations below the bubble. The center of the bubble is now well above the center of the original perturbation, presumably due to the effect of buoyancy.

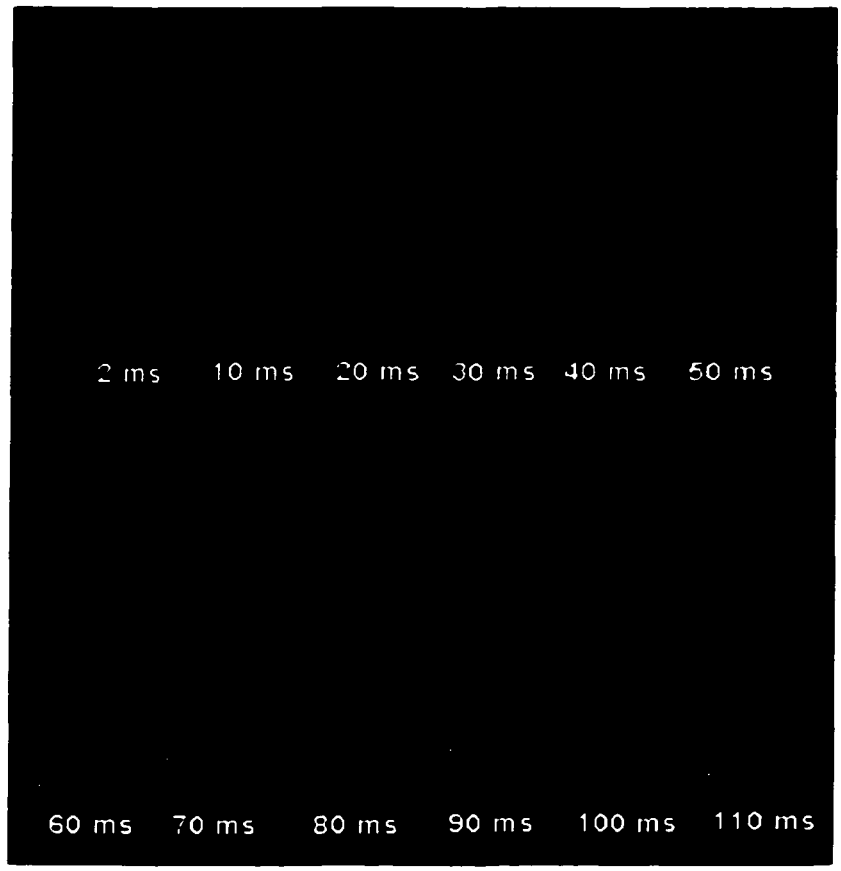


Figure 5.8. Development of drill hole structure in 100% glycerol. Drilling was performed in normal gravity at 80Watts.

The destabilisation of the cylindrical drill hole is an inevitable result of a Rayleigh -Taylor instability associated with a cylindrical cavity in a liquid medium [57]. Phenomenologically, metamorphosis from a cylindrical structure to one involving the structure of the latter images of Figure 5.8 can be described using the following simple model.

Assume that an initially cylindrical cavity exists as the result of a pressure balance

between vapourisation from the laser beam tending to open the cavity, and surface tension and hydrostatic pressures tending to close the cavity. The pressure associated with surface tension for a cylindrical cavity is $p_\gamma=\gamma/r$, where γ is the surface tension of the liquid at the wall and r is the radius of the hole. If one assumes that the pressure and wall temperature in the cylindrical cavity is initially constant, then any localised perturbation in the pressure acting on the wall will result in a change in the radius within that region. The radial perturbation can be either towards smaller r or larger r and hence the local variation in surface tension pressure can be either positive or negative.

If the shift is towards larger radius, the closing pressure associated with surface tension is reduced and the wall will continue to expand. The vapourisation pressure will fall off as the wall radius expands, but the natural tendency for pressure equalization within the cavity will counter losses from direct laser vapourisation. This growth will in general proceed in an unhindered manner, causing a localized ballooning of the drill hole wall which evolves towards a spherical growth in the drill hole several times the initial cavity radius.

If the shift is to smaller radius (higher closing pressure), the collapse pressures will exceed the expansion pressure and the perturbation will grow. In the absence of any restoring force, the perturbation will evolve into a collapse. One mechanism that counters a developing constriction is an increase in local vapourisation pressure due to

higher laser intensity at smaller radii. This localised excess pressure will act as a braking force to the collapsing wall. Unlike the perturbation at large radii, the restoring force can exceed the closing force. This alone does not ensure that a full collapse cannot happen however as fluid momentum can act to delay the reversal of the collapse, and if this is large, reversal of the collapse will not occur.

Full or partial collapse of a region of the drill hole is significant, as it has a profound effect on the stability of all regions of the drill hole below the closure. Momentary interruption of the beam due to a closure will upset the pressure balance in the sub-closure cavity, halting any expansion or initiating contraction of the cavity. The collapse time calculations carried out in Chapter 4 for drill holes in glycerol and water give an indication of the relative effect of fluid momentum. With collapse times for glycerol estimated to be about ten times that of water, the glycerol can be considered to be less likely to undergo collapse. The relative stability of the drill hole in glycerol compared to its lower viscosity counterparts is the key factor in allowing the growth of large radius features such as those on *Figure* 5.8.

This is not to say that drill holes in glycerol never experience total collapse, but the frequency at which this occurs is low enough that stable radial growth can be established. The sequence of frames shown in *Figure* 5.8 shows no evidence of complete collapse but it only covers roughly 0.1seconds from the initiation of the drill.

To get a sense of the longer term dynamics in glycerol drilling without resorting to frame averaging, a Dipix P360F frame grabber was configured to store video data as digitized single line segments of pixels across the drill hole perpendicular to the direction of drilling. *Figure* 5.9 Illustrates typical locations along a drill hole. By digitizing line segments from consecutive frames and writing the pixel data sequentially to a file, a temporal image of the cross section of the drill hole depth was produced. Post processing of the grayscale image files with a threshold filter produces a well defined drill hole diameter vs. time display.

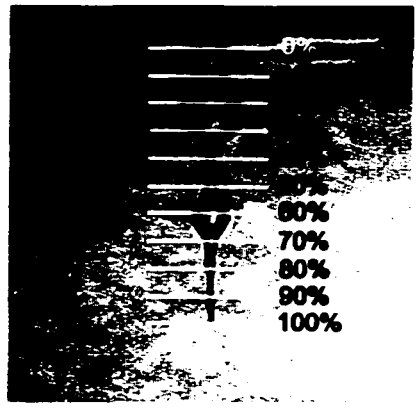


Figure 5.9 Typical locations of pixel line segments used to generate temporal line profiles.

A family of such displays taken from different depths is shown in *Figure* 5.10. Data was obtained from the same experiment as in *Figure* 5.8. The line profiling was taken at depths representing percentages of the maximum observed penetration over the

course of a 10 second long drill. Digitization was performed over typically 400 individual frames, representing 800ms of drilling. While this technique inherently limits the resolution along the beam axis, the total time represented is almost 80 times that of *Figure* 5.8 and the time resolution is limited only by the 500 Hz framing rate.

Each line profile represents a time line showing the passage of bubbles past a fixed point within the hole. Line profiles have been stacked on top of one another in order that the migration of drill hole features can be easily seen. Growth and subsequent contraction of the drill hole diameter at deeper depths is mimicked at shallower depths at a later time. At some point in the growth, a migrating bubble's upper boundary reaches a threshold proximity to the constricted entrance of the drill hole where the constriction is no longer stable and a rapid venting of the bubble occurs. This occurrence is marked on the line profile display by an abrupt reduction in the drill hole diameters at shallower depths, and generally initiation of new deep penetration features. Once the collapse is complete, the newly created deep feature assumes the role of the primary bubble in the drill hole and the process tends to repeat itself.

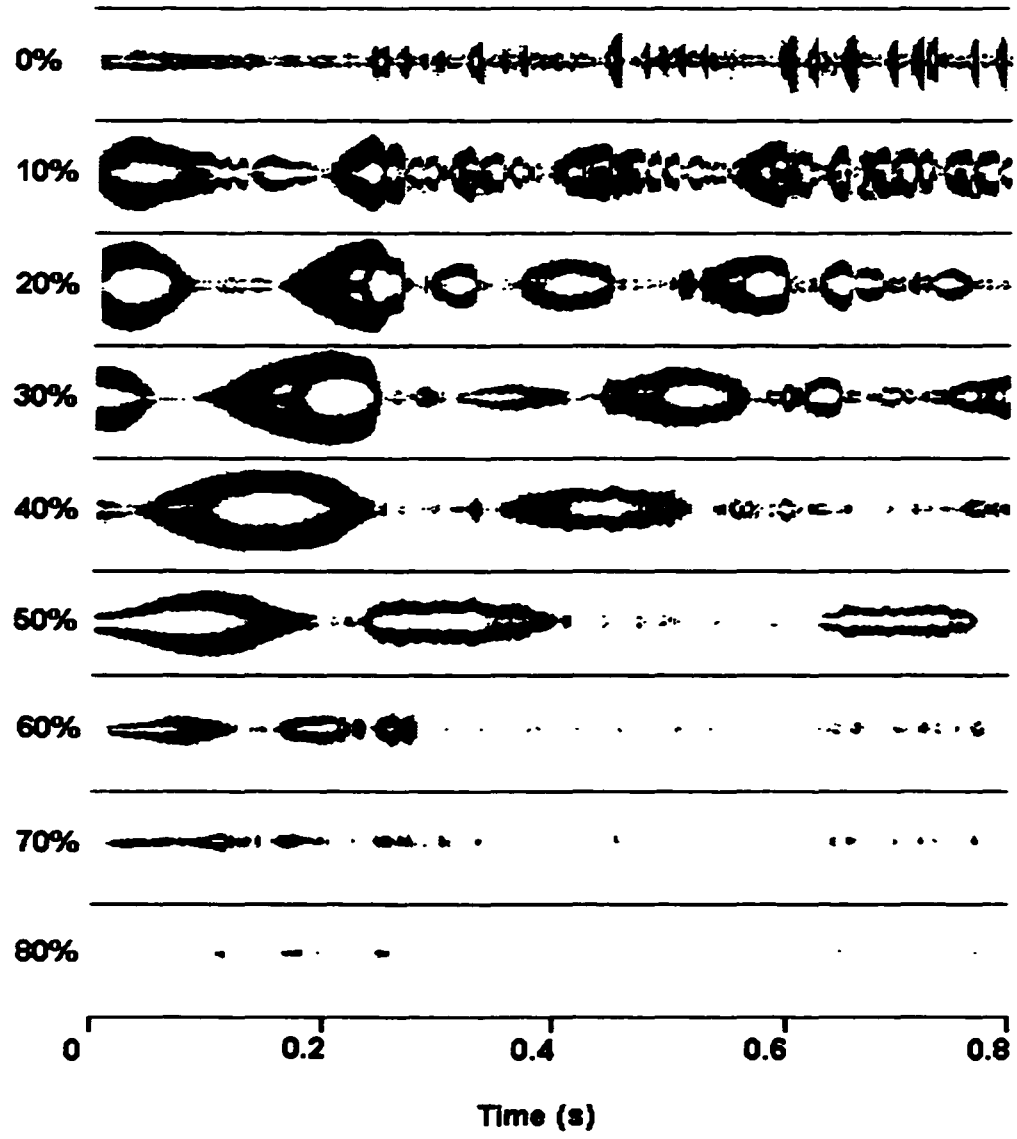


Figure 5.10. Binarized drill hole radius profiles (vertical dimension) versus time (horizontal) for drilling of glycerol at a laser power of 40 Watts in normal gravity. The profiles are normalised to the maximum depth throughout the entire drill. The duration of the time base is approximately 0.80s.

The buoyancy effect was also studied using this line profiling method for 80 Watt drilling carried out in normal and low gravity and line profiles are shown in *Figures* 5.12 and 5.13 respectively. In normal gravity, 80 Watt and 40 Watt drilling shows similar behaviour. Contrasting this is the zero-g drill which demonstrates virtually none of the radial drill hole dynamics associated with normal gravity drilling. Instead, the drill hole rapidly assumes a narrow conical profile including a single dominant subsurface bubble located coaxially with the slender drill hole. The evolution of the drill hole profile is quite simple from this point onward. The primary bubble undergoes a more or less monotonic expansion without migration towards the surface until the constricted entrance aperture of the drill hole destabilises and the bubble rapidly vents to the atmosphere. This event is highlighted on the line profile chart by the rapid radial change which takes place throughout all of the shallower (less than ½ full penetration) depth profiles at about the 0.35 second point. The bubble venting process, like in the normal gravity case, allows unattenuated beam incidence deeper into the material and this is reflected by line profile activity increasing at deeper (greater than ½ full penetration) depths as soon as the bubble begins to vent. Though the line profile duration was insufficient to capture the full cycling of the process, observation of the video data indicates that the spiking during the venting "seeds" the drill hole with the beginnings of the next primary bubble and the process repeats itself.

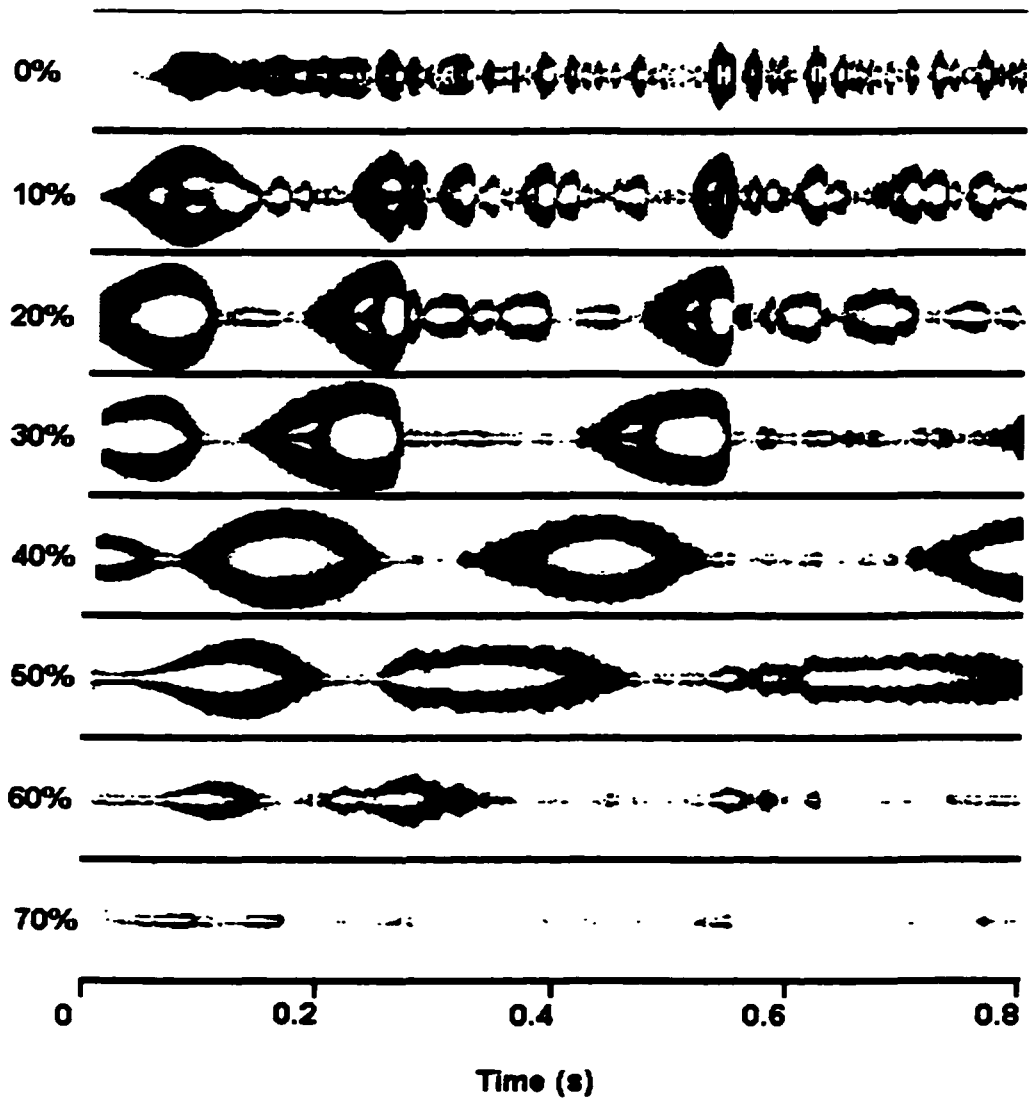


Figure 5.11. Binarized drill hole radius profiles (vertical dimension) versus time (horizontal) drilling of glycerol at a laser power of 80 Watts in normal gravity. The profiles are normalised the maximum depth throughout the entire duration of the drilling.

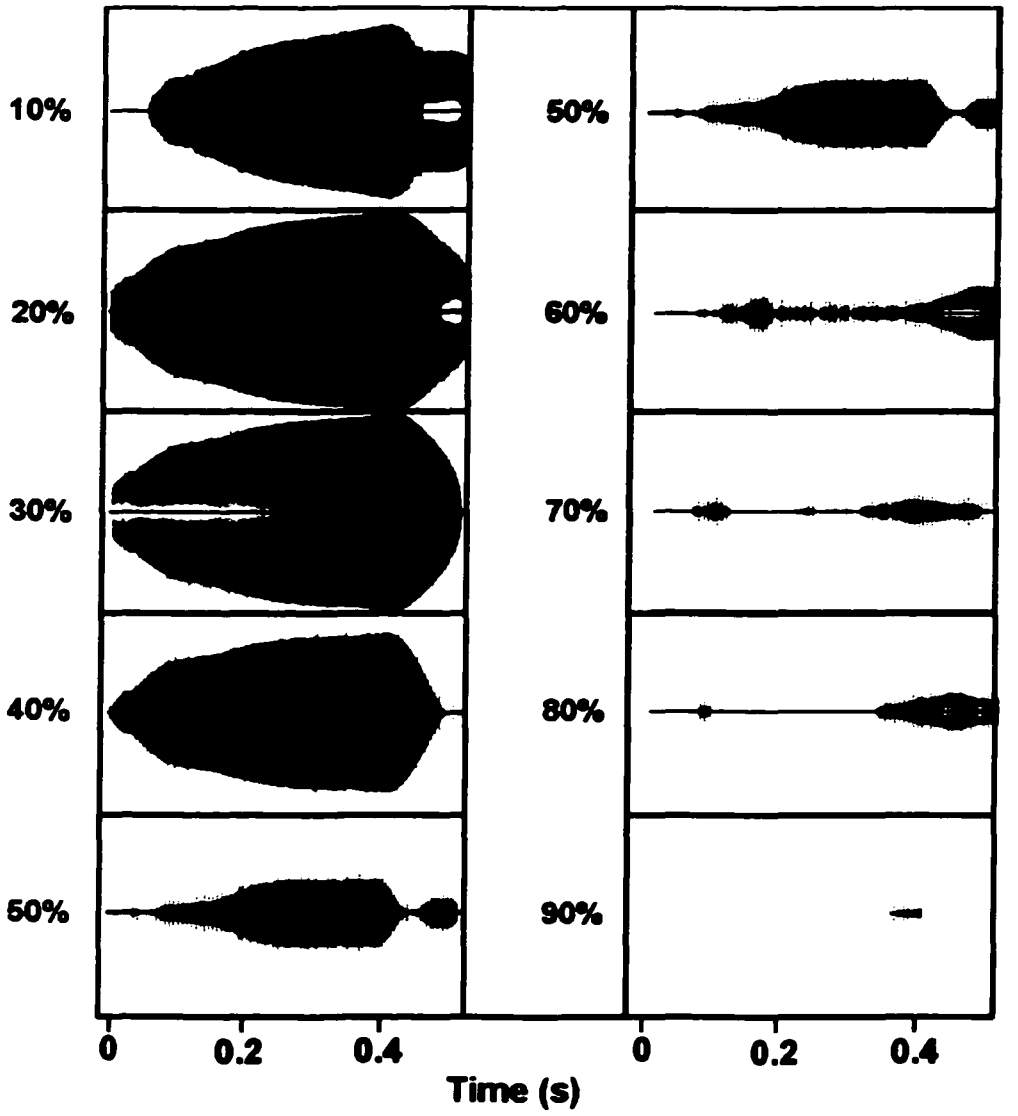


Figure 5.12. Binarized drill hole radius profiles (vertical dimension) versus time (horizontal) for drilling of glycerol at a laser power of 80 Watts in low gravity. The profiles are normalised to the maximum depth throughout the entire duration of the drilling.

The large scale departure in the behaviour between the normal and low gravity

glycerol drilling can be explained by comparing buoyancy and hydrostatic pressure effects. Both act to accelerate dynamical processes within the drill hole. Buoyancy acts to draw vapour bubbles to the surface and the larger the bubble, the stronger the effect. Hydrostatic pressure acts in conjunction with surface tension to provide closing pressure on the hole, which must be overcome by the vapourisation pressure in order to maintain the drill hole. When these two parameters are eliminated from the process, the dynamics are stabilized. This is seen clearly in the case of pure glycerol, for as the line profiles of *Figure* 5.12 indicates, the low gravity drilling of glycerol shows fewer dynamical effects than in normal gravity. For comparative purposes, a sequence of five consecutive frames (1/30 seconds apart) of low gravity glycerol drilling are shown in *Figure* 5.13. This can be contrasted against the seven frame consecutive sequence shown in *Figure* 4.1 for normal gravity glycerol drilling.

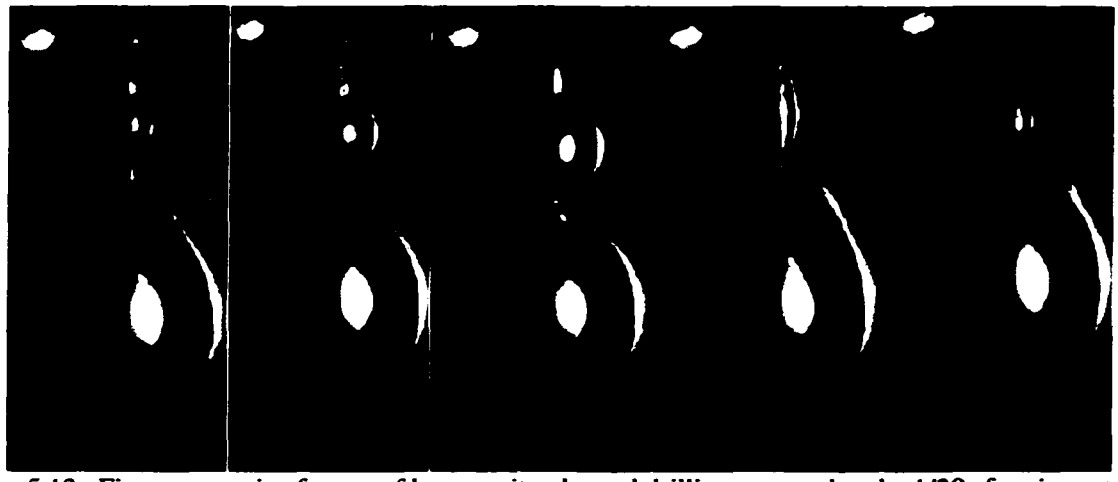


Figure 5.13. Five consecutive frames of low gravity glycerol drilling captured at the 1/30s framing rate of standard NTSC video.

The process dynamics for both low and normal gravity glycerol drilling both tend to show cyclic behaviour. The periodicity of the two processes however, are considerably different. Inspection of the normal gravity line profile of *Figure* 5.11 show completion of the first cycle within about 200ms. The low gravity drill line profile however falls short of capturing a full cycle over it's full duration of 500ms.

5.3. Fluid Motion Phenomena

The fluid motion induced by laser penetration processing plays an important role in determining the final characteristics of any particular laser treatment. The large number of variables associated with the fluid motion however makes its study quite parametrically dependent. This section summarizes observations of fluid flow characteristics surrounding the drill hole for a variety of materials in varying gravity. Glycerol-water mixtures of 100%-0%, 66%-34%, and 0%-100% respectively were studied allowing insight into the flow dynamic dependence on differing material properties. Gelatin was also studied to ascertain differences between a bounded and semi-unbounded liquid region.

5.3.1. 100% Water

Flow patterns during laser drilling of water have been studied in a variable gravity environment by Mueller [16]. The keyholing regime in water is characterized by a high downward reaction flow both in low and normal gravity. Flow in low gravity tends to be somewhat more collimated than in normal gravity, but the general circulation pattern remains the same. This is shown in *Figure* 5.14.

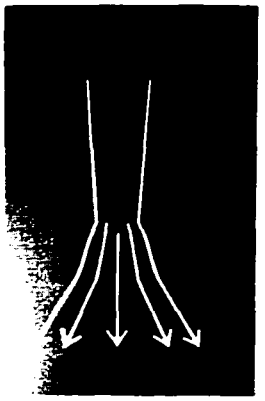


Figure 5.14 Frame average of water drilling in normal gravity with liquid flow lines overlaid on the image.

5.3.2. 66% Glycerol – 34% Water Mixture

Ground (1-g) and aircraft (0-g) based drilling of 66% glycerol 34% water was performed with similar beam intensities. The flow characteristics of the 66% mixture

were well suited to visualisation via holographic interferometry. Sequences of interferograms are shown in *Figure* 5.15. Interference fringes are evident throughout the entire field of view, but the highest density of fringes involves the disturbance evolving from the top of the field of view associated with the laser drilling. The disturbance rapidly extends beyond the drill hole as bubbles and heated fluid are ejected from the bottom of the hole in reaction to the vapour jet escaping from the top.

The keyhole, which is not directly observable with this technique, initially takes the form of a deep cavity of roughly cylindrical shape, then subsequently destabilises into a dynamic structure involving regions of both expansion (bubbles) and constriction. The average hole depth does not appear to vary significantly with g-level and was found to be ≈8 mm for our experiments.

Reaction flow from the root of the drill hole proceeds in a similar manner to that in water, and initially proceeds as a plume of heated liquid and vapour. Unlike water however, the plume develops a mushroom-like appearance as it migrates into the cooler more viscous surroundings. This difference in plume structure is a result of a larger viscosity differential between the reaction flow and the surrounding liquid in the glycerol-water mixture. The plumes associated with the mixture evolve similarly in low and normal gravity up to t = 1 s, after which differences become apparent. The mushroom shaped plume in low gravity continues to grow in size and migrate deeper into the fluid

while in normal gravity, the braking effect of buoyancy slows the advancement of the plume. In normal gravity the plume eventually halts and returns towards the surface, with a stable and symmetric return flow, which takes the shape of a prolate half sphere.

Another disturbance can be observed radiating outward from the drill hole near the surface of the liquid. As with the plumes, significant differences between g-levels do not arise until after 1 second when it becomes apparent that the radial propagation rate in normal gravity is greater than that in low gravity. The disturbance is caused by heated surface liquid which is redirected outward at the surface. The same density differences that generate the contrast in the holographic images lead to increased surface bound flow in normal gravity through density driven (buoyancy) convection.

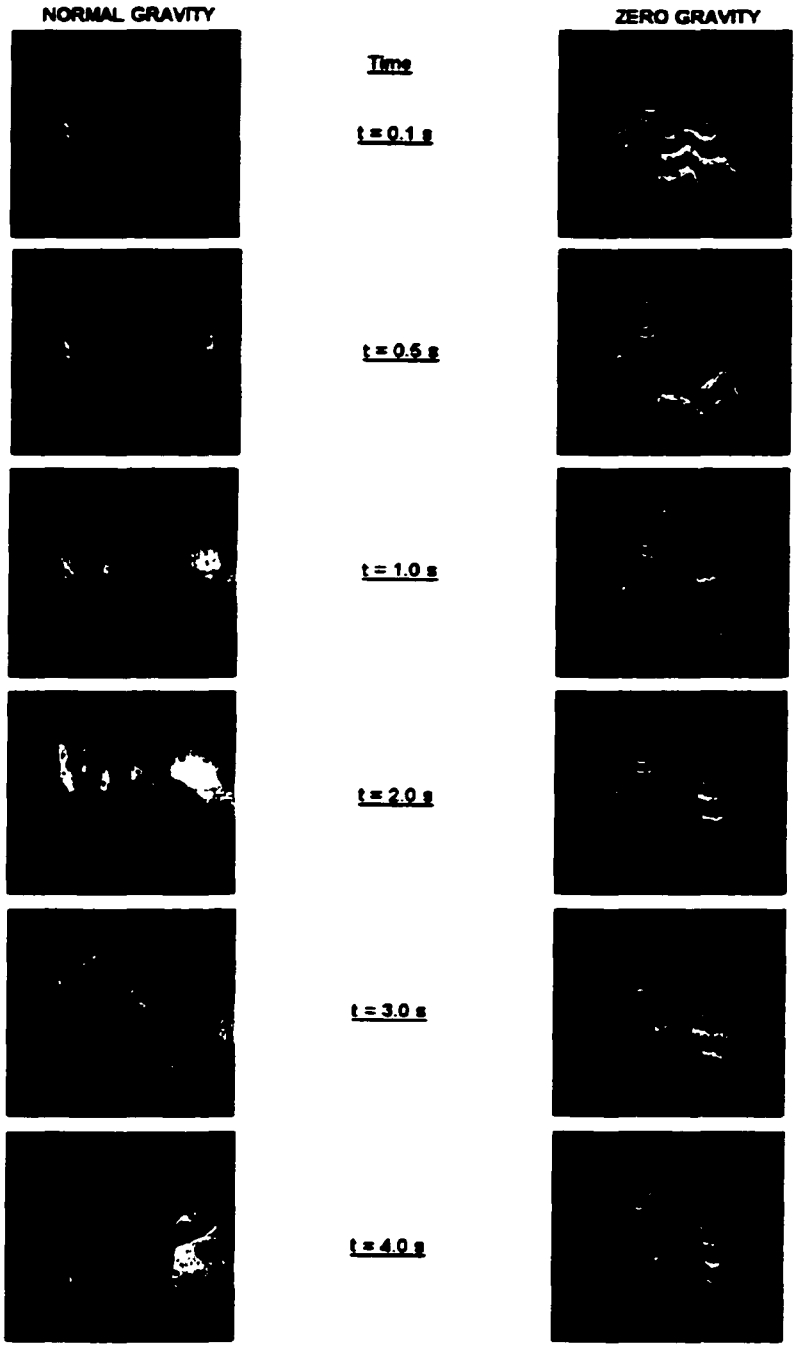


Figure 5.15 Sequences of interferograms comparing fluid flow between drilling in normal and zero gravity of a 66% glycerol - 34% water mixture

5.3.3. 100% Glycerol

As shown previously, laser drilling of glycerol produces no reaction flow deeper into the liquid. This results from the high viscosity of glycerol. The relative stability of the hole allows large bubbles to form along its length. When drilling takes place in the presence of gravity, buoyancy acts to draw these bubbles to the surface, with the growth of new bubbles deep within the hole replacing surfacing bubbles. In a process analogous to pulling a string of beads through a liquid, surrounding fluid is drawn to the surface as the drilling process creates a buoyancy driven viscous pump, drawing fluid coaxially towards the surface along with bubble migration.

This effect is clearly shown in *Figure* 5.16, for glycerol in normal gravity. The image shows several arcing dark tracks in the liquid surrounding the drill hole. These tracks actually arise from migration of tiny bubbles entrapped in the glycerol prior to drilling.

Low gravity drilling of 100% glycerol shows no evidence of bulk fluid motion. This is not surprising, given the lack of drill hole dynamics observed under these conditions.



Figure 5.16 Cumulative frame average of several seconds drilling in normal gravity in 100% glycerol liquid. Bubbles suspended within the fluid trace out their paths, revealing the widespread bulk fluid motion induced by the pumping action of the drill hole. The arrows indicate the direction of the flow.

5.3.4. Gelatin

Drilling of gelatin in a variable gravity environment provides insight into both gravity effects within a bounded system as well as comparative data for the liquid state drilling. *Figure* 5.17 shows both 0 and 1.8-g drilling into gelatin and illustrates how low gravity may affect hole morphology.

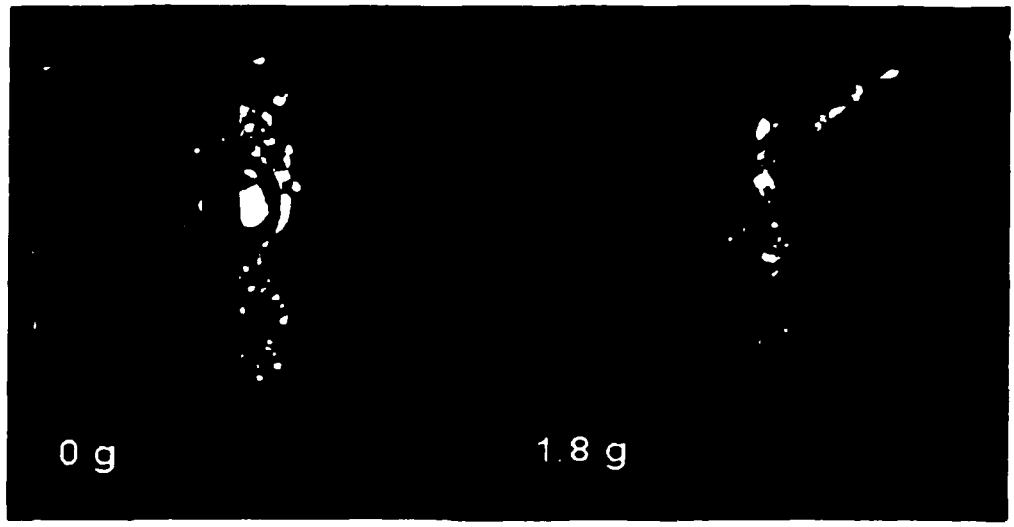


Figure 5.17 Drilling of gelatin at 0 and 1.8-g. Laser power: 70 Watts.

A schematic of the flow patterns during drilling is shown in *Figure* 5.18. In the presence of gravity, buoyancy has the effect of assisting bubbles ejected from the root of the drill hole to flow back to the surface. The bubbles help to entrain the return flow and a smooth, symmetric flow field is established. When the downward axial stream of reaction flow encounters the phase boundary it forces the stream to mushroom and reverse its direction, rising along the outer wall of the drill hole. The surface bound flow is constricted to a waist at roughly one third of the melt pool depth. While much of the surface bound flow is reintroduced into the downward core stream of reaction flow, some is drawn through the waist to the surface. With another boundary at the surface, the flow splits into outward and inward radial flows. The inward flow is immediately returned

into the reaction flow stream, while the outward flow, encountering the radial boundary of the melt pool is forced downwards. A viscous pumping action analogous to that observed in glycerol (*Figure* 5.16), helps to drive this flow pattern. The overall flow field can be simplified into two recirculating toroidal flow fields (*Figure* 5.19), which exhibit a certain degree of cross-coupling to one another. It is interesting to note that the characteristic "wine glass" profile of the melt pool seen here mimics transverse profiles of laser penetration welds in metals [58].

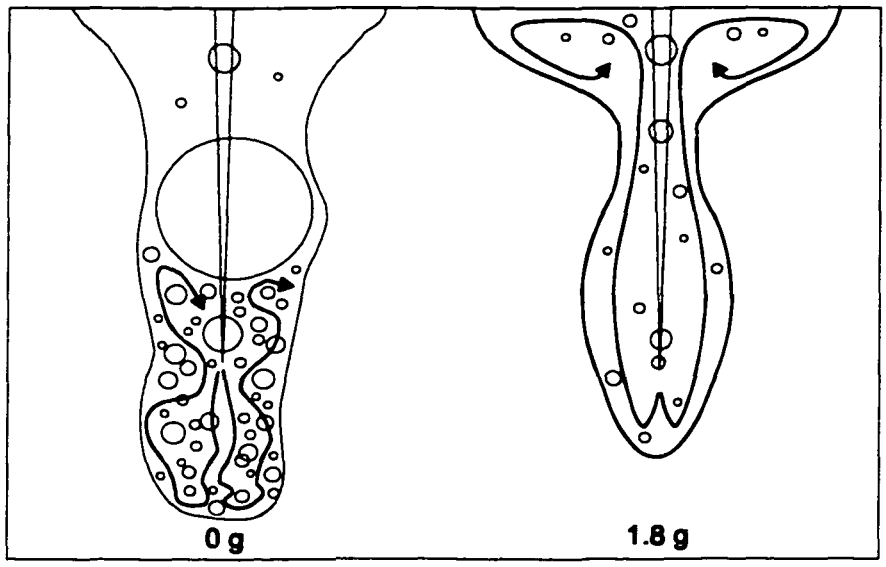


Figure 5.18 Schematic illustration of drilling at low and high gravity showing the differing flow patterns playing a role in shaping the molten pool.

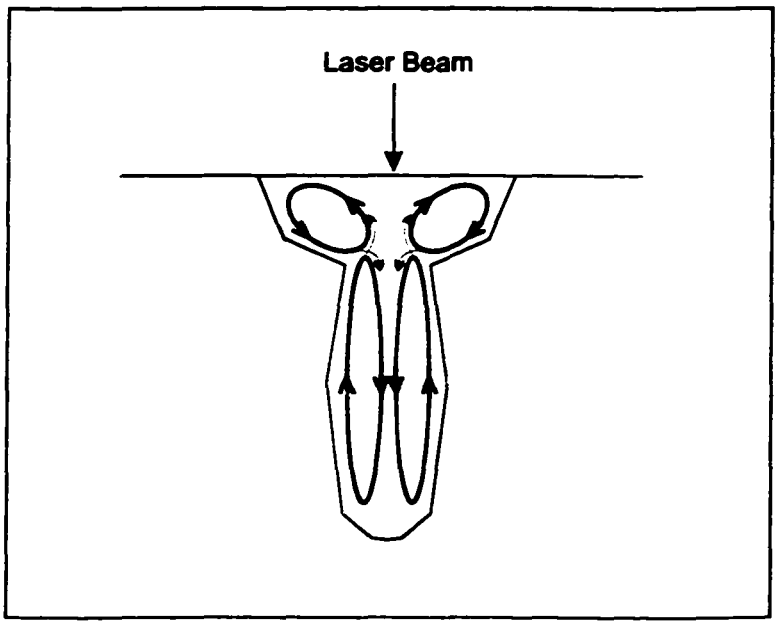


Figure 5.19 Section view of twin toroidal steady state flow pattern established during laser drilling of gelatin in the presence of gravity.

Without the influence of buoyancy, and constrained by a non-liquid boundary, ejected bubbles rapidly collect at the root of the drill hole. Bubbles and heated liquid are redirected towards the surface by the gelatin phase boundary, but the return flow is maintained by the reaction flow momentum. In the absence of hydrostatic pressure, large bubbles such as can be seen (*Figure* 5.17) to form along the hole and swell to form a barrier for reaction flow back to the surface. These sporadic blockages combined with unassisted reaction flow disrupt the cylindrical flow symmetry and hence the symmetry of the molten zone.

This demonstrates a significant difference in dynamical processes between low

and normal gravity drilling in gelatin. If this process is representative of the dynamics in an industrial process, one can foresee potential problems with low gravity processing.

Chapter Six

Discussion

6.1. Holographic Results

Real time differential holographic interferometry was successfully applied to laser processing of fused quartz in low and in normal gravity. Analysis of the holographic data allowed the temperature distribution in the fused quartz to be extracted. The holographic data that was analyzed however, did not provide enough fringe resolution to infer temperature values over the entire image field. The resulting temperature field data was limited to radially distant regions from the drill hole. An analytical model using prolate

spheroidal coordinates was attempted, but proved to be non-physical. Numerical solution of an isothermal prolate half sphere yielded a temperature field that agreed with the experimental data well at the surface, but predicted deeper thermal penetration and higher radial conduction below the surface than measured holographically.

The main source of the discrepancy between experiment and the model arises from differences in the boundary conditions. The prolate half-spheroidal cavity used to model the hole does not match microscopic profiles of experimental drill hole walls. The major difference between experiment and model however, is the assumption of an isothermal drill hole wall. Heating times of the order of two seconds observed in the drilling into preexisting holes retard the advancement rate of the heat front in comparison with the isothermal boundary condition.

While drilling in quartz reaches a thermal equilibrium after two to three seconds, the initial phase may be better represented with an *isoflux* boundary condition rather than an isothermal surface.

The results are somewhat limited in resolution, but nonetheless represent the first application of real time differential holography to the problem of heat transfer in laser penetration processing. This serves to demonstrate the feasibility of applying the technique of real time differential holographic interferometry in this application.

6.2. Laser Drilling With a Modulated Beam

Under certain circumstances, drilling into a fluid with an intensity modulated laser beam generates stable drill hole structures. Such structures are related to both the modulation frequency and to the material properties of the target liquid. Two series of experiments were carried out on water and glycerol with somewhat different results due to changes in the experimental apparatus.

In the first series of experiments, water drilling exhibited little to no dependence on beam modulation frequency, while glycerol demonstrated a structural metamorphosis observed in video frame averages of the drilling over the range of modulation frequencies. Despite the changes observed in the frame averaged structure, *stable* structures were not observed in the first series of experiments.

The second series of experiments were carried out with improved apparatus and the addition of acoustic monitoring. Drilling in glycerol showed a clear transition from an unstable to a highly stable structure, in the form of a single spherical bubble coaxially superimposed on a slender cylindrical cavity. This structure was attributed to a resonant coupling of the modulated beam to the drill hole. Stable structures were not observed in water, but frame averages revealed a previously unobserved metamorphosis of the structural envelope over the range of modulation frequencies.

The presence of resonant structures was found to depend on both the modulation frequency and the laser intensity. Drilling at higher intensity produced onset of resonant structure at lower frequencies. Resonant behaviour was observed over a range of modulation frequencies but the bandwidth of the resonant mode was limited by destabilisation of the captive bubble at higher frequencies. Drill hole dynamics above the resonant state destabilisation frequency however, were not found to be similar to the behaviour observed below the onset frequency.

Acoustic emission from the drilling was transformed into frequency spectra for comparison with structural observations. Glycerol and water emission spectra tended to exhibit similar (relative) spectral characteristics, indicating that the emissions were being influenced by a frequency response function of systematic origin. Resonance conditions in the drill hole were characterised acoustically by significantly enhanced emissions in the 0.5 to 2kHz band.

The first attempt at modeling the resonant behaviour focused on the spherical captive bubble which defined the structural resonant state. Geometric behaviour of the bubble was studied in the form of bubble radius, $r(t)$ vs. bubble depth, $z(t)$ and $r(t)$ vs. modulation frequency, f_m. The frequency dependence of $r(t)$ vs. f_m was similar to that of the family of spherical harmonics $Y_m^l(\theta,\phi)$ which indicated that spherical harmonic structures superposed on the captive bubbles originated from "l" states ranging from l=8

to l=11. Bubble radius vs. frequency behaviour appears to be intensity independent, with a linear dependence on the inverse frequency. No physical explanation for this could be provided.

The remaining process models are all based upon the keyhole collapse formulation presented by Kroos et al [25,26,27]. By first extending the model to include the effects of viscosity, collapse times for water and glycerol were calculated over a dimensionless temperature (T^*) range from 0-1, where 0 is room temperature and 1 is the boiling temperature of the liquid. Closing times for water are found to be weakly and monotonically dependent on fluid temperature while glycerol hole closure times exhibit much stronger temperature dependence which includes closing time minima near T^*=0.2. The glycerol collapse time minima were located such that plots of predicted fundamental mode frequency, f_0 vs. T^* for water and glycerol shared two common points. The initial (pre-collapse) radius of the cavity was found to have a strong effect in the computation of the closing time and because of this, the results were presented over a range of initial radii. With the exception of low (dimensionless) temperatures, the model predicts fundamental mode frequencies between 1 and 3.7kHz for both water and glycerol (see *Figure* 4.47). Furthermore, the model indicates that water and glycerol should exhibit identical fundamental mode frequencies at certain temperatures, and are never more than approximately 30% different from one another.

It was recognized that the temperature at the drill hole wall will in general be much higher than in the surrounding bulk fluid, and the model was recalculated, using high temperature values for surface tension and low temperature values for density and viscosity. The results (summarized in *Table* 4.6) predict fundamental mode frequencies between 150 and 300Hz for glycerol, and between 1250 and 3300Hz for water, depending on the initial drill hole radius. This two temperature form of the model effectively explains why resonance is observed in glycerol but not in water, however it predicts just one frequency for each drill hole radius.

The final iteration of the model makes a continuous band of resonant frequencies possible by introducing a small degree of taper into the drill hole wall. The modification is justified in terms of real drill hole geometry, and if each point along the axis is considered separately (based on the cylindrical model calculations), a continuum of collapse frequencies results.

6.3. Initiation of the Drill Hole

Drill hole initiation rates were studied for solid glycerol, liquid glycerol and acrylic. A simple model describing the depth vs. time ($z(t)$) behaviour was developed by

solving the expression for the velocity of the vapour front in *Equation* 1.1 for $z(t)$ assuming the laser beam follows a Beer Lambert exponential attenuation as it penetrates into the material. The expression for $z(t)$ contains three unknown parameters; the initial velocity (v_o), the beam attenuation coefficient (α), and the video synchronization offset time (t_o). These parameters could be determined by curve fitting to experimental $z(t)$ data and the surface laser intensity could subsequently be obtained in a straightforward manner from v_o.

Drilling into solid glycerol was first parameterized using the above model yielding an average α=250 m^{-1}, and v_o=0.75 m/s, resulting in a surface intensity of I_o=1.8×10^9 W/m^2.

Application of curve fitting to drilling into liquid glycerol yielded a poor fit, underestimating v_o by more than 10 times. This discrepancy is attributed to the much greater influence of convective mechanisms when drilling into liquids.

Curve fitting was also applied to the drilling of acrylic to study differences between the Lumonics VFA 1700 and Melles Griot CRF1200 lasers. The average attenuation coefficient was found to be α=117 m^{-1} for both lasers. From the calculations of v_o, beam intensities were computed and plotted relative to the recorded laser power. The data for the Melles Griot laser was taken at three separate power levels, and the intensity vs. power relationship demonstrates a linear dependence without an intercept, as

expected. The Lumonics laser drilling data was obtained at a single power level and hence no trend could be established. The Lumonics data point fell far above the trend line established by the Melles Griot experiments, indicating much higher intensity per watt than the Melles Griot laser. The exercise demonstrated clearly that using laser power as a baseline variable can be misleading, particularly in cases where more than one laser is used in a series of experiments.

6.4. Dynamic Behaviour

6.4.1. Drill Hole Dynamics

Glycerol was the only fluid which provided slow enough dynamic response to be captured using a high speed camera. The high viscosity associated with glycerol is presumed to be the factor which separates its dynamic behaviour from water and glycerol-water mixtures. The high speed camera allowed the initial development of a drill hole to be tracked and a model fitting the observations has been proposed in which radial perturbations of a cylindrical drill hole initially in equilibrium result in large localised radial growth of the drill hole (i.e. bubbles). Perturbations towards smaller radii experience restorative pressure from increased laser intensity due to the beam intensity distribution. When combined with the slower collapse dynamics of a high viscosity

liquid, the drill hole is more stable and permits the formation of large bubbles along the beam axis.

Time dependent dynamics in both low and normal gravity were studied by mapping the radial fluctuations of the drill hole as a function of time at fixed depths. A regular pattern emerged in which a single large scale bubble tends to dominate the hole profile. In normal gravity this bubble rapidly migrates to the surface due to its buoyancy and vents at the surface, momentarily providing an opening deep into the liquid. This venting bubble allows the laser beam to penetrate deep into the liquid where rapid vapourisation generates a new bubble nearer to the root of the drill hole. The process then repeats itself at a cycle period of about 0.2 seconds.

In low gravity, a similar process takes place, without the effect of buoyancy or hydrostatic pressure. This results in a much larger and slower moving bubble than in normal gravity and a cycle period of about 0.5 seconds.

6.4.2. Fluid Flow

Several distinctly different flow patterns have been identified in Section 5.3. By comparing these patterns one can identify the parameters responsible for fluid flow.

As we have seen, the difference in viscosity between liquids is primarily responsible for differing flow behaviour. In water and in a 66% glycerol – 34% water mixture in both normal and low gravity, a reverse reaction flow dominates the bulk fluid motion. The higher viscosity glycerol-water mixture naturally does not support nearly as deep a reverse flow as in water. In between the viscosity of 100% glycerol and 66% glycerol–34% water, the liquid no longer allows reverse reaction flow. At this stage, buoyancy becomes a factor in determining the bulk fluid motion. Viscous drag on bubbles attached to the drill hole act to draw surrounding fluid with them. In the presence of buoyancy (gravity), the bubbles move towards the surface, generating a bulk flow exactly opposed to the reaction flow observed in the other liquids. Under low gravity conditions, all flow is suppressed.

Insight into the effects of the solid/liquid phase boundary on the flow patterns can be obtained by comparing drilling in gelatin to that in pure water. In normal gravity drilling of gelatin, the deep expanding reaction flow plume seen in the water drilling is redirected by the phase boundaries into a symmetric recirculating flow consisting of two counter rotating toroids. In the low gravity drilling of gelatin, the lack of buoyancy acts to disrupt the symmetry of the flow pattern, resulting in an irregularly shaped molten region with a large amount of entrapped vapour near the root of the melt.

6.5. Improvements and Further Opportunities

6.5.1. Holographic Imaging and Fringe Analysis

The holographic imaging technique proved to be quite viable and stable both for ground and aircraft based experiments. Similarly, the fringe analysis technique demonstrated its capability to reduce *resolvable* interference fringes to isothermal contours. The restrictions of the technique amount to a problem of limited resolution. Isotherm results were of limited usefulness because they were restricted to regions radially removed from the proximity of the drill hole. Temperature distributions in the immediate vicinity of the drill hole were impossible to infer and unfortunately, it is this region which is of the greatest significance in determining the post processing material properties of the work piece.

In order to experimentally measure temperatures close to the drill hole, individual interference fringes must be resolved near to the drill hole wall. While this may prove too challenging, simply enhancing the imaging resolution would be a start. Data for the fused quartz data was recorded by CCD camera to an NTSC video recorder which has a resolution of 240×480 pixels. The camera was oriented in such a way that the 240 pixel resolution was in the direction perpendicular to the drill hole. Because of radial symmetry involved, this limits the entire temperature distribution (determined by the

fringes) to be mapped into a maximum of 120 pixels. While video based data acquisition has the advantage of recording information over a long period of time at 30 frames per second, this speed is not required in the case of holographic interferometry. Present day digital cameras have resolutions of 1200×1600 pixels and can easily be integrated into an experimental platform. If the wide aspect of the image frame were used in the radial direction, the effective fringe resolution in the radial direction would be improved by a factor of 6.6 times. In addition, the cylindrical symmetry of the process allows an increase in resolution by a factor of two, if the drill hole axis is offset to the camera's frame edge, rather than centered in the frame.

Another simple means of enhancing the resolution of the system is to zoom in on the region of interest. The holographic configuration on the LAMPS test bed was adjusted to capture the entire 25mm by 25mm holographic plate. Optics could be selected to allow imaging of just a small portion of the holographic plate. The drawback to this approach is that while imaging camera resolution increases, holographic camera resolution decreases. A better solution, though more complex would be to place a beam expanding telescope between the object and the holographic plate, acting as a zoom lens to the imaging camera, but also allowing the full resolution of the holographic plate to be used for generating the reference hologram.

The above recommendations all pertain to enhancing image resolution to achieve

better results. Temperatures near the drill hole wall approach that of the melting temperature of the material, and high temperature gradients are expected in this region. In order to be able to resolve individual fringes in a high temperature gradient region, interference fringes should be associated with large temperature differences. In effect, materials which exhibit extremely low (fringe to fringe) thermal resolution are better suited for resolving temperature fields close to the drill hole.

In Appendix A, *Equations* A.10 and A.11, the phase difference is shown to be linearly dependent on the overall temperature difference, the linear thermal expansion coefficient of the material, and the rate of change of the index of refraction with respect to temperature. Low melting temperature materials, or materials exhibiting reduced sensitivity to thermally induced optical path differences would lower the thermal resolution of the holography, resulting in increased fringe resolution close to the drill hole.

A final issue that needs to be considered to truly enhance the resolution of the holographic method is systematic error. Improving resolution aids little if the signal to noise ratio is not sufficiently high to make use of the resolution. Two sources of systematic error were identified within the holographic interferometry module. The first was related to the mechanical isolation of the testbed, which while generally only a minor issue for ground based and low gravity experiments, high-g experiments were rendered

unusable as a result of mechanical vibrations. Figure 6.1 shows a video frame of an interferogram while under a high-g load.

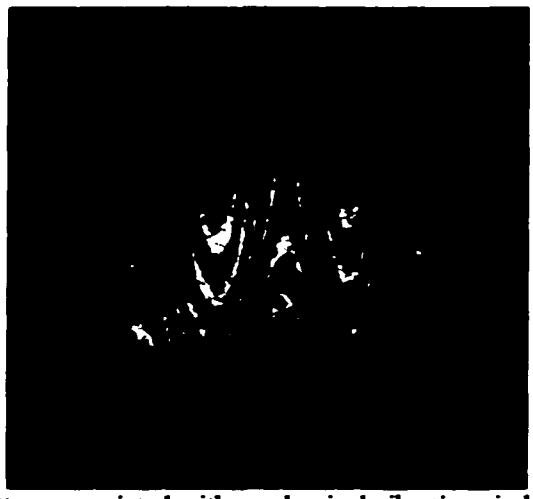


Figure 6.1 Distorted fringe pattern associated with mechanical vibrations induced in the system during the high-g maneuver.

The second source of systematic error comes from the holographic plate, which is extremely sensitive to microparticle contamination. Generally, any dust contamination on a holographic plate acts as a diffraction centre which takes the form of a small circular fringe within the true path difference fringe pattern. These defects can be seen in *Figures* 3.4-3.6. A much more contaminated interferogram is shown in Figure 6.2. This interferogram was the result of a holographic exposure during a flight in which a large number of particulates remained in the LAMPS enclosure. The particles were permanently entrapped in the holographic plate as a result of the thermal erasure process

utilized by the holographic camera.

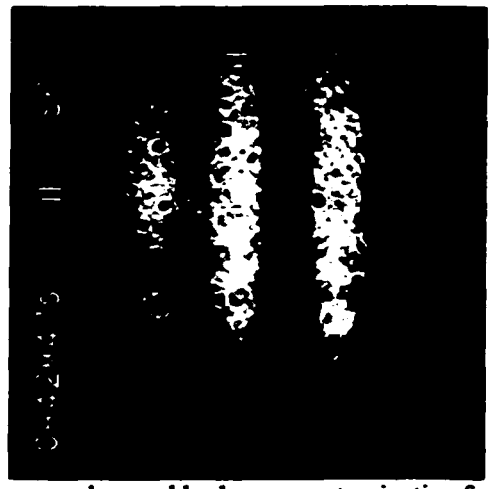


Figure 6.2 Holographic interferogram obscured by heavy contamination from dust particles.

The solution to the vibration problem involves improving the characteristics of the test bed isolation mounts to achieve isolation in low, normal, and high gravity environments. The contamination problem can only be solved by ensuring that the environment within the enclosure remains as clean as possible. The weakness is in the flight based fume extraction which uses the aircraft's overboard venting system, consisting of a 25mm diameter pipe. When the low volume flow of this system is combined with the 100mm aperture intake pipe, fume extraction is ineffective.

Reducing the intake aperture to 25mm and locating it as close as possible to the entry point of the drill hole would improve the efficiency of fume extraction. Even this

measure may not prove effective during the low gravity maneuver however, since there is no directional preference for the heated effluent from buoyancy. Some form of air knife could be employed to further protect the plate, however care would have to be taken to ensure that no ambient entrained flow was allowed to reach the surface of the plate.

6.5.2. Modulated Beam Drilling

Many aspects of the modulated beam experiments can be expanded or improved upon. Two independent series of experiments using different experimental apparati yielded two distinctly different behavioural responses in glycerol and water. Clarification of the systematic contributions to the observed behaviour would be necessary. Of all of the experimentation carried out throughout the research, the modulated beam drilling experiments were the only ones *not* carried out in a variable gravity environment. Replication of the modulated beam experiments in low gravity would determine if hydrostatic pressure (which is ignored in the models) alters the behaviour.

Acoustic recording of the emissions was problematic. Aside from the background and electronic noise issues dealt with in Chapter four, other systematic problems existed. The microphone was placed in a closed rectangular air space above the surface of the liquid. Acoustic damping foam lining the walls of the enclosure will have

reduced, but not entirely eliminated internal reflections in the enclosure. Vapour and spatter build up on the microphone may also alter the frequency response characteristics of the device. A better approach would be to use a submerged microphone (hydrophone). The hydrophone would still be susceptible to vessel reflections and resonance, however these would be at a great deal higher frequency than similar frequencies in air. The impulse response characteristic of the system could be measured and used to normalise the spectra associated with laser processing.

Electronically modulated drilling experiments provided the most stable frequencies, but were limited in bandwidth. Modulation frequency limitations associated with both electronic and mechanical modulation prevented definitive observation of a resonant transition in water drilling. Other laser manufacturers, (e.g. Trumpf, Synrad) provide pulse width modulated controlled output capable of more than 10kHz[18] which could make this possible.

Experimentation can easily progress to solids as well. With a relatively small amount of effort, a vessel could be designed that could contain frozen water or glycerol in such a way as to allow imaging and acoustic recording similar to the liquid experiments.

[18] Trumpf lasers can produce modulation output up to 90kHz, however the relative laser intensity modulation diminishes greatly above 10 kHz.

Both drilling and welding experiments could be performed with a modulated laser beam, making the research more relevant to industrial processes.

6.5.3. Drill Hole Dynamics

Pure glycerol provided the only venue for following the evolution and dynamics of the drill hole, due to its relatively slow dynamical response to laser irradiation. Even this required imaging at 500Hz to capture in detail. It would be of interest to image less viscous liquids with cameras capable of 1kHz or more framing rate. If drill hole dynamics still prove to be too fast for this framing rate, then higher concentration mixtures of glycerol-water could be used. Ideally the mixture would still be thin enough to exhibit reverse reaction flow. *Figure* 6.3 shows how the viscosity is altered by addition of water to pure glycerol. Aside from a pure water baseline, mixture data is only presented for mixtures from pure glycerol to 50% (weight fraction) glycerol.

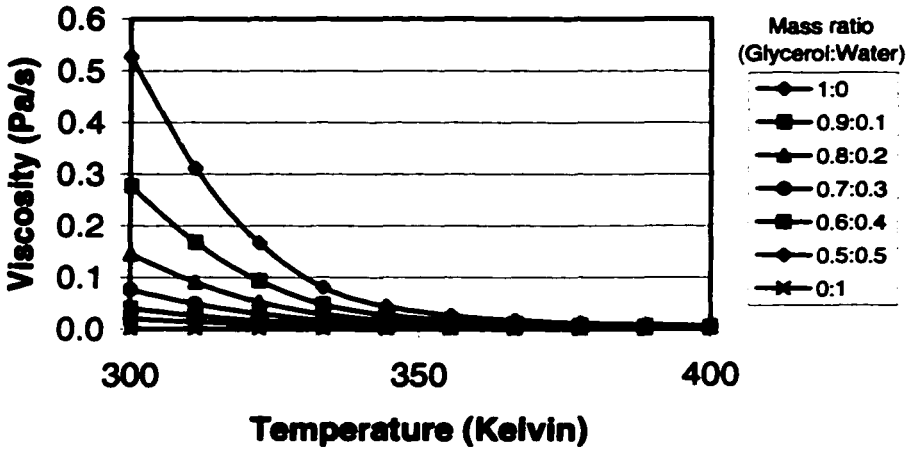


Figure 6.3 Viscosity dependence of glycerol – water mixtures (from [49]). Low temperature values are strongly effected by addition of water.

The adjustable nature of a glycerol-water mixture makes it an ideal tool for continued work on laser penetration processing dynamics. The viscosity could be varied to explore the transition region separating the downward (reaction) flow regime from the upward (viscous pump) flow regime. A continuously tunable viscosity opens up entire new resonance investigation opportunities with a modulated beam as well.

6.6. Closing Remarks

The variety of experimentation throughout the course of this research was broad,

yet the goal always remained the same: To further the basic understanding of the dynamics of laser penetration processing. To this end, numerous advances have been made.

The thermal dynamics of fused quartz drilling was experimentally measured in the first known application of real time differential holography to the problem and compared with a numerical model developed in prolate spheroidal coordinates. An analytical model developed in prolate spheroidal coordinates proved to be non-physical due to the simplifying assumptions required in the process of solving the problem. The numerical model fitted the experimental data reasonably well near the surface, but differences between model and experiment increased with increasing depth into the quartz. The mismatch is thought to arise primarily from using an isothermal boundary condition at the drill hole wall rather than an isoflux condition. The exercise nonetheless still represents the first known application of real time differential holographic interferometry to laser processing.

Important new advances into laser interaction mechanisms in a two phase system have been achieved through the various experiments performed on liquids. Stable structures observed in modulated beam glycerol drilling were successfully described with a drill hole collapse model.

Drill hole initiation into solids was effectively modeled using energy conservation

in conjunction with exponential beam attenuation along the length of the drill hole. A failure of the model to describe drill hole initiation in liquid glycerol served to highlight the differences in the drill hole initiation process for solids and liquids. The model also proved its use as a beam intensity diagnostic when applied to acrylic drill hole initiation.

Drilling experiments on glycerol, water, gelatin, and glycerol/water mixtures were compared which highlighted the relative effect of viscosity, gravity and solid phase boundaries on the dynamics of laser drilling. Descriptive models were presented which outline plausible mechanisms for various phenomena including drill hole initiation in glycerol, drill hole dynamics in glycerol, and bulk fluid flow around the drill hole.

The *comprehensive* description of laser penetration processing has continued to elude investigators, however the work in this thesis has significantly advanced the understanding of keyhole dynamics. Transparent dielectric materials, even in liquid form have provided a valuable tool for investigation of the dynamics associated with laser penetration processing. Given the number of opportunities cited above for further work, it appears that much more knowledge can yet be gained from these materials.

Bibliography

1. Maiman, T.H. *Nature* **187**, 493 (1960)
2. Duley, W.W. "Laser Processing and Analysis of Materials", Plenum (1983)
3. Steen, W. M. "Laser Material Processing", Springer-Verlag (1991)
4. Migliore, L. (ed.) "Laser Materials Processing", Marcel Dekker (1996)
5. Crafter, R.C. and Oakley, P.J. (eds.) "Laser Processing in Manufacturing", Chapman and Hall (1993)
6. LIW "Electron and Laser Beam Welding", Elsevier Science (1986)
7. Duley, W.W. "Laser Welding", John Wiley and Sons (1998)
8. Rykalin, N. Uglov, A.A. and Kokora, A. "Laser Machining and Welding", Franklin Book Co. (1978)
9. Dawes, C. "Laser Welding", Mcgraw Hill (1992)
10. Geskin and Leu "High Energy Beam Manufacturing Techniques", Amer. Soc. of Mech. Eng. (1989)
11. Grigoryants, A.G. "Basics of Laser Material Processing", CRC press (1994)
12. Anisimov, S. Khokhlov, V.A. "Instabilities in laser-matter interaction", CRC Press (1995)
13. Hannicke, L. "Laser technology within the Volvo Car Corporation", *Proc. 5th Lasers in Manufacturing* (1988)

14. Ferguson, N. "Report on laser hemming progect", *private correspondence between Magna ATC and Ford Advanced Vehicle Technology Group* (1999)

15. Waddell, W. Davies, G. M. "Laser welded tailored blanks in the automotive industry", *Weld Met. Fabrication*, March (1995)

16. Mueller, R. "The Effect of Low Gravity on Laser Keyhole Welding Dynamics", *York University PhD. Thesis*, (1994)

17. Hardy, S. C. "The Motion of Bubbles in a Vertical Temperature Gradient", *Journal of Colloid and Interface Science*, Vol. 69 No. 1 (1978)

18. Hughes, T.P. "Plasmas and Laser Light", John Wiley and Sons (1975)

19. Arata, Y. and Miyamoto, I. "Wall-Focusing effect of Laser beam", *Proc. 2nd Int. Symp. of JWS* (1975)

20. Swift-hook, D. T. and Gick, A. E. F. "Penetration welding with lasers: Analytical study indicates that present laser beam welding capabilities may be extended tenfold", *Welding Research Supplement*, November, (1973)

21. Duley, W.W. "CO_2 Lasers: Effects and Applications", Academic Press (1976)

22. Banas, C. "High Power Laser Welding", *Industrial Laser Annual Handbook*, 69-86 (1986)

23. Carslaw, H. C. and Jaeger, J. C. "Conduction of Heat in Solids", 2nd ed., Clarendon Press (1959)

24. Andrews, J. G. and Atthey, D. R. "Hydrodynamic limit to penetration of a material by a high power beam", *J. Phys. D: Appl. Phys.* **9**, 2181-2194 (1976)

25. Kroos, J. Gratzke, U, and Simon, G. "Towards a self-consistent model of the keyhole in penetration laser beam welding", *J. Phys. D: Appl. Phys.* **26**, 474-480 (1993)

26. Kroos, J. Gratzke, U, Vicanek, M. and Simon, G. "Dynamic behaviour of the keyhole in laser welding", *J. Phys. D: Appl. Phys.* **26**, 481-486 (1993)

27. Klein, T. Vicanek, M. Kroos, J. Decker, I. and Simon, G. "Oscillations of the keyhole in penetration laser beam welding". *J. Phys. D: Appl. Phys.* **27**, 2023-2030 (1994)

28. Dowden, J. Davis, M. and Kapadia, P. "Some aspects of the fluid dynamics of laser welding", *J. Fluid Mech.* **126**, 123-146 (1983)

29. Lindl, Widl, *Proc. Laser in der Fertigung München*, (1993)

30. Otto, A. Deinzer, G. and Geiger, M. "Control of Transient Processes During CO_2-Laser Welding", *SPIE Proc. Laser Material Processing* (1994)

31. Duley, W. W. and Young, W.A., *Journal of Applied Physics*, **44**, 4236, (1973)

32. Arata, Y. Abe, N. and Oda, T. "Beam Hole Behaviour During Laser Beam Welding", *Proc. ICALEO* (1983)

33. Mueller, R.E Duley, W.W. Maclean, S. Garneau M. Tryggvason, B. Evans, W.F.J. "Laser Welding of Plastics in Low and High Gravity Environments", *Journal of laser Applications* **1** (3), p22 (1989)

34. Mueller, R.E. Bird, J. and Duley, W.W. "Laser drilling into an absorbing liquid", *J. Appl. Phys.* **71** (2), p551, (1992)

35. Williams, R.K. "JSC Reduced Gravity Program Users Guide" *NASA Document* JSC-22803, NASA Washington, (1987)

36. Duley, W. W. and Mueller, R. E. "Laser materials processing in space", *Proc. 40th Intl. Astronautical Congress* (1989)

37. Anonymous, MELLLES GRIOT CRF-1200 sealed CO2 laser documentation.

38. Gu, H., *U. of Waterloo MSc. Thesis* (1995)

39. Arata, Y. Maruo, H. Miyamoto, I. and Takeuchi, S. "Dynamic Behaviour of Laser Welding", *Arata Transcripts, Doc.* IV-222-77 (1977)

40. Morse, P. Feshbach, H. "Methods of Theoretical Physics", McGraw-Hill (1953)

41. Boyce, W. E. and DiPrima, R. C. "Elementary Differential Equations and Boundary Value Problems", John Wiley and Sons, 3rd ed. (1977)

42. Teertstra, P. "Heat Conduction in Regions Surrounding Oblate Spheroidal Bodies", *U. of Waterloo MSc. Thesis* (1992)

43. Yovanovich, M. M. Course notes from U. of Waterloo Mech. Eng. 651, (1993)

44. ESCO Products Inc. "A1" fused quartz data sheets.

45. Anonymous, "Surfer Topographic generation software", Ver.4.12, Golden Software, (1989)

46. Duley, W. W. Olfert, M. Bridger, P. and Mao, Y. L. "What CO_2 Laser Welding of Liquids Tells Us About Penetration Welding of Metals", *Proc. ICALEO* (1992)

47. Duley, W. W. Olfert, M. Bridger, P. Bird, J. and Mueller, R. "Basic Physical Phenomena During Laser Processing of Materials": *Proc. LAMP* (1992)

48. Landau, L.D. and Lifshitz, E.M. "Fluid Mechanics", Pergamon Press (1959)

49. Anonymous, "Prode PPP Material property calculation software", Ver.1.1.d, *http://www.prode.com*

50. Weast, R.C. (Ed.) "Handbook of Chemistry and Physics", 50th ed. CRC press (1969)

51. Ried, R. C. Prausnitz, J. M. and Sherwood, T. K. "The Properties of Gases and Liquids", 3rd ed. McGraw-Hill (1977)

52. Vargaftik, N. B. "Tables on the thermophysical properties of liquids and gases- in normal and dissociated states", 2nd Ed. John Wiley & Sons

53. Dunn, I. Bridger, P. and Duley, W.W. "Observation of stable waveguide propagation for CW CO_2 laser radiation in liquid water", *J. Phys. D., Appl. Phys.* (in press 1993)

54. Miyamoto, I. Maruo, H. Arata, Y. "Intensity profile measurements of focused CO_2 laser beam using PMMA", *Proc. ICALEO'84*, Laser Institute of America, Toledo Ohio, p313, (1984)

55. Meyerhofer, D. "Measurement of the beam profile of a CO_2 laser", *IEEE Journal of Quantum Electronics* QE-4: 969-970

56. Whitehouse, D. Nilsen, C. "Plastic burn analysis (PBA) for CO_2 laser beam diagnostics", *Proc. ICALEO,* Laser Institute of America, Toledo Ohio (1990)

57. Rayleigh, Lord "On the Instability of Cylindrical Fluid Surfaces", *The London, Edinburgh and Dublin Philisophical Magazine* **34** 177 (1892)

58. Arata, Y. Abe, N. and Oda, T. "Beam Hole Behaviour during Laser Beam Welding", *Proc. ICALEO'83* (1983)

59. Becker, F. Mier, G. E. A. Wegner, H. "Fringe Pattern Analysis of Interferometric Fringes", *Appl. Opt.* **20**, 18 (1981)

60. Vest, C. M. "Interferometry of strongly refracting axisymmetric phase objects", *Applied Optics,* **14**, No 7, (1975)

61. Bracewell, R.N. "The Fourier Transform and its Applications", McGraw-Hill (1986)

62. Bradley, J. W. "Density determination from axisymmetric iterferograms", *AIAA Journal,* **6**, 6, (1968)

63. Hansen, E. W. and Law, P. L. "Abel Inversion by Kalman Filtering", CH1945-5/84/0000-0308, *IEEE,* (1984)

64. Hansen, E. W. and Law, P.L. "Recursive Methods for Computing the Abel Transform and its Inverse", *JOSAA,* **12**, 4, (1985)

65. Balasubramanian, R. "The application of the least squares finite element method to Abel's integral equation", *Int. J. for Num. Meth. in Engineering,* **14**, 201-209 (1979)

66. Kalal, M. and Nugent, W.C. "Abel inversion using fast Fourier transform", *Appl. Opt.* **27**, 10, 1956-1959 (1988)

67. Bennet, F. D. Carter, W. C. and Bergdolt, V.E. *J. Appl. Phys.* **23**, (1952)

68. Merzkirtch, W. and Erdman, W. *Appl. Phys.* **2**, (1973)

69. Vest, C. M. "Holographic Interferometry", John Wiley & sons (1979)

70. Nestor, O. H. and Olsen, H. N. "Numerical methods for reducing line and surface probe data", *SIAM Rev.* **2**, (1960)

71. Cremers, C. J. and Birkebak, R. C. "Applications of the Abel Integral Equation to Spectrographic Data", *Appl. Opt.* **5**, 1057-1064 (1962)

72. Edels, H. Hearne, K. and Young, A. "Numerical solutions to the Abel integral equation", *J. Math. Phys.* **41**, 62-75 (1962)

73. Langois, P. Bouchard, M. Harvey, E. Gingras, D. and Pawluczyk, R. "Development of a Laser Material Processing Program for research in Microgravity (LAMPS-Phase IIb): Optical Visualization System", National Optics Institute document INO 91-0902-2D0RFI (1992)

74. Beyer, W. H. "CRC Standard Mathematical Tables", CRC Press (1981)

75. Jahnke, E. "Tables of Functions With Formulae and Curves", Dover (1945)

Appendix A

Holographic Data Reduction to Temperature Field Information

A.1 GENERAL FRINGE INTERPRETATION

In general, given the interferometry setup described in chapter 2, thermal disturbances of the object will generate a two dimensional interference pattern which is recorded by a camera. Defining this fringe plane as the x-y plane, the expression for the intensity distribution within the two dimensional fringe pattern is given by [59]:

$$I(x,y) = I_o(x,y) + I_1(x,y)\cos\left[\frac{2\pi}{\lambda}\Delta\Phi(x,y)\right] \qquad \text{A.1}$$

where I_o is associated with an incoherent background illumination, I_1 is the product of the square roots of the reference and object beam intensities, and $\Delta\Phi$ is the optical path difference (OPD) between the reconstructed original beam and the current perturbed

beam. We can express the OPD in terms of the index of refraction of the perturbed medium as follows:

$$\Delta\Phi(x,y) = \int_{z1}^{z2} \{n(x,y,z) - n_0\} dz \qquad \text{A.2}$$

and for destructive interference (i.e. dark fringes) for example we would have:

$$\Delta\Phi(x,y) = \frac{2m-1}{2}\lambda \qquad \text{A.3}$$
$$m = \pm 1, \pm 2, \pm 3, \cdots$$

In reality, the OPD not only depends on the change of index of refraction, but also on small physical dimension changes induced by thermal dilation of the material. Consider the one dimensional model shown in figure A.1 in which a thickness t of material with an undisturbed (room temperature) index of refraction n_o is heated to some temperature $T>T_o$. The index of refraction of the heated material is now n and the thickness is now $t+\delta t$. The optical paths of the undisturbed and disturbed beams are only different from each other over the thickness $t+\delta t$.

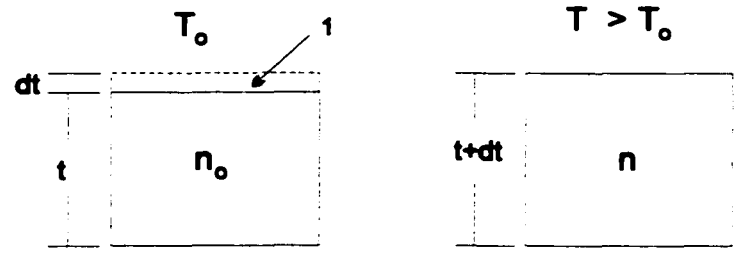


Figure A.1. Simple one dimensional model of material undergoing expansion as a result of uniform heating.

The optical paths of the undisturbed and disturbed beams are respectively:

$$\Phi_0 = n_0 t + 1 \cdot \delta t \qquad \text{A.4}$$

$$\Phi_1 = nt + n \cdot \delta t \qquad \text{A.5}$$

where it is assumed that the index of refraction of the medium surrounding the disturbed medium is unity. The OPD is thus given by:

$$\Delta\Phi = \Phi_1 - \Phi_2 = (n - n_0)t + (n - 1)\delta t \qquad \text{A.6}$$

Assuming that the change in index of refraction is small, we can rewrite the index in the disturbed medium as $n = n_0 + \delta n$, with $\delta n << n_0$, and substitute into eqn. A.6:

$$\Delta\Phi \cong (n - n_0)t + (n_0 - 1)\delta t \qquad \text{A.7}$$

where we have neglected second order terms. The expansion δt can be expressed in terms of the linear thermal expansion coefficient c as:

$$\delta t = ct(T - T_0) = ct\delta T \qquad \text{A.8}$$

Now we use the fact that δn is very small and write the index as:

$$n = n_0 + \delta n \cong n_0 + \frac{dn}{dT}\delta T \qquad \text{A.9}$$

Using equations A.8 and A.9 we can write equation A.7 in terms of the temperature difference and the index of refraction gradient:

$$\Delta\Phi = K(T - T_0)t \qquad \text{A.10}$$

where

$$K = \frac{dn}{dT} + c(n_0 - 1) \qquad \text{A.11}$$

This simple model can easily be extended to general temperature distributions $T(x,y,z)$ and geometry as follows:

$$\Delta\Phi(x,y) = K\int_{z1}^{z2}[T(x,y,z) - T_0]dz \qquad \text{A.12}$$

where the limits $z1$ and $z2$ on the integral denote the boundaries of the disturbed zone and are generally dependent on x and y. Beyond the boundaries of the disturbed zone however, the integrand is zero and therefore mathematically, the limits $z1$ and $z2$ can be extended to $\pm\infty$.

A.2 AXISYMMETRIC PHASE OBJECTS

The interference pattern generated by the thermal processing of fused quartz arises from path differences introduced to the object beam by axisymmetric temperature fields which alter the local index of refraction in the quartz. If we assume that the object is a phase object, (meaning that refraction is negligible and the light only experiences phase changes), then equation A.12 remains valid [19]. Figure A.2 shows the geometry of how ray of light traverses an axisymmetric phase object.

[19]Although in general, this assumption may not be valid, it has been demonstrated [60] that even strongly refracting systems yield accurate estimates of the temperature field as long as the camera which records the interferogram is focused on the center plane of the phase object. This was the case in our experiments.

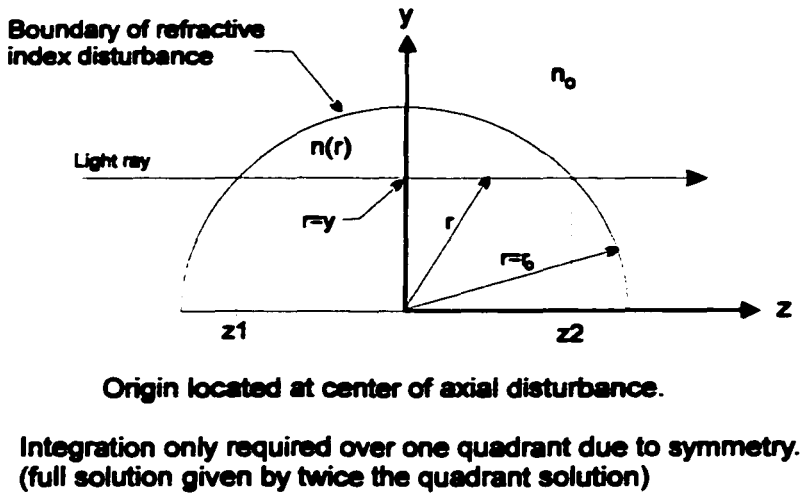


Figure A.2. Diagram showing geometry of a light ray traversing an axisymmetric index of refraction (temperature) disturbance.

The symmetry is denoted about the x axis with the ray traveling in the z direction. The boundary of the disturbance is denoted by the semicircle of radius r_o. Let us introduce the following change of variables into eqn. A.12:

$$z = \sqrt{r^2 - y^2} \qquad \text{A.13}$$

and hence,

$$dz = \frac{rdr}{\sqrt{r^2 - y^2}} \qquad \text{A.14}$$

Substitution into equation A.12 gives:

$$\Delta\Phi(x,y) = 2K\int_{r=y}^{r=r_o} \frac{T(r) - T_0}{\sqrt{r^2 - y^2}} rdr \qquad \text{A.15}$$

As before, since the integrand vanishes for $r > r_o$, we can replace the upper limit of the integral in eqn. A.15 with infinity:

$$\Delta\Phi(x,y) = 2K\int_{r=y}^{r=\infty} \frac{T(r)-T_0}{\sqrt{r^2-y^2}} r dr \qquad \text{A.16}$$

It should be noted that the x dependence is not explicit in the above equations as they are valid for any plane x = *constant*. The integral in equation A.16 is recognized as the Abel transform [61] of $T(r)$ - T_0. Fortunately, inversion formulas are known for the Abel transform [62] which allow us to express the unknown temperature difference as a function of the OPD which is directly attainable from the interferogram. Inversion of equation A.16 gives:

$$T(r)-T_0 = -\frac{1}{\pi K}\int_{y=r}^{r_0} \frac{\frac{d(\Delta\Phi)}{dy}}{\sqrt{r^2-y^2}} dy \qquad \text{A.17}$$

A.3 IMPLEMENTATION OF SOLUTION (NOI)

The nature of the interferogram itself limits the knowledge of the OPD to a discrete number of locations. Numerous techniques have been developed involving either numerical methods [63..66] or data approximation schemes [67..72] which allow solution of equation A.17. The technique employed by the National Optics Institute involves curve fitting to experimental data [73]. The OPD from equation A.3 is rewritten in terms of the fringe shift $\delta(y)$:

$$\Delta\Phi = \lambda\delta(y) \qquad \text{A.18}$$

Substituting for $\Delta\Phi$ in equation A.17 we then have:

$$T(r)-T_0=-\frac{\lambda}{\pi K}\int_{y=r}^{r_0}\frac{\frac{d\delta}{dy}}{\sqrt{r^2-y^2}}dy \qquad \text{A.19}$$

The function $\delta(y)$ can be represented by a polynomial of order M-1:

$$\delta(y)=\sum_{k=1}^{M}a_k y^{k-1} \qquad \text{A.20}$$

which when differentiated, is given by:

$$\frac{d\delta}{dy}=\sum_{k=1}^{M}(k-1)a_k y^{k-2} \qquad \text{A.21}$$

When equation A.21 is substituted into equation A.19, we have:

$$T(r)-T_0=-\frac{\lambda}{\pi K}\sum_{k=1}^{M}(k-1)a_k\int_{y=r}^{r_0}\frac{y^{k-2}}{\sqrt{y^2-r^2}}dy \qquad \text{A.22}$$

The general solution of the integral in eqn. A.22 can be obtained by consultation of standard mathematical tables [74].

Even powers of y:

$$\int_{y=r}^{r_0}\frac{y^{2m}}{\sqrt{y^2-r^2}}dy=\frac{(2m)!}{2^{2m}(m!)^2}\left[\sqrt{r_0{}^2-r^2}\sum_{j=1}^{m}\frac{j!(j-1)!}{(2j)!}(r^2)^{m-1}(2r_0)^{2j-1}+r^{2m}\ln\left(\frac{r_0+\sqrt{r_0{}^2-r^2}}{r}\right)\right] \qquad \text{A.23}$$

Odd powers of y:

$$\int_{y=r}^{r_0}\frac{y^{2m+1}}{\sqrt{y^2-r^2}}dy=\left[\sqrt{r_0{}^2-r^2}\sum_{j=0}^{m}\frac{(2j)!(m!)^2}{(2m+1)!j!}(4r^2)^{m-1}r_0{}^{2j}\right] \qquad \text{A.24}$$

Where the index m = 0, 1, 2, 3.... in both equations. A.23 and A.24. The full solution was thus implemented from eqn. A.22, with equations. A.23 and A.24 substituted

appropriately for even and odd powers of y. Due to the rather complex nature of the calculations[20], the reduction of the interferometry data was carried out on Sun workstations.

[20]In fact, the solution of the Abel transformation entails only part of the computing requirement for full analysis of the data. Considerable computing resources are involved in first reducing the grayscale interferograms to contour fields indicating the families of optical path differences.

Appendix B

Prolate Spheroidal Coordinates

The prolate spheroidal coordinate system (consisting of coordinates η, θ, ψ) can be generated from the more familiar circular cylindrical coordinates r, ψ, z through the following conformal transformation:

$$w = z + ir = a\cosh(\eta + i\theta) \qquad \text{B.1}$$

with a defined as positive. By expanding the hyperbolic cosine and equating real and imaginary terms, we obtain the following expressions:

$$\begin{aligned} z &= a\cosh\eta\cos\theta \\ r &= a\sinh\eta\sin\theta \end{aligned} \qquad \text{B.2}$$

This then relates to Cartesian coordinates as follows:

$$\begin{aligned} x &= a\sinh\eta\sin\theta\cos\psi \\ y &= a\sinh\eta\sin\theta\sin\psi \\ z &= a\cosh\eta\cos\theta \end{aligned} \qquad \text{B.3}$$

The variables θ, and ψ are easily eliminated from eqns. B.3 to obtain:

$$\frac{x^2}{(a\sinh\eta)^2}+\frac{y^2}{(a\sinh\eta)^2}+\frac{z^2}{(a\cosh\eta)^2}=1 \qquad \text{B.4}$$

For constant a and η, we can readily see that eqn. B.4 represents an ellipsoid of revolution about the z axis. Furthermore, since $\cosh\eta > \sinh\eta$ for all values of η, we see that the shape of the ellipsoid is indeed prolate. Denoting the minor semi-axis as b, and the major semi-axis as c, we can easily deduce the following relation for the constant a:

$$a^2 = b^2 - c^2 \qquad \text{B.5}$$

We can also readily express η in terms of the semi-axes as follows:

$$\eta = \tfrac{1}{2}\ln\frac{b+c}{b-c} \qquad \text{B.6}$$

Alternatively, had we eliminated η and ψ from eqns. B.3, we would have found that θ = constant gives rise to hyperboloids of two sheets. θ ranges from 0 to π in an analogous manner to the θ variable in spherical coordinates.

Finally, the variable ψ is not effected by the conformal transformation at all and retains the same definition as in the circular cylindrical coordinate frame. The range is from 0 to 2π with 0 representing the semi-infinite half plane extending along the positive

x axis. *Figure* B.1 shows families of θ = constant and η = constant contours in the $\psi = 0,\pi$ plane.

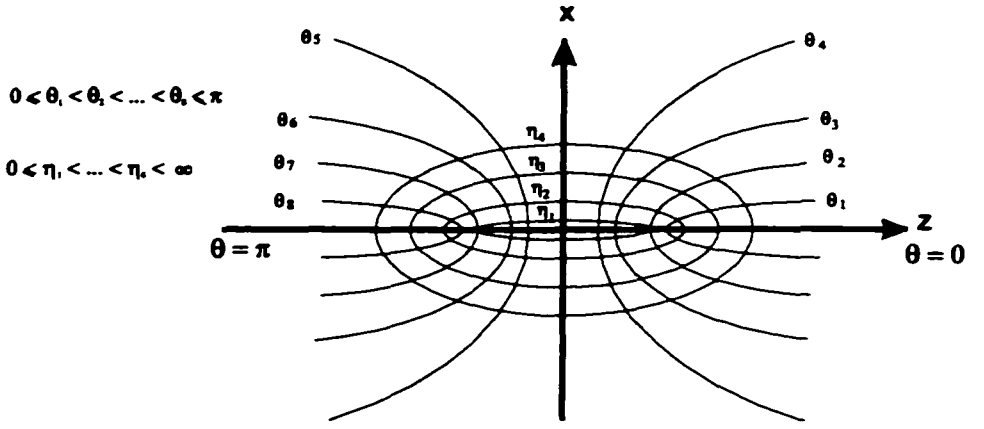


Figure B.1. Contours associated with constant η prolate spheroids, and constant θ hyperboloids, viewed in the x-z plane.

Appendix C

Analytical Solution of Heat Conduction in Prolate Spheroidal Coordinates

The general approach taken in solving multivariable heat conduction problems involves a technique known as separation of variables. It is assumed that the temperature function can be separated into a product of single variable functions. The time dependence is factored out first:

$$T(\eta,\theta,t)=U(\eta,\theta)\phi(t) \qquad \text{C.1}$$

Substitution of *Equation* C.1 into *Equation* 3.2 gives:

$$\frac{\nabla^2 U}{U}=\frac{1}{\alpha\phi}\frac{d\phi}{dt}=\pm\lambda^2 \qquad \text{C.2}$$

where the equality of two independent functions implies that they must be a constant, $\pm\lambda^2$ and mathematically either sign is possible. The reality governing the heat flow however indicates that the negative sign is the physically correct choice. Thus, *Equation* C.2 can be broken into the following two differential equations:

$$\frac{d\phi}{dt} + \lambda^2\alpha\phi = 0 \qquad \text{C.3}$$

$$\nabla^2 U + \lambda^2 U = 0 \qquad \text{C.4}$$

Equation C.3 can immediately be solved to obtain:

$$\phi(t) = c_t e^{-\alpha\lambda^2 t} \qquad \text{C.5}$$

where c_t is some constant.

To solve *Equation* C.4, we assume that we can also separate the spatial dependence into a product of single variable functions:

$$U(\eta,\theta) = H(\eta)\Theta(\theta) \qquad \text{C.6}$$

By substituting *Equation* C.6 into *Equation* C.4 with the use of the simplified Laplacian used in *Equation* 3.4, the following two ODE's are generated:

$$\frac{d}{d\xi}\left[(1-\xi^2)\frac{dH}{d\xi}\right] + (\beta - \lambda^2 a^2 \xi^2)H = 0 \qquad \text{C.7}$$

$$\frac{d}{d\mu}\left[(1-\mu^2)\frac{d\Theta}{d\mu}\right] + (\beta - \lambda^2 a^2 \mu^2)\Theta = 0 \qquad \text{C.8}$$

where β is the second separation constant, and we have made the substitution $\xi = \cosh\eta$,

and $\mu = \cos\theta$. By making the substitution $\beta = p(p + 1)$, *Equations* C.7 and C.8 are recognized as Legendre equations, having as solutions the associated Legendre functions:

$$H = AP_p(\lambda a, \xi) + BQ_p(\lambda a, \xi) \qquad \text{C.9}$$

$$\Theta = CP_p(\lambda a, \mu) + DQ_p(\lambda a, \mu) \qquad \text{C.10}$$

where $P_p^{\lambda a}(x)$, and $Q_p^{\lambda a}(x)$, are associated Legendre functions of the first and second kind respectively and A, B, C, D are constants.

In order to complete the solution, the boundary conditions given in *Equations* 3.5-3.8 will need to be re-expressed in terms of the new variables. Furthermore, because the Legendre functions are easier to deal with when their arguments lie within the range $-1 \le x \le 1$, further normalisation of the variables will first be performed. Since $\mu = \cos\theta$ already lies within the range, no further normalisation is required for this variable. In the case of $H(\xi)$, we can perform a very simple normalisation of the form:

$$\xi^* = \frac{\xi}{\cosh a}, \qquad \frac{1}{\cosh a} \le \xi^* \le 1 \qquad \text{C.11}$$

where in making this somewhat arbitrary normalisation, we have limited the range of η to $0 \le \eta \le a$. Effectively, this limits the validity of the solution to short times, where one can still assume that $T(\eta=a) = T_\infty$.

Extending the normalisation to the temperature variable as well, the dimensionless temperature is introduced as:

$$T^* = \frac{T - T_\infty}{T_0 - T_\infty}, \qquad 0 \le T^* \le 1 \qquad \text{C.12}$$

where T is the absolute temperature, T_∞ is the infinite field absolute (room) temperature, and T_0 is the drill hole wall temperature. The boundary conditions then transform in the new variables to:

$$\left.\frac{\partial T^*}{\partial \mu}\right|_{\mu=0} = 0 \quad \text{, or} \quad \left.\frac{\partial \Theta}{\partial \mu}\right|_{\mu=0} = 0 \qquad \text{C.13}$$

$$\left.\frac{\partial T^*}{\partial \mu}\right|_{\mu=\pm 1} = 0 \quad \text{, or} \quad \left.\frac{\partial \Theta}{\partial \mu}\right|_{\mu=\pm 1} = 0 \qquad \text{C.14}$$

$$T^*|_{\xi=1} = 0 \quad \text{, or} \quad H|_{\xi^*=1} = 0 \qquad \text{C.15}$$

$$T^*|_{\xi=1/\cosh a} = 1 \text{ , or} \quad H|_{\xi^*=1/\cosh a} = c_H \qquad \text{C.16}$$

where the term c_H in *Equation* C.16 is some constant.

Let us consider the μ dependent equation first. Since $\Theta(\mu)$ is given by Legendre functions (*Equation* C.9) we have a relationship for their derivatives which is:

$$(1-x^2)\frac{d}{dx}P_n^m(x) = (n+1)xP_n^m(x) - (n-m+1)P_{n+1}^m(x) \qquad \text{C.17}$$

with a similar expression for Q_n^m. However, $Q_n^m(\mu)$ becomes unbounded at $\mu = 1$, as does its derivative, and hence we must have the constant $D = 0$ in *Equation* C.10 to satisfy the boundary condition of *Equation* C.14.

The resulting form for the $\Theta(\mu)$ is then $\Theta(\mu) = CP_n^m(\mu)$, and consideration of the

boundary conditions of *Equation* C.13 and C.14 further allows constraints to be placed on the parameters m, and n. The boundary conditions imply that the derivative of $P_n^m(\mu)$ must vanish at $\mu = 1$ and $\mu = 0$. At $\mu = 1$ this requirement can be satisfied if m and n are integers and $n \geq m$. At $\mu = 0$, the first term of *Equation* C.17 vanishes leaving the expression:

$$\frac{d}{dx} P_n^m(\mu)\Big|_{\mu=0} = \frac{(n-m+1)}{1-\mu^2} P_{n+1}^m(\mu)\Big|_{\mu=0} = 0 \qquad 3.26$$

The term $1 - \mu^2$ in the denominator gives rise to a singularity at $\mu = 1$ *unless* the Legendre function can be written as $P_{n+1}^m(\mu) = (1-\mu^2) f(\mu)$, where the function $f(\mu)$ exists at $\mu = 1$. In order to satisfy the homogeneity of *Equation* C.18, we require either $f(\mu)\big|_{\mu=0} = 0$, or $n - m + 1 = 0$, with the latter possibility being precluded by the constraints already placed on m and n. The function f will satisfy the constraints imposed on it if it can be written as $f(\mu) = \mu \cdot g(\mu)$, where $g(\mu)$ is a function which is bounded at $\mu=0$. The Legendre function satisfying the above constraints can thus be written as:

$$P_{n+1}^m(\mu) = (1-\mu^2) \cdot \mu \cdot g(\mu) \qquad C.19$$

To simplify the problem as much as possible, it will be assumed that the solution can be represented by the lowest order Legendre function having the form of *Equation* C.19. To this end, if one restricts the parameters n and m to the condition $n=m$ then $P_n^m(\mu)$ can be

expressed in a simplified form given by [75]:

$$P_n^n(\mu) = \frac{(2n)!}{2^n n!}(1-\mu^2)^{\frac{n}{2}} \qquad \text{C.20}$$

which when differentiated yields:

$$\frac{d}{d\mu}P_n^n(\mu) = \frac{-n(2n)!}{2^n n!}\mu(1-\mu^2)^{\frac{n}{2}-1} \qquad \text{C.21}$$

It is immediately clear upon inspection of *Equation* C.21 that Legendre functions of the form specified in *Equation* C.20 satisfy the boundary conditions given in *Equations* C.13 and C.14 for all values of $n \geq 2$. The simplest non-constant solution is then given by $P_2^2(\mu)$ and therefore the solution can be written as:

$$\Theta(\mu) = CP_2^2(\mu) = c_\Theta(1-\mu^2) \qquad \text{C.22}$$

where c_Θ is some constant yet to be determined.

The solution of the radial-like function $H(\xi^*)$, proceeds in a similar manner to the theta function solution. When the boundary condition of *Equation* C.16 is imposed on the general solution (*Equation* C.9), the unbounded behaviour of $Q_n^m(1)$ implies that the constant B of *Equation* C.9 must be zero, leaving behind the following:

$$H(\xi^*) = AP_n^m(\xi^*) \qquad \text{C.23}$$

Since both of the spatial solutions are expressed in terms of the same separation constants which are related to m and n, the same constraints arrived at in the previous solution will

be applied to the radial-like solution. Namely, the simplest solution corresponding to n=m=2 will be assumed, yielding:

$$H(\xi^*) = AP_2^2(\xi^*) = 3A(1-\xi^{*2}) \qquad \text{C.24}$$

Finally, applying the boundary condition of *Equation* C.16, the solution can be written as

$$H(\xi^*) = \frac{C_H}{1-(\frac{1}{\cosh a})^2}(1-\xi^{*2}) \qquad \text{C.25}$$

Combining the three solutions from *Equations* C.5, C.22, and C.25, the full solution can be written as:

$$T(\xi^*, \mu, t) = \frac{C_H C_\Theta C_t}{1-(\frac{1}{\cosh a})^2}(1-\xi^{*2})(1-\mu^2)e^{-\alpha\lambda^2 t} \qquad \text{C.26}$$

Recalling the definitions of ξ^* and μ in terms of η and θ, *Equation* C.26 can be rewritten,

$$T(\eta, \theta, t) = \frac{C_H C_\Theta C_t}{1-(\frac{1}{\cosh a})^2}(1-(\frac{\cosh\eta}{\cosh a})^2)(1-\cos^2\theta)e^{-\alpha\lambda^2 t} \qquad \text{C.27}$$

In principle, the "constant" term in *Equation* C.27 can now be solved for using the isothermal boundary condition of *Equation* 3.8, however upon setting η=0 in *Equation* C.27, it becomes clear that there is no way of satisfying the boundary condition for all time and theta values. Even if the theta dependence were removed, the solution still intrinsically depends on a separate and independent time factor.

The solution arrived at analytically describes a static spatial distribution of the temperature field which is uniformly scaled by the time dependent solution which is

clearly non physical. During the course of the solution, several assumptions were made to simplify the mathematics as much as possible, of which one or more may have destroyed the realisation of a solution. Unfortunately, the weakest assumption was likely the very first assumption, that of the separability of $T(\eta, \theta, t)$. The implication of a separable temperature field function is that the temperature field can be described by a static spatial field globally scaled by a temporal function. An analytical solution to the transient heat flow problem therefore does not exist.